

AD-A151 978

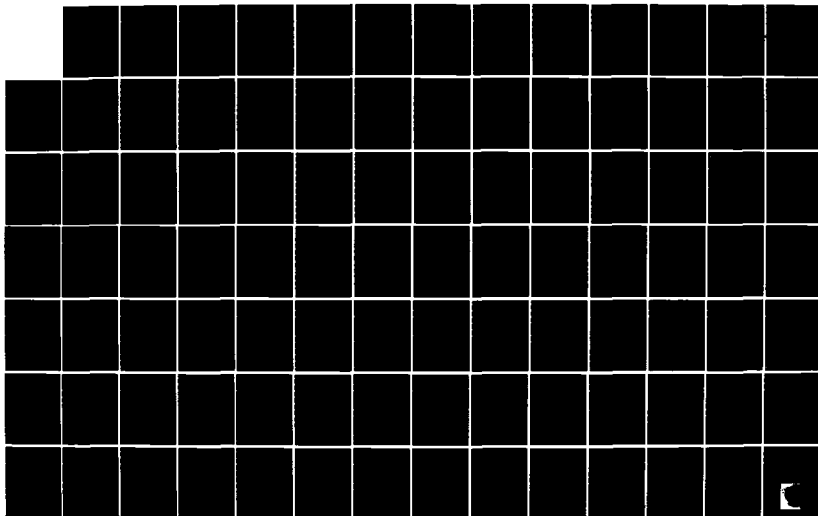
MECHANICAL ASPECTS OF INTERFACES AND SURFACES IN
CERAMIC CONTAINING SYSTEMS(U) CALIFORNIA UNIV BERKELEY
DEPT OF MATERIALS SCIENCE AND MINERA.

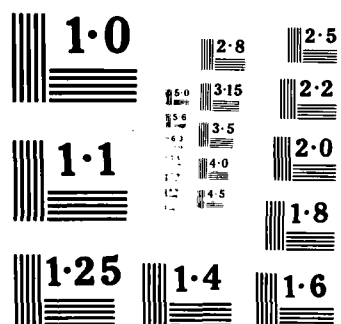
1/3

UNCLASSIFIED

A G EVANS ET AL. 14 DEC 84 N00014-81-K-0362 F/G 20/11

ML





2

AD-A151 978

MECHANICAL ASPECTS OF INTERFACES AND SURFACES IN CERAMIC CONTAINING SYSTEMS

Annual Report to
Office of Naval Research
Contract No.: N00014-81-K-0362
January 1, 1984 - December 31, 1984

by

A. G. Evans
University of California
Berkeley, California 94720

and

Z. B. Ahmad, P. W. R. Beaumont, E. D. Case,
M. D. Drory, K. T. Faber, Y. Fu, D. G. Gilbert,
C. H. Hsueh, D. Johnson-Walls, D. B. Marshall,
M. Rühle and S. Williams

DTIC FILE COPY



This document has been approved
for public release and sale; its
distribution is unlimited.

85 03 06 016

| REPORT DOCUMENTATION PAGE | | READ INSTRUCTIONS BEFORE COMPLETING FORM |
|--|-----------------------|---|
| 1. REPORT NUMBER | 2. GOVT ACCESSION NO. | 3. RECIPIENT'S CATALOG NUMBER |
| 4. TITLE (and Subtitle) Mechanical Aspects of Interfaces and Surfaces In Ceramic Containing Systems | | 5. TYPE OF REPORT & PERIOD COVERED Annual Report Jan. 1, 1984 - Dec. 31, 1984 |
| | | 6. PERFORMING ORG. REPORT NUMBER |
| 7. AUTHOR(s) A. G. Evans | | 8. CONTRACT OR GRANT NUMBER(s) N00014-81-K-0362 |
| 9. PERFORMING ORGANIZATION NAME AND ADDRESS Dept. of Materials Science and Mineral Engineering University of California Berkeley, California 94720 | | 10. PROGRAM ELEMENT PROJECT, TASK AREA & WORK UNIT NUMBERS |
| 11. CONTROLLING OFFICE NAME AND ADDRESS Office of Naval Research, Code 471 Arlington, VA 22217 | | 12. REPORT DATE December 14, 1984 |
| | | 13. NUMBER OF PAGES |
| 14. MONITORING AGENCY NAME & ADDRESS (if different from Controlling Office) | | 15. SECURITY CLASS. (of this report) Unclassified |
| | | 15a. DECLASSIFICATION/DOWNGRADING SCHEDULE |
| 16. DISTRIBUTION STATEMENT (of this Report) See distribution list. Do not release to NTIC | | |
| 17. DISTRIBUTION STATEMENT (of the abstract entered in Block 20, if different from Report) | | |
| 18. Supplementary Notes | | |
| 19. KEY WORDS (Continue on reverse side if necessary and identify by block number) Ceramic matrix composites, metal/ceramic bonded systems, particulate toughened polymers, interface bonding, interface friction, crack blunting, edge effects, fracture toughness, matrix cracking, indentation fracture, metal/ceramic interfaces. <i>behavior</i> | | |
| 20. ABSTRACT (Continue on reverse side if necessary and identify by block number) The mechanical behavior of various multicomponent materials have been investi- gated. The systems studied include ceramic matrix composites, metal/ceramic bonded systems and polymer particulate composites. Experimental observations of fracture behavior have been used to develop criteria that identify the fracture parameters pertinent to structural design. For example, the matrix cracking strength and the ultimate tensile strength have emerged as important parameters in ceramic composite failure. Micromechanics models of mechanical behaviors have also been developed, whenever experimental knowledge | | |

20. ABSTRACT (continued)

sufficiently characterizes the important physical features. Matrix cracking in composites and edge effects in metal/ceramic bonded systems are examples of phenomena that have been comprehensively modelled.

Wignalls - applied Research included: 7-1-78

Letter in file

INTRODUCTION

Research during FY 1984 has considered four areas, concerned with the mechanical behavior of materials: monolithic ceramics, ceramic matrix composites, ceramic/metal bonded systems, and polymer matrix materials. Water drop impact damage on brittle systems has also been investigated.

The research on monolithic ceramics represents the conclusion of several years of study related to the fracture toughness of polycrystalline ceramics. The emphasis of the present research (Paper I) has been on the development of a comprehension of microcrack toughening in single phase anisotropic ceramics, such as Al_2O_3 . The study illustrates how the stress, strain characteristics of a microcracking system can be derived and then used to predict trends in the fracture toughness. The dilatational strain associated with the microcracking is thereby determined to be the major toughening mechanism. The dilatation is, in turn, related to the thermal expansion anisotropy and the grain size.

Thermal fracture studies (Paper II) describe a technique for evaluating edge flaw populations in ceramic devices: notably, multilayer capacitors. The study, performed on standard capacitors, revealed that the edge flaws are more serious than the surface flaws and hence, that capacitor fracture upon soldering or thermal cycling is strongly influenced by edge damage. The concept of thermal stress testing to obtain flaw populations is also shown to be applicable to other components, such as turbine valves and turbocharger rotors. The procedure may be used for evaluation or proof testing purposes.

The research on ceramic matrix composites (Papers III & IV) presents an analysis of the mechanical behavior of a SiC/LAS composite with

uniaxial reinforcement. The study reveals that the tensile properties are dictated by a matrix cracking stress and an ultimate tensile strength, whereas the fracture toughness is not a relevant material parameter. Comprehensive investigation of matrix cracking indicates that, in this composite, the good tensile properties derive from an absence of chemical bonding between the fiber and matrix. Furthermore, the matrix cracking stress is determined to vary with the frictional shear resistance of the interface, the fracture toughness of the matrix and with the thermal expansion difference between fiber and matrix (via the residual stress).

Studies of the mechanical properties of ceramic/metal bonded systems (Papers V, VI, VII) have begun to investigate the effects of thermal and elastic anisotropy and of metal plasticity on the mechanical strength. In particular, plasticity in the metal is determined to profoundly effect several aspects of mechanical behavior. For example, crack blunting has been observed at the interface of $\text{Al}_2\text{O}_3/\text{Nb}$, due to plastic flow in the metal, resulting in interface strengthening. Additionally, stress, strain hysteresis due to metal plasticity has been used to eliminate residual stress in $\text{Al}_2\text{O}_3/\text{Cu}$ strips. The influence on fracture behavior of stress concentrations at edges, due to mismatch in elastic modulus, has also been studied.

Polymer matrix particulate composites exhibit toughness characteristics similar to those previously studied in ceramics (viz, transformation and microcrack toughening). Hence, models of rubber toughening and glass toughening of polymers have been developed (Papers VIII, IX) using concepts based on stress, strain hysteresis. In these instances, the dilatation of the material due to plastic expansion of

the matrix around debonded, or cavitated, second phases has been studied and used to predict trends in the toughness. The trends reveal synergistic effects. Particularly strong synergism was identified in rubber toughened systems wherein toughening by rubber stretching across the crack faces was determined to be multiplicative with debonding and shear banding in the process zone.

Finally, the research studies on water drop impact damage have involved the development of schemes for statistical damage characterization, pertinent to the influence of the damage on infrared transmission losses. Three aspects of this issue have been addressed. Techniques developed for characterizing the spatial variation in crack damage (Papers XI, XII) allow experimental results evaluated for a wide variety of impact conditions and target materials to be unified. In particular, the inner damage radius and the number density of cracks have now been fully characterized. Theoretical studies (Paper X) have involved the development of a computer model to simulate the crack damage. The model is based on the fracture mechanics of cracks engulfed by the short stress pulse generated by drop impact. Inertial effects of the crack faces are a particularly important aspect of the model. The computer scheme thereby allows the stress pulse to activate statistically distributed, small pre-existing surface cracks and create a distribution of crack damage. The simulation has, thus far, successfully predicted the number density of cracks in the damage zone, by incorporating stress pulse attenuation.

TECHNICAL ARTICLES
1984

Monolithic Ceramics

- I. Y. Fu and A. G. Evans, "Some Effects of Microcracks on the Mechanical Properties of Brittle Solids, I - Stress, Strain Relations, II - Microcrack Toughening."
- II. D. B. Marshall, D. Johnson-Walls, M. D. Drory, A. G. Evans and K. T. Faber, "Evaluation of Reliability in Brittle Components by Thermal Stress Testing."

Ceramic Matrix Composites

- III. D. B. Marshall and A. G. Evans, "Failure Mechanisms in Ceramic-Fiber/Ceramic Matrix Composites."
- IV. D. B. Marshall and A. G. Evans, "The Mechanics of Matrix Cracking in Brittle-Matrix Fiber Composites."

Ceramic/Metal Bonded Systems

- V. A. G. Evans and M. Ruhle, "On the Mechanics of Failure in Ceramic/Metal Bonded Systems."
- VI. C. H. Hsueh and A. G. Evans, "Residual Stresses in Metal/Ceramic Bonded Strips."
- VII. C. H. Hsueh and A. G. Evans, "On Residual Stresses and Cracking in Metal/Ceramic Systems for Microelectronics Packaging."

Polymers

- VIII. A. G. Evans, Z. B. Ahmad, D. G. Gilbert, and P. W. R. Beaumont, "Mechanisms of Toughening in Rubber Toughened Polymers."
- IX. A. G. Evans, S. Williams and P. W. R. Beaumont, "On the Toughness of Particulate Filled Polymers."

Water Drop Impact

- X. E. D. Case and A. G. Evans, "A Computer-Generated Simulation of Water Drop Impact Damage."
- XI. E. D. Case, K. M. Louie and A. G. Evans, "Statistical Analysis of Damage Induced by Water Drop or Water Jet Impact."
- XII. E. D. Case and A. G. Evans, "Inner Radius of Water Drop Impact Damage Field."

CHAPTER I-a

SOME EFFECTS OF MICROCRACKS
ON THE MECHANICAL PROPERTIES
OF BRITTLE SOLIDS

I. Stress-Strain Relations

Y. Fu and A. G. Evans

SOME EFFECTS OF MICROCRACKS ON THE
MECHANICAL PROPERTIES OF BRITTLE SOLIDS

I. STRESS, STRAIN RELATIONS

by

Y. Fu and A. G. Evans

Department of Materials Science and Mineral Engineering,
University of California, Berkeley, CA 94720

ABSTRACT

An analysis of microcracking in a brittle polycrystalline aggregate is presented. The analysis is based on the combined influence of the residual stress and the applied loads. Microcrack densities are predicted as a function of load and correlated with acoustic emission measurements. The non-linear characteristics of the stress-strain curves of microcracking materials are calculated, as required for subsequent evaluation of microcrack toughening in brittle materials.

I. INTRODUCTION

Localized residual stresses typically form in polycrystalline brittle solids, due to thermal expansion anisotropy.¹⁻⁴ The residual field often induces a stress intensity of sufficient magnitude that microcracks nucleate,⁵ especially when present in conjunction with appreciable applied stresses. The resultant microcracks influence the mechanical properties of the material, in addition to having important effects on optical and thermal properties. The intent of this article is to describe the source of the microcracks and to evaluate the stress, strain response of materials subject to stress induced microcracking. The associated effects of microcracks on crack propagation are presented in a companion paper.⁶

In the present paper, the stresses that result from expansion anisotropy are firstly assessed. Then, fracture concepts that account for observations of thermal microcracks are discussed. Thereafter, the concepts are used to predict the microcracking that occurs upon application of applied loads and hence, to predict stress, strain relations for microcracking brittle solids. Experimental measurements that relate to stress induced microcracking are, where available, correlated with the predictions.

2. RESIDUAL STRESSES

The analyses of the residual stress caused by expansion anisotropy were originally concerned with the stresses induced within grains. The results of such analyses, obtained using variational principles,

revealed stresses of the form,²

$$\sigma_{ij} = M_{ijkl} (\sigma_{kl})_o$$

$$(\sigma_{ij})_o = C_{ijkk}(\alpha_o - \alpha_k)\Delta T \quad (1)$$

where α_o is the thermal expansion coefficient of the polycrystalline aggregate and α_k is the thermal expansion coefficient along the k-axis of the grain, ΔT is the cooling range, C_{ijkl} is a compliance tensor and M_{ijkl} is a relaxation tensor. However, since microcracks in polycrystalline brittle solids typically occur along grain boundaries^{5,7}, the stresses along boundaries are deemed more pertinent for present purposes.

Grain boundary stresses are conveniently analyzed using the Eshelby procedure.^{5,8} In this procedure, the first step entails removal of the microstructural entities, followed by unconstrained straining. Then, surface forces are applied to restore the entities to their original shape, whereupon they are reinserted into the body. Finally, interface tractions are imposed to establish stress continuity in the system. For polycrystalline solids subject to thermal expansion anisotropy, it can be shown⁹ that the grain boundary stresses may be adequately assessed using four anisotropic grains, contained within an isotropic matrix with the average properties of the polycrystal (fig. 1). With this approach, the stresses σ_{ij}^T within each grain, due to application of surface forces, are given by

$$\begin{aligned}
\sigma_{zz}^T &= E\Delta\alpha\Delta T \cos 2\theta_n / (1+\nu) \\
\sigma_{yy}^T &= E\Delta\alpha\Delta T \cos 2\theta_n / (1+\nu) \\
\sigma_{xy}^T &= E\Delta\alpha\Delta T \sin 2\theta_n / (1+\nu)
\end{aligned}
\tag{2}$$

where,

$$\begin{aligned}
\Delta\alpha &= \alpha_1 - (\alpha_1 + \alpha_2)/2 \\
&= \alpha_2 - (\alpha_1 + \alpha_2)/2;
\end{aligned}$$

the subscripts 1 and 2 refer to the principal strains, and θ_n is the angle between the axis of maximum contraction in grain n and the grain boundary plane.

These stresses are modified during the final step in the sequence, when interface tractions P_i (fig. 2) - equal in magnitude but opposite in sign to the surface forces - are applied around the grain boundaries after insertion into the matrix. Resultant stresses, evaluated for two dimensional grain arrays, with several grain orientations, are presented in fig. 3.

The stresses can be considered to comprise of two principal components: uniform stresses at the grain facet center and singular stresses near the grain corner. The uniform stresses, σ_{ij}^M , originate from the mismatch between the two grains adjacent to the grain boundary of interest and are given by;

REFERENCES

1. W. Boas and R. W. K. Honeycombe, *Nature*, 153, (1944) 495.
2. V. A. Likhachev, *Soviet Physics-Solid State*, 3, 6, (1961) 1330.
3. W. R. Buessem, L. E. Cross and A. K. Goswami, *J. Am. Ceram. Soc.* 49, (1966) 1.
4. W. R. Buessem and F. F. Lange, *Interceram*, 15, 3, (1966) 229.
5. A. G. Evans, *Acta Met.*, 26, (1978) 1845.
6. Y. Fu and A. G. Evans, companion paper.
7. A. G. Evans and D. R. Clarke, "Thermal Stresses in Severe Environments" (1980), D. P. H. Hasselman and R. A. Heller, eds., Plenum Publishing Co., New York.
8. J. D. Eshelby, *Proc. Roy. Soc.* A241, (1957) 376.
9. Y. Fu, "Microfracture in Brittle Solids", M.S. Thesis, University of California, Berkeley, 1980.
10. J. A. Kuszyk and R. C. Bradt, *J. Am. Ceram. Soc.*, 56, (1978) 420.
11. S. L. Dole, O. Hunter, Jr., F. W. Calderwood and D. J. Bray, *J. Am. Ceram. Soc.*, 61 (1976) 241.
12. H. J. Siebeneck, D. P. H. Hasselman, J. J. Cleveland and R. C. Bradt, *J. Am. Ceram. Soc.*, 241 (1976).
13. R. C. Pohanka, R. W. Rice and B. E. Walker, Jr., *J. Am. Ceram. Soc.*, 59 (1976) 71,
14. J. J. Cleveland and R. C. Bradt, *J. Am. Ceram. Soc.*, 61, (1978), 478.
15. R. W. Davidge, *Acta Met.*, 29 (1981) 1696.

6. CONCLUDING REMARKS

An approach for predicting the trends in microcracking with applied stress has been developed. The model is restricted to two dimensional grain arrays and excludes interaction between neighboring microcracks. Nevertheless, the model appears to provide information regarding the influence of thermal microcracks on the elastic properties of brittle solids, consistent with the grain size dependence of Young's modulus. In addition, predicted trends in microcrack density with applied load are in qualitative accord with acoustic emission measurements.

Finally, the analysis predicts non-linear loading and linear unloading characteristics, with load cycle hysteresis. Such nonlinearities are deemed to be important in the evaluation of toughening, as discussed in the companion paper.

facets, f . Hence, from eqn (23), trends in θ are expected to satisfy the relation,

$$\theta \sim \chi m(\sigma_1 - \sigma_{th})(1+\nu)/E \quad (27)$$

where χ is a dilatational parameter which characterizes the strain relieved by microcrack formation. This permanent strain also has an important influence on the crack growth resistance of a microcracking material.⁶

Direct experimental observations of tensile⁺ non-linear stress, strain behavior (and of the associated permanent strain) have not been reported in tests on brittle materials. The inability to obtain such observations derives from the premature incidence of tensile failure, that occurs due to the localized coalescence of microcracks, before an appreciable net density of microcracks has been created by the applied stress. However, large densities of microcracks are more probable in the process zone around major cracks, where microcrack coalescence does not induce complete failure, due to the constraint of the uncracked elastic matrix. The stress, strain characteristics of the process zone are thus expected to exhibit non-linearity as discussed in the accompanying paper.⁶

⁺Compression tests reveal substantial non-linearity, due to microcracking. However, different effects exist in compression obviating a direct correlation with the tensile behavior emphasized in the present analysis.

microcrack density (eqn 24). The overall principal strains deduced in this manner are ($\sigma_1 > \sigma_{th}$);

$$e_1 = s_1 [1 - kv(1 + C - Bs_1)] / (1 + C - Bs_1) \quad (26)$$

$$e_2 = s_2 [1 - v(1 + C - Bs_2/k) / k] / (1 + C - Bs_2/k)$$

where $e = (1 + v) / \Delta \alpha \Delta T$, with

$$B = pgm\ell^3/9$$

and,

$$C = B(\sqrt{\ell^5/s_c} - 1)$$

The stress/strain response is linear below the threshold (fig. 12), but thereafter becomes nonlinear, since the microcrack propensity increases continuously with stress. The nonlinear loading response resembles that of a work-hardening material. However, since the elastic modulus is reduced by the irreversible microcracking process, unloading occurs with a reduced secant modulus, as depicted schematically in fig. 13. The stress, strain curve thus exhibits hysteresis, and the associated energy dissipation is the source of wake effects on the crack propagation resistance, as discussed in the companion paper.⁶

Another feature of the stress-strain curve, that can be addressed only qualitatively with the present analysis, is the existence of a permanent strain (fig. 13). The permanent dilatation derives from the relief of the residual tensile stress by the facet microcracks, as depicted in fig. 8. Furthermore, the permanent strain ϵ should scale with the residual strain, $\Delta \alpha \Delta T$, and with the fraction of microcracked

where the coefficient m between 0 and 2 that depends on the grain geometry and the ratio, $k = \sigma_2/\sigma_1$. The microcrack density N may thus be obtained as

$$N \approx pgm(\sigma_1 - \sigma_{th})(1+\nu)/2E\alpha\Delta T \quad (24)$$

Evidence for the incidence of microcracking during the application of stress has been obtained using acoustic emission measurements.²⁰ These measurements indicate the existence of a microcrack threshold and suggest that the fraction of cracked facets, significantly above the threshold, satisfies the relation,

$$f = \lambda \sigma_1^q \quad (25)$$

where q and λ are coefficients. Data for Al_2O_3 ²⁰ yield $q \sim 10$. The facet fracture predictions obtained with the present analysis, plotted using logarithmic axes (fig. 11), suggest similar post-threshold behavior, with $q \sim 3$ to 10 (at least over the narrow range of facet fracture probabilities typically encountered prior to specimen fracture, $f < 5\%$). However, additional acoustic emission data are clearly needed to permit adequate assessment of the implications of the present analysis.

5.4 The Stress/Strain Curve

The strain response due to microcracking can be estimated by coupling the relations for the elastic moduli (eqn 14) with the

is expected to increase. Following the general relation for the effective stress (eqn 18), it may be specified that microcracking occurs at facets where the configuration parameters, θ_1 , θ_2 and ϕ satisfy the relation

$$H(v_1, v_2, \phi, s_1, s_2) > \ell_c^S / \ell \quad (20a)$$

subject to,

$$- \frac{(\cos 2v_1 + \cos 2v_2)}{2} + s_1 \sin^2 \phi + s_2 \cos^2 \phi > 0 \quad (20b)$$

The corresponding points in the configuration domain (fig. 9) occupy a volume V , that depends on s_1, s_2 and ℓ / ℓ_c^S . The fraction f of facets microcracked is

$$f = V / \pi^3 \quad (21)$$

and the microcrack density N is

$$N = pgV / 2\pi^3 \quad (22)$$

Numerical integration, based on both Gaussian and Monte Carlo methods, may be used to calculate f and hence, N , from eqn (20). The results are shown in figs. 10.

Inspection of fig. 10 reveals that the fraction f of microcracked facets is approximately proportional to $(\sigma_1 - \sigma_{th})$, such that

$$f \approx m(\sigma_1 - \sigma_{th})(1+\nu) / E\Delta\alpha\Delta T \quad (23)$$

where

$$\begin{aligned}
 H(v_1, v_2, \phi, s_1, s_2) \equiv & 1/2 + (1/2)\cos(2v_1-2v_2) + \sin^2\phi + s_2^2 \cos^2\phi \\
 & -\cos 2v_1 \cos 2v_2 (s_1 \sin^2\phi + s_2 \cos^2\phi) \\
 & +(\sin 2v_1 + \sin 2v_2)(s_1 - s_2) \sin\phi \cos\phi
 \end{aligned}$$

with $s_1 = \sigma_1(1+\nu)/E\Delta\alpha\Delta T$ and $s_2 = \sigma_2(1+\nu)/E\Delta\alpha\Delta T$.

5.2 The Threshold Stress

When the grain facet size in the material is less than the critical size ℓ_c^S , stress induced microcracking initiates at a threshold stress, σ_{th} . This threshold pertains to the grain facet subject to the maximum normal tension, due to superposition of the applied and residual fields. Hence, if σ_1 is the maximum principal tension, the effective stress at the cracking threshold becomes,

$$\sigma = \sigma_1 + E\Delta\alpha\Delta T/(1+\nu) \quad (18)$$

Hence, from eqn (8), the threshold stress can be deduced as

$$\sigma_{th} = \left(\sqrt{\ell_c^S/\ell} - 1 \right) E\Delta\alpha\Delta T/(1+\nu) \quad (19)$$

5.3 The Microcrack Density

As the applied stress, σ_1 exceeds σ_{th} , additional grain facets satisfy the microcracking criterion and the microcrack number density N

Stress induced microcracking arises because the stresses on the grain boundaries associated with the applied loads superpose on the residual stress and exceed the critical condition. The trends in microcracking can be analytically determined for two dimensional grain arrays (fig. 1). Such arrays are characterized by the crystallographic orientations of the adjacent grains, θ_1 , θ_2 , and the angle, ϕ , between the facet and the stress axis. With $0 \leq \theta_1, \theta_2, \phi \leq \pi$, all possible combinations of θ_1, θ_2 and ϕ occupy a cubic domain (fig. 9). Each volume element in the domain is equally populated with facets having the corresponding θ_1 , θ_2 and ϕ . The applied stresses, resolved onto the grain facet, are thus given by

$$\begin{aligned}\sigma_{yy}^a &= \sigma_1 \sin^2 \phi + \sigma_2 \cos^2 \phi \\ \sigma_{xy}^a &= (\sigma_1 - \sigma_2) \sin \phi \cos \phi\end{aligned}\tag{16}$$

These stresses are linearly superimposed upon the residual stresses (equation (3)) to obtain the total stresses

$$\begin{aligned}\sigma_{yy} &= -\frac{E\Delta\alpha\Delta T}{1+\nu} \frac{(\cos 2\theta_1 + \cos 2\theta_2)}{2} + \sigma_1 \sin^2 \phi + \sigma_2 \cos^2 \phi \\ \sigma_{xy} &= \frac{E\Delta\alpha\Delta T}{1+\nu} \frac{(\sin 2\theta_1 + \sin 2\theta_2)}{2} + (\sigma_1 - \sigma_2) \sin \phi \cos \phi\end{aligned}\tag{17}$$

such that the effective stress becomes

$$\sigma = [H(\theta_1, \theta_2, \phi, s_1, s_2)]^{1/2} E\Delta\alpha\Delta T/(1+\nu)\tag{18}$$

If it is now assumed that the number density of microcracks in the two dimensional grain array (eqn 12) is of approximate applicability to the three dimensional polycrystal, the elastic modulus of a polycrystal containing facet-sized cracks ($\ell = 2a$), becomes

$$\bar{E}/E \approx 1 - \left(\frac{pg\ell^3}{9\pi} \right) \cos^{-1} \sqrt{\ell^5/\ell} \quad (15)$$

A comparison of eqn (15) with experimental measurements¹⁸ (fig. 7) indicates that the modulus trend is adequately predicted, by adopting $pg \approx 20/\ell^3$ as the facet density. However, for a typical equiaxed structure, with 12 facets per grain, the facet density is more closely approximated by $pg = 6/\ell^3$. Consistency between the data and the present model is thus incomplete. The discrepancy is due, presumably, to the two dimensional nature of the facet cracking analysis. Nevertheless, the relatively close prediction of modulus trends, based on the facet density used in fig. 7 should provide a reasonable basis for further analysis of stress induced microcracking.

5. STRESS/STRAIN RELATIONS

5.1 General Considerations

The formation of microcracks reduces the elastic modulus of a material, as described in the preceding section. Consequently, stress induced microcracking necessarily results in a non-linear stress strain curve, as depicted in fig. 8. Furthermore, load cycle hysteresis develops, and contributes to the toughening, as discussed in the companion paper.⁶

The number of microcracks per unit volume in the two dimensional array is thus,

$$N = p(g/2) \cos^{-1} \sqrt{\ell_c^3/\ell} \quad (12)$$

where p is the number of facets per grain and g is the number of grains in unit volume.

4. THE ELASTIC MODULI

Modulus measurements¹⁸ provide a useful basis for validating predictions of thermal microcracking. A randomly oriented three dimensional array of circular microcracks of radius a modifies the elastic properties in accord with the relations¹⁹

$$\begin{aligned} \frac{\bar{E}}{E} &= 1 - \frac{16}{45} \frac{(1-\bar{\nu}^2)(10-3\bar{\nu})}{(2-\bar{\nu})} \cdot N \langle a^3 \rangle \\ \frac{\bar{\mu}}{\mu} &= 1 - \frac{32}{5} \frac{(1-\bar{\nu})(5-\bar{\nu})}{(2-\bar{\nu})} \cdot N \langle a^3 \rangle \end{aligned} \quad (13)$$

where μ is the shear modulus and \bar{E} , $\bar{\nu}$, and $\bar{\mu}$ refer to the microcracked body. Furthermore, over the important range, $\bar{E} \geq 0.2E$, the following approximation pertains,

$$\bar{E}/E = \bar{\nu}/\nu \approx 1 - (16/9)N\langle a^3 \rangle \quad (14)$$

subject to;

$$\cos 2\theta_1 + \cos 2\theta_2 \leq 0$$

The preceding criterion can be used to evaluate the number density of cracked facets in a polycrystal provided that crack interaction effects are neglected⁺. Specifically, in a material with a large number of randomly oriented grains of uniform facet size ℓ , all possible facet configurations (θ_1, θ_2) in a two dimensional array occupy a square domain (fig. 5), and each area element in the domain is equally populated. Points in the domain that satisfy equation (9) correspond to microcracked grain boundary facets. Hence, the fraction f of thermally microcracked facets is

$$f = A_1/A \quad (10)$$

where A_1 is the area encompassed by equation (9) and A is the total area (π^2). Integrating over A_1 , yields the relation plotted in fig. 6,

$$f = \frac{1}{\pi} \cos^{-1} \sqrt{\ell^5/c/\ell} \quad (11)$$

⁺The residual compression between cracked facets (fig. 4) tends to inhibit coalescence, except in a few localized regions of the microstructure.

effective stress and β is a coefficient. In particular, since first cracking obtains on boundaries subject to the maximum residual stress, $\sigma = E\Delta\alpha\Delta T/(1+\nu)$, the critical facet size is;

$$l_c^s [E\Delta\alpha\Delta T/(1+\nu)]^2 = \beta (K_c^b)^2 \quad (6)$$

Comparison with experimental measurements reveals that eqn (6) indeed affords an adequate description of microcracking, with $\beta \approx 3.5, 5, 7, 10, 15$

Trends in microfracture on facets larger or smaller than l_c^s may be assessed by noting that crack extension, along grain facets,¹⁶ is generally predicated on an effective stress⁺,

$$\sigma = \sqrt{\sigma_{yy}^2 + \sigma_{xy}^2} \quad (7)$$

Such crack extension occurs provided that the tensile normal stress, $\sigma_{yy} > 0$. Hence, the fracture of facets larger than the critical size can be expected to proceed in accord with the inequality

$$\begin{aligned} l/l_c^s &> [E\Delta\alpha\Delta T/(1+\nu)]^2 \sigma^2 \\ &\equiv [E\Delta\alpha\Delta T/(1+\nu)]^2 [(\sigma_{yy}^M)^2 + (\sigma_{xy}^M)^2]^{-1} \end{aligned} \quad (8)$$

Inserting the stresses σ_{ij}^M from eqn (3), yields the microcrack criterion pertinent to a two dimensional grain array,

$$l/l_c^s > 2[1 + \cos(2\theta_1 - 2\theta_2)]^{-1} \quad (9)$$

⁺Coplanar crack extension typically occurs when the strain energy release rate exceeds a critical value and hence when the normal and shear stresses satisfy eqn (7).

size undoubtedly depends on the scale effect contained in the logarithmic singularity, $\ln(l/x)$, which allows the stress to be sustained over a larger area of grain facet as l increases.⁵ Consequently, larger grain facets, subject to the same residual stress amplitude, are more susceptible to microfracture. However, the details of the nucleation subject to the logarithmic singularity are not well known. One postulate^{5,7} is that the stress singularity acts in conjunction with an extrinsic inhomogeneity (e.g. voids, second phase inclusions) at the grain junction. Then, when l is large enough, the precursor becomes unstable and nucleates into a microcrack.

After nucleation, the microcrack propagates along the grain facet, motivated by the net residual stresses, σ_{yy}^M and σ_{xy}^M . Finally, the microcrack is arrested at the neighboring junctions, because the adjacent boundary facets are generally subject to residual compression (fig. 4).

Detailed knowledge of the microcrack nucleation mechanism is not an essential prerequisite for selecting a viable microcrack nucleation criterion. An adequate criterion may be obtained by dimensional analysis and expressed in terms of the critical facet size l_c^S and the uniform stress σ_{ij}^M . Specifically, the parameters involved in fracture have dimensions that suggest facet cracking subject to the inequality,^{5,10,15}

$$l\sigma^2 \geq \beta(K_c^b)^2 \quad (5)$$

where K_c^b is the fracture toughness of the grain boundary, σ is an

$$\begin{aligned}\sigma_{yy}^M &= -E\Delta\alpha\Delta T(\cos 2\theta_1 + \cos 2\theta_2)/2(1+\nu) \\ \sigma_{zy}^M &= E\Delta\alpha\Delta T(\sin 2\theta_1 + \sin 2\theta_2)/2(1+\nu)\end{aligned}\quad (3)$$

The stresses near the facet corner exhibit a logarithmic singularity, such that

$$\begin{aligned}\sigma_{yy}(x) &= [1+F_1(\theta_1, \theta_2, \theta_3)\ln(\ell/x)]\sigma_{yy}^M \\ \sigma_{xy}(x) &= [1+F_2(\theta_1, \theta_2, \theta_3)\ln(\ell/x)]\sigma_{xy}^M\end{aligned}$$

where ℓ is the grain facet length and F_1, F_2 are functions of the grain orientation parameters θ_n .

The singular stresses are of obvious importance in determining microcrack nucleation.^{5,7} However, the singular terms introduce major complexity when analyzing multiple microcracking in polycrystalline arrays. Consequently, since the singular stresses scale with the uniform stresses (eqn 4), the potential for using the non-singular stress to predict microcrack trends, is explored in the subsequent section.

3. THERMAL MICROCRACKING

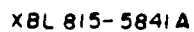
Experimental observations¹⁰⁻¹⁴ indicate that thermal microcracking occurs when the grain facets exceed a critical size, ℓ_c^s . The intent of the present section is to establish a generalized microcracking criterion, using ℓ_c^s as a parameter. The existence of a critical facet

16. K. T. Faber and A. G. Evans, Acta Met., 31 (1983) 577.
17. D. B. Marshall, J. Am. Ceram. Soc., in press.
18. E. D. Case, J. R. Smith and O. Hunter, J. Mater. Sci. 15, (1980)
149.
19. B. Budiansky and R. J. O'Connell, Int. J. Solid Struct., 12 (1976)
81.
20. A. G. Evans, M. Linzer, and L. R. Russell, Mat. Sci. Eng. 15, 253
(1974).

FIGURE CAPTIONS

- Fig. 1 The four anisotropic grains with an isotropic matrix used for residual stress analysis.
- Fig. 2 A summary of the interface tractions, P_i , imposed to achieve stress continuity in the final step of the Eshelby sequence.
- Fig. 3 Stress distributions calculated for four grain arrays with three different relative grain orientations.
- Fig. 4 A schematic illustrating the tendency for the residual stress to alternate between tension and compression on adjacent facet pairs. The compression induces crack arrest and allows for stable microcracking.
- Fig. 5 A schematic illustrating the grain facet configurational domain and the configuration points corresponding to thermally microcracked facets: $\sigma_R = E\Delta T\Delta\alpha/(1+\nu)$.
- Fig. 6 A plot of the trend in facet microfracture with facet size, above critical, l_c^S .
- Fig. 7 Trends in the elastic modulus with grain facet size predicted by the analysis, compared with data for $MgTi_2O_5$ ($l_c^S \approx 1.5 \mu m$, $E = 248 \text{ GPa}$) and Fe_2TiO_5 ($l_c^S \approx 1.5 \mu m$, $E = 172 \text{ GPa}$).
- Fig. 8 A schematic stress-strain curve for a microcracking brittle solid.
- Fig. 9 The configurational domain used for the analysis of stress induced microcracking.

- Fig. 10 The effects of stress on the microcrack density a) uniaxial stress, (b) biaxial stress.
- Fig. 11 A logarithmic plot of the trend in microcrack density with stress, indicating approximate linearity above the threshold, within the data range, qualitatively consistent with acoustic emission measurements.
- Fig. 12 A predicted stress-strain curve for a material with a grain facet size below the critical value for thermal microcracking, subject to an equibiaxial stress ($k = 1$).
- Fig. 13 Stress-strain curves for complete loading cycles illustrating the hysteresis.



27

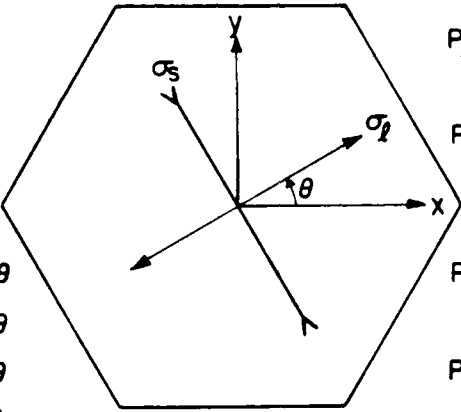
$$\begin{aligned}
 P_x &= \sigma_l^T \sin \theta \cos \theta \\
 &\quad - \sigma_s^T \cos \theta \sin \theta \\
 P_y &= \sigma_l^T \sin \theta \sin \theta \\
 &\quad + \sigma_s^T \cos \theta \cos \theta
 \end{aligned}$$

$$\begin{aligned}
 P_x &= -\sigma_l^T \sin(\pi/3 - \theta) \cos \theta \\
 &\quad - \sigma_s^T \cos(\pi/3 - \theta) \sin \theta \\
 P_y &= -\sigma_l^T \sin(\pi/3 - \theta) \sin \theta \\
 &\quad + \sigma_s^T \cos(\pi/3 - \theta) \cos \theta
 \end{aligned}$$

$$\begin{aligned}
 P_x &= -\sigma_l^T \sin(2/3\pi - \theta) \cos \theta \\
 &\quad - \sigma_s^T \cos(2/3\pi - \theta) \sin \theta \\
 P_y &= -\sigma_l^T \sin(2/3\pi - \theta) \sin \theta \\
 &\quad + \sigma_s^T \cos(2/3\pi - \theta) \cos \theta
 \end{aligned}$$

$$\begin{aligned}
 P_x &= \sigma_l^T \sin(2/3\pi - \theta) \cos \theta \\
 &\quad + \sigma_s^T \cos(2/3\pi - \theta) \sin \theta \\
 P_y &= \sigma_l^T \sin(2/3\pi - \theta) \sin \theta \\
 &\quad - \sigma_s^T \cos(2/3\pi - \theta) \cos \theta
 \end{aligned}$$

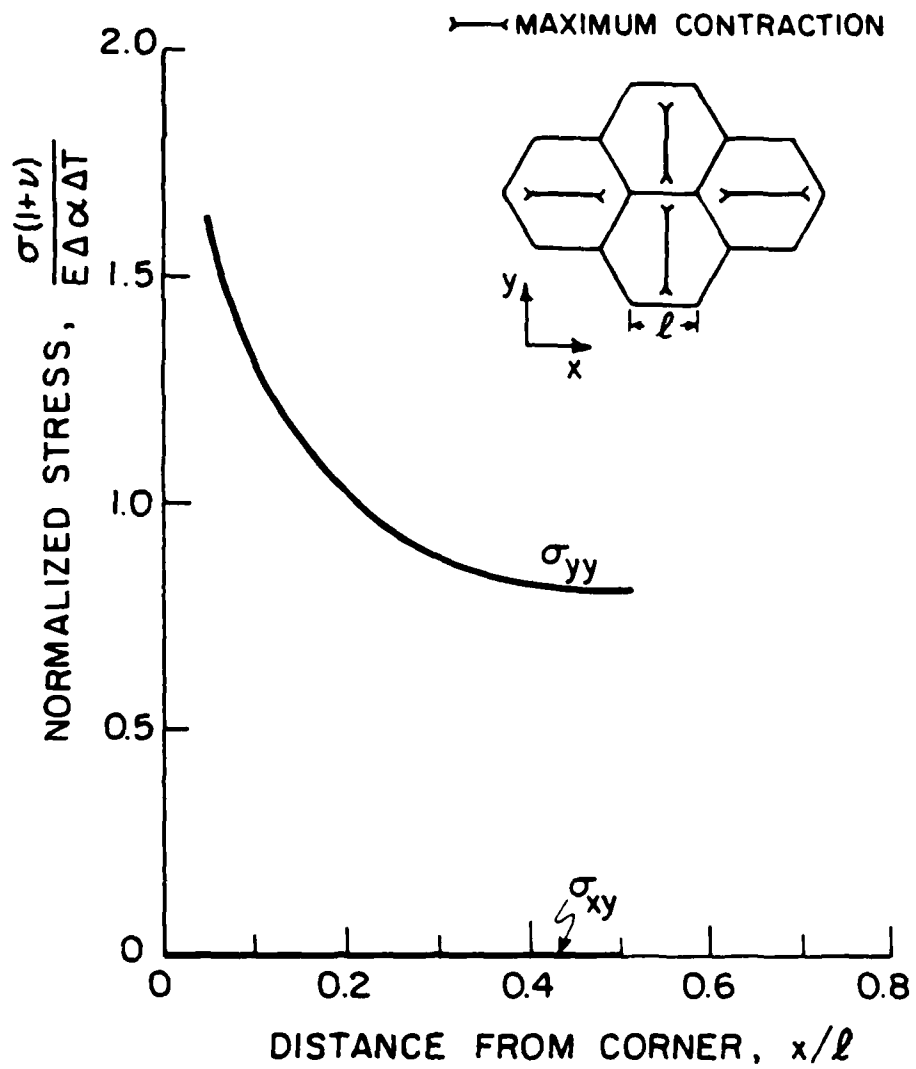
$$\begin{aligned}
 P_x &= \sigma_l^T \sin(\pi/3 - \theta) \cos \theta \\
 &\quad + \sigma_s^T \cos(\pi/3 - \theta) \sin \theta \\
 P_y &= \sigma_l^T \sin(\pi/3 - \theta) \sin \theta \\
 &\quad - \sigma_s^T \cos(\pi/3 - \theta) \cos \theta
 \end{aligned}$$

$$\begin{aligned}
 P_x &= -\sigma_l^T \sin \theta \cos \theta \\
 &\quad + \sigma_s^T \cos \theta \sin \theta \\
 P_y &= -\sigma_l^T \sin \theta \sin \theta \\
 &\quad - \sigma_s^T \cos \theta \cos \theta
 \end{aligned}$$


$$\begin{aligned}
 \sigma_{xx} &= \sigma_l^T \cos^2 \theta + \sigma_s^T \sin^2 \theta \\
 \sigma_{yy} &= \sigma_l^T \sin^2 \theta + \sigma_s^T \cos^2 \theta \\
 \sigma_{xy} &= (\sigma_s^T - \sigma_l^T) \sin \theta \cos \theta
 \end{aligned}$$

XBL 815-5842

Fig. 2



XBL815-5843

Fig. 3a

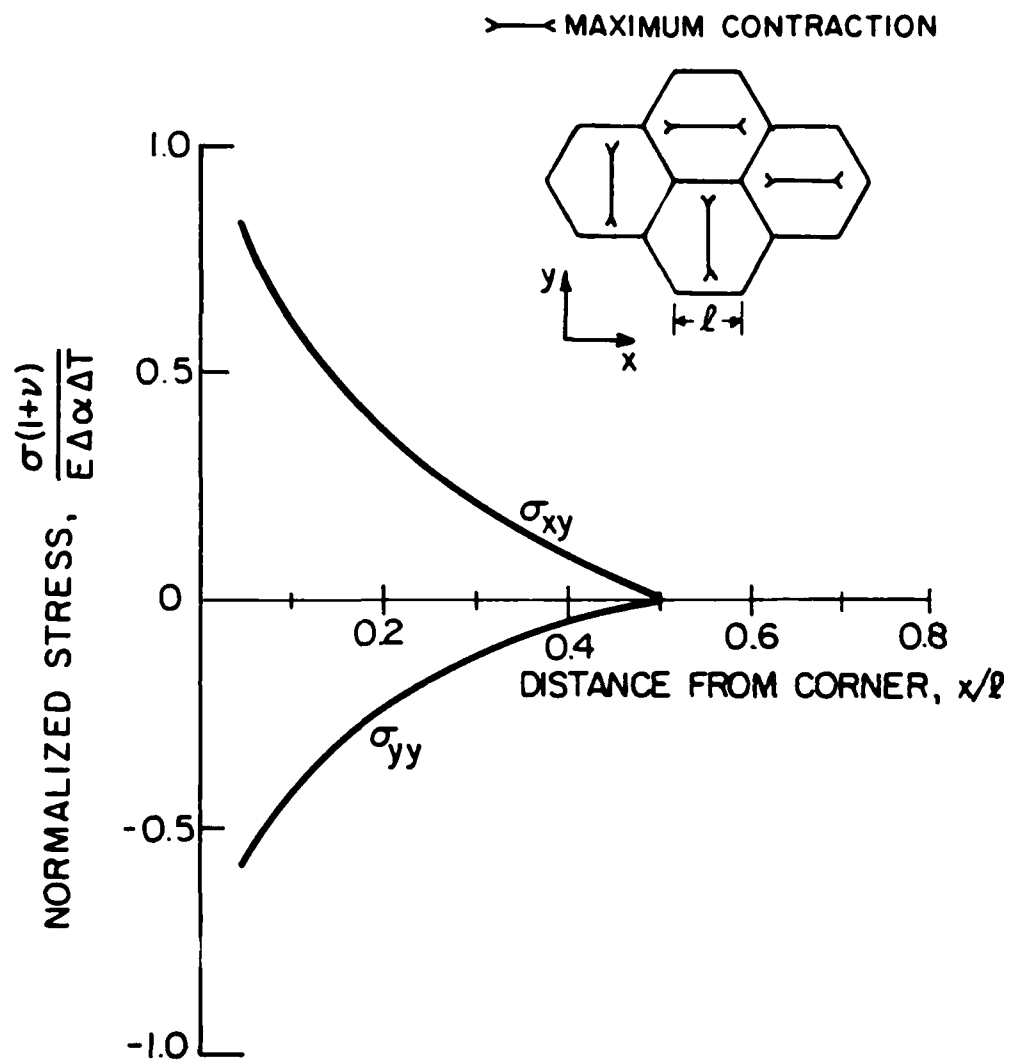
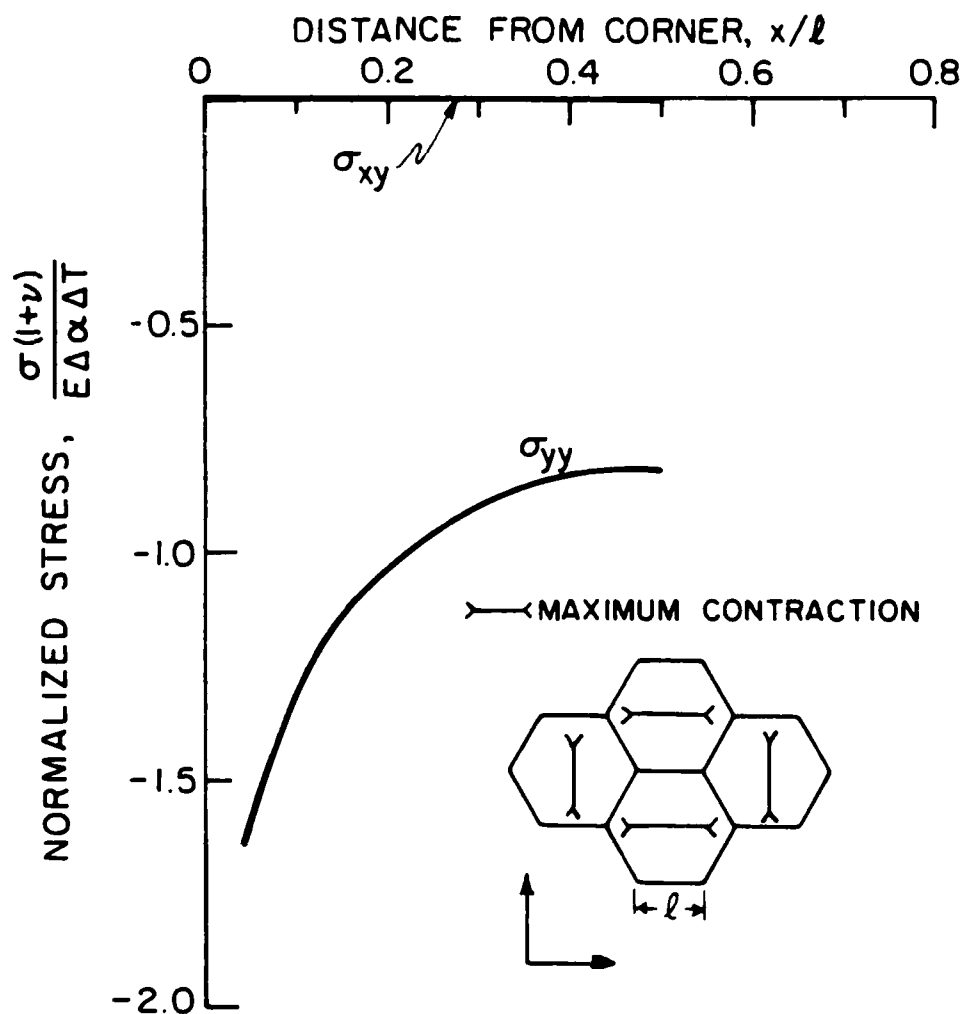
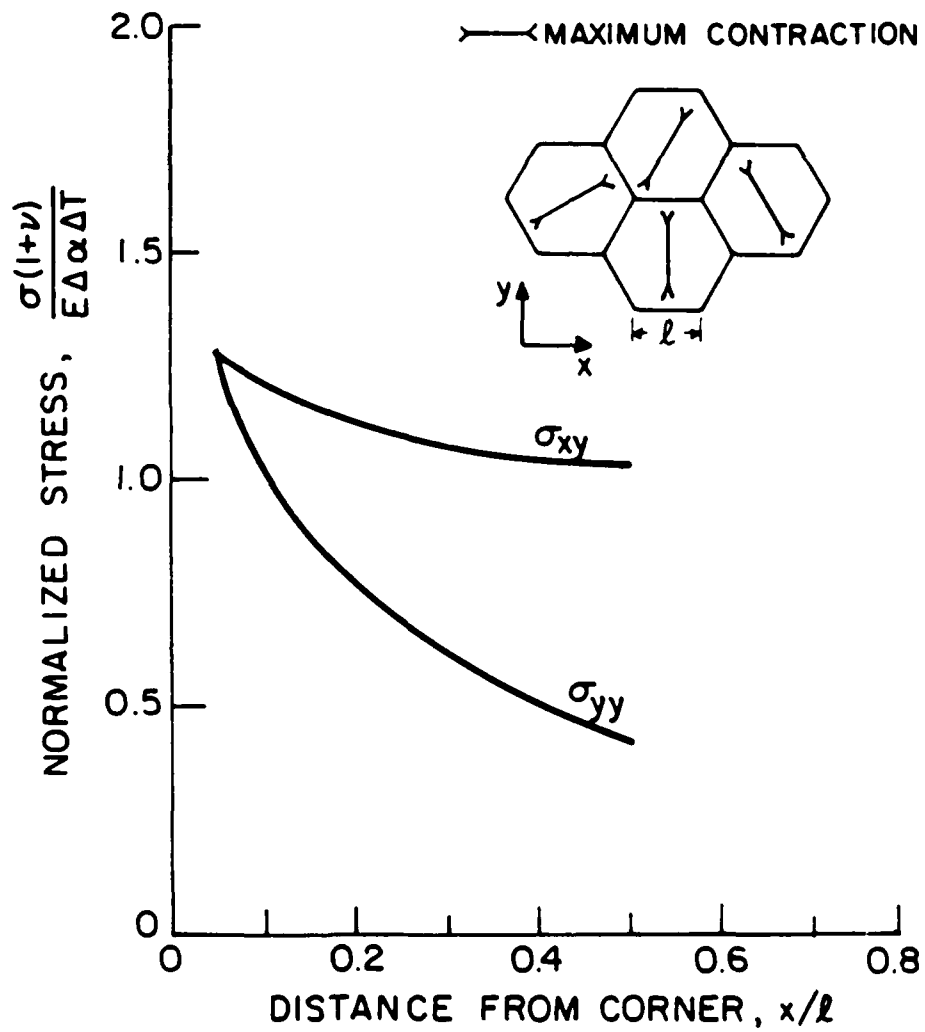


Fig. 3b



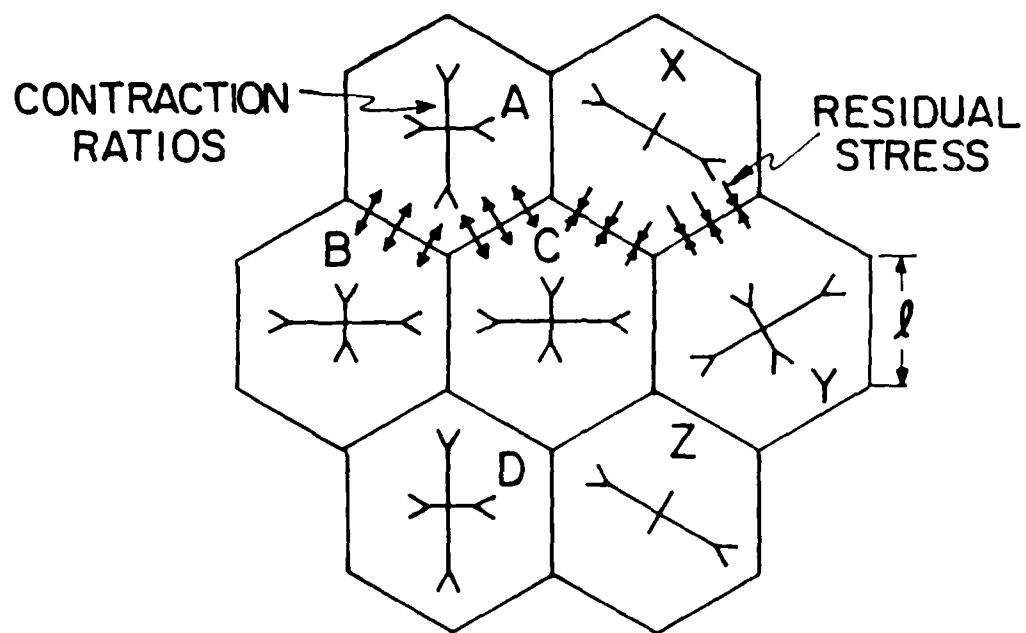
XBL 815-5845

Fig. 3c



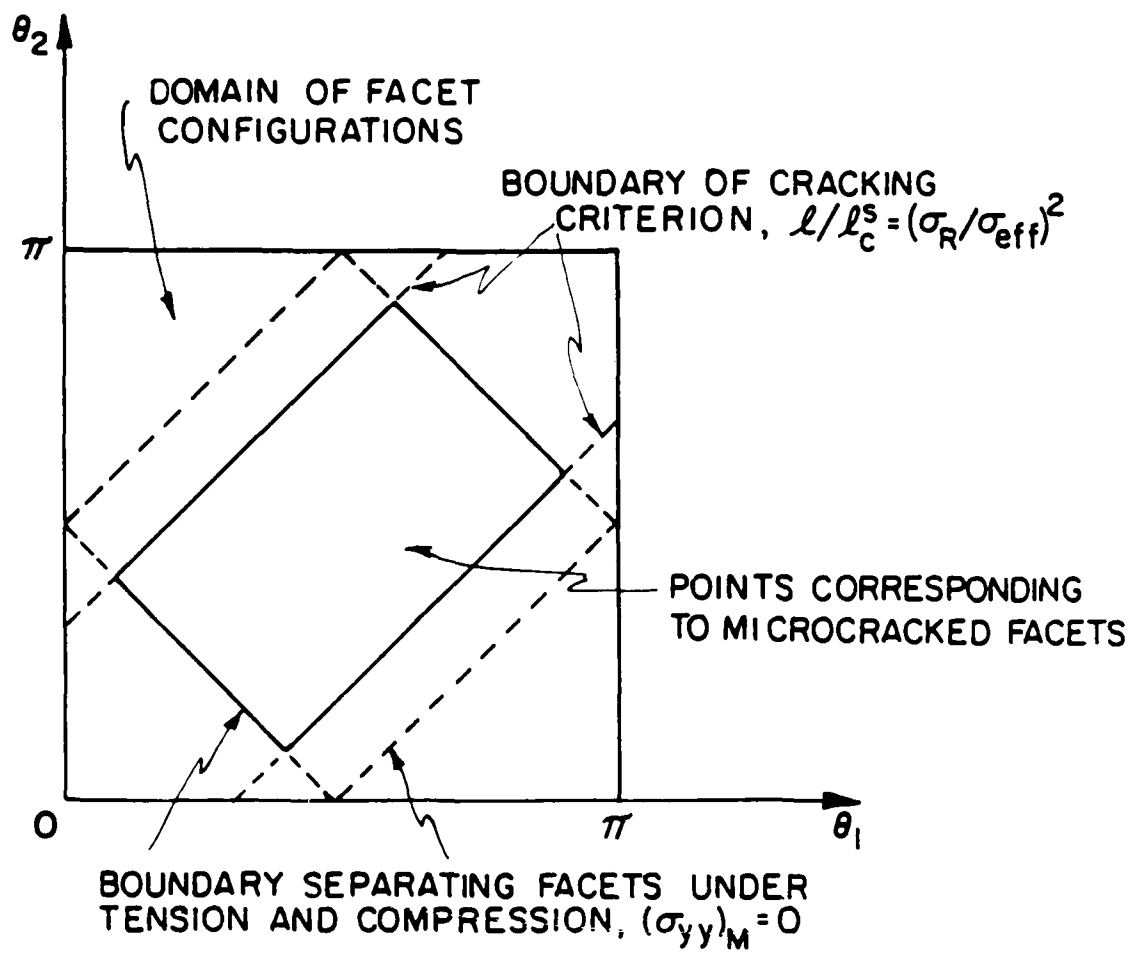
XBL 815-5846

Fig. 3d



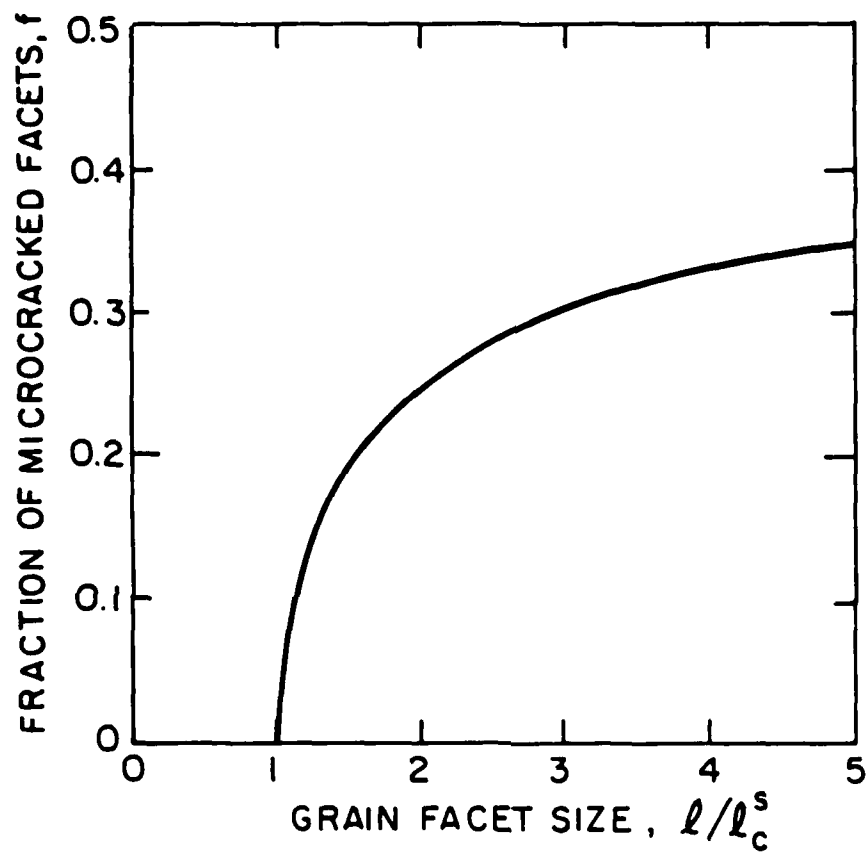
XBL 839-11653

Fig. 4



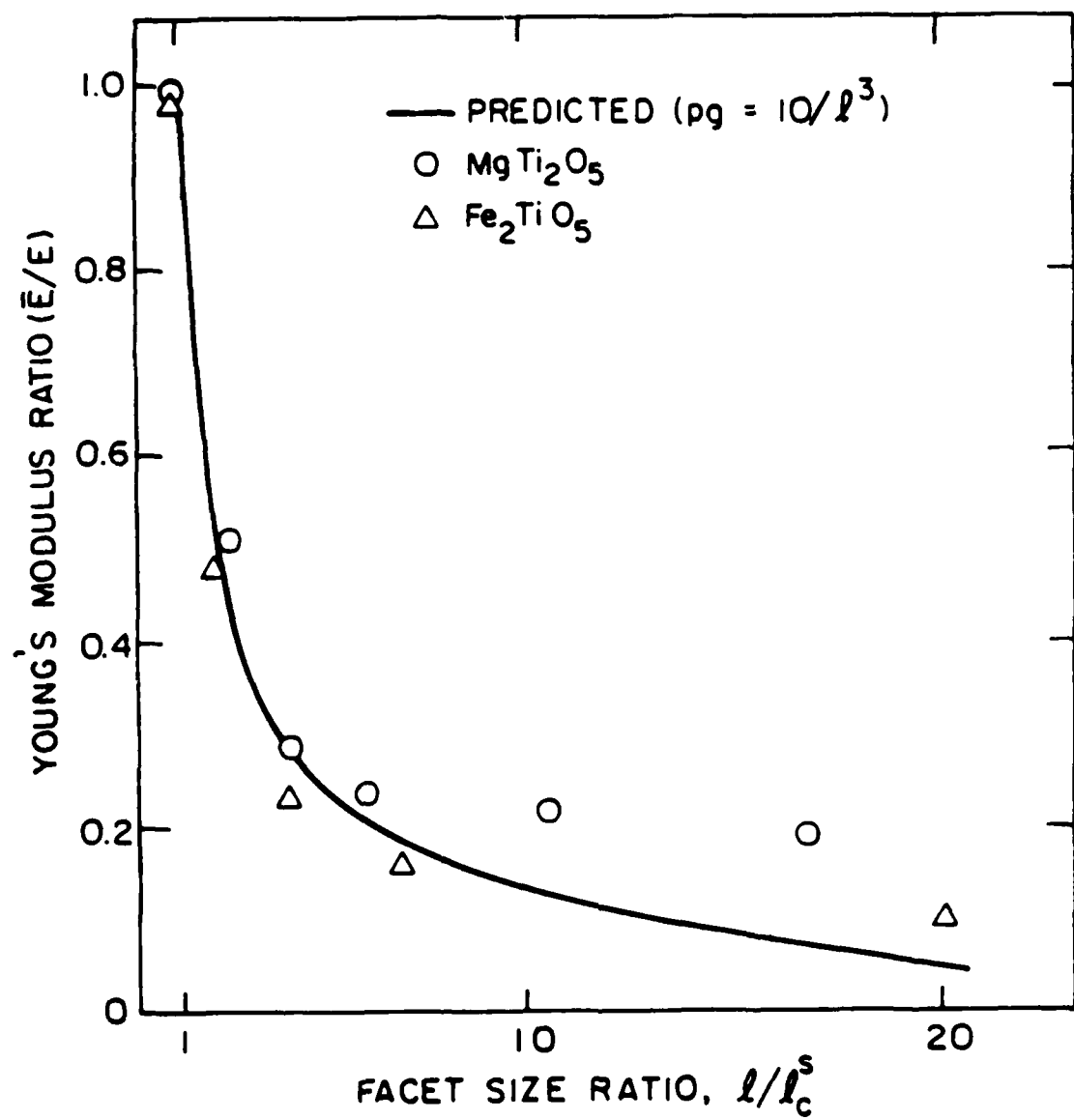
XBL 839-6352

Fig. 5



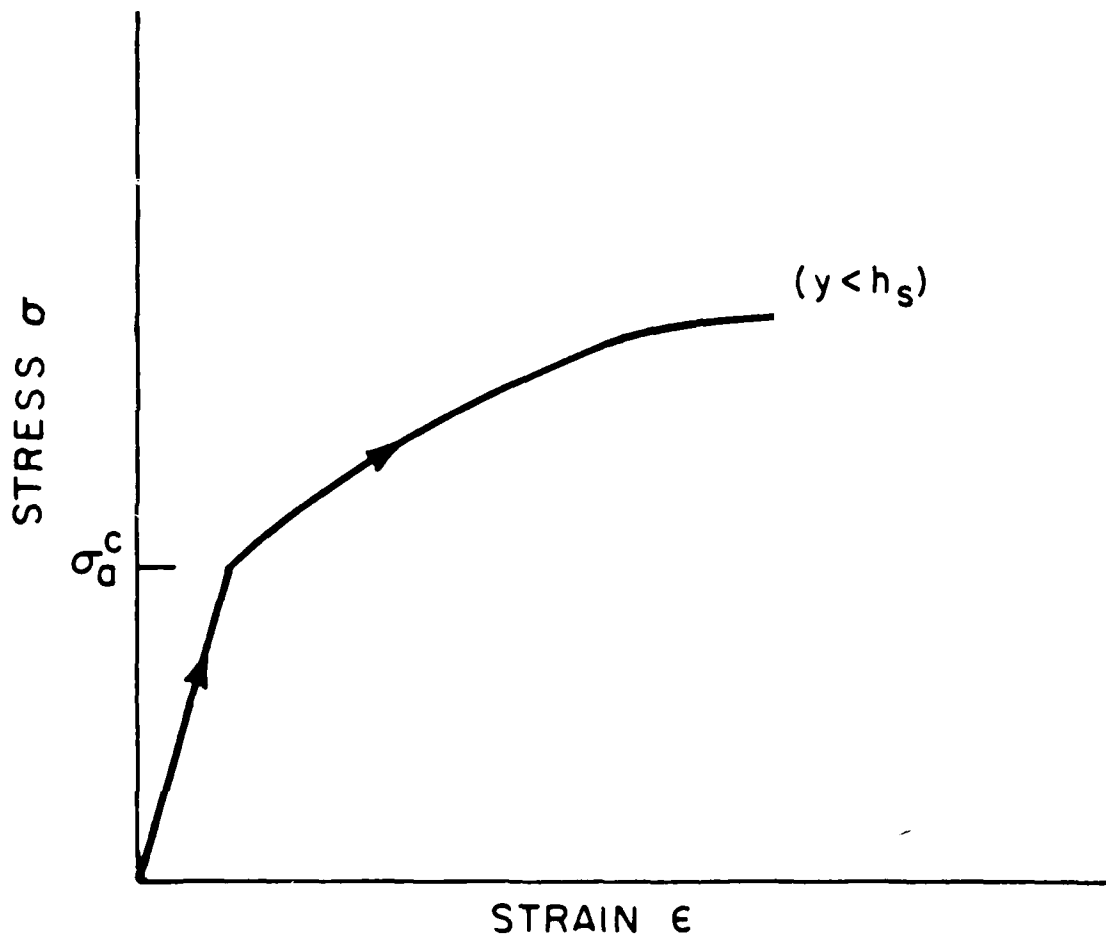
XBL 839-6353

Fig. 6



XBL 841-6527

Fig. 7



XBL83 9- 6341A

Fig. 8

considerations. In particular, the translation of the microcrack zone that accompanies crack advance results in energy dissipation, associated with the energy changes that occur in the remote, fully unloaded, elements of the zone wake ($x = -\infty$). This energy change is characterized by a residual energy density $U(y)$, derived directly from the hysteresis in the stress/strain curve and the permanent strain (fig. 3), such that the change in toughness is given by;²⁶

$$(1-\nu^2)(K_C^\infty)^2/E = (1-\nu_s^2)(K_C^L)^2/E_s + 2 \int_0^h U(y)dy \quad (7)$$

where h is the process zone width.

Evaluation of the toughening due to the energy deposited in the process zone wake requires further comprehension of relationships between the process zone width and the crack tip stress field, as well as trends in $U(y)$ with distance from the crack surface. A detailed determination of these relationships requires explicit calculation of the crack tip stress field in the presence of the process zone. Such calculations are beyond the scope of the present analysis. However, in the analagous problem of a martensitic crack tip process zone, Budiansky et al.²⁶ established that the stress field in the vicinity of the process zone boundary can be expressed in terms of the linear crack tip field relations, but with a stress intensity factor dictated by the mean value between the remote and local stress intensities,

$$K = (K^\infty + K^L)/2 \quad (8)$$

It is assumed that similar behavior obtains at the microcrack process

$$\frac{K_c^\infty}{K_c^0} = \frac{[1-v^2(1-2N_s\ell^3/9)]^{1/2}(1-f_s)}{(1-v^2)^{1/2}(1-2N_s\ell^3/9)^{1/2}} \quad (5)$$

where N_s is the microcrack density at saturation. Further refinement is achieved by assuming that about half of the facets are subject to microcracking at saturation⁺, whereupon $v \approx 1/4$, $f_s \approx 0.5$ and $N_s \approx 3/\ell^3$. With this choice of saturation parameters, the toughness ratio becomes

$$\frac{K_c^\infty}{K_c^0} \approx 0.9 \quad (6)$$

Thus, there is a slight decrease in toughness in the presence of a frontal microcrack zone irrespective of the grain facet size, the microcrack process zone size and the permanent strain. Consequently, it is concluded that the frontal process zone is ineffective as a toughening mechanism.

3. STEADY STATE PROPAGATION

3.1 General Considerations

In steady state, the microcrack process zone is of uniform width (fig. 4), characteristic of the asymptote in the R-curve. The fracture toughness in this configuration can be determined from energy balance

⁺This assumption is consistent with the notion, introduced above, that the residually compressed facets do not microcrack, in a discrete sense, prior to macrocrack extension.

microcracking and f_s is the fraction of microcracked facets in the saturation zone. However, the subsequent results are not particularly sensitive to the specific choice of the degradation function.

The crack growth criterion, used in conjunction with an analysis of the local stress intensity in the presence of the process zone, permits evaluation of the influence of the frontal microcrack zone on the fracture toughness. The near tip field can be ascertained by noting that J is path independent for the frontal process zone, because all volume elements experience monotonic straining. Hence, if a contour is taken outside the process zone,

$$J = (1-\nu^2)(K^\infty)^2/E \quad (2)$$

where K^∞ is the stress intensity associated with the applied loads, ν is Poisson's ratio and E is Young's modulus. The corresponding J for a contour within the saturation zone at the crack tip, is;

$$J = (1-\nu_s^2)(K^l)^2/E_s \quad (3)$$

where K^l is the local stress intensity. Equating J from eqns (2) and (3) and setting K^l equal to the critical value for the degraded material, K_C^l , the measured toughness, K_C^∞ becomes,

$$\frac{K_C}{K_C^0} = \left[\frac{(1-\nu_s^2)}{(1-\nu^2)} \frac{E}{E_s} \right]^{1/2} (1-f_s) \quad (4)$$

Using the moduli and Poisson's ratios determined for microcracked material (eqn (14) in part I), we obtain

equals the threshold stress¹, σ_{th} . Close to the crack tip, the stress field and the microcrack density vary rapidly. The material response in this region, although critical to the analysis of crack extension, is not well understood. For present purposes it is assumed that microcracking saturates, such that the stress-strain response exhibits linearity at large strains (fig. 3) - with a slope dictated by the modulus E_s of the microcrack saturated material. This assumption allows the near tip crack field to be characterized by a stress intensity factor, K , and thereby, permits a rational choice for the crack growth criterion, as discussed below. This assumption is predicated on the notion that those facets subject to appreciable residual compression¹ will not be amenable to stress induced microcracking, prior to extension of the primary crack tip.¹⁶ The alternate approach (required in the absence of a saturation condition) would entail the use of J to characterize the crack tip field, coupled with an appropriate crack growth criterion.

The microcracks in the process zone immediately ahead of the crack tip deteriorate the local fracture resistance. An estimate of this deterioration, expressed in terms of a critical stress intensity factor K_c , establishes a tangible criterion for the prediction of crack growth. Studies on porous glasses²⁷ indicate that an appropriate choice might be;

$$K_c^l \approx K_c^0 [1 - f_s] \quad (1)$$

where K_c^0 is the fracture resistance of the material without

A recently established continuum mechanics description of martensitic transformation toughening^{25,26} has features similar to microcrack toughening: specifically, the existence of nonlinearity and hysteresis in the stress/strain response of the process zone²⁶ (Fig. 2). Studies by McMeeking and Evans²⁵ and Budiansky et al²⁶ revealed that R-curve behavior is inherent in martensitic transformation toughening, originating from the gradual unloading of the process zone wake which forms during crack propagation. The purpose of the present study is to establish a similar continuum mechanics description of microcrack toughening, as needed to quantify the toughening process, to identify the physical origin of the R-curve and to clarify the toughness measurements obtained with various tests. For this purpose, the non-linear characteristic of a microcracking medium is used.¹ The fracture energies may then be calculated both at the initiation of crack propagation and at the steady-state crack propagation stage, corresponding to the two extremities on the R-curve. Correlations between the results of the theoretical analysis and experimental data are also presented.

2. INITIAL CRACK PROPAGATION

The configuration of the system at the initiation stage of crack propagation is shown schematically in Fig. 2. The macrocrack is originally in a microcrack-free medium and a frontal microcrack zone develops as the load gradually increases. The microcrack zone is enclosed by the contours on which the maximum principal stress

I. INTRODUCTION

In single phase anisotropic polycrystalline materials, the occurrence of microcracking is associated with the microstructural residual stresses arising from thermal contraction mismatch among randomly oriented grains, as discussed in the accompanying paper.¹ In the presence of a discrete macrocrack, subject to load, the crack tip stress field induces microcracks at the nearby boundary facets to form a microcrack process zone. This process zone is expected to modify the fracture toughness.²⁻¹⁶ In particular, the microcracked process zone is more compliant than the un-microcracked region.¹⁶ Hence, the crack tip stress singularity is relaxed. However, the microcracks adjacent to the macrocrack tip deteriorate the local fracture resistance of the medium.^{11,16} Counteracting effects are thus in evidence.

An important characteristic of the microcrack toughening process is the existence of resistance (R) curve behavior^{9,12-15} (Fig. 1), wherein the fracture resistance is a monotonically increasing function of the crack tip advance distance Δa , rather than a single-valued parameter. Several experimental observations of prominent R-curve behavior have been reported.^{14,15} Yet, the basis for its existence has not been well established and confusion often arises among experimental toughness measurements obtained with different tests¹⁷⁻²⁴ (e.g. notch beam and double cantilever beam tests) which monitor fracture instability at different stages of crack propagation. Furthermore, most of the theoretical analyses^{7,8,10,12} attempting to simulate microcrack toughening have not incorporated the R-curve effect.

SOME EFFECTS OF MICROCRACKS ON THE
MECHANICAL PROPERTIES OF BRITTLE SOLIDS

II. Microcrack Toughening

by

A. G. Evans and Y. Fu

Department of Materials Science and Mineral Engineering
University of California, Berkeley, CA 94720

ABSTRACT

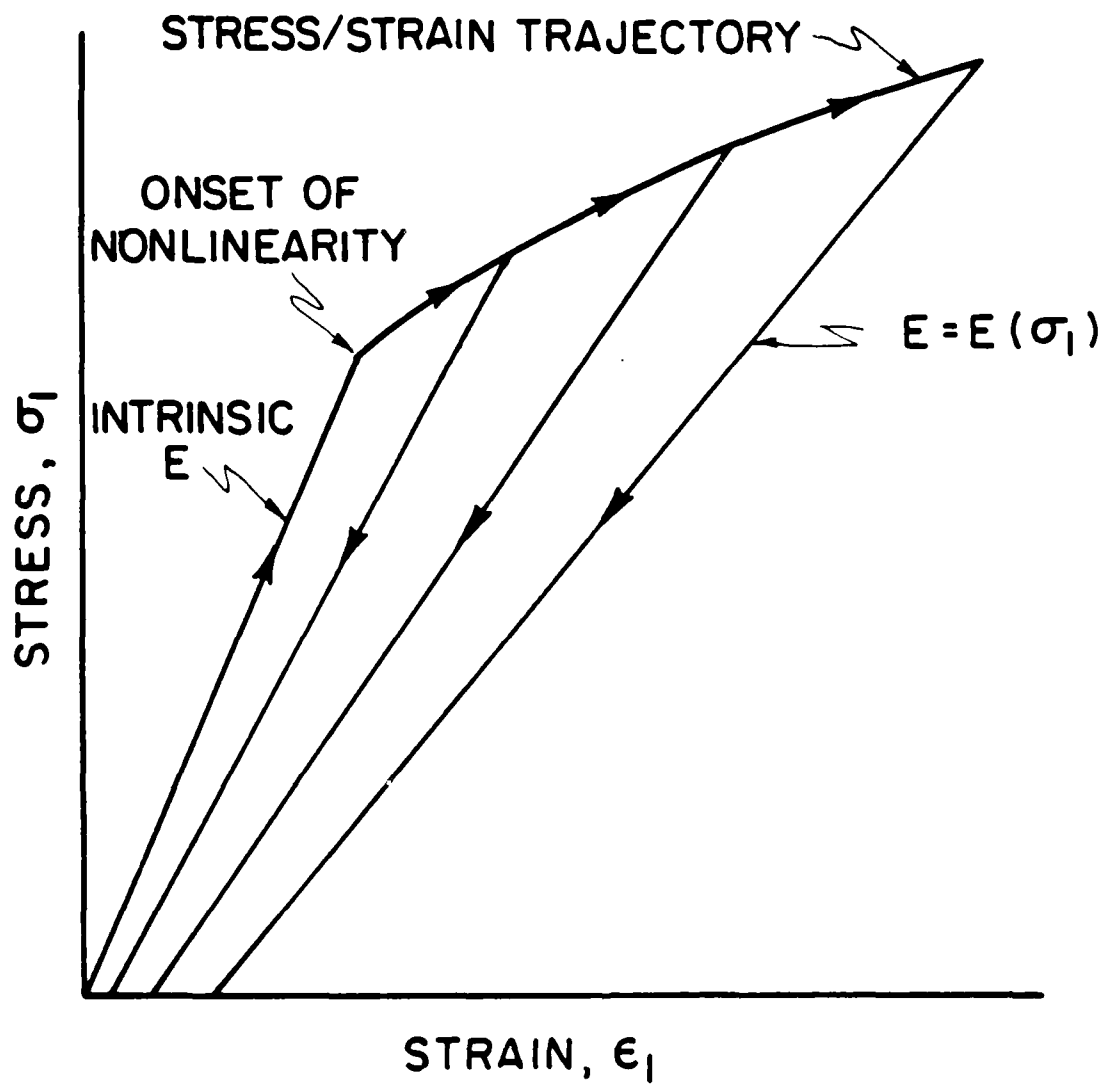
The stress-strain characteristics of a microcracking material are used as the basis for computations of the fracture toughness, by applying a line integral formulation, pertinent to frontal and steady-state microcrack process zones. The calculated toughness is used to predict the trends in toughness with grain size and specimen geometry. The trends are correlated with experimental data.

CHAPTER I-b

SOME EFFECTS OF MICROCRACKS
ON THE MECHANICAL PROPERTIES
OF BRITTLE SOLIDS

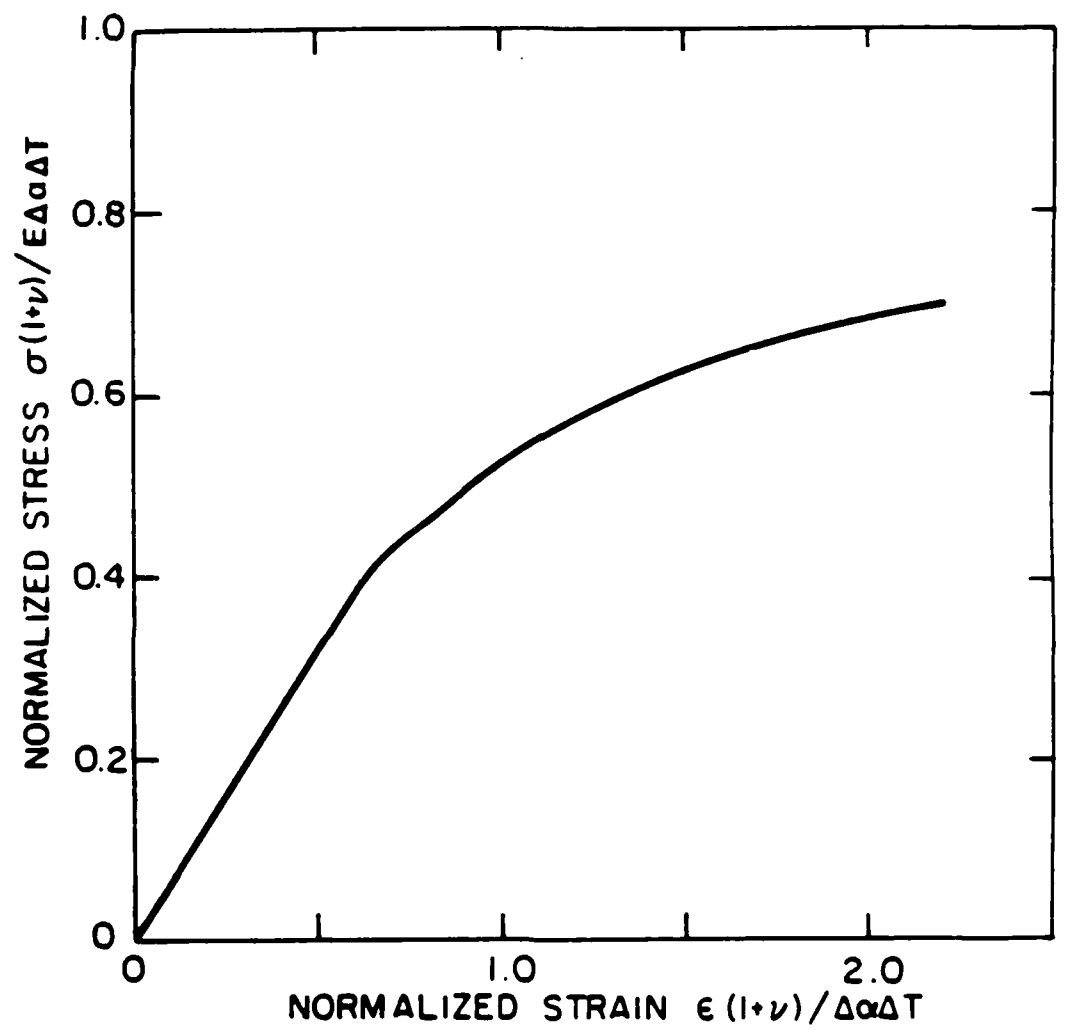
II. Microcrack Toughening

Y. Fu and A. G. Evans



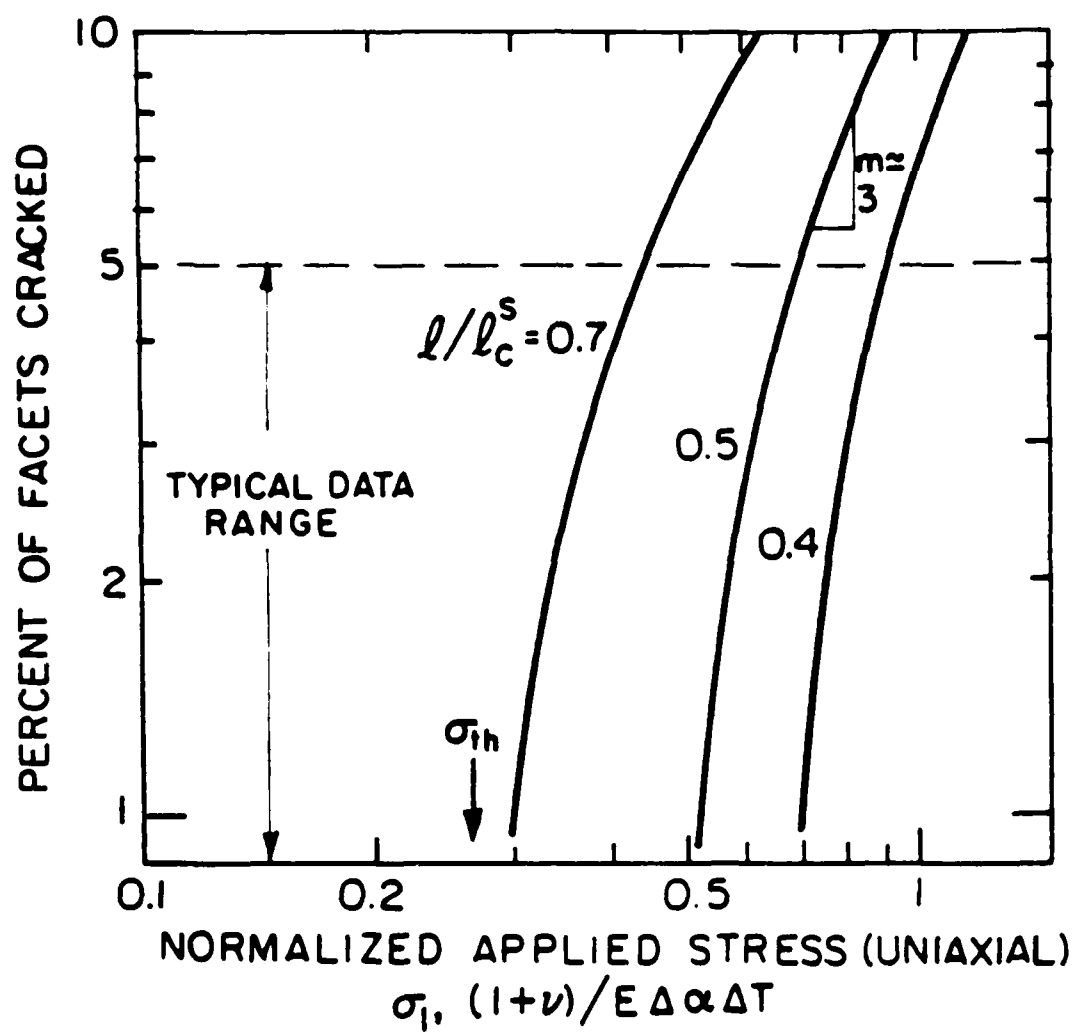
XBL 8410- 7408

Fig. 13



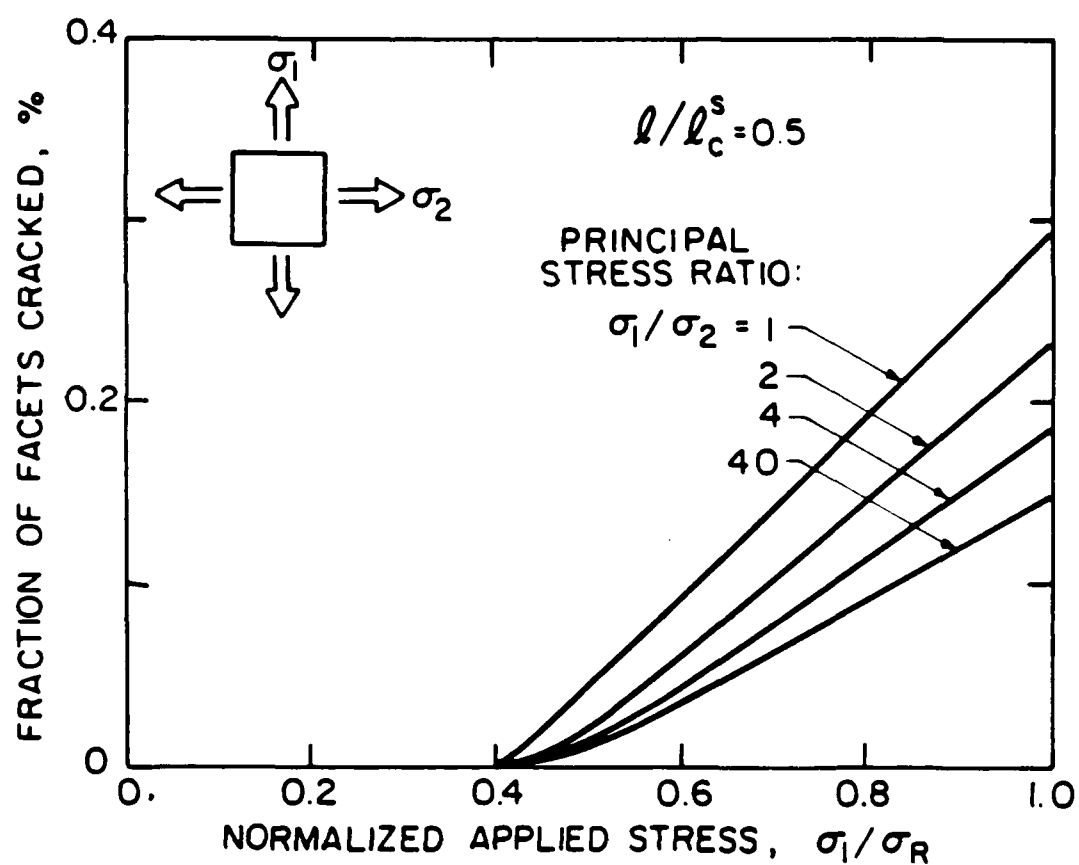
XBL 839-6340A

Fig. 12



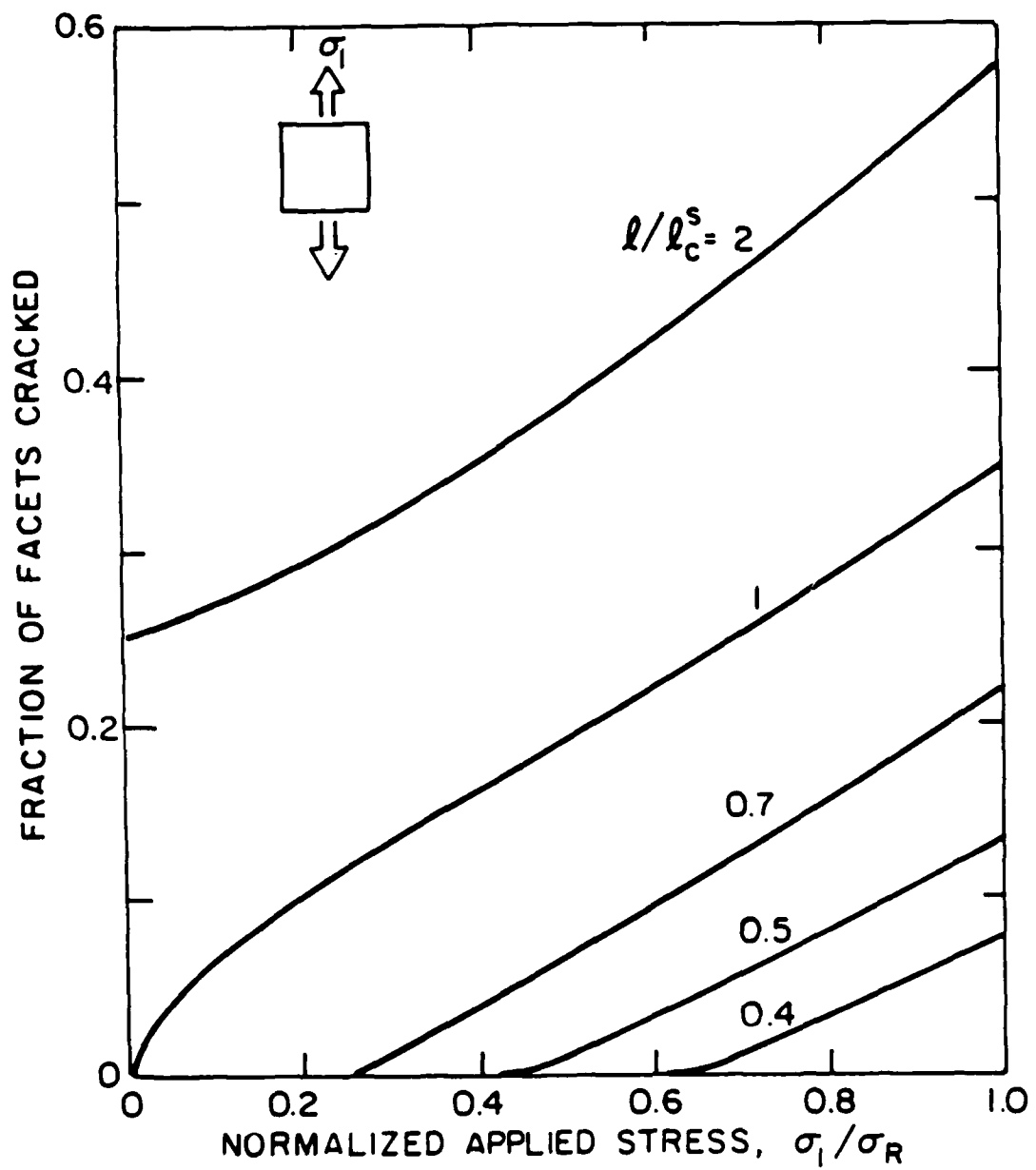
XBL 839-6361 B

Fig. 11



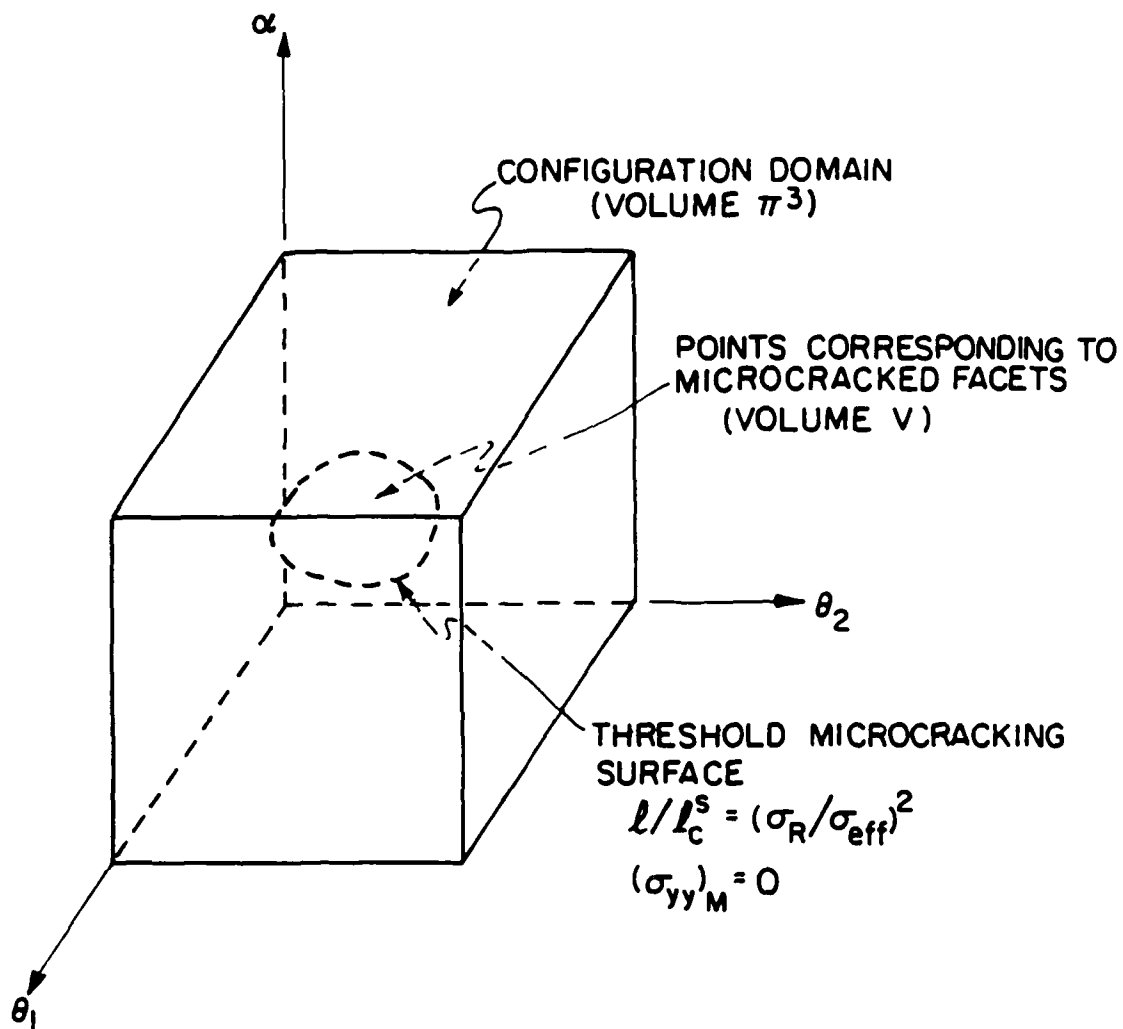
XBL 839-6358A

Fig. 10b



XBL 839-6357A

Fig. 10a



XBL 839-6356

Fig. 9

zone boundary. With this assumption, the width of the process zone can be related to the threshold stress, such that

$$h \approx \frac{(K_c^\infty + K_c^l)^2}{16\sigma_{th}^2} \quad (9)$$

Within the process zone, $y < h$, the linear crack field relations also indicate that each strip element, dy (fig. 4), experiences a peak stress, $\hat{\sigma}$, in the vicinity of the crack tip (fig. 5). This peak stress is of paramount significance because it dictates the residual energy density, $U(y)$, ascribed to each element (fig. 6). For present purposes, it is assumed that a reasonable estimate of $\hat{\sigma}$ can also be obtained from the linear field relations, with amplitude determined by the mean stress intensity. This assumption gives;

$$\hat{\sigma} \approx \frac{K}{2\sqrt{y}} \quad (10)$$

It is recognized that this approximation is most appropriate near the zone boundary ($y \rightarrow h$), but inappropriate near the crack tip ($y \rightarrow 0$) where the field is dominated by K_c^l . The result obtained with eqn (10) should thus constitute an upper bound. Furthermore, the results derived in this way only have validity when the process zone h is fully contained within the test specimen. Hence, the analysis is restricted to conditions wherein, $\sigma_{th} > 0$.

3.2 The Energy Density

The energy density $U(y)$ in eqn (7) can be obtained directly from the area under the stress-strain curve (fig. 6), as

$$\begin{aligned}
U(y) = & \frac{(1+k)\sigma_{th}^2}{E} \left\{ \frac{\hat{\sigma}/\sigma_{th}}{1+c - (\hat{\sigma}/\sigma_{th})} + 2\nu^2 c \left(\frac{\hat{\sigma}}{\sigma_{th}} \right)^2 - (1+2\nu^2 c) \frac{\hat{\sigma}}{\sigma_{th}} \right\} \\
& + \frac{(1+k)\sigma_{th}^2 \chi^2 m(1+\nu)}{6E} \left\{ \left(\frac{\hat{\sigma}}{\sigma_{th}} \right)^2 - 1 \right\} \\
& + \frac{\sigma_{th}^2 \chi^2 m^2 (1+\nu^2)}{36E(1-\nu)} \left\{ \frac{\hat{\sigma}}{\sigma_{th}} - 1 \right\}^2
\end{aligned} \tag{11}$$

where χ is a dilatational coefficient of order unity, m is a microcrack density parameter in the range $1/4$ to 2 , k is a coefficient determined by the principal stress ratio, σ_1/σ_2 , and C is a facet size parameter, as defined in Part I. The first term in eqn (11) is due to the unloading of the more compliant microcracked material elements (fig. 6), while the other two terms are provided by the residual energy in the wake, due to the permanent dilatation. It is noted that $U(y)$ decreases as σ/σ_{th} decreases and tends to zero at the zone boundary ($\hat{\sigma} = \sigma_{th}$, or $y = h$), because there can be no stress-strain hysteresis or permanent dilatation as the microcrack density approaches zero.

3.3 The Steady State Toughness

The energy deposited in the process zone wake can be ascertained by integrating the energy density (eqn 11) over the zone width, h . For this purpose, it is noted that, within the saturation zone ($y < h_s$), the

peak stress $\hat{\sigma}_s$ is approximately invariant with y ($U(y) \approx U(h_s)$), while in the remainder of the zone ($h_s < y < h$), the peak stress decreases with y , as expressed by eqn (10). It is thus convenient to evaluate the residual energy in two parts,

$$\int_0^h U(y) dy = \int_0^{h_s} U(y) dy + \int_{h_s}^h U(y) dy. \quad (12)$$

Hence, incorporating $U(y)$ from eqn (11), $\hat{\sigma}$ from eqn (10) and h from eqn (9), integration of eqn (12) gives;

$$2 \int_0^h U(y) dy = \frac{1-\nu^2}{E} K^2 \left\{ \frac{1+k}{4(1-\nu^2)} Q(C,D,\nu) - \frac{(1+k)\chi_m}{6(1-\nu)} \ln D + \frac{(\chi_m)^2(1+\nu)}{144(1-\nu)^2} (D-1-2\ln D) \right\} \quad (13)$$

where K is given by eqn (8),

$$Q(C,D,\nu) = \frac{D}{1+C-C/D} + 2\nu^2 C(1-2\ln D) + \frac{2(1-D)}{1+C} - (1-2\nu^2 C)(2-D) - \frac{2C}{(1+C)^2} \ln [(1+C)D-C]$$

and

$$D = 2\sigma_{ch} \sqrt{h_s} / K$$

Inserting eqn (13) into eqn (7) the energy balance relation becomes

$$\frac{1-\nu^2}{E} (K_C^\infty)^2 = \frac{1-\nu_s^2}{E_s} (K_C^l)^2 + \frac{1-\nu^2}{4E} (K_C^\infty + K_C^l)^2 \left\{ \frac{1+k}{4(1-\nu^2)} Q(C,D,\nu) \right. \\ \left. - \frac{(1+k)\chi_m}{6(1-\nu)} \ln D + \frac{(\chi_m)^2(1+\nu)}{144(1-\nu)^2} (D - 1 - 2\ln D) \right\} \quad (14)$$

and the toughness K_C^∞ in the presence of a steady-state process zone is given by

$$\frac{K_C^\infty}{K_C^o} = \frac{S/8 + \sqrt{4/S - 11S/80}}{1-S/4} \quad (15a)$$

where

$$S = \frac{(1+k)}{4(1-\nu^2)} Q(C,D,\nu) - \frac{(1+k)\chi_m}{6(1-\nu)} \\ + \frac{(\chi_m)^2(1+\nu)}{144(1-\nu)^2} (D - 1 - 2\ln D)$$

The corresponding fracture energy \mathcal{G}_C^∞ is;

$$\frac{\mathcal{G}_C^\infty}{\mathcal{G}_C^o} = \frac{S/8 + \sqrt{4/S - 11S/80}}{1-S/4} \quad (15b)$$

Final solutions for the trends in toughness require that further information be provided regarding the saturation zone width, h_s . The most plausible assumption, as noted above, regards saturation as a state defined by a saturation density, N_s , of microcracks. With this

assumption, a saturation stress can be derived from eqn (24) in part I which, in conjunction with eqn (9) gives,

$$\sqrt{h_s} = \frac{K/2\sigma_{th}}{\left\{ 1 + [2m(\sqrt{\ell_c^s/\ell} - 1)]^{-1} \right\}} \quad (16a)$$

and thus

$$D = \frac{2m(\sqrt{\ell_c^s/\ell} - 1)}{1 + 2m(\sqrt{\ell_c^s/\ell} - 1)} \quad (16b)$$

Substituting D from eqn (16) into eqn (14) determines the toughness. Specific results are presented in the following section.

4. TRENDS IN TOUGHNESS

4.1 Effects of Grain Size on Steady State Toughness

The general solution for the toughness (eqn 15) can be used to predict variations in fracture energy with grain size, based on ℓ_c^s as a material parameter, as plotted in fig. 7, for specific choices of the coefficient m and assuming $f_s = 0.5$. The trends, schematically illustrated in fig. 8, indicate two opposing influences. The permanent dilatational component of the toughness (the second and third terms in S) increases with increase in grain size, while the toughening attributed to the increased compliance (the first term in S) increases with decrease in grain size. Consequently, a minimum toughness obtains.

Additionally, as $\ell \rightarrow \ell_c^S$, the microcrack zone boundary reaches the specimen boundaries. Some of the permanent strain induced residual energy is thus relaxed and the toughness becomes smaller than the value predicted by eqn (15). Furthermore, when $\ell > \ell_c^S$, a proportion of the microcracks form thermally. These microcracks do not contribute to the toughness, because they do not participate in the stress-strain hysteresis. Consequently the toughness must diminish with increase in grain size, beyond ℓ_c^S . Hence, a toughness maximum must occur at ℓ_c^S , as schematically represented on fig. 8.

The trend toward an increase in toughness with increase in grain size, due to dilatation, is reflected in the corresponding changes in the threshold stress σ_{th} and the zone width, h . As ℓ increases, σ_{th} decreases, and the permanent dilatation increases, causing the residual energy per unit thickness of process zone to decrease. Meanwhile, the zone width increases (eqn 16b). The net effect is a total energy, integrated through the process zone, that becomes larger as ℓ increases. Consequently, the change in zone width dominates the trend in toughness. Similar behavior is encountered in transformation toughening²⁶ and in ductile fracture.

The preceeding dilatational effect contrasts with that for compliance toughening. For the latter, the energy density varies more strongly with $\hat{\sigma}$, due to the increased compliance on unloading (fig. 6). Consequently, in this instance, the energy density changes more rapidly with grain size than the zone width, resulting in a toughness that decreases with increase in grain size.

Another grain size feature concerns the ability of a crack to sustain a discrete microcrack process zone. A prior analysis¹⁶ revealed that, in single phase polycrystals, the grain size was required to exceed $\sim 0.4\ell_c^S$ in order to permit process zone development. The preceding toughness characteristics should thus be considered subject to truncation when $\ell \leq 0.4\ell_c^S$, unless modes of microcracking other than thermal expansion anisotropy are present (e.g. twins or slip bands).

4.2 Effects of Specimen Geometry

Fracture toughness tests conducted with a sawn notch, such as the single edge notched bend (SENB) specimen, entail an initial configuration with no microcrack process zone (except for microcracks introduced by sawing). Consequently, initial growth from the notch occurs with only a frontal process zone and hence, the measured toughness should be similar to the intrinsic toughness. Conversely, with cantilever beam tests (DCB, DT etc), experiments are frequently conducted with a precrack, formed by prestressing or by stable crack extension. A microcrack process zone forms over the surface of the precrack. Further crack growth during the toughness measurement process is thus conducted in the presence of a process zone wake. Hence, the steady state toughness should be more pertinent. This difference in fracture behavior, in the presence of an initial process zone wake, is considered to be the principal reason for the discrepancy between the SENB and DCB toughness measurements on Al_2O_3 and other

anisotropic oxides.¹⁷⁻²⁴

4.3 Comparison with Experiment

Experimental measurements of the variation of toughness of an anisotropic oxides with grain-size, using cantilever beam methods, generally indicate the existence of a peak toughness¹⁰ (fig. 7). Recalling from the preceding section that cantilever beam methods yield steady state behavior, the peak in toughness should coincide with the critical grain size for thermal microcracking (fig. 8). On this basis, comparison with the predicted toughness (fig. 7) indeed suggests that the toughness below the peak can be reasonably attributed to the dilatation caused by the microcracks in the process zone. However, the data do not confirm the existence of the compliance toughening predicted at small grain size.

5. CONCLUDING REMARKS

An analysis of toughening based on the non-linear, irreversible stress-strain characteristics of a microcracking solid has been presented. An important contribution to the toughness due to the microcrack induced dilatation has been predicted at grain sizes below the size at which thermal microcracking initiates. The trends are apparently consistent with experimental data. However, the comparison with experiment has required the assumption that discrete microcracking saturates near the crack tip when about half of the facets have failed. Thereafter, macrocrack propagation proceeds by the

failure of the remaining facets. This assumption is based on the recognition that about half of the facets along the crack front are subject to residual tension and thus, are amenable to discrete microfracture. However, additional study of this concept is clearly demanded before further progress can be achieved.

A predicted increase in toughness at small grain sizes, due to a compliance effect, is not confirmed by experimental data. It has been presumed that the effect is not observed because a discrete microcrack zone cannot be sustained at small grain sizes. Observations of microcrack process zones are needed to further investigate this issue.

Finally, it has been noted that a peak in toughness should occur at grain sizes equivalent to the grain size for thermal microfracture, λ_c^s . This peak obtains because the thermal microcracks do not contribute to the toughening. The specific trend in toughness above λ_c^s could be predicted using the procedures described in this paper, provided that the density of thermal microcracks is known at each grain size.

REFERENCES

1. Y. Fu and A. G. Evans, this volume.
2. R. G. Hoagland, C. W. Marschall, A. R. Rosenfield, G. Hollenberg and R. Ruh, Mater. Sci. Eng., 15, (1) 51 (1974).
3. C. C. Wu, S. W. Freiman, R. W. Rice and J. J. Mecholsky, J. Mater. Sci., 13, 12, 2659 (1978).
4. R. G. Hoagland, G. T. Hahn and A. R. Rosenfield, Rock Mech., 5, (2), 77 (1973).
5. R. G. Hoagland, J.D. Embury and D. J. Green, Scr. Metall., 9, (9) 907 (1975).
6. A. G. Evans, ibid., 10, (1), 93 (1976).
7. F. E. Buresch, "Fracture Mechanics of Ceramics," vol. 4, pp. 835, edited by R. C. Bradt, D. P. H. Hasselman and F. F. Lange, Plenum Press, N.Y. (1978).
8. W. Kreher and W. Pompe, J. Mater. Sci. 16, (3), 694 (1981).
9. R. G. Hoagland and J. D. Embury, J. Am. Ceram. Soc., 63, (7) 404 (1980).
10. R. W. Rice, S. W. Freiman and P. F. Becher, J. Am. Ceram. Soc., 64 (6), 345 (1981).
11. A. G. Evans and K. T. Faber, J. Am. Ceram. Soc., 64 (7) 394 (1981).
12. N. Claussen, B. Mussler and M. V. Swain, J. Am. Ceram. Soc., 65, (1), C-14 (1982).
13. B. Musller, M. V. Swain and N. Claussen, J. Am. Ceram. Sci., 65,

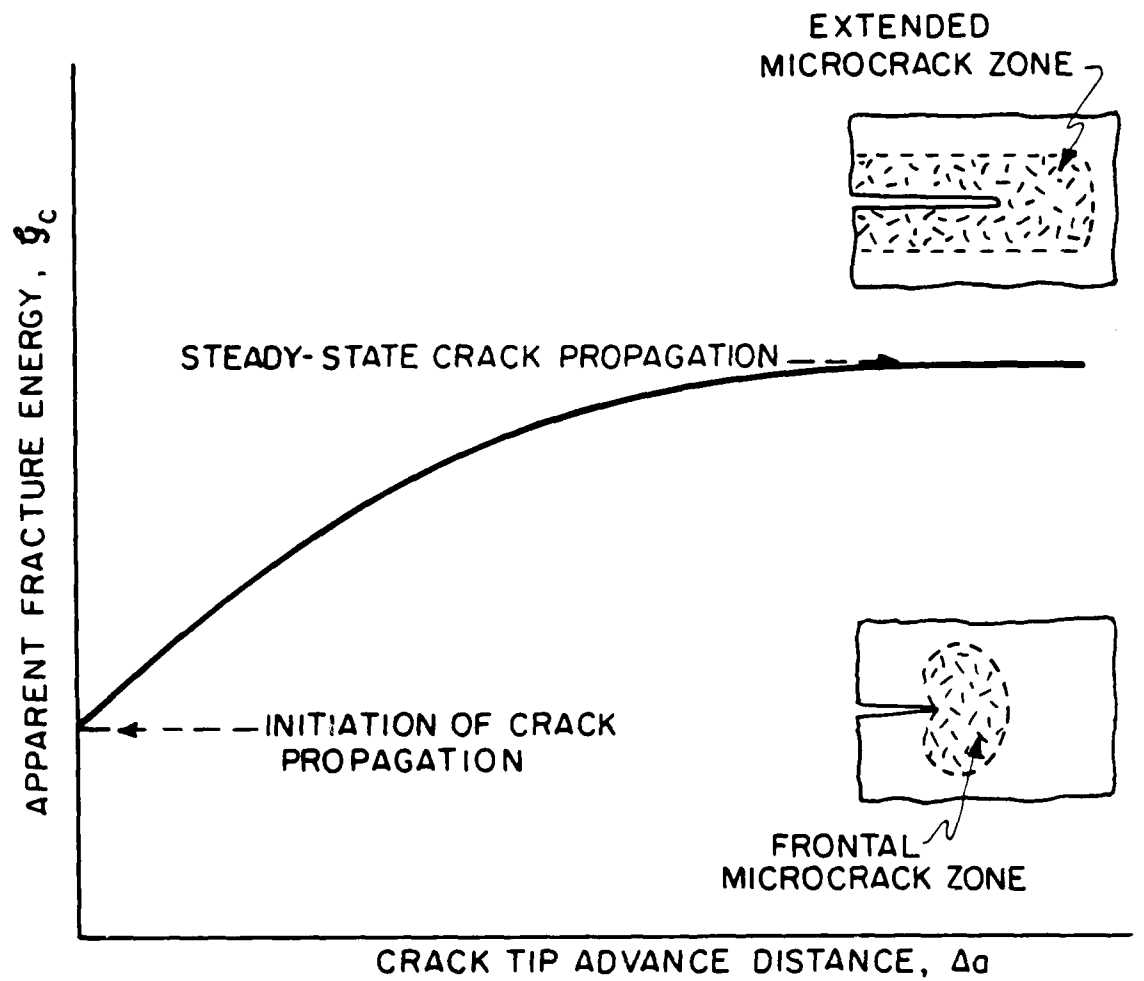
- (11), 566 (1982).
14. H. Hubner and J. Jillek, *J. Mater. Sci.*, 12, 117 (1977).
 15. R. Knehans and R. Steinbrech, *J. Mater. Sci. Letters*, 1, 327 (1982).
 16. Y. Fu and A. G. Evans, *Acta Met.*, 30, 1619 (1982).
 17. L. A. Simpson, *J. Am. Ceram. Soc.*, 56, 11, 610 (1973).
 18. B. J. Dalgleish, P. L. Pratt and J. Sanford, "Science of Ceramics," vol. 8, pp. 659, edited by P. Popper, The British Ceramic Soc., Stoke-on-Trent, England (1976).
 19. P. L. Pratt, "Fracture '77", vol. 3, pp. 909, edited by D. M. R. Taplin, Univ. of Waterloo Press, Waterloo, Canada (1977).
 20. A. G. Evans and G. Tappin, *Proc. Br. Ceram. Soc.*, 20 275 (1972).
 21. N. Claussen, P. Pabst and C. P. Lahmann, *ibid.*, 25 139 (1975).
 22. R. F. Pabst, "Fracture Mechanics of Ceramics," vol. 2, pp. 556, edited by R. C. Bradt, D. P. H. Hasselman and F. F. Lange, Plenum Press, N.Y. (1974).
 23. G. D. Swanson, *J. Am. Ceram. Soc.*, 55 (1), 48 (1972).
 24. S. W. Freiman, K. R. McKinney and H. L. Smith, pp. 659 in Ref. 27.
 25. R. M. McMeeking and A. G. Evans, *J. Am. Ceram. Soc.*, 65 (5), 242 (1982).
 26. B. Budiansky, J. Hutchinson and J. Lambropoulos, *Int. J. Solids & Structures*, 19, 337 (1983).
 27. J. Zwiessler and A. Adams, "Fracture Mechanics of Ceramics," edited by R. C. Bradt, D. P. H. Hasselman, F. F. Lange and A. G. Evans, Plenum Press, N.Y. (1983), vol. 6, p. 211.

Figure Captions

- Fig. 1 A schematic of a resistance (R) curve in which the fracture energy increases monotonically as the crack advances.
- Fig. 2 Frontal process zone configuration which forms at the initiation of crack growth in an originally microcrack-free medium.
- Fig. 3 The nonlinear stress-strain characteristic of elements inside the process zone. At saturation, E_s remains constant, as dictated by the microcrack number density N_s .
- Fig. 4 Extended process zone configuration during steady state crack propagation.
- Fig. 5 Normalized principal stress distribution along the dashed strip in fig. 4.
- Fig. 6 The energy density associated with each strip corresponds to the shaded hysteresis area.
- Fig. 7 Predicted trends in toughness with facet size for two values of m . Also shown are data obtained for Al_2O_3 . Reasonable

agreement at $\ell < \ell_c^s$ obtains for $m \approx 2$.

Fig. 8 A schematic illustration of trends in toughness with facet size.



XBL 839-6339

Fig. 1

ratio of ~ 0.92 (Fig. 5). However, in the as-indented state the corner cracks have appreciably lower strengths than the surface cracks (strength ratio 0.84), presumably because of differences in the residual fields. Therefore, since the capacitors were tested in the as-indented state, the strengths of the corner flaws were taken to be 0.84 of the strength of the equivalent surface flaw. With an additional factor of 0.9 to account for the relative strengths of Knoop and Vickers surface flaws,⁸ the strength of the corner flaws is given by Eq. (1) with $A = 1.527$. Thus, with 5 N Knoop indentation corner cracks in the capacitors, a critical temperature difference of 395°C was measured and a strength of 3 MPa was calculated.

III. THERMAL STRESS ANALYSIS

1) Calculation at Peak Stress

The thermal stress caused by an imposed temperature differential ΔT can be expressed in the general form:⁹

$$\sigma = [E\alpha\Delta T/(1 - \nu)] f_1(bh/k) f_2(kt/C\rho b^2) f_3(z/b, r/b, a/b) \quad , \quad (2)$$

where α is the thermal expansion coefficient, k the thermal conductivity, C the specific heat, ρ the density, h the heat transfer coefficient, t the time, b the specimen width, a the jet width, z and r are position coordinates, and f_1 , f_2 and f_3 are configuration dependent functions. If the parameters α , k , C and h are independent of temperature within the ΔT range selected, Eq. (2) becomes, for a given test configuration and material, and a given time:

ing's modulus, and H is the hardness. The toughness and hardness parameters were obtained from the dimensions of the indentation cracks and the contact pressure⁵ ($K_C = 1.0 \text{ MPa}\cdot\text{m}^{1/2}$, $H = 10 \text{ GPa}$). With these values and $E = 147 \text{ GPa}$ for BaTiO_3 , Eq. (1) yields $S = 70 \text{ MPa}$ for $P = 5 \text{ N}$. The corresponding value of T was found to be 385°C .

Controlled corner flaws were also introduced by indentation. In this case the capacitors were mounted in pairs with their edges butted together. A Knoop indenter was loaded with its tip between the two capacitors, such that one of the long diagonals of the indenter contacted each capacitor normal to the edge. This technique produced well-defined corner cracks. Further experiments were then done to establish an empirical relation between the lengths of corner and surface flaws (an expression analogous to Eq. (1) for the strength of corner flaws is not available). For this purpose, two sets of glass flexure bars were prepared. One set were indented in the center of the respective tensile test surfaces with a Knoop indenter at 12 N load. The other set were indented on their edges using the same method employed to produce corner cracks in the capacitors. In this case the load on the Knoop indenter (N) was chosen such that the radii of the corner and surface cracks were equal. Half of the bars in each set were broken in four-point bending in the indented state, and the other half were annealed to remove residual contact stresses prior to strength testing. The results are summarized in Table I. The difference in strengths of annealed and as-indented specimens reflects the influence of the residual stress. For the annealed bars, the small strength difference between corner and surface cracks (strength ratio = 0.96) is consistent with existing stress intensity factor analyses,^{6,7} which suggest a strength

prior to fracture was used to define the critical temperature differential, ΔT_c . The failure probabilities for corner and surface flaws are plotted as a function of ΔT_c in Fig. 3.

A special technique was required for the optical detection of cracks. (Cracks oriented normal to the as-received surfaces of the capacitors are not visible using conventional optical microscopy, unless dye penetrants are used.) The method, which is generally suitable for translucent materials, is illustrated in Fig. 4. Direct illumination is restricted to a small region within the field of view, and the crack is placed outside that region, in an area which is indirectly illuminated by backscattered light from within the material. Scattering from the crack surfaces causes a change of contrast across the crack (Fig. 4).

(2) Calibration Experiments

Both the analytical and the finite element stress calculations (Section 3) require experimental calibration. This was achieved by measuring ΔT_c for capacitors containing controlled flaws with known failure stresses.

For the surface flaw configuration, the controlled flaws were created by indenting the central test area with a Vickers pyramid at a load of 5 N. The fracture stress for Vickers indentation flaws is given by⁴

$$S = A \left(\frac{K_c}{E} \right)^{1/6} P^{-1/3}, \quad (1)$$

where $A = 2.02$, K_c is the fracture toughness, P is the indenter load, E is the

eries of thermal shock tests, which involved heating the capacitor to a temperature ΔT above ambient, impinging a rapid flow of helium at ambient temperature to the desired area, and determining the critical temperature differential, ΔT_c , to cause fracture. The corresponding thermal stresses were determined using an analytical approximation for the peak stress and finite element analysis for more detailed stress distributions.

1) Test Procedure and Results

Tests were conducted by inserting the capacitors into a holder which provided thermal insulation (using fibrous SiO_2) to all surfaces except the upper test surface (Fig. 2). The test surface was then positioned (by means of a translation stage) beneath the gas jet nozzle within a preheated furnace. For evaluation of the surface flaws, the gas was delivered to the center of the test surface by an alumina tube (1.5 mm inner diameter). For corner flaws, the perimeter of the test surface was exposed to the gas jet by using a tube of rectangular section with an insert to protect the central portion of the surface from the direct gas flow. After permitting the temperature to equilibrate, the helium flow was initiated by a solenoid valve, and allowed to impinge into the capacitor for ~ 60 s. The capacitor was then removed from the furnace and inspected for cracks in an optical microscope.

An incremental test sequence was used for each capacitor. Specifically, the temperature was increased in 10°C intervals until subsequent optical examination revealed a fracture. The fracture event was always characterized by the appearance of a single crack about 1 - 2 mm in length passing through the test area directly beneath the gas stream. The maximum temperature reached

I. INTRODUCTION

Evaluation of the mechanical reliability of ceramic components requires knowledge of flaw populations.^{1,2} Generally, this information is obtained from statistical analysis of mechanical strength measurements, using specimens of simple shape such as flexure bars. This approach is based on the assumption that the flaw population in the bars is the same as that in the component. The inability, in general, to verify this correspondence represents a severe shortcoming of the approach.

In this paper a method for evaluating strength characteristics of surface flaws, directly on actual components, is described. The strength measurements are obtained by applying a well-defined transient thermal stress to the surface, using an impinging gas jet.³ The thermal stress can be applied to selected localized areas, thus enabling spatial variations of flaw populations to be assessed. The method is demonstrated by evaluating flaw populations at two locations in multilayer BaTiO₃ capacitors. The results are then used to predict the reliability of the capacitors in typical service conditions.

II. EXPERIMENTAL

The capacitors were plates with dimensions $6 \times 5 \times 1$ mm. They were tested in the as-received state, with surfaces which had been exposed to a tumbling treatment (Fig. 1). Flaw populations were assessed in two locations; in the center of the faces of the plates (surface flaws) and along the perimeter of the faces (corner flaws). This was done by subjecting each capacitor to a

EVALUATION OF RELIABILITY OF BRITTLE COMPONENTS BY
THERMAL STRESS TESTING

D. Johnson-Walls, M.D. Drory and A.G. Evans
Department of Materials Science and Mineral Engineering
University of California
Berkeley, CA 94720

D.B. Marshall
Rockwell International Science Center
1049 Camino Dos Rios
Thousand Oaks, CA 91360

K.T. Faber
Department of Ceramic Engineering
Ohio State University
Columbus, OH 43210

ABSTRACT

A thermal stressing technique has been applied to evaluate two distinct flaw populations (surface and corner) in BaTiO_3 multilayer capacitors. The mechanical reliability of the capacitors was deduced by relating the thermal stress response to the mechanical strength of the material. The surface flaw population alone yields relatively high survival probabilities, whereas incorporation of the corner flaw population severely reduces the probability of survival.

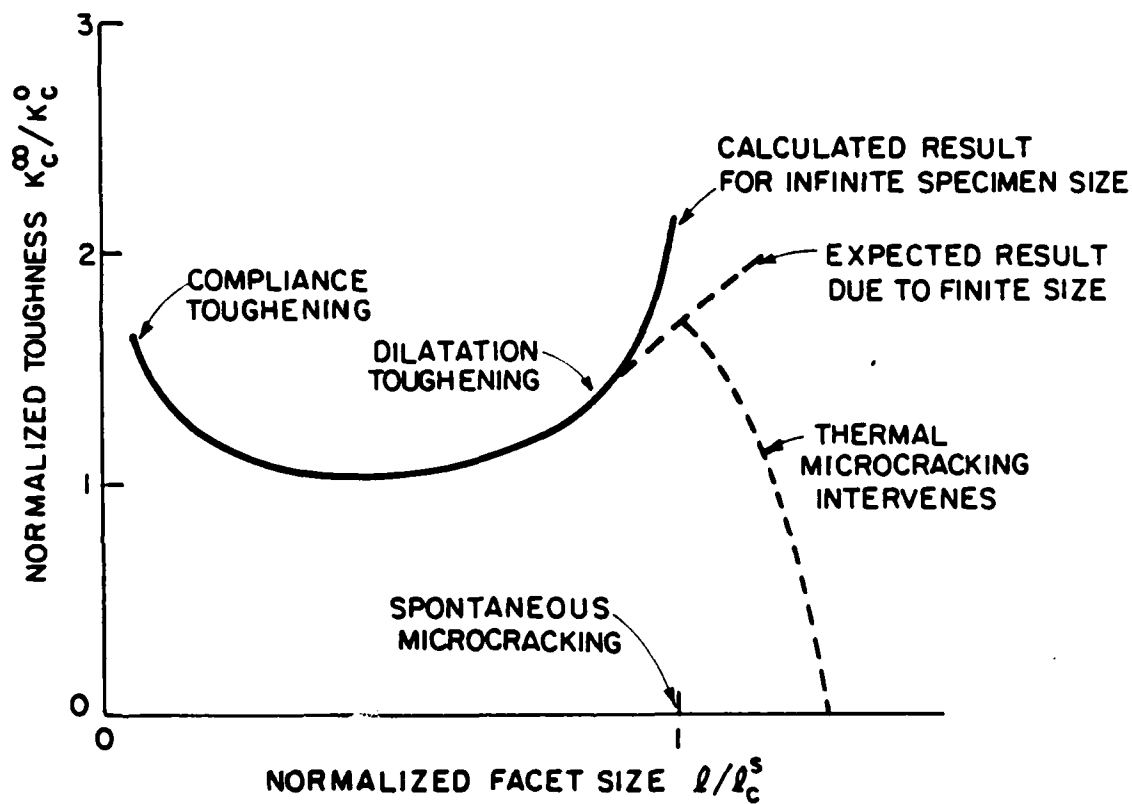
CHAPTER II

EVALUATION OF RELIABILITY IN BRITTLE COMPONENTS

BY THERMAL STRESS TESTING

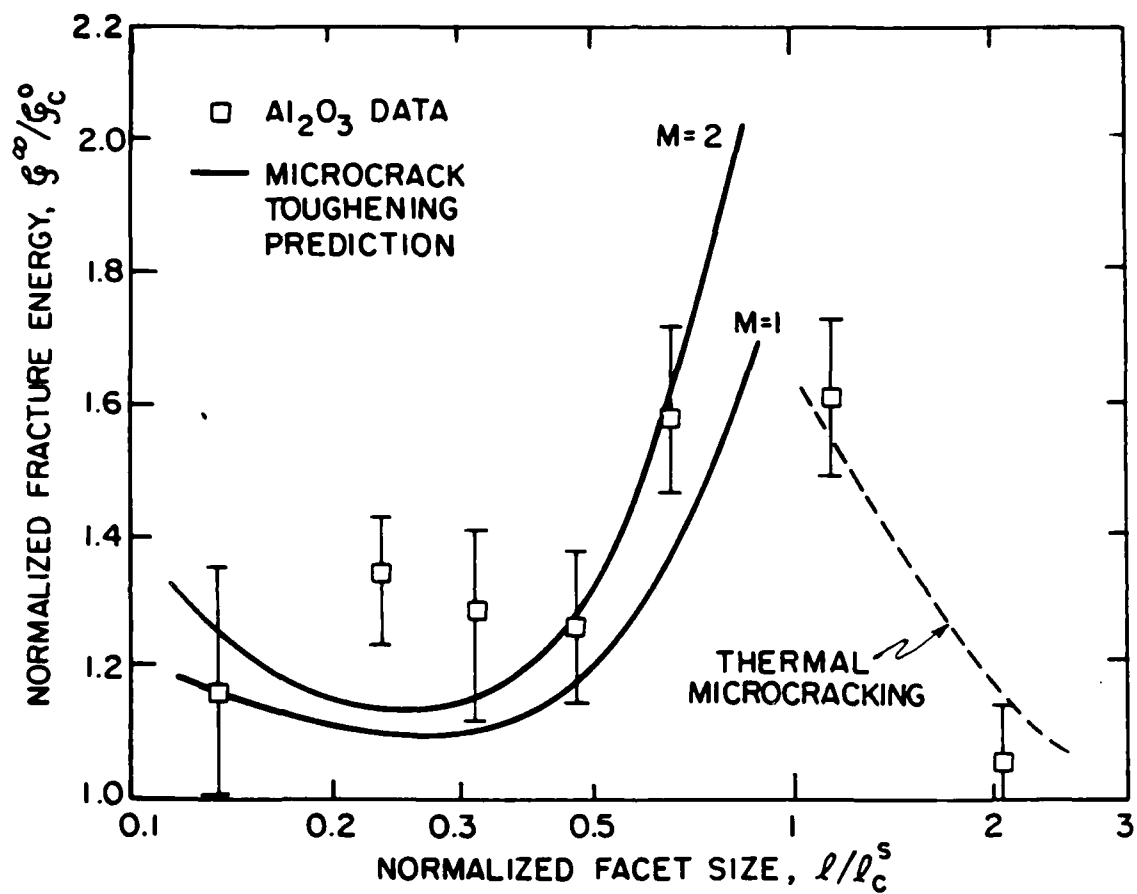
D. B. Marshall, D. Johnson-Walls, M. D. Drory, A. G. Evans and

K. T. Faber



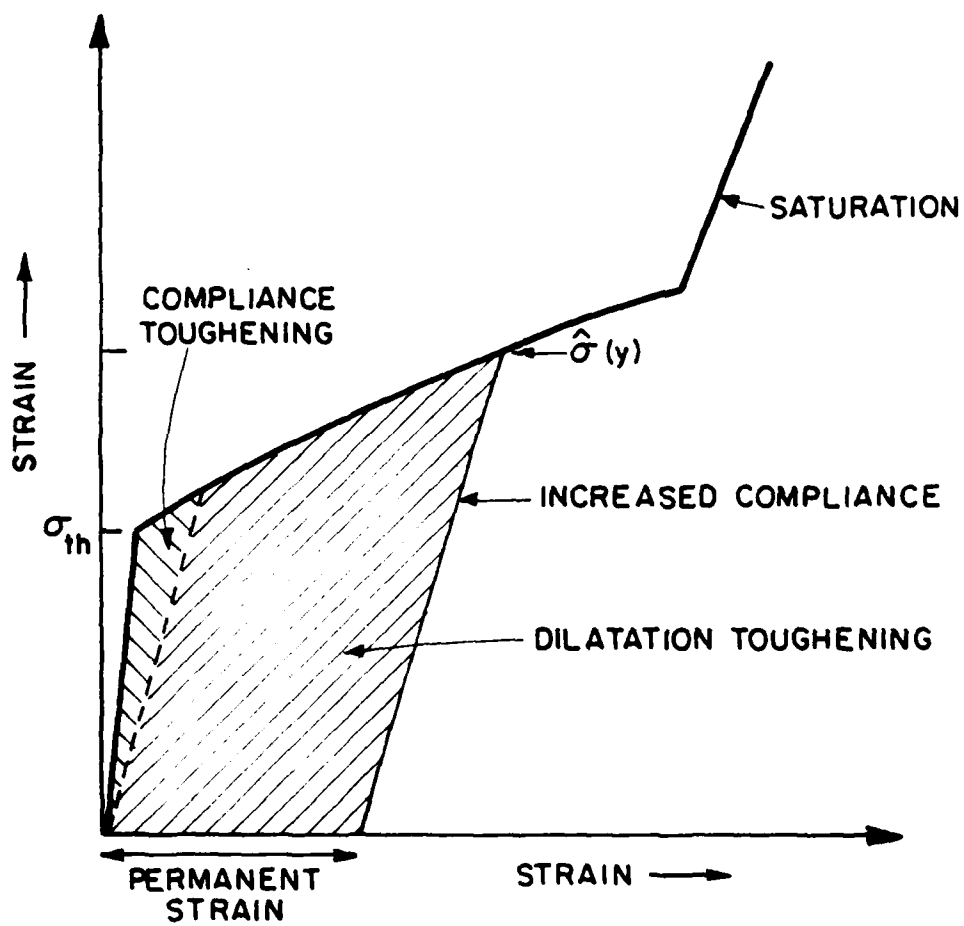
XBL84 4-6885

Fig. 8



XBL 8410-7409

Fig. 7



XBL 844-6884

Fig. 6

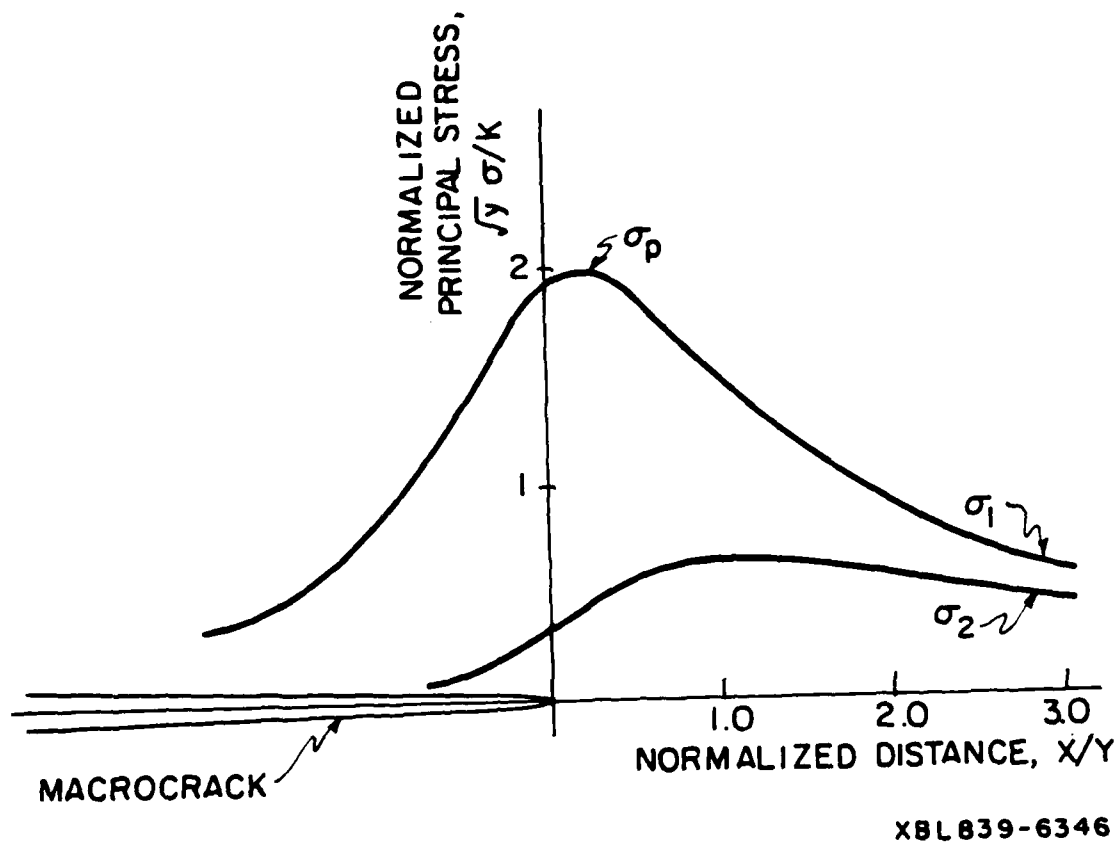
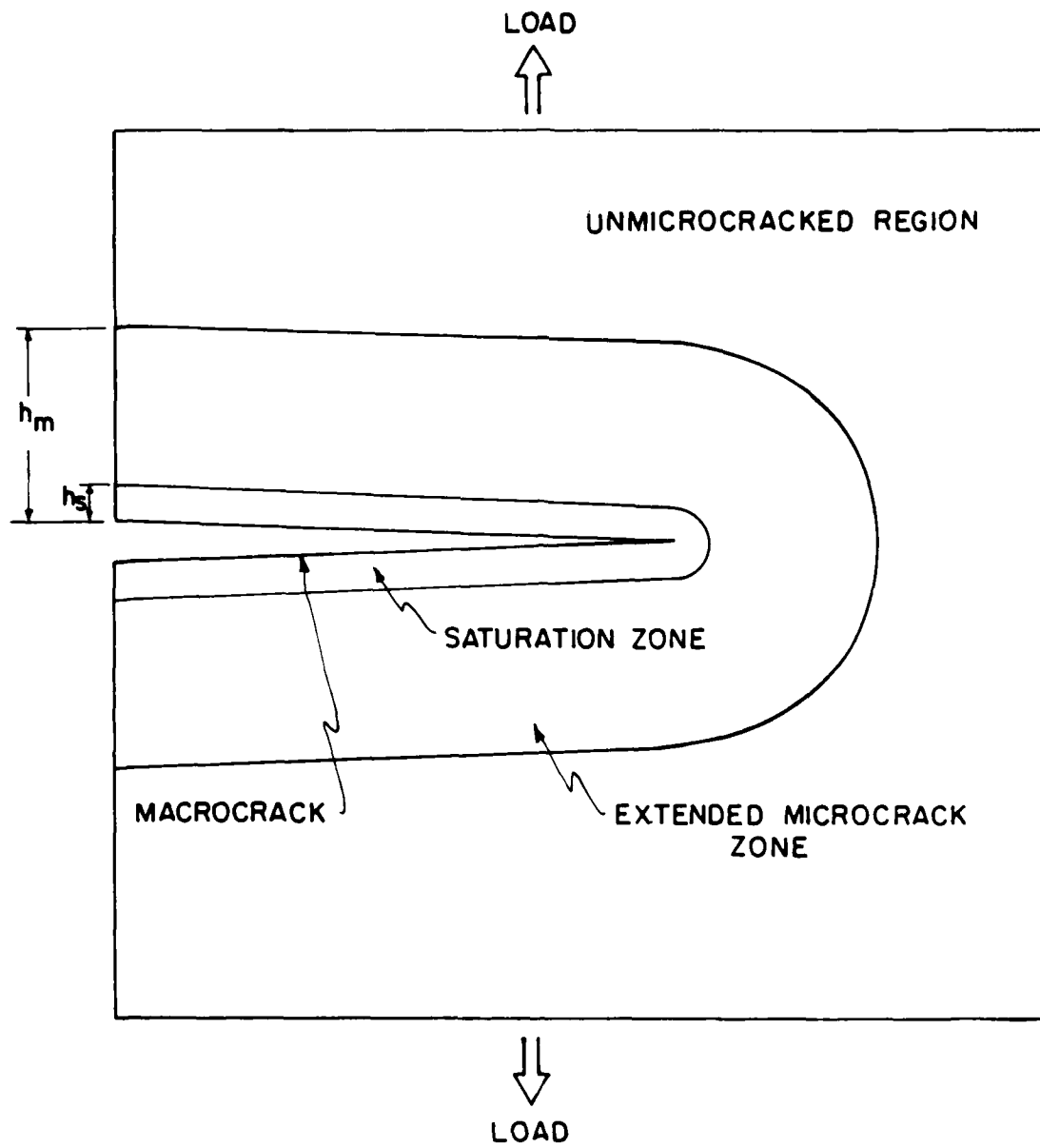
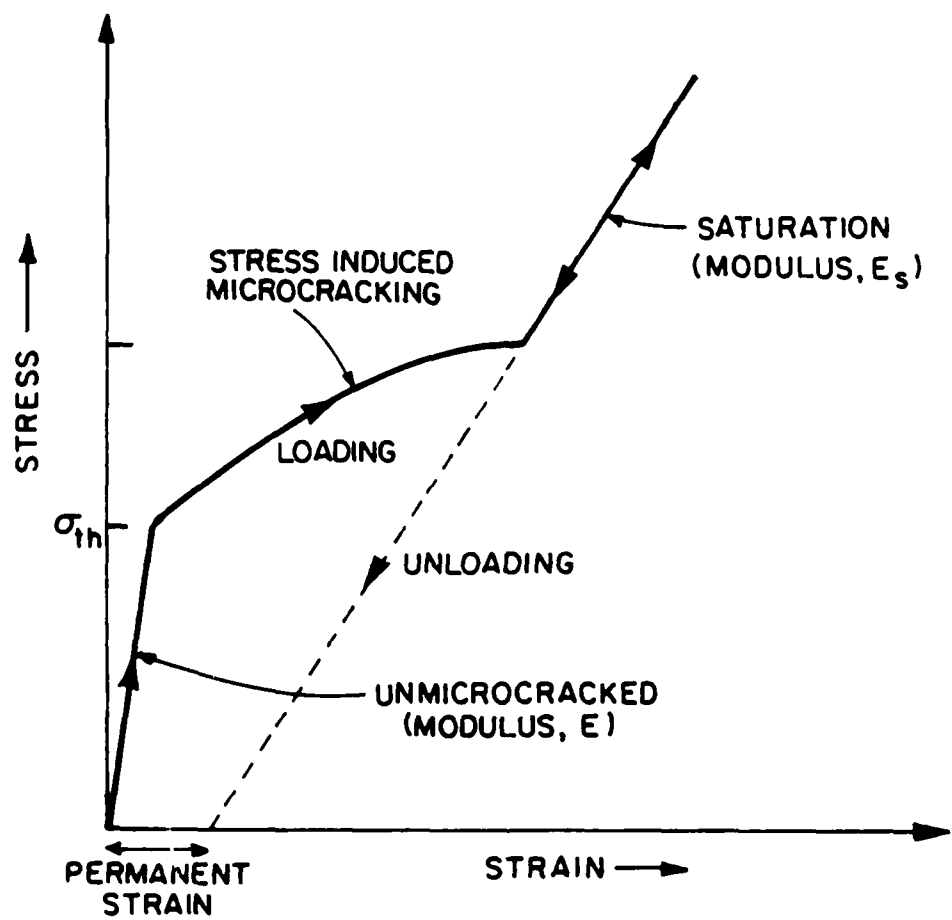


Fig. 5



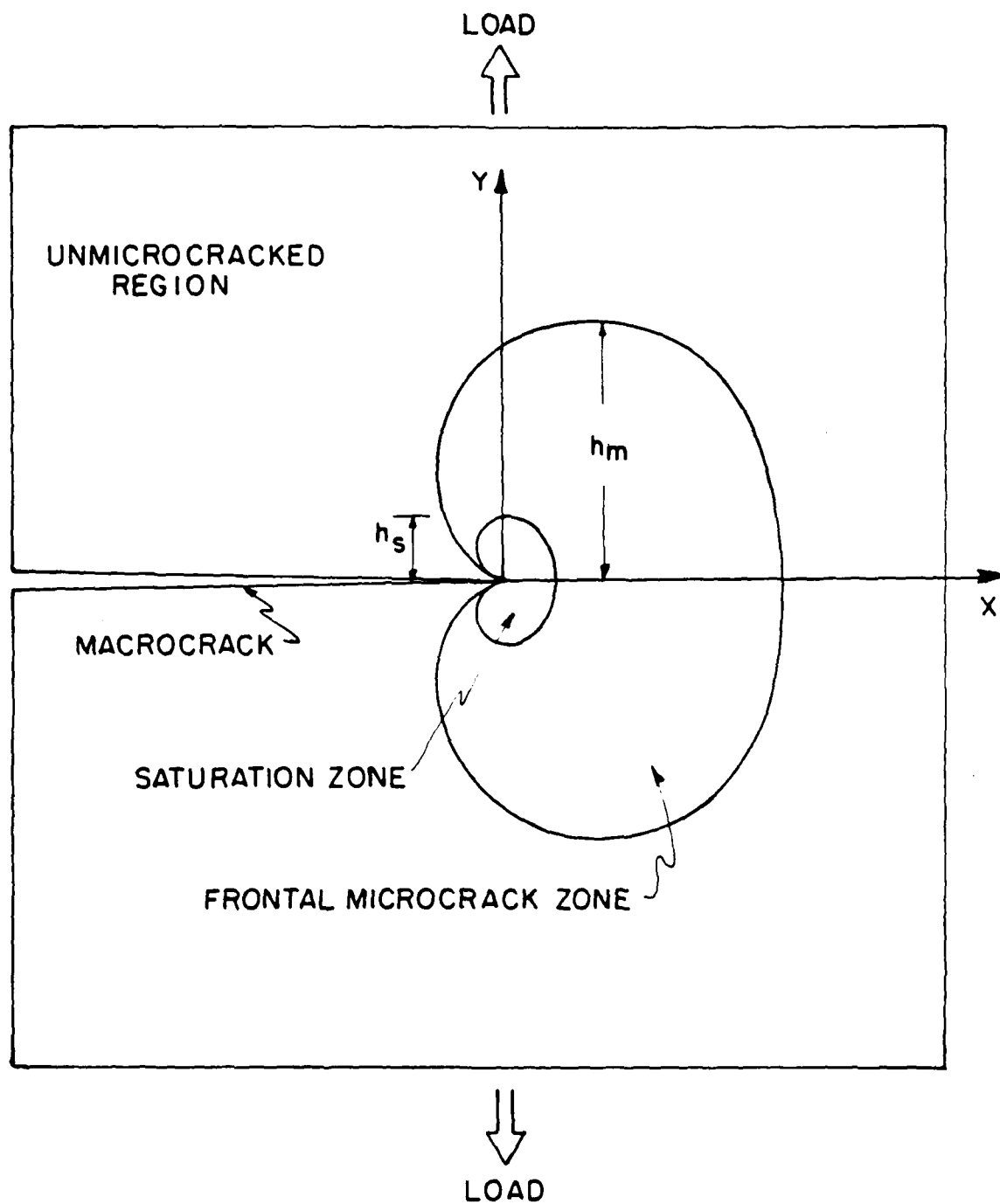
XBL 839-6350

Fig. 4



XBL 844-6883

Fig. 3



XBL 839-6349

Fig. 2

$$\sigma = \lambda \Delta T \quad , \quad (3)$$

where λ is a configuration dependent constant. The constant λ can be calibrated using the measurements in Section II(2) to give expressions for the peak stresses for each of the test configurations (the peak stress must occur at a fixed time after commencement of the gas flow if k , C and ρ are independent of temperature within the pertinent range). The data in Section II(2), combined with Eq. (3), give $\lambda = 0.182 \text{ MPa} \cdot ^\circ\text{C}^{-1}$ for the peak stress in the surface flow configuration and $\lambda = 0.134 \text{ MPa} \cdot ^\circ\text{C}^{-1}$ for the peak stress in the corner flow configuration.

(2) Finite Element Calculations

The thermal stress distribution for the surface flow test was determined using a finite element technique. The following material properties were used in the analysis; $k = 2.93 \text{ Js}^{-1}\text{m}^{-1} \text{ C}^{-1}$, $\alpha = 8.5 \times 10^{-6} \text{ C}^{-1}$, $C = 418.6 \text{ J Kg}^{-1} \text{ C}^{-1}$, $\rho = 4900 \text{ Kg m}^{-3}$, and $E = 147 \text{ GPa}$. Initial calculations indicated that the tensile stress in the vicinity of the jet center is maximum ($\hat{\sigma}$) at $t = 2 \text{ s}$ (Fig. 6a). This is the stress that dictates the onset of thermal fracture at the critical temperature ΔT_c . Therefore, all subsequent calculations were done at $t = 2 \text{ s}$.

The stress calculation requires a calibration of the pertinent heat transfer coefficient, h . The calibration was obtained from the control thermal shock tests using precracked capacitors, in combination with computations of $\hat{\sigma}$ for various values of h at the critical temperature difference ΔT_c measured

for the precracked capacitors ($\Delta T_c = 385^\circ\text{C}$). A plot of the computed $\hat{\sigma}$ versus h is shown in Fig. 6b. The calibrated value of h , determined by setting $\hat{\sigma}$ equal to the strength of the indentation crack ($\hat{\sigma} = 70 \text{ MPa}$), is $h = 2560 \text{ J s}^{-1}\text{m}^{-1} \text{C}^{-1}$.

Subsequent calculations using the calibrated h provided the required stress distribution (Fig. 6c). It is noted that the peak tensile stress occurs directly beneath the jet and is approximately uniform and equibiaxial over a central radius of $\sim 0.6 \text{ mm}$ (i.e., approximately half of the jet radius). Beyond this region the tangential stress decreases rapidly with radial position and becomes compressive outside the jet perimeter. Therefore, failure would be expected to originate predominantly from the central region, in accord with the experimental observations.

IV. FAILURE PROBABILITIES

(1) Flaw Populations

The strength characteristics of the surface and corner flaws can be deduced from the measured critical temperatures (Fig. 3) and the calibrated relations between the peak stress and ΔT_c (Eq. 3). The resulting failure probabilities are plotted in Fig. 7. In equating the peak stress to the flaw strength in Fig. 7, gradients in the thermal stress (Fig. 6d) have been neglected. However, over the range of strengths in Fig. 7 the corrections due to stress gradients were found to be less than 4%.

The data in Fig. 7 may be used to evaluate the statistical parameters that characterize the flaw distributions. For weakest link statistics using the Weibull assumption, the cumulative failure probability is given by¹⁰

$$P = 1 - \exp\left[-\int_A (S/S_0)^m dA\right], \quad (4)$$

where A is the area tested, m is the shape parameter, and S_0 is a scale parameter. In the present experiments failure originated from within an area of uniform biaxial stress in the surface flaw test and from an area of uniform uniaxial stress in the corner flaw test. Therefore, Eq. (4) reduces to

$$P = 1 - \exp[A_s (S/S_0^s)^m] \quad (5a)$$

for the surface flaw tests (A_s is the area of uniform biaxial stress) and

$$P = 1 - \exp[L_e (S/S_0^e)^m] \quad (5b)$$

for the corner flaw tests (L_e is the length of edge tested). The data in Fig. 7, plotted according to Eqs. (5a) and (5b), provide the statistical parameters summarized in Table II.

(2) Capacitor Reliability

Capacitors are subject to in-service failure during thermal cycling. A finite element analysis of the stresses that develop during typical cycling indicates that the stress on the upper surface, σ_u , is approximately uniform

(~ 10 MPa) and the stress on the lower surface is given approximately by¹¹

$$\sigma_x \sim \sigma_0(1 + |x/2b|) \quad , \quad (6)$$

where $\sigma_0 \sim 20$ MPa is the stress at the center line (OY, Fig. 1) of the capacitor surface.

The mechanical reliability of the capacitors can be estimated by inserting this stress distribution and the statistical parameters into Eq. (4). The survival probability thus becomes:

$$\begin{aligned} -\ln(1 - P) = & 2w(\sigma_0/S_0^s)^{m_s} \int_0^b [1 + (x/2b)]^{m_s} dx + 2bw(\sigma_u/S_0^s)^{m_s} \\ & + 2(\sigma_0/S_0^e)^{m_e} \int_0^b [1 + (x/2b)]^{m_e} dx + 2b(\sigma_u/S_0^e)^{m_e} \quad , \end{aligned} \quad (7)$$

where w is the capacitor width (Fig. 1). The first two terms represent the survival probability associated with the surface flaw population at the lower and upper surfaces, while the last two terms refer to the corner flaw population. The failure probability evaluated by substituting the statistical parameters from Table II into Eq. (7) is 5×10^{-4} . This value is consistent with practical experience. It is noted that the failure probability evaluated from Eq. (7) by considering the surface flaw population alone is only 6×10^{-8} . Therefore, the failure of the capacitors during this thermal cycling is dominated by the corner flaws.

These estimates of failure probability involve extensive data extrapolation, from the strength levels $\sim 55 - 85$ MPa used for experimental characterization to stresses < 30 MPa. Such extrapolation introduces several uncertainties. First, alternative flaw populations can, in general, emerge at strength levels outside the data range. Second, at the lower strength levels the strength-controlling flaws are larger than the flaws used for the data collection, and thus more likely to be influenced by stress gradients. However, the agreement between calculated and observed failure probabilities suggests that these effects are not important in the present experiments.

V. CONCLUSIONS

A thermal stress method for evaluating surface flaw populations in ceramic components has been demonstrated. The stress is applied using gas jets to induce local thermal transients, and the stresses are deduced from calibration tests using controlled precracks. The method can, in principle, be applied to components of complex shape to evaluate statistical parameters in situ and to perform proof testing. It can also be used to evaluate multiple, spatially separated flaw populations.

In the present experiments on multilayer capacitors, corner flaws were identified as the primary source of failure during typical in-service thermal cycling. This result implies that the capacitor reliability could be improved by modifying fabrication procedures to reduce the severity of corner flaws.

ACKNOWLEDGEMENTS

Funding for this work was supplied by the U.S. Office of Naval Research (Contract No. N00014-79-C-0159) for D.J., M.D.D. and AGE, by Rockwell International Independent Research and Development for DBM, and by the National Science Foundation (DMR-8351476), in conjunction with IBM Corp., 3M Co., Eastman Kodak and PPG Industries, for KTF.

REFERENCES

1. A.G. Evans, "Mechanical Behavior of Materials," (Ed. K.J. Miller and R.F. Smith) Pergamon Press, Oxford, Vol 1 (1980) p. 279.
2. S.M. Wiederhorn, "Fracture Mechanics of Ceramics," (Ed. R.C. Bradt, F.F. Lange and D.P.H. Hasselman) Plenum Press, New York (1974) p. 613.
3. K.T. Faber, M.D. Huang and A.G. Evans, "Quantitative Studies of Thermal Shock in Ceramics Based on a Novel Test Technique," J. Amer. Ceram. Soc., 65 [5] 296-301 (1981).
4. P. Chantikul, G.R. Anstis, B.R. Lawn and D.B. Marshall, "A Critical Evaluation of Indentation Techniques for Measuring Fracture Toughness: II, Strength Method," J. Amer. Ceram. Soc., 64 [9] 539-43 (1981).

5. G.R. Anstis, P. Chantikul, B.R. Lawn and D.B. Marshall, "A Critical Evaluation of Indentation Techniques for Measuring Fracture Toughness: I Direct Crack Measurements," J. Am. Ceram. Soc. 64 [9] 533-538 (1981).
6. F.W. Smith, A. F. Emery and A.S. Kobayashi, "Stress Intensity Factors for Semi-Circular Cracks, Part II - Semi-Infinite Solid," J. Appl. Mech. Trans. ASME, 34, Series E, 953-59 (Dec. 1967).
7. A.S. Kobayashi and A.N. Eneanya, "Stress Intensity Factors of a Corner Crack," in Mechanics of Crack Growth, ASTM STP 590, American Society for Testing and Materials, 1976, pp 477-95.
8. D.B. Marshall, "Controlled Flaws in Ceramics: A Comparison of Knoop and Vickers Indentation," J. Amer. Ceram. Soc. 66 [2] 127-131 (1983).
9. J.C. Jaeger, "Thermal Stresses in Circular Cylinders," Phil. Mag. 36[257] 418-28 (1945).
10. A. Freudenthal, in Fracture (Ed. H. Liebowitz), Academic Press, Vol. II, Ch. 6 (1968).
11. D. Blanchet, Draper Labs, Interlab Memorandum DB 81 16.

Figure Captions

Fig. 1 Ceramic (BaTiO_3) multilayer capacitor on substate showing surface crack (S), and corner crack (C).

Fig. 2 Schematic of thermal shock test for evaluating (a) surface flaw population and (b) corner flaw population.

Fig. 3 Thermal shock results (probability of failure vs ΔT_c) for surface and edge flaw tests.

Fig. 4 Optical technique for detection of cracks. (a) Schematic of crack placed outside the directly illuminated region, in an area illuminated by backscattered light from within the capacitor. (b) Optical micrograph of thermal shock induced crack, obtained using the method in (a).

Fig. 5 Normalized stress intensity factors as a function of angular orientation for semi-circular surface and corner cracks (after Refs. 6 and 7).

Fig. 6 Finite element stress calculations:

- (a) Variation of peak stress with time after commencement of gas flow, using dimensionless coordinates.
- (b) Variation of peak stress with heat transfer coefficient, for $\Delta T_c = 385^\circ\text{C}$.
- (c) Variation of radial and tangential stresses with radial distance on the test surface.
- (d) Variation of radial stress with distance below the test surface.

Fig. 7 Weibull plots of strength distributions for surface and corner flaw populations (data from Fig. 3).

Table I

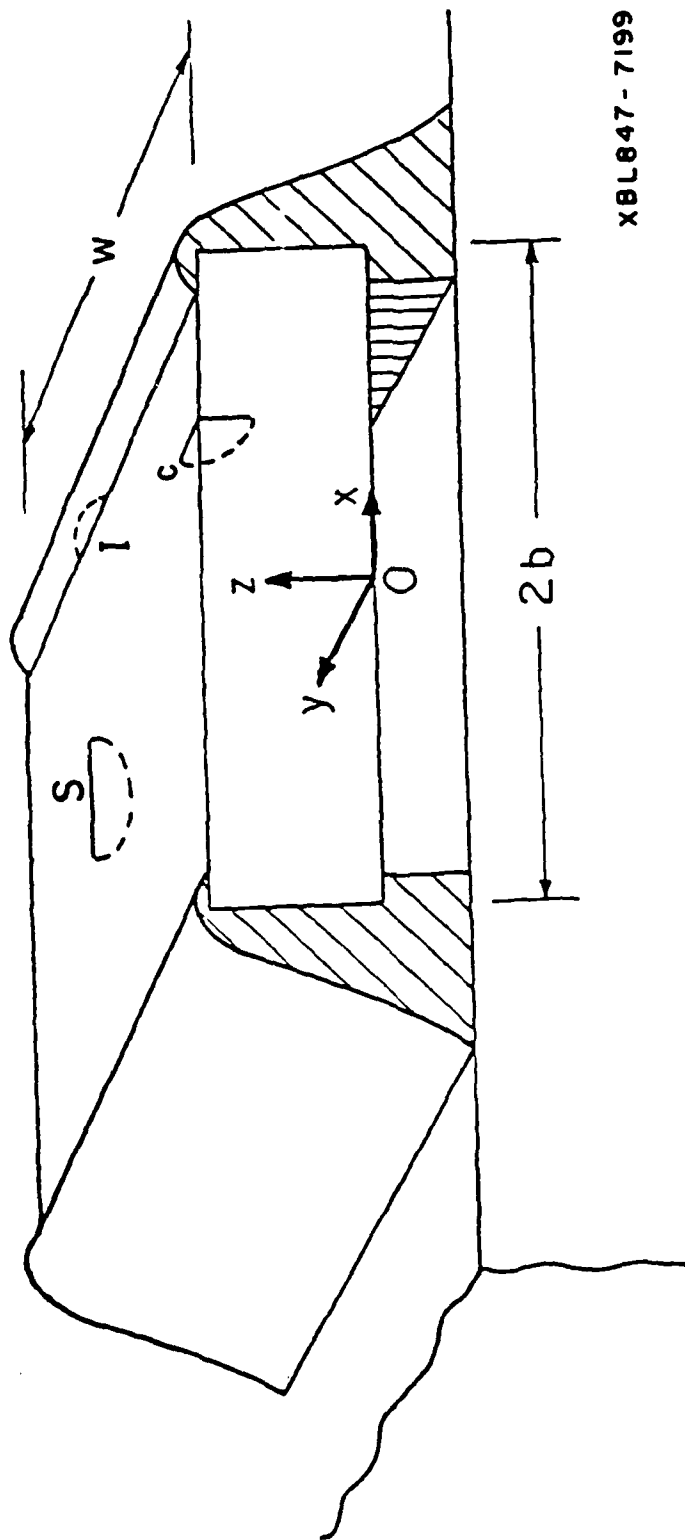
Bend Strengths of Glass Flexure Bars Containing Controlled Flaws

| Flaw Type | As-Indented | Annealed | $\frac{S_{\text{annealed}}}{S_{\text{as-indented}}}$ |
|--|------------------|------------------|--|
| Surface | 39.4 \pm 3 MPa | 48.4 \pm 5 MPa | 1.23 |
| Corner | 33.2 \pm 4 MPa | 46.6 \pm 5 MPa | 1.41 |
| $R = S_{\text{corner}}/S_{\text{surface}}$ | 0.84 | 0.96 | |

Table II

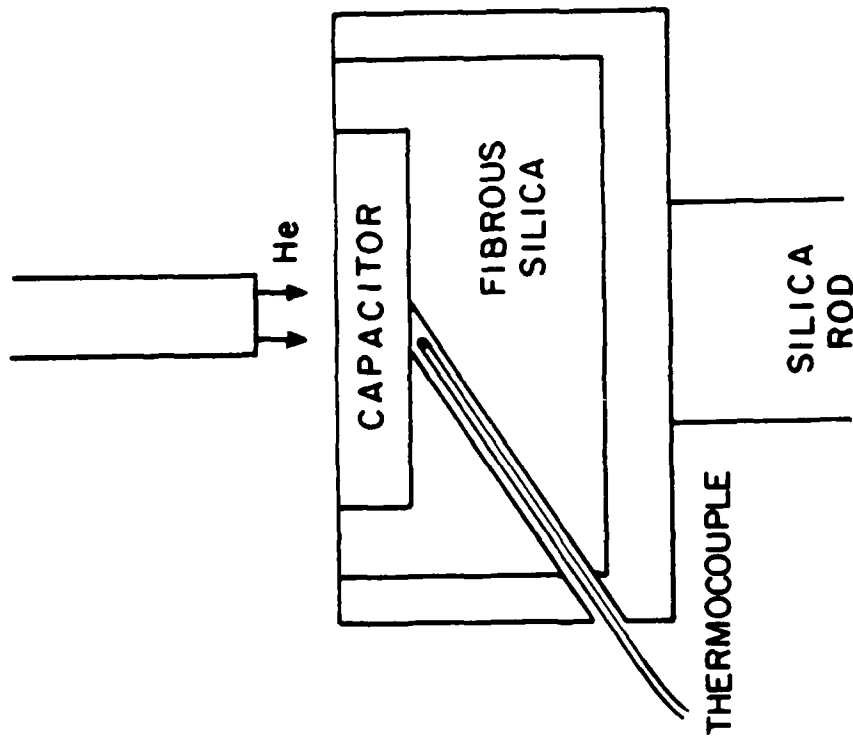
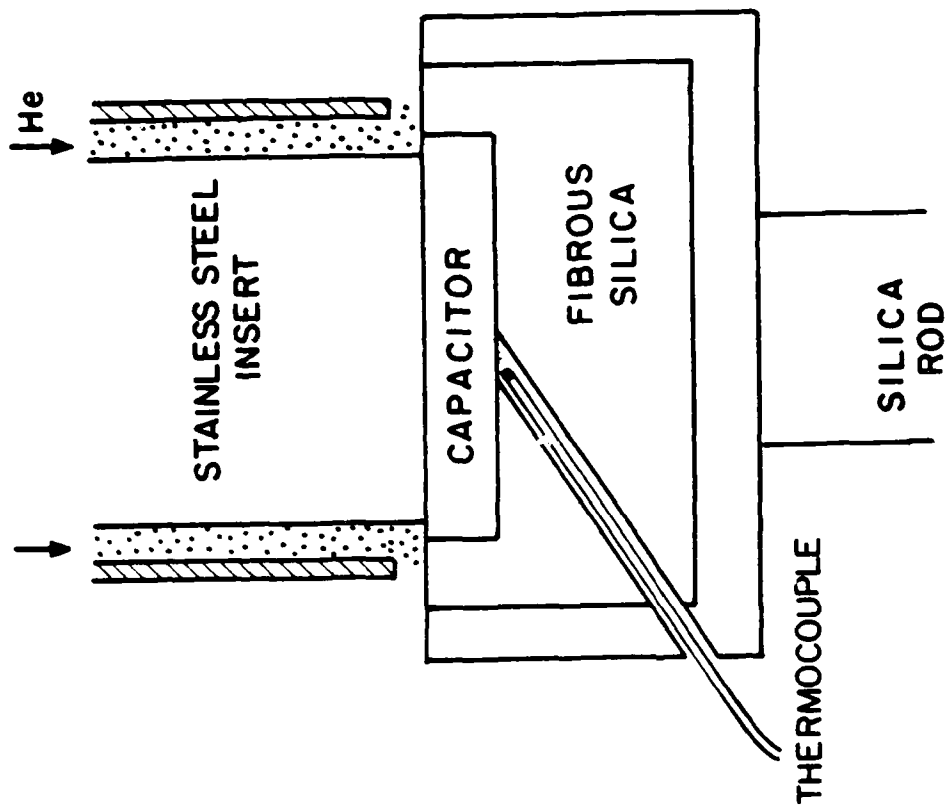
Statistical Failure Parameters

| Flaw Population | m | $S_0(\text{uniaxial})$ | $S_0(\text{equibiaxial})$ |
|-----------------|-----|-----------------------------|--------------------------------|
| Surface | 18 | | 38.5 MPa $(\text{m}^2)^{1/18}$ |
| Corner | 9.3 | 39.0 MPa $\text{m}^{1/9.3}$ | - |



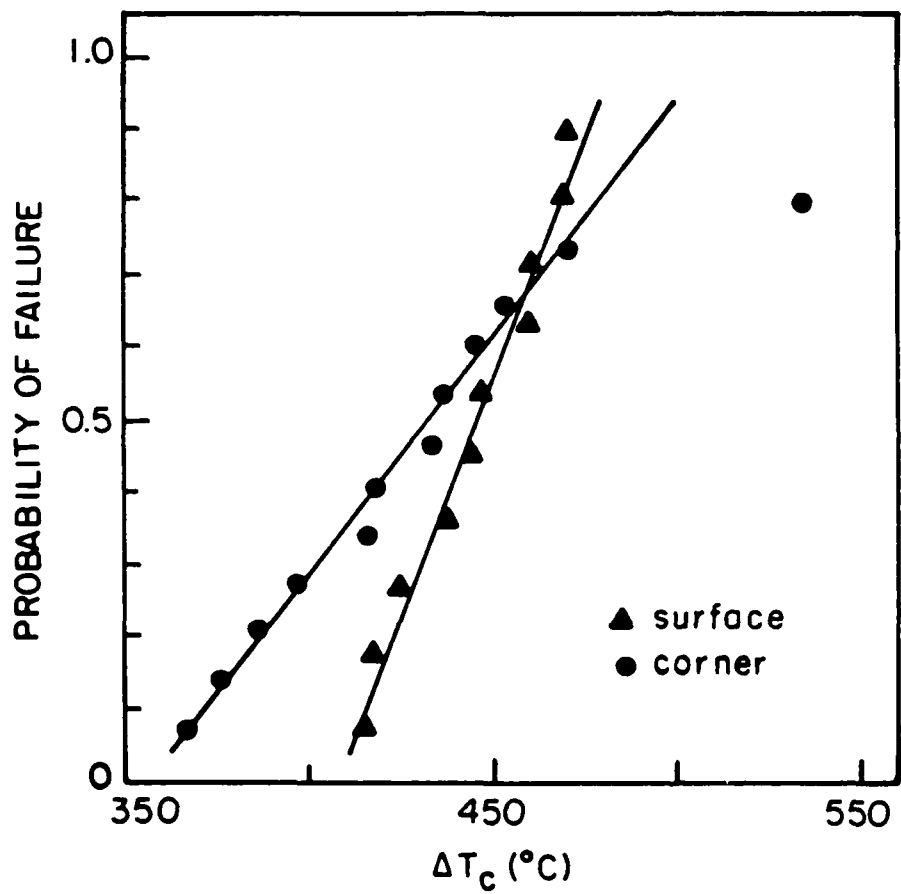
XBL847-7199

Fig. 1



X BL 847-7200

Fig. 2



XBL 849-7392

Fig. 3

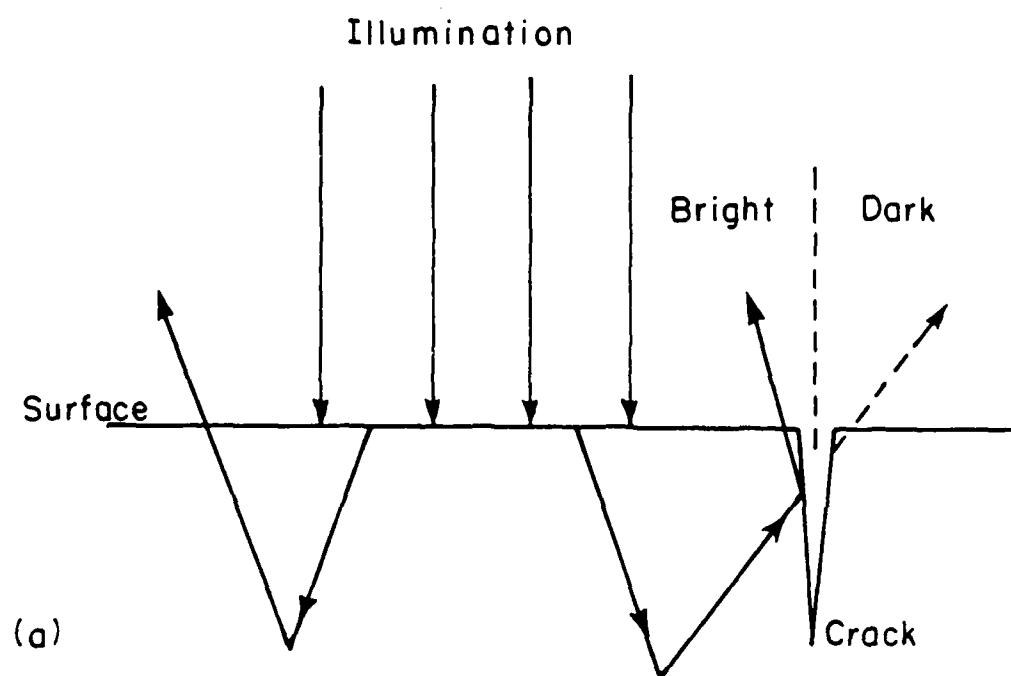


Fig. 4

AD-A151 978

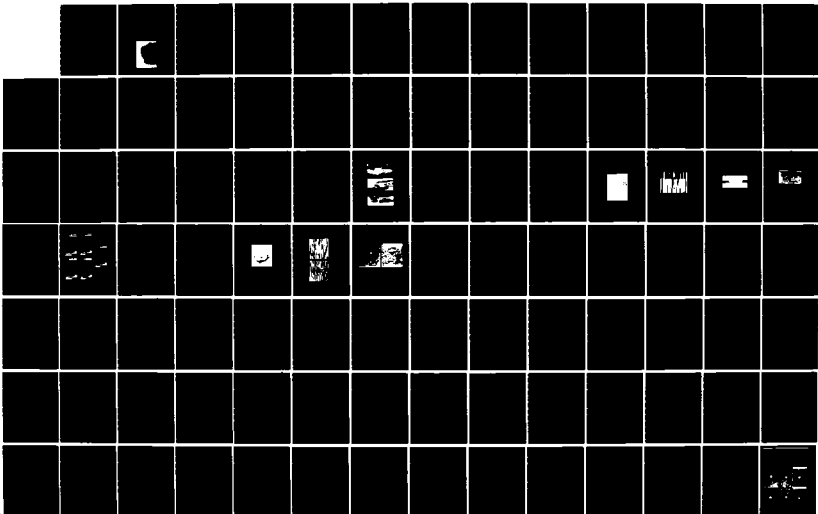
MECHANICAL ASPECTS OF INTERFACES AND SURFACES IN
CERAMIC CONTAINING SYSTEMS(U) CALIFORNIA UNIV BERKELEY
DEPT OF MATERIALS SCIENCE AND MINERA.

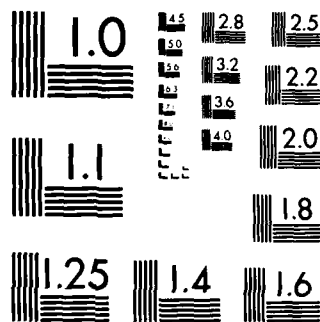
2/5

UNCLASSIFIED

A G EVANS ET AL. 14 DEC 84 N00014-81-K-0362 F/G 20/11

NL





MICROCOPY RESOLUTION TEST CHART
NATIONAL BUREAU OF STANDARDS 1963 A

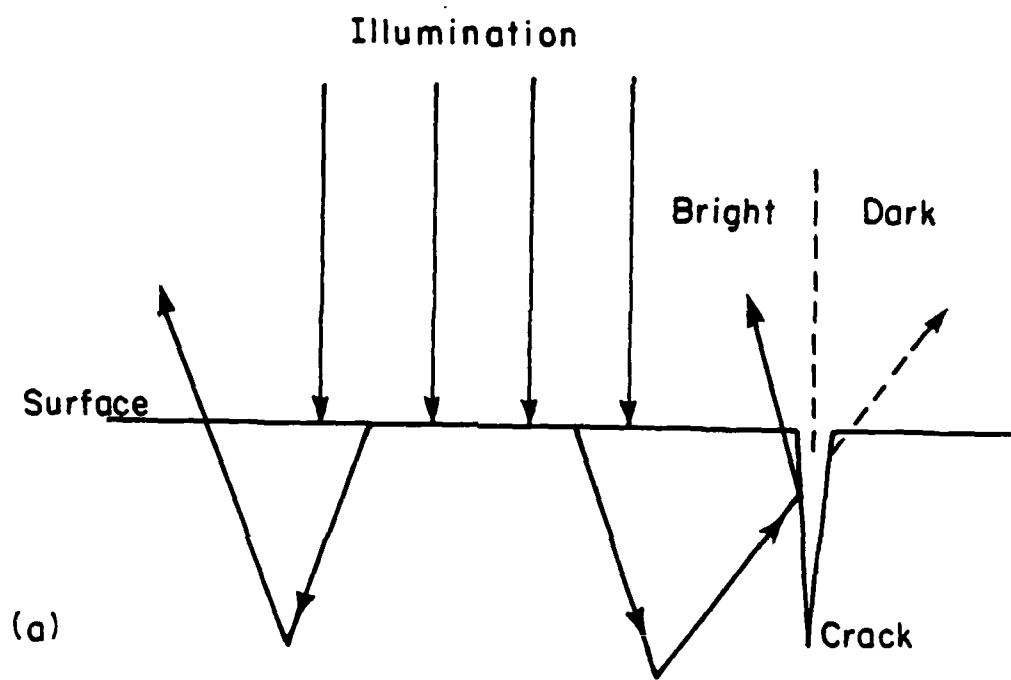
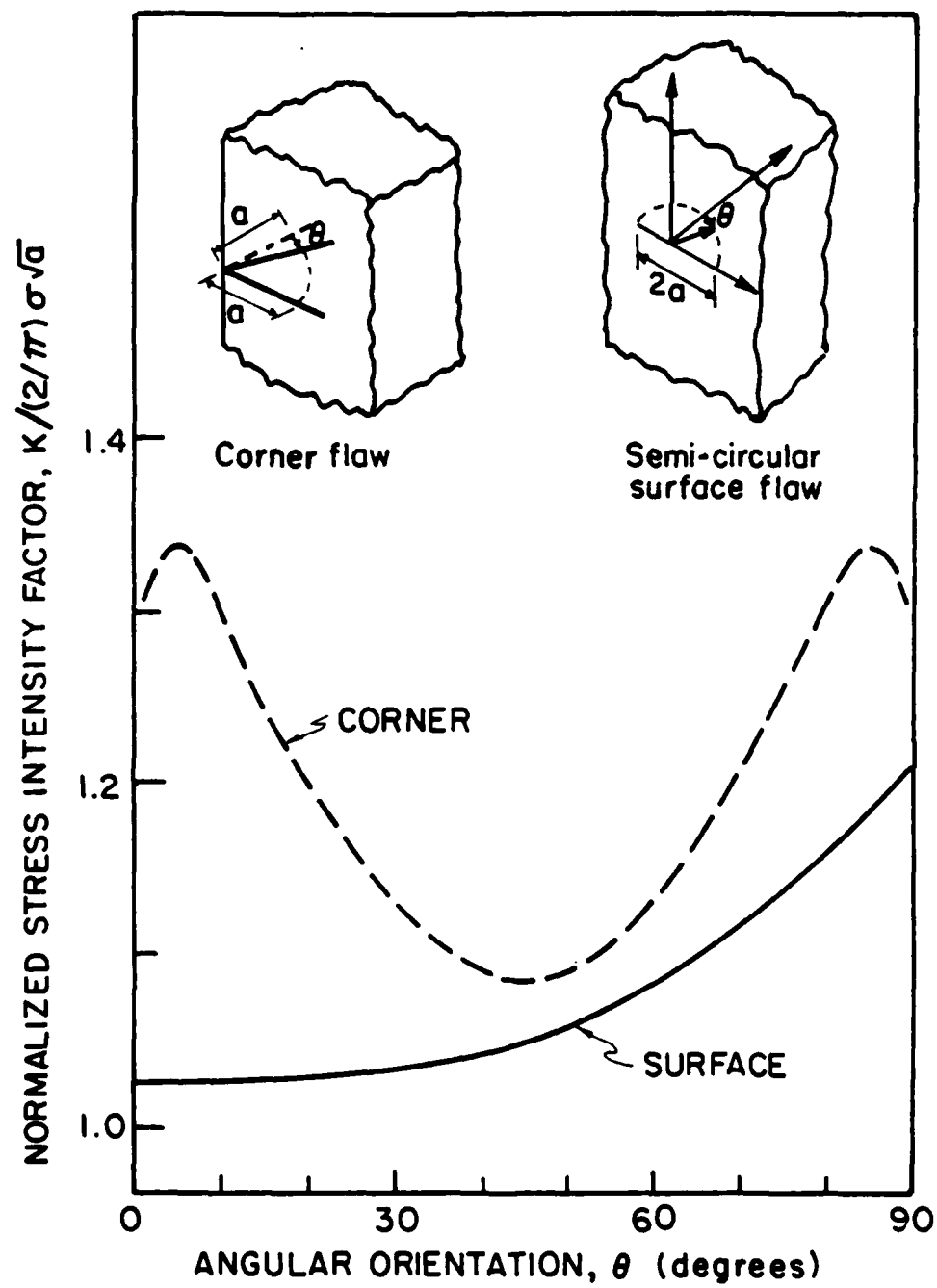
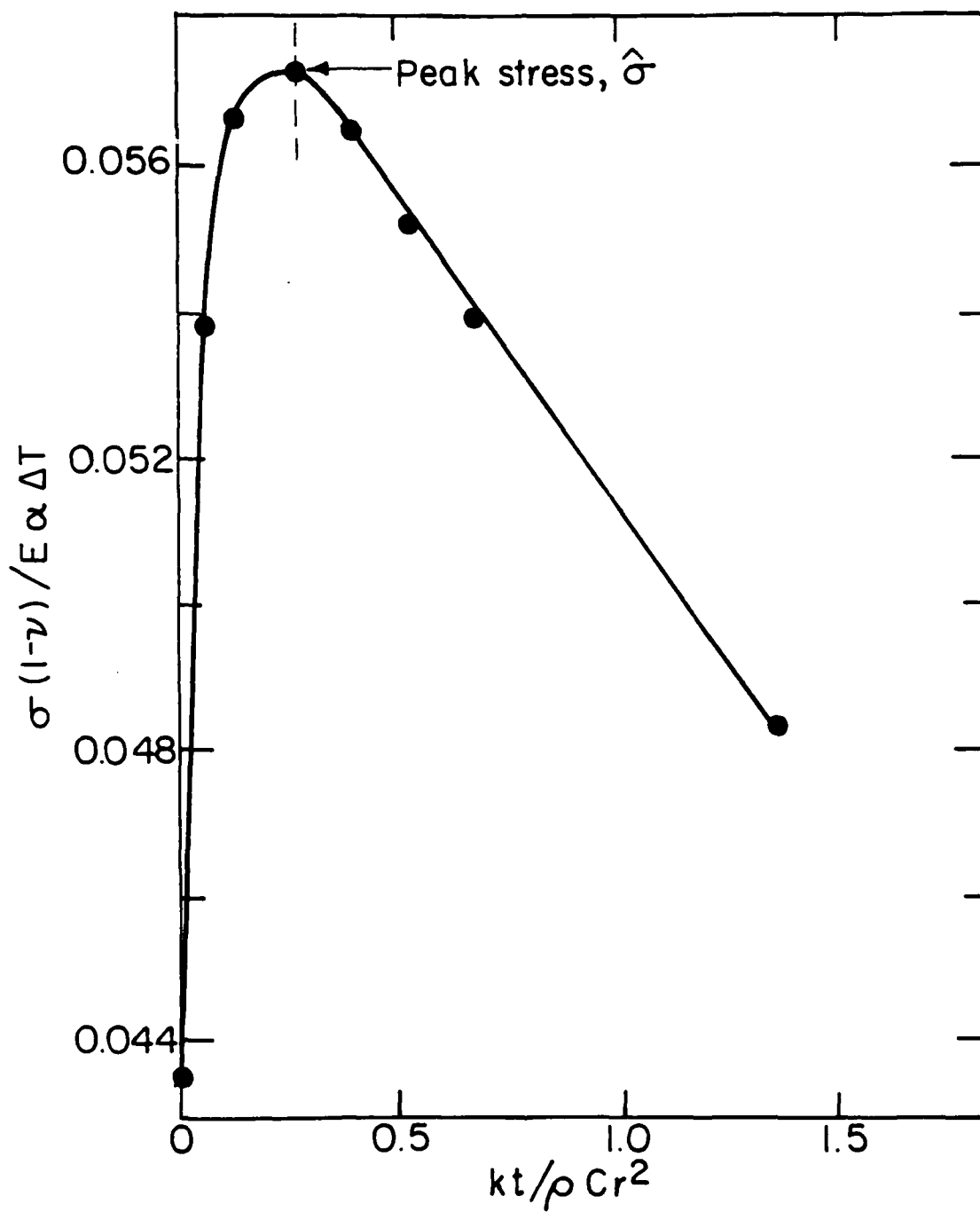


Fig. 4



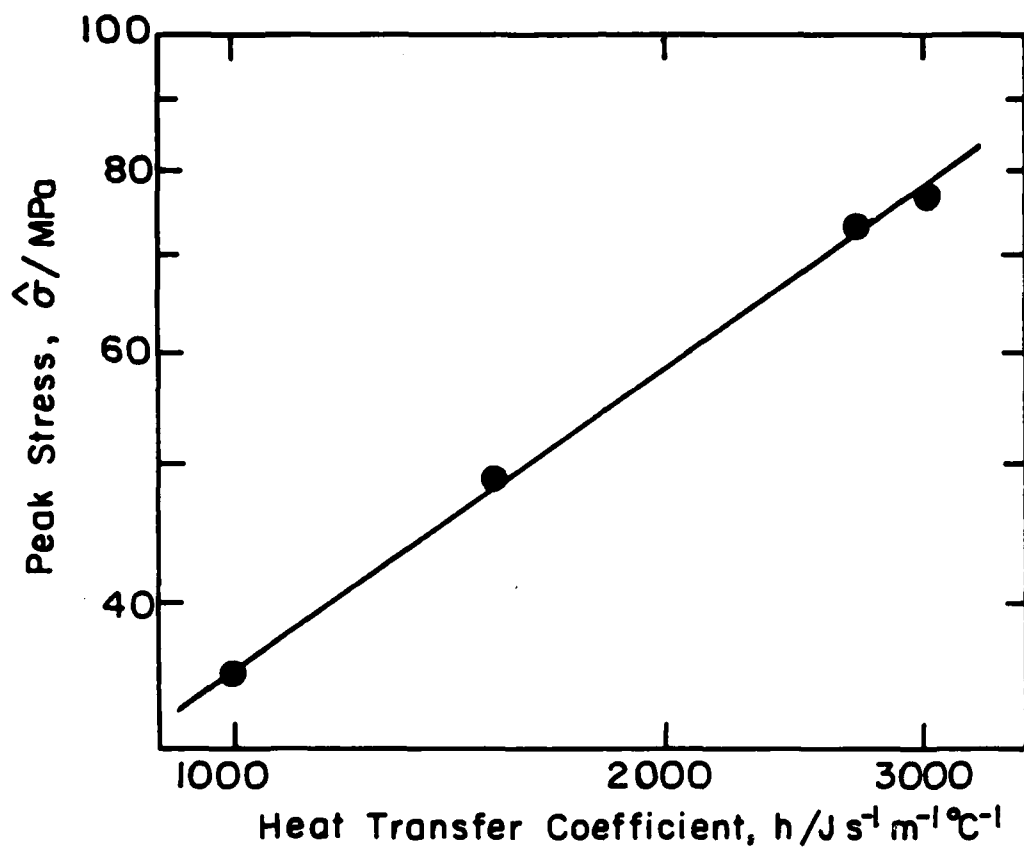
XBL 847-7201

Fig. 5



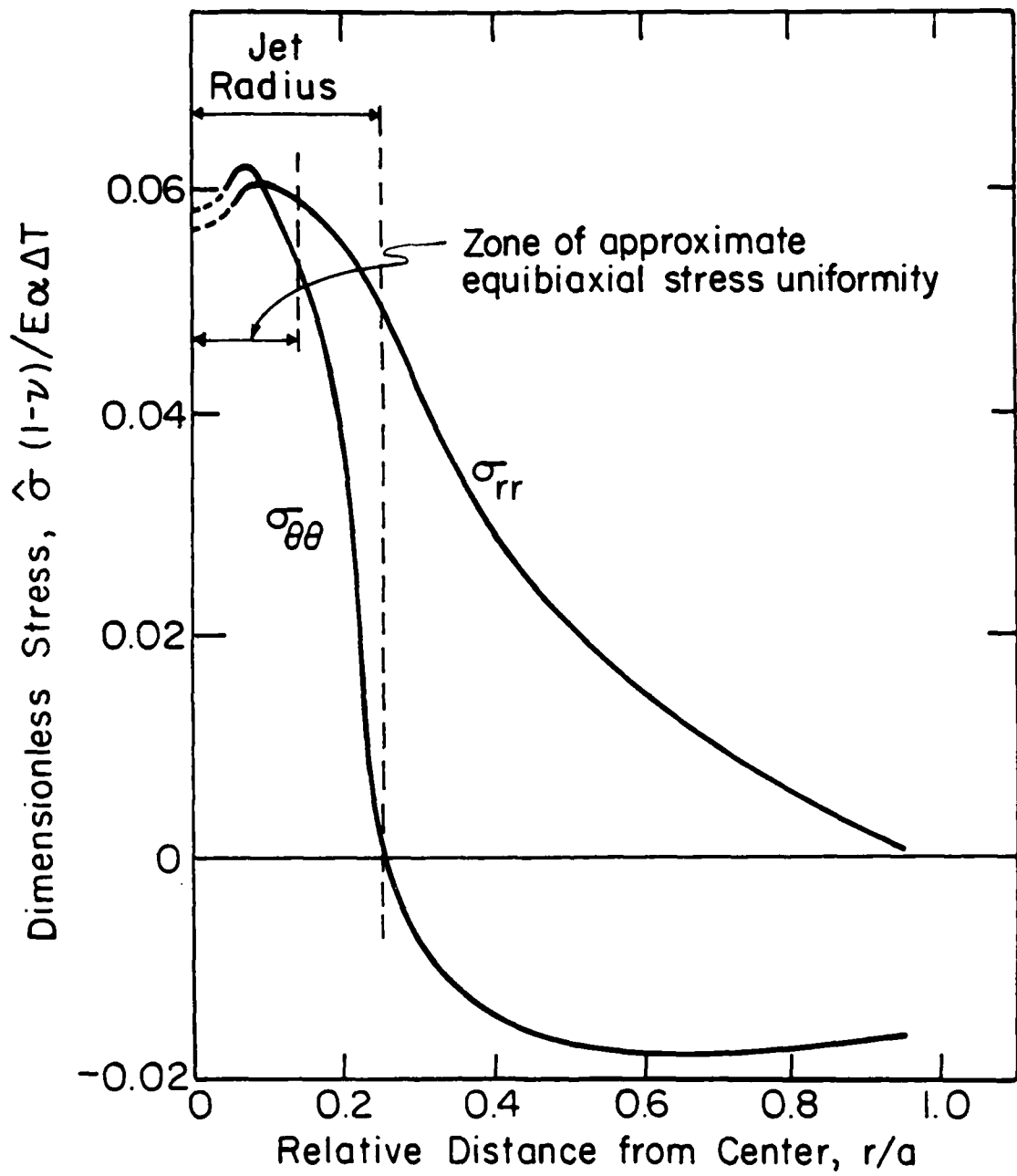
XBL 822-5214A

Fig. 6a



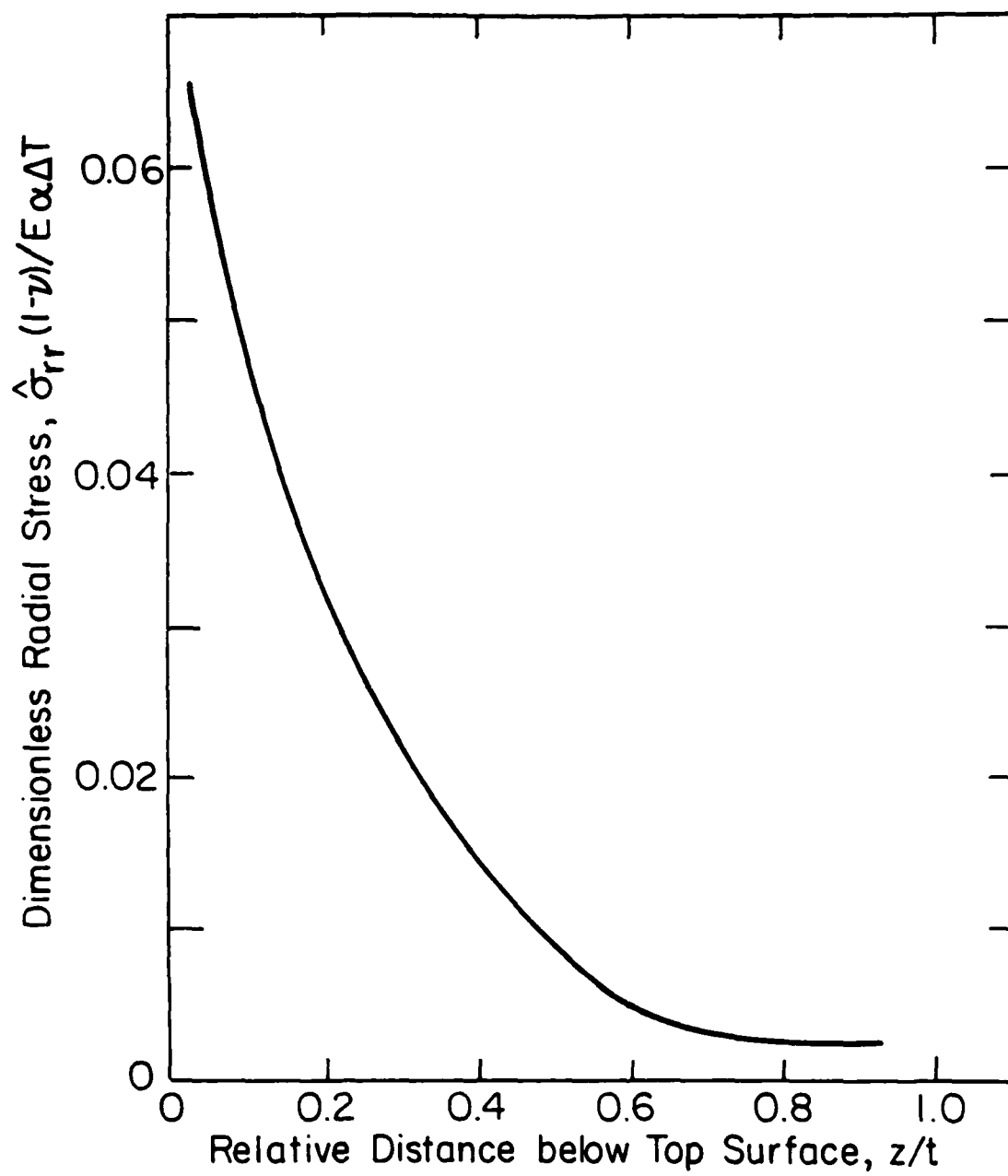
XBL822-5209

Fig. 6b



XBL 822-5212 A

Fig. 6c



XBL 822 5213 A

Fig. 6d

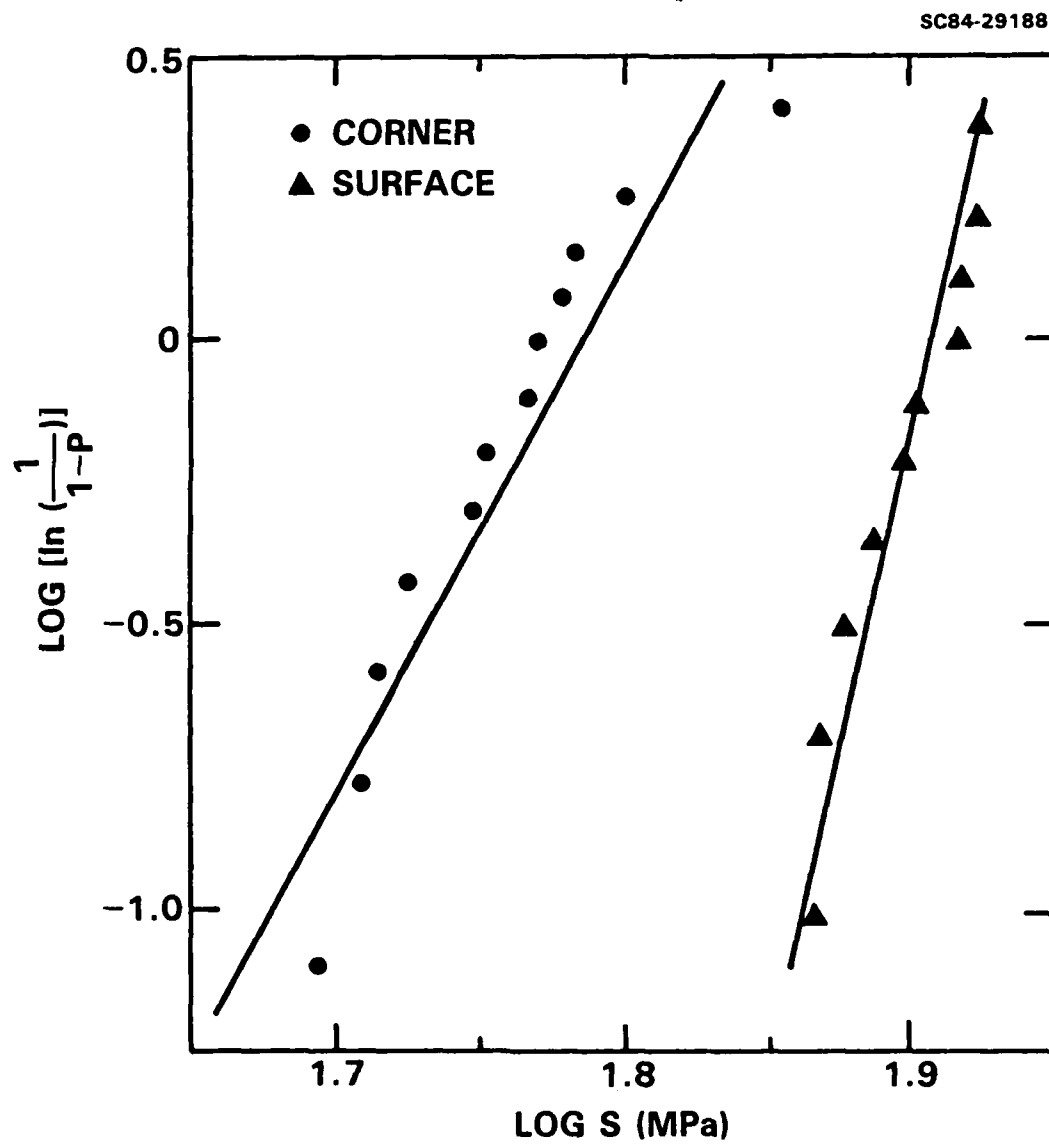


Fig. 7

CHAPTER III

FAILURE MECHANISMS IN
CERAMIC-FIBER/CERAMIC MATRIX COMPOSITES

D. B. Marshall and A. G. Evans

FAILURE MECHANISMS IN CERAMIC-FIBER/CERAMIC-MATRIX
COMPOSITES

D.B. Marshall

Rockwell International Science Center
1049 Camino Dos Rios
Thousand Oaks, CA 91360

A.G. Evans

Department of Materials Science and Mineral Engineering
University of California
Berkeley, CA 94720

ABSTRACT

Mechanisms of failure in a unidirectional SiC-fiber/glass-ceramic composite are investigated using in situ observations during tensile and flexural loading. These experiments show that failure in tension occurs in several stages (similar to certain other brittle fiber composites): multiple matrix cracking, followed by fiber fracture and pullout. In flexural loading the failure process is more complex. Consequently, the flexural test cannot be used for measurement of tensile strength (although it can be used for measurement of the stress for matrix cracking). The application of conventional fracture mechanics to describe tensile failure is discussed. The in situ observations provide direct indication of the importance of frictional bonding between the matrix and fibers. Some novel methods for measuring the frictional forces and residual stresses are investigated, and the influence of surface damage on strength is assessed.

I. INTRODUCTION

The reinforcement of brittle materials with high strength fibers can yield composites of very high "toughness". This was first demonstrated using carbon fibers in glass and glass-ceramic matrices.¹⁻³ More recently, the availability of continuous SiC fibers has led to development of glass and glass-ceramic composites⁴⁻⁶ which are more resistant to high temperature oxidation than the carbon fiber composites. Since the motivation for developing these materials is to utilize their high "toughness" in structural applications, an understanding of the mechanisms by which they fail is needed, both for material evaluation and as a basis for design.

The failure of the SiC/glass-ceramic composite under mechanical loading is so unlike the failure of monolithic ceramics that the role of conventional fracture mechanics concepts in describing the failure is unclear. The complexity of the failure process can be seen in Fig. 1, which shows specimens from two tests that are commonly used to evaluate these materials; beams loaded in four-point bending for strength measurement and a notched beam loaded in bending for fracture toughness measurement. In the strength tests failure occurs either in compression or in shear but never in tension, so calculation of a tensile strength from this loading configuration is clearly invalid. In the fracture toughness test failure occurs by delamination parallel to the fibers and normal to the notch. Therefore, calculation of a fracture toughness using fracture mechanics relations based on coplanar extension of a single crack from the notch is also invalid.

The aim of this paper is to investigate the mechanisms of failure in a SiC/glass-ceramic composite under tensile loading, and to define test configurations that give meaningful measurements of material properties. Direct in situ observations are used to define failure mechanisms and to indicate the role of fracture mechanics. These observations show that fracture mechanics can be usefully applied in the initial stage of tensile failure. An analysis will be reported separately.⁷ Frictional slipping is observed at the fiber/matrix interface in the presence of matrix cracks, thus providing strong circumstantial evidence that there is no chemical bonding between the fibers and matrix. Novel methods for measuring the frictional stress between the fibers and matrix are explored. Finally, since residual stresses are generally expected in composites, owing to differences in thermal contraction between the fibers and matrix, methods for estimating such stresses are briefly assessed.

II. EXPERIMENTAL

Specimens for flexure and tension testing (Fig. 2(A)) were cut from a plate of a composite material consisting of approximately 50% uniaxially aligned SiC fibers in a lithium alumino silicate glass-ceramic matrix.* All specimens were oriented with the fibers parallel to the prospective applied tension, and the test surfaces were polished with diamond to allow observation of cracking.

A schematic of the experimental arrangement used to observe the surface of the tensile test specimens during loading is shown in Fig. 2(B). The specimens were accurately located in set positions in the grips and held by both

*United Technologies Research Center.

8. D.B. Marshall and B.R. Lawn, "An Indentation Method for Measuring Stresses in Tempered Glass Surfaces," J. Amer. Ceram. Soc. 60[1-2] 86-87 (1977).
9. M.G. Mendiratta, T.I. Mah, and S.K. Ehlers, "Mechanics of Ductility, Toughness and Fracture in Complex High Temperature Materials, Section 3: Ceramic-Ceramic Composites," Interim Technical Report, Systems Research Laboratories April, 1983.
10. R.J. Roark, Formulas for Stress and Strain, 4th ed.; Chapter 10, McGraw-Hill, New York and London, 1965.
11. D.B. Marshall, "A Simple Method for Measuring Matrix-Fiber Frictional Stresses in Ceramic Composites," submitted to J. Amer. Ceram. Soc.
12. J. Aveston, G.A. Cooper and A. Kelly, "Single and Multiple Fracture," pp. 15-26 in the Properties of Fiber Composites, Conf. Proc. Nat. Physical Lab., IPC Science and Technology Press Ltd., Surrey, England, 1971.
13. J. Aveston and A. Kelly, "Theory of Multiple Fracture of Fibrous Composites," J. Mater. Sci. 8[3] 352-62 (1973).
14. J. Cook and J.E. Gordon, "A Mechanism for the Control of Crack Propagation in All-Brittle Systems," Proc. Roy. Soc. Lond. A282 508-520 (1964).

REFERENCES

1. R.A.J. Sambell, A. Briggs, D.C. Phillips and D.H. Bowen "Carbon Fiber Composites with Ceramic and Glass Matrices, Part 2 - Continuous Fibers," J. Mater. Sci. 7[6] 676-681 (1972).
2. D.C. Phillips, "Interfacial Bonding and the Toughness of Carbon Fiber Reinforced Glass and Glass-Ceramics," J. Mater. Sci. 9[11] 1847-54 (1974).
3. D.C. Phillips, "The Fracture Energy of Carbon-Fiber Reinforced Glass," J. Mater. Sci. 7[10] 1175-91 (1972).
4. K.M. Prewo and J.J. Brennan, "High Strength Silicon Carbide Fiber Reinforced Glass Matrix Composites," J. Mater. Sci. 15[2] 463-8 (1980).
5. K.M. Prewo and J.J. Brennan, "Silicon Carbide Yarn Reinforced Glass Matrix Composites," J. Mater. Sci. 17[4] 1201-6 (1982).
6. J.J. Brennan and K.M. Prewo, "Silicon Carbide Fiber Reinforced Glass-Ceramic Matrix Composites Exhibiting High Strength and Toughness," J. Mater. Sci. 17[8] 2371-83 (1982).
7. D.B. Marshall and A.G. Evans, "A Fracture Mechanics Analysis of Matrix Cracking in Fiber Composites," to be published.

The present results also emphasize that the peak load bearing capacity and ultimate separation of a tensile specimen are not controlled by the extension of a single crack. Therefore, fracture mechanics parameters based on the extension of a single crack (e.g., fracture toughness, work of fracture, etc.) cannot be defined in relation to this stage of the failure process. Rather, prediction of the peak load requires statistical analysis of fiber fracture and pullout, including the effects of frictional forces exerted by the matrix on the fibers.¹⁷

Finally, some remarks are made concerning the bonding at the fiber/matrix interface. The present measurements of the frictional shear stress, the matrix cracking stress, the crack spacing, and the residual matrix stress are largely consistent with an unbonded interface. This conclusion derives from the realization that, to obtain the observed crack spacing ($2d = 400 \mu\text{m}$) in the presence of bonded fibers, debonding must occur over length $\geq 200 \mu\text{m}$. Calculations¹⁵ indicate that such debond lengths could only be achieved at the observed matrix cracking stress (290 MPa), (and for the small residual tension that exists at the interface), if the debond toughness, G_d , is $\leq 10^{-2} G_c^m$, i.e., $G_d \leq 0.4 \text{ Jm}^{-2}$. Such small levels of fracture resistance are unknown in covalent and ionic bonding. An unbonded interface (or perhaps a very weak Van der Waals bond) is thus implied.

where K_C^m is the toughness of the matrix. With $\tau = 2.0$ MPa and $K_C^m = 2$ MPa·m^{1/2},¹⁶ Eq. (7) gives $\sigma = 307$ MPa. This is in reasonable agreement with the stress measurements in Section III(1) (290 ± 20 MPa).

Flexural tests can be used for measurement of the stress at which matrix cracking occurs, for this is the first damage to occur (provided that the ratio of loading-span to beam-thickness is sufficiently large). However, once the first crack forms the uniformity of the beam is destroyed and the stresses in the beam are no longer related solely to the applied load and specimen dimensions. Then the relation between the peak load and the failure stress (compression or shear) is obscure. If this nonuniformity of the beam is ignored an apparent paradox arises when apparent strengths in tension and bending are compared. The observation of compressive failure in a uniform flexure beam would imply that the strength in compression is lower than the strength in tension. However, the apparent compressive strength measured in the bend test is higher than the tensile strength obtained from a tension test (800 MPa vis-a-vis 500 MPa). Similar results have been obtained in a study using another SiC/glass-ceramic composite (magnesium-alumino silicate),⁸ where it was suggested that the strength difference in the two tests may be due partly to flaw statistics. However, the strain gauge measurements in Fig. 7 show that when the matrix is cracked the true stress on the compressive surface is higher than the apparent stress calculated from the flexural load. (And the stress on the tensile surface must be lower.) Thus, the maximum load bearing capacity is ~ 1300 MPa in compression, and ~ 500 MPa in tension.

are determined by fiber failure and pullout. This failure sequence is characteristic of several other brittle composites, and requires the strength of the fibers to be sufficiently high to support the full applied load when the matrix fails,^{12,13} and the bonding between the fibers and matrix to be purely frictional or sufficiently weak for substantial debonding to occur ahead of the crack.¹⁴ In the tension tests described in Section III(1) matrix cracking occurred at an applied stress $\sigma_a = 290$ MPa, and the volume fraction of fibers was 0.5. Therefore, after a crack passed completely through the matrix the true stress in the fibers where they bridged the crack was ~ 600 MPa. This stress is considerably lower than the as-fabricated strengths of the fibers (~ 2 GPa⁶).

The formation of the first crack in the matrix is amenable to analysis by fracture mechanics.^{7,12,15} An important result of one of these analyses⁷ is that, with the crack being bridged by unbroken fibers, the applied stress required to extend the crack becomes independent of the crack size. This implies that the stress for matrix cracking is not degraded by the existence of large flaws, in contrast to the response of monolithic ceramics. This conclusion is supported by the results in Section III(3), where the introduction of large controlled flaws did not degrade the matrix cracking stress. The fracture mechanics analysis provides a relation between the matrix stress and microstructural parameters;^{7,12,15}

$$\sigma = 1.82 [K_c^m \tau E_f V_f^2 V_m (1 + E_f V_f / E_m V_m)^2 / E_m R]^{1/3} \quad (8)$$

fibers at various orientations relative to the fibers (ranging from radial to tangential), without systematic deflection of the cracks. These results suggest that the residual stresses normal to the fibers are small.

Residual stresses parallel to the fibers influence the opening of matrix cracks (Appendix). Thus, in principle, measurements such as those in Fig. 9 can be used to determine the magnitude of the residual stress. This is most conveniently done by extrapolating the linear portions of the loading and unloading curves to zero strain, to give intercepts u_0 and u_c . For zero residual stress $u_0 = -u_c$, whereas for a residual stress σ_R^m in the matrix (Appendix)

$$u_0 + u_c = 4 \sigma_R^m d / E_m \quad . \quad (7)$$

The accuracy of the data in Fig. 9 is limited by optical resolution, and is only sufficient to give broad limits for σ_R^m . Noting that $u_0 = 0.2 \pm 0.4 \mu\text{m}$ and $u_c = -0.2 \pm 0.4 \mu\text{m}$ (from Fig. 9), Eq. (7) gives $\sigma_R^m = 0 \pm 80 \text{ MPa}$, confirming that residual stresses, if they exist, are indeed small (it can be shown from these results that the residual stress normal to the interface is less than 20 MPa).

IV. DISCUSSION

The observations of Section III(1) show that failure of the unidirectional SiC glass-ceramic composite, in tensile loading parallel to the fibers, occurs in several stages. After initial linear elastic loading to a critical stress, multiple regularly spaced cracks form in the matrix. Further load increase is nonlinear, and the peak load-bearing capacity and final separation

Noting that $2d = 400 \text{ } \mu\text{m}$, (from Section III(1)), $V_f = V_m = 0.5$, $E_m = 85 \text{ GPa}$, $R = 8 \text{ } \mu\text{m}$, and $\delta = 0.5 \pm 0.1 \text{ } \mu\text{m}$ (Fig. 9), Eq. (5) yields $\tau = 2.4 \pm 0.5 \text{ MPa}$.

A third estimate of the frictional stress can be obtained from the spacing of the matrix cracks. The crack spacing is given by¹²

$$2d \approx \sigma_c R / 2\tau V_f (1 + E_f V_f / E_m V_m) \quad . \quad (6)$$

With $\sigma_c = 290 \text{ MPa}$ (from Section III(1)), Eq. (6) gives $\tau = 1.7 \text{ MPa}$. Thus, the three independent estimates of the frictional stress are consistent, within experimental accuracy.

(5) Residual Stresses

Residual stresses in composites arise both from differences in thermal contraction of the fibers and matrix and from unrelaxed volume changes associated with crystallization and phase changes. These stresses influence matrix fracture in two ways. Stresses parallel to the fibers superimpose directly on the applied stress, whereas stresses normal to the fiber axes affect the frictional forces between the fibers and matrix.

Residual stresses can be detected on a small scale by monitoring their effect on controlled cracks introduced by indentation.⁸ This method proved to be unsuitable for use on longitudinal sections because of disruption of the crack pattern by subsurface fibers of unknown location. However, indentations on transverse sections provided information pertinent to stresses normal to the fiber axes. Examples are shown in Fig. 12. The indentation cracks approach

the corners of the indentation contacted the matrix at the edge of the hole left by the depressed fiber, as shown in Fig. 10:

$$u = (b-a) \cot \psi \quad (3)$$

where 2ψ is the angle between opposite edges of the indenter ($2\psi = 74^\circ$ for the Vickers pyramid). The force applied to the fiber was calculated from the dimension of the residual hardness impression on the fiber surface

$$F = 2a^2 H \quad (4)$$

where the hardness, $H = 13$ GPa, was obtained by indenting other fibers at lower loads which did not cause the indenter to touch the matrix. For the example in Fig. 10(B), $F = 0.23$ N and $u = 3.0$ μ m, giving $\lambda = 1.7$ mm (smaller than the specimen thickness, $t = 7$ mm) and $\tau = 2.0$ MPa. Similar measurements from twenty other fibers gave $\tau = 2.5 \pm 0.9$ MPa.

A second estimate of the frictional stress can be obtained from the hysteresis in the crack opening (Fig. 9). Within the range where the crack opening curves are linear the difference in opening, Δ , at a given strain during the loading and unloading half cycles is (Appendix)

$$\Delta = 4d^2 \tau V_f / RV_m E_m \quad , \quad (5)$$

where $2d$ is the spacing of the multiple matrix cracks, V_f and V_m are the volume fractions of fibers and matrix, and E_m is the Young's modulus of the matrix.

indented configuration in Fig. 11(A). Only at a higher flexural load (Fig. 11(B)) did one of the indentation cracks normal to the applied tension extend to form a matrix crack.

(4) Frictional Stress

The magnitude of the frictional stress at the fiber/matrix interface can be measured directly using an indentation method,¹¹ which is illustrated in Fig. 10. In this technique a Vickers indenter is loaded onto the center of a fiber in a polished section normal to the fiber axis. The force applied to the fiber causes sliding and depresses the surface of the fiber a distance, u , below the matrix surface. The frictional stress, τ , and the distance, λ , over which the matrix and fiber slide can then be calculated from measurement of the distance u , and the force, F , applied to the fiber:¹¹

$$\tau = F^2 / 4\pi^2 u R^3 E_f \quad (1)$$

and

$$\lambda = 2\pi R^2 u E_f / F \quad (2)$$

where R is the fiber radius and E_f is the Young's modulus of the fiber ($E_f = 200 \text{ GPa}^6$). Equations (1) and (2) require λ to be smaller than the specimen thickness, t , and much larger than the fiber radius.

The value of u in Eqs. (1) and (2) is the fiber depression at maximum load. This was conveniently measured by choosing the indentation load such that

(2) Matrix Cracking

Observations of cracks during an unload/reload cycle (Fig. 8) provide a direct indication of the influence of the reinforcing fibers on matrix cracking. From a comparison of Figs. 8(B) and 8(D) it is clear that the crack opening, at a given strain, is larger during unloading than during loading. More extensive measurements of crack surface displacements during the load/unload cycle are shown in Fig. 9. These observations imply that the fibers exert frictional forces on the matrix, which tend to oppose crack closure during unloading and resist crack opening during loading. Therefore, frictional forces must play an important role in inhibiting the initial extension of the first crack through the matrix. Several estimates of the frictional shear stress are presented in Section III (4).

(3) Effect of Surface Damage on Matrix Cracking

Some flexural tests were done with the tensile test surfaces containing controlled flaws introduced by Vickers and Knoop indentation. Indentation loads ranged from 2 to 100 N. The lower loads produced cracks smaller than some of the fiber spacings, whereas the high loads produced cracks and chipping which extended across more than ten fibers. In all of these tests the stress at which the first matrix cracking occurred was not altered by the presence of the indentation flaws. In fact, in most cases the first matrix crack did not even initiate from the indentation. This is illustrated in Fig. 11(A) which shows the tensile surface of a beam loaded in flexure to the stage at which the first matrix crack formed. The surface also contains cracks generated by Vickers indentation at 5 N load. These cracks have not extended beyond their as-

tirely by the intact fibers bridging the crack. Further small increase of load caused formation of multiple regularly spaced cracks in the matrix throughout the central test area (Fig. 4). The spacing of the cracks was about 400 μm . After the formation of multiple cracks, further loading caused occasional additional cracks in the central area and in the areas further from the center where the cross section became larger (Fig. 2(A)). A large part of the additional deflection was due to pull out of the fibers from the matrix and the associated increase in crack opening. The peak load was determined by fiber failure, which continued in the region of relatively rapid load drop beyond the peak. At deflections beyond the peak the opening of one of the cracks became very large (Fig. 5(A)), and final separation involved the pulling of broken fibers through the blocks of matrix formed by the multiple cracking in the central test area (Fig. 5(B)). The response in the flexure test was similar, except that the matrix cracks penetrated only to about the midplane of the beam (Fig. 6), and the crack openings on the tensile surface did not become large enough to cause complete fiber pullout before compressive failure occurred in the opposite surface.

The formation of multiple matrix cracking in only half of the flexure bar has important consequences. In particular, the cracks destroy the macroscopic uniformity of the beam and render calculation of stress based on a uniform beam invalid. This is illustrated by a comparison of the compressive stresses calculated from beam bending formulae with the stresses indicated by a strain gauge on the compressive surface (Fig. 7). The apparent compressive strength calculated from the bending load would be 780 MPa, whereas the compressive strength obtained from the strain gauge is 1330 MPa.

these materials the appearance of being very "tough." Similar curves have been reported for flexure tests of a SiC/magnesium-alumino-silicate glass ceramic⁹ and carbon-fiber/glass-ceramic composites.¹

Although the general appearance of the load-deflection curves for flexure and tension are similar, several important details differ. On each of the plots in Fig. 3 an apparent stress scale is indicated as well as the load scale. For the flexure test this stress refers to the tension (or compression) calculated from the measured load using the relation for a uniform beam in bending.¹⁰ For the tension test the apparent stress was obtained from the measured load divided by the cross-sectional area of the test section. In both tests the onset of nonlinear deflection occurred at the same stress, $\sigma_c = 290 \pm 20$ MPa. However, the peak apparent stress was higher in bending than in tension (800 MPa vis-a-vis 500 MPa). Also, the onset of nonlinear deflection in the tension test was marked by a distinct load drop, and was followed by other load drops at higher loads, whereas in the flexure test load drops were not detected. The curves also differ in the relative deflections in the regions of linear load increase, nonlinear load increase, and decreasing load. Therefore, calculation of the work done by the loading system to cause failure (i.e., "work of fracture") clearly does not give a quantity which is a material property, independent of loading configuration.

The direct observation of the tensile surfaces during loading provides insight into the characteristics of the load/deflection curve. In both the flexure and tension tests the onset of nonlinear deflection coincided with the formation of a single matrix crack. In the tension test this crack passed completely through the central test section, and the applied load was supported en-

III. RESULTS

(1) Failure Mechanisms

Initially some general features of the flexural failure of the SiC/glass-ceramic composite are examined. In tests where the ratio of the separation of the inner and outer loading points, $d-e$, to the beam thickness, h , is large (i.e., $(d-e)/h \geq 8$) failure involves buckling of the fibers and fragmentation of the matrix on the compressive side of the beam (Fig. 1(A)). When the ratio $(d-e)/h$ is small (i.e., less than ~ 5) failure occurs by cracking along the neutral plane between the inner and outer loading points, where the shear stresses are highest (Fig. 1(B)). This change of fracture mechanism is consistent with the change in the ratio of the maximum compressive stress to the maximum shear stress as the loading configuration changes. The ratio of maximum compression to maximum shear in four-point flexure is $4(d-e)/h$, and the failure mode is determined by whichever of these stresses first exceeds the corresponding strength. Therefore, small values of $(d-e)/h$ tend to induce failure by shear. Similar reasoning might suggest that the observed compressive failure in Fig. 1(A) is consistent with a higher strength in tension than in compression (since maximum compression and tension in a uniform rectangular beam are equal). However, other observations indicate that the beam does not remain uniform during the flexure test.

The general features of the load/deflection curves for flexure and tension tests are shown in Fig. 3. In both cases an initial linear elastic region is followed by nonlinear load increase to a maximum, followed by continuous load decrease. It is the noncatastrophic decrease in load that gives

clamping and epoxy glue. The grips were loaded through balls located at positions colinear with the specimen axis, thus ensuring good alignment. The grips could be set either in a loading fixture on the stage of an optical microscope, or on a conventional tensile testing machine. When used in the horizontal position on the microscope stage the weight of the grips was counter-balanced by springs, and force measurements were made using a strain gauge load cell in the load train.

In the tests used to observe flexure bars during loading, the fixture could be mounted in several positions on the microscope stage to allow observation of either the tensile surface or the side of the bar. The inner and outer loading points in these experiments were separated by 13 mm and 45 mm, and the specimen dimensions were about 50 × 6 × 3 mm. Some specimens were tested with as-polished surfaces. Others had controlled flaws introduced into their polished test surfaces by loading with Vickers or Knoop indenters.

Two sets of experiments were performed using Vickers indentations on polished sections normal to the fibers. In one experiment the fiber/matrix bonding was investigated by loading the indenter in the center of a fiber and measuring the relative displacements of the fiber and matrix at a given load. In the other experiment the indentation was located in the matrix and the radial cracks generated by the indentation were used to investigate residual stresses.⁸

15. B. Budiansky, A.G. Evans and J.W. Hutchinson, to be published.
16. B.J. Pletka and S.M. Wiederhorn; pp. 745-59 in Fracture Mechanics of Ceramics, Vol. 4. Edited by R.C. Bradt, D.P.H. Hasselman, and F.F. Lange, Plenum, New York, 1978.
- 17.

APPENDIX

Calculations of Crack Opening During Loading and Unloading

Consider a section of composite between two matrix cracks of spacing $2d$ (Fig. A1(A)). Before the cracks are formed the residual stresses σ_R^f and $-\sigma_R^m$ exist in the fibers and matrix, such that the sections of fiber and matrix are respectively extended and compressed from their relaxed states (Fig. A1(B)) by $2z_0^f = 2(\sigma_R^f/E_f)d$ and $2z_0^m = 2(\sigma_R^m/E_m)d$. The application of stress, σ_a , larger than a critical value, σ_c , causes matrix cracking and slipping between fibers and matrix over a distance d , as illustrated in Fig. A1(C). The average strain in the composite is $\epsilon_c = z/d$ (Fig. A1(C)), and the crack opening can be written

$$u_0 = 2(z - \delta - z_0^m) = 2d(\epsilon_c - \delta/d - \sigma_R^m/E_m) \quad , \quad (A1)$$

where the distance δ is given by

$$\delta = \tau V_f d^2 / R V_m E_m \quad . \quad (A2)$$

Further increase of the applied stress to a peak value σ_u , followed by a reduction to σ_a , causes reverse slipping between the matrix and fibers. Reverse slip initiates at the crack surface and extends along the interface as the applied stress is reduced. Budiansky et al.¹⁵ have shown that, for $\sigma_a \lesssim \sigma_u - \sigma_c$, the reverse slip extends fully over the length d , as depicted in Fig. A1(D). Then the crack opening is

$$u_c = 2(z + \delta - z_0^m) = 2d(\epsilon_c + \delta/d - \sigma_R^m/E_m) \quad . \quad (A3)$$

Thus, Eqs. (A1) and (A3) represent the linear portions of the loading and unloading curves in Fig. 9 (except that the strain in Fig. 9 is measured on the compressive surface and, therefore, differs by a constant factor from the average strain on the tensile surface, ϵ_c).

The frictional stress τ can be evaluated from the difference in crack opening at a given strain, (Eqs. A1 to A3);

$$\Delta = u_c - u_0 = 4\tau V_f d^2 / RV_m E_m \quad . \quad (A4)$$

The residual stress in the matrix can be obtained from the sum of the (extrapolated) crack openings at $\epsilon_c = 0$ (Eqs. A1 and A3);

$$u_c + u_0 = 4d \sigma_R^m / E_m \quad . \quad (A5)$$

FIGURE CAPTIONS

- Fig. 1 Specimens of SiC/glass-ceramic composite after flexural testing. (A) Rectangular beam tested in 4-point loading. Separation of inner and outer load points is 16 mm, specimen thickness is 2 mm. (B) As in (A), but with specimen thickness 3.5 mm, separation of inner and outer load points 10 mm. View shows right half of specimen with load points indicated by arrows. (C) Rectangular beam containing a notch (cut with a diamond saw) and tested in 4-point loading with the notch in the center of the tensile test area.
- Fig. 2 Schematic diagrams of (A) the tensile test specimen, (B) the tensile test fixture used for in situ observations.
- Fig. 3 Load-deflection curves for (A) flexure and (B) tension tests. An apparent stress is also indicated on each plot. For the flexure test this was calculated from the measured load, assuming a uniform beam in bending. For the tension test it was obtained from the measured load divided by the cross-sectional area of the test section.
- Fig. 4 Tensile surface of a flexure specimen, loaded beyond the linear region of the load-deflection curve. Width of field 1.5 mm. Brightly reflecting regions are polished cross sections of fibers, grey regions are the matrix.
- Fig. 5 (A) Matrix crack in tension specimen, loaded beyond the peak load (apparent stress = 200 MPa). Width of field 550 μm . (B) Tensile test specimen extended far beyond the peak load condition. Width of field 12 mm.
- Fig. 6 Side view of area between inner load points of a flexure beam, showing matrix cracks confined to the tensile half of the beam.

- Fig. 7 Comparison of apparent stresses in the compressive surface of a flexure beam, one calculated from strain gauge measurements, and the other calculated from the measured load assuming a uniform beam in bending.
- Fig. 8 Sequence of optical micrographs showing a matrix crack on the tensile surface of a four-point flexure beam during an unload/reload cycle. (A) to (C) decreasing load; (C) to (A) increasing load. Stresses obtained from strain gage on compressive surface; (A) 600 MPa, (B) 210 MPa, (C) zero, (D) 210 MPa, (E) 600 MPa. Note that the crack is not visible in (C), and that the crack opening is larger in (B) than in (D). Width of each micrograph 166 μm .
- Fig. 9 Plot of separation of crack surfaces in tensile surface of a flexure beam during loading, unloading, and reloading. Measurements from optical micrographs similar to Fig. 8. Strains obtained from strain gage on compressive surface. Note that absolute accuracy of crack opening measurements is limited by optical resolution ($\sim \pm 0.4 \mu\text{m}$). However, since all micrographs were taken under effectively identical conditions, the uncertainty in the differences is considerably lower (provided that the crack openings are $\geq 1 \mu\text{m}$).
- Fig. 10 (A) Schematic of indentation method used to measure matrix-fiber frictional stress. (B) Scanning electron micrograph showing a fiber that was indented with a Vickers pyramid at 0.5 N load. The edges of the pyramid contacted the matrix at the edge of the hole left by the indented fiber. Width of field 32 μm .
- Fig. 11 Vickers indentation in tensile surface of flexure beam (A) apparent stress = 300 MPa. Note crack in matrix near the indentation, but the indentation crack has not grown. (B) Apparent stress = 310 MPa. The indentation crack has extended partly through the matrix. Width of field 534 μm .
- Fig. 12 (A) and (B); Indentation cracks in matrix, formed by loading a Vickers pyramid at 2 N. Note that the cracks are not deflected as they approach the fibers.

Fig. A1. Schematic showing relative displacements of matrix and fibers between two matrix cracks.

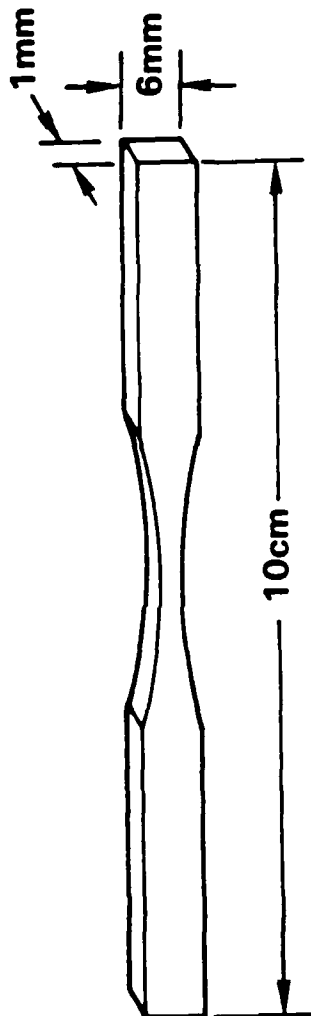
- (A) Single fiber and surrounding matrix before cracking. σ_R^m and σ_R^f are residual stresses. Prospective crack planes are AA' and BB'.
- (B) Displacements required to relax residual stresses.
- (C) Displacements of fiber and matrix after applying stress σ_a to the composite ($\sigma_a > \sigma_c$).
- (D) Displacements of fiber and matrix after increasing σ_a to σ_u , then reducing σ_a to a value $< (\sigma_u - \sigma_c)$.

SC84-28371

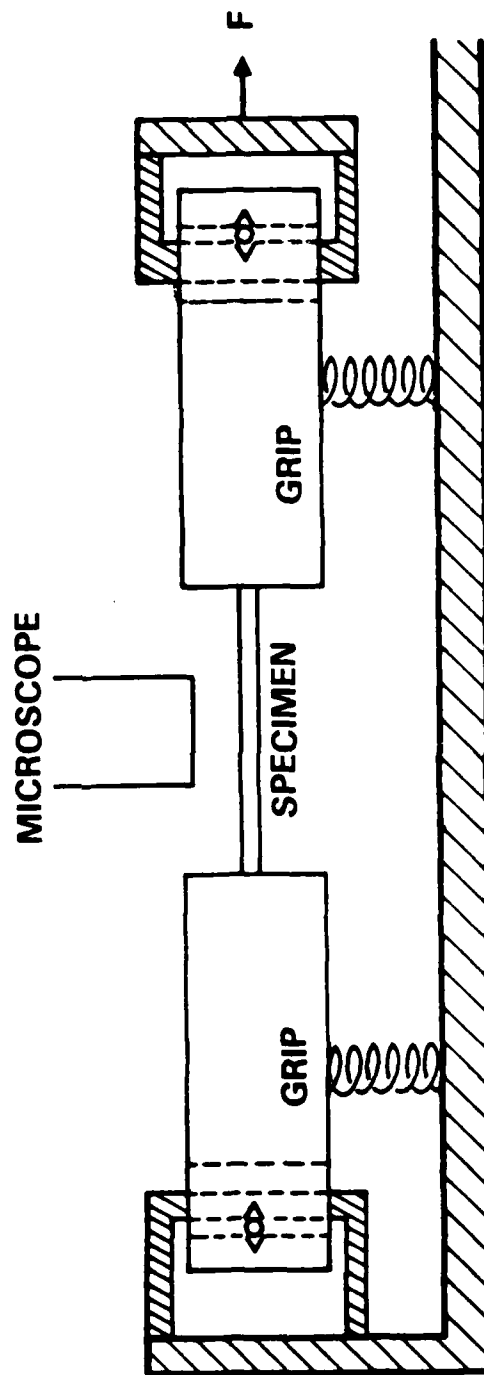


Fig. 1

SC84-27198



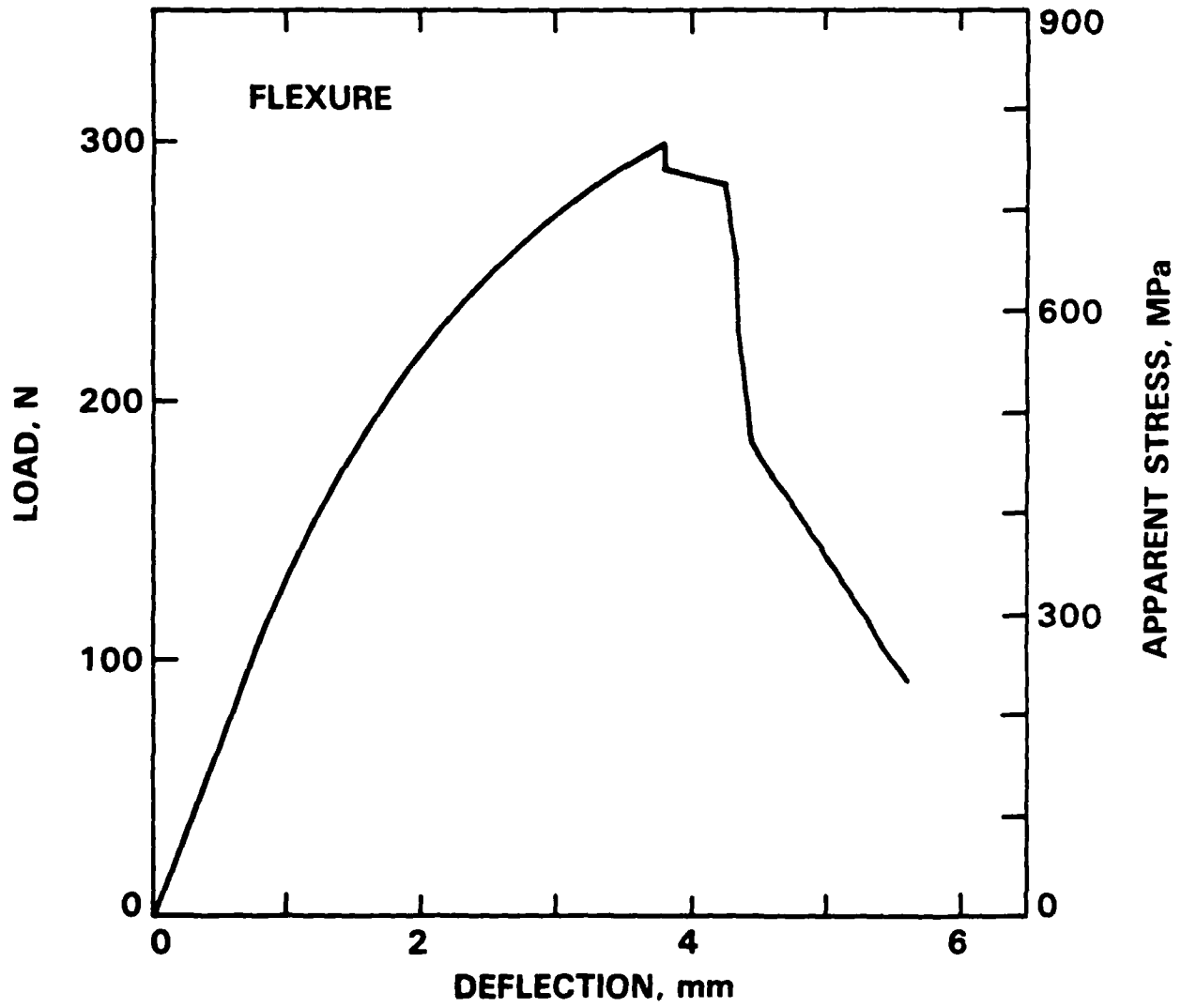
(A)



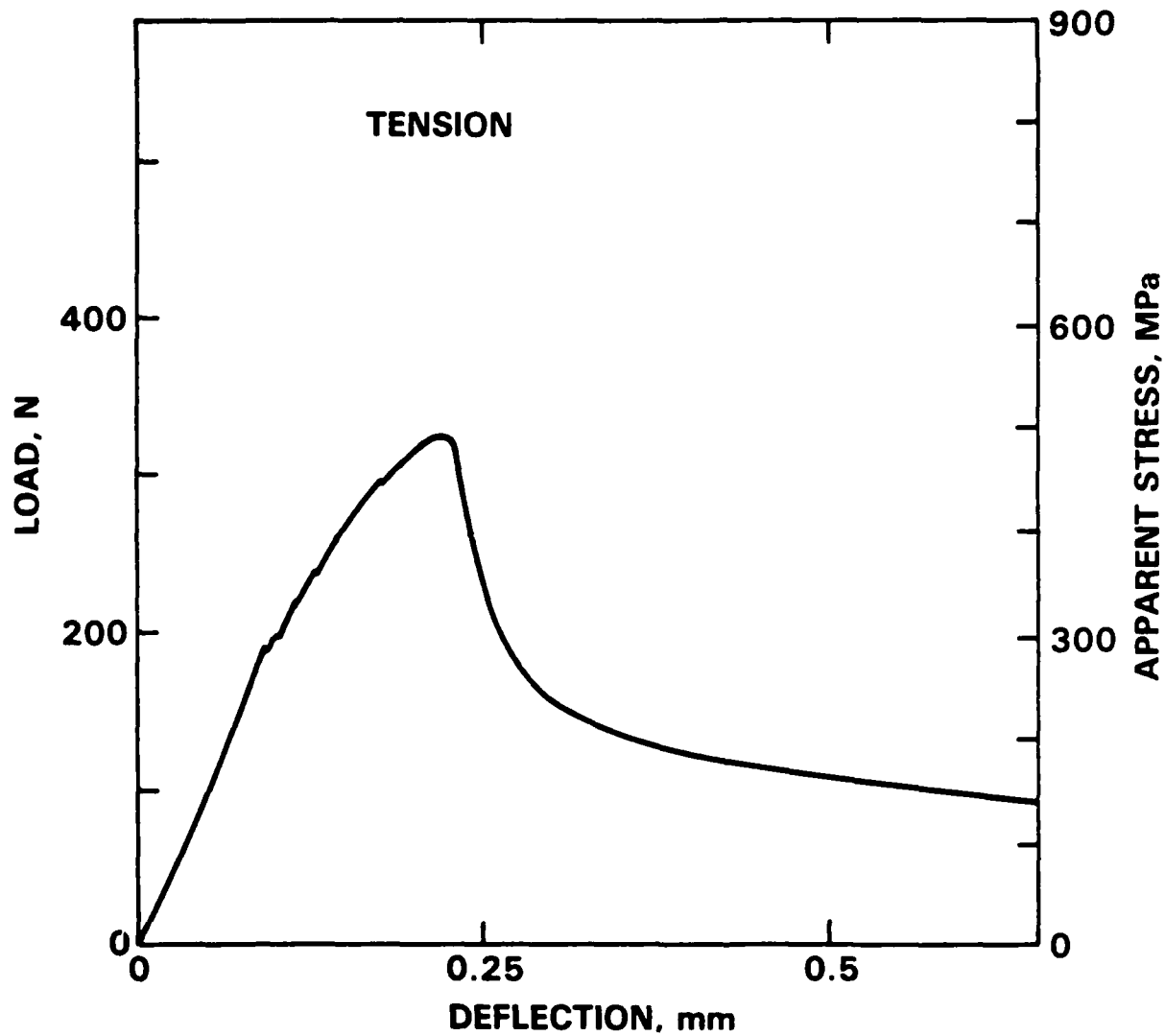
(B)

Fig. 2

SC84-27197



SC84-27196



SC84-28372

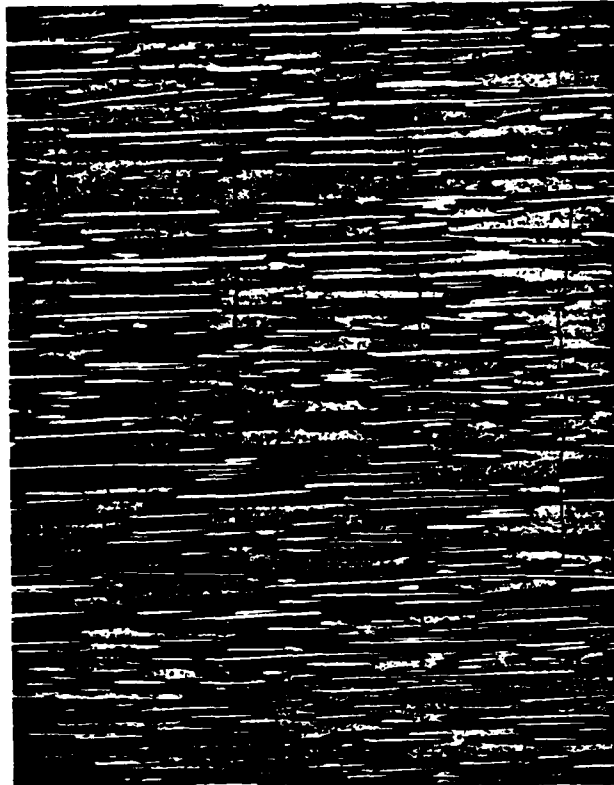


Fig. 4

SC84-28373



Fig. 5A

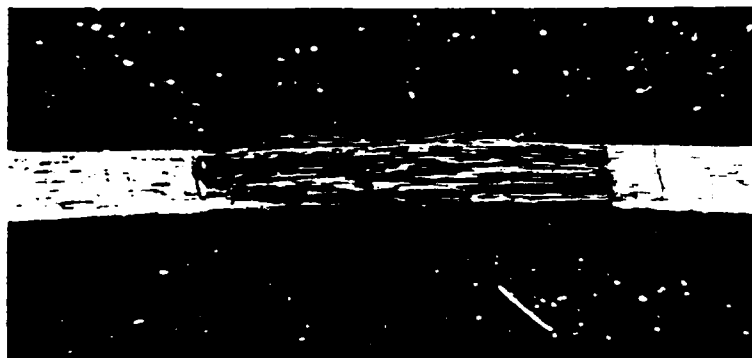


Fig. 5B

SC84-28374



Fig. 6

intensity method. Finally, several implications of the analysis for matrix cracking in various composite systems are discussed.

2. STRESS INTENSITY FORMULATION OF MATRIX CRACKING

Separation of the surfaces of a matrix crack which is bridged by uniaxially aligned reinforcing fibers (Fig. 1) requires some sliding of the matrix over the fibers. In general, this would require debonding followed by sliding against frictional forces. However, it appears that in successfully reinforced ceramic composites, there is no chemical bond between the fibers and matrix. The present analysis is concerned with such unbonded composites, in which the sliding of the matrix over the fibers is resisted only by frictional forces.

The restraining effect of the fibers causes a reduction in both the crack opening and the crack tip stresses. Relations between these quantities and the remotely applied stress, σ_∞ , can be evaluated by imagining the crack in Fig. 1 to be formed in two steps. First, all of the bonds across the prospective crack plane (in the fibers as well as the matrix) are cut and the stress σ_∞ is applied (Fig. 2a) causing the crack to open. In the second step tractions, T , are applied to the end of each fiber. The magnitude of T is chosen such that the fiber ends displace relative to the matrix and allow the fibers to be rejoined (Fig. 2b). In a continuum approximation ($c \gg$ fiber spacing) this procedure is equivalent to applying a distribution of closing pressure $p(x)$ to the crack surfaces:

generally deterministic, but rather are sensitive to distributions of flaws. Second, the energy balance analysis was based on a comparison of energies before and after complete cracking of the matrix, whereas a rigorous thermodynamic treatment of crack growth requires examination of energy changes that accompany incremental changes in crack length. These deficiencies are addressed in the present study.

It is convenient to distinguish between large and small cracks as a basis for further analysis. Large cracks experience a crack opening, u , which asymptotically approaches (but cannot exceed) the equilibrium separation, u_0 , of the completely failed matrix (i.e., two half planes connected by fibers (Fig. 1)). This limiting separation is approached beyond a characteristic distance, c_0 , from the crack tip. Within that region the net force in the intact fibers that bridge the crack must exactly balance the applied force. In this case the crack tip stress concentration is induced exclusively over the length c_0 , and the stress needed to extend the crack must be independent of the total crack length. Crack growth in this region is referred to as steady state growth. Conversely, for short cracks (i.e., $c < c_0$) the entire crack contributes to the stress concentration, such that the stress required to propagate a crack is sensitive to the crack length (as it is in monolithic materials).

Crack growth can be evaluated using either energy balance or stress intensity considerations. The general formalism for the stress intensity approach is presented in the following section. Then the steady state crack is examined using both stress intensity and energy balance approaches in order to establish the equivalence of the two independent methods of analysis. The growth characteristics of short cracks are then evaluated using the stress

1. INTRODUCTION

The reinforcement of brittle materials with high strength brittle fibers can yield composites that undergo large tensile strains prior to failure. In such materials prefailure damage initiates with the formation of multiple, regularly spaced cracks in the matrix.¹ This damage mode requires the strain-to-failure of the matrix to be less than that of the fibers, and the fibers to have sufficient strength to remain intact after a crack passes completely through the matrix. Materials that have been observed to behave in this manner include cement and plaster reinforced by glass, steel, or asbestos fibers,²⁻⁶ and glasses and glass ceramics reinforced by carbon⁷⁻⁹ and SiC^{10,11} fibers.

The ultimate load bearing capacity of the composite may substantially exceed the load for matrix cracking. Nevertheless, the first matrix crack is of prime concern because matrix fracture signifies the onset of permanent damage, the loss of protection provided by the matrix against corrosion and oxidation of the fibers, and the likelihood of an enhanced susceptibility to degradation due to cyclic loading. Despite the importance of the first matrix crack, a complete fracture mechanics analysis does not exist. Some aspects of the problem have been addressed by Aveston, Cooper and Kelly.¹ Specifically, assuming that the matrix possesses a characteristic strength, independent of strength-controlling defects, they rationalized the regularity of the matrix cracking. They also used an energy balance analysis to introduce a dependence of strength on microstructure and account for certain increases in matrix strength observed in systems containing small diameter fibers. However, this analysis has two limitations. First, the cracking strengths of glasses and ceramics are not

ABSTRACT

Matrix fracture in brittle-matrix fiber composites is analyzed for composites that exhibit multiple matrix cracking prior to fiber failure and which have purely frictional bonding between the fibers and matrix. The stress for matrix cracking is evaluated using a stress intensity approach, with the influence of the fibers that bridge the matrix crack being represented as closure tractions at the crack surfaces. Long and short cracks are distinguished. Long cracks approach a steady-state configuration, for which the stress intensity analysis and a previous energy balance analysis are shown to predict identical dependence of matrix cracking stress on material properties. For short cracks an approximate analytical solution is derived and used to estimate the range of crack sizes over which the steady state solution applies.

THE MECHANICS OF MATRIX CRACKING IN BRITTLE-MATRIX
FIBER COMPOSITES

D.B. Marshall

Rockwell International Science Center
1049 Camino Dos Rios
Thousand Oaks, CA 91360

and

A.G. Evans

Department of Materials Science and Mineral Engineering
University of California
Berkeley, CA 94720

CHAPTER IV

THE MECHANICS OF MATRIX CRACKING
IN BRITTLE-MATRIX FIBER COMPOSITES

D. B. Marshall and A. G. Evans

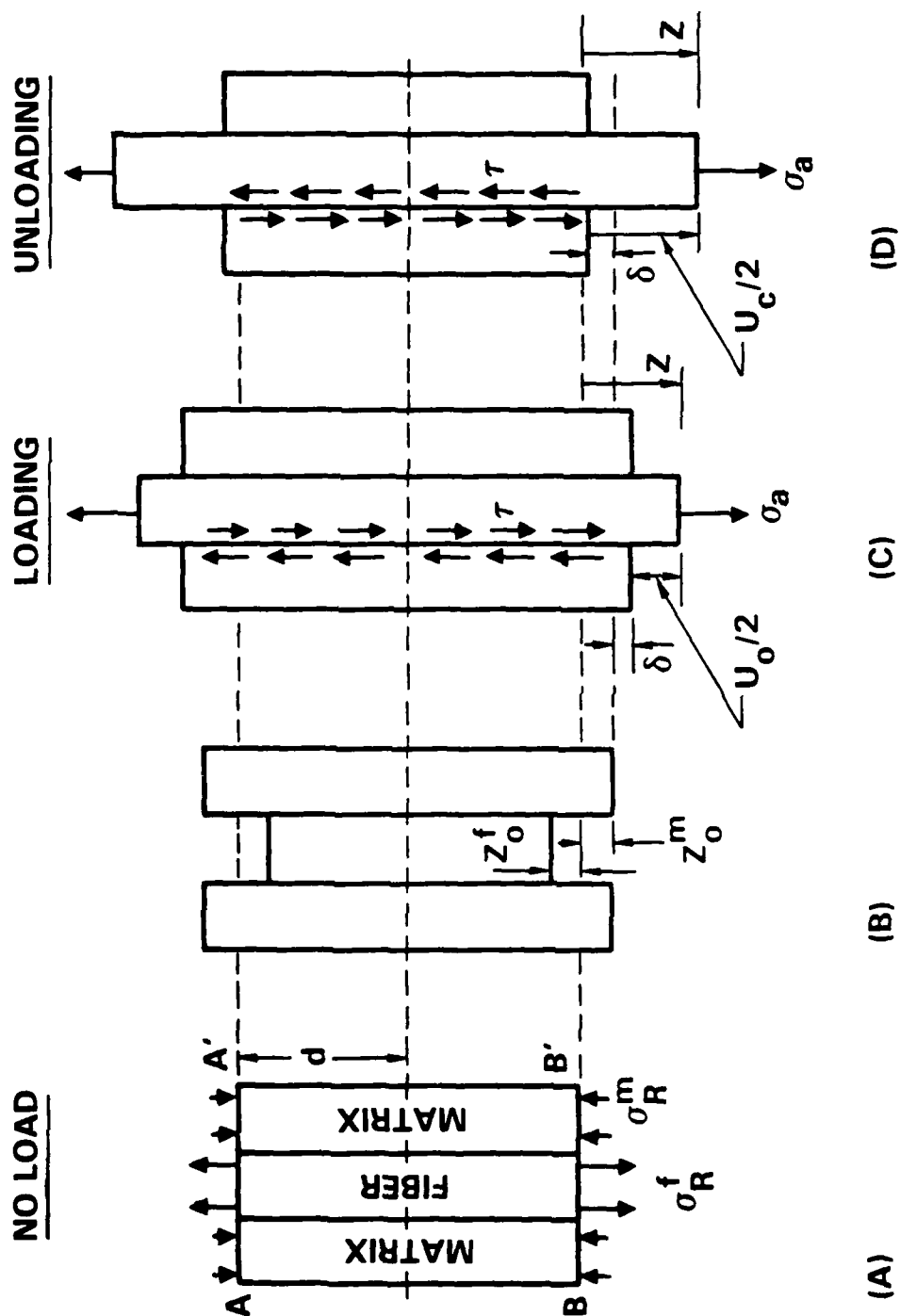


Fig. A(1)

SC84-28378

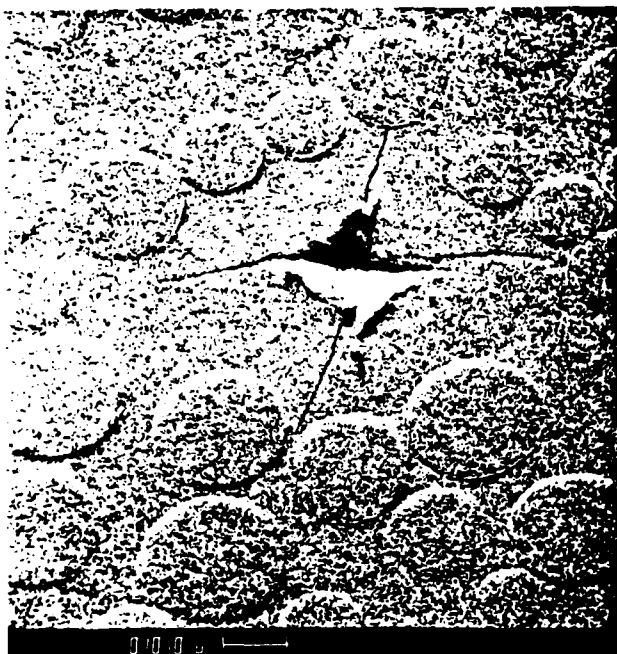


Fig. 12

SC84-28377

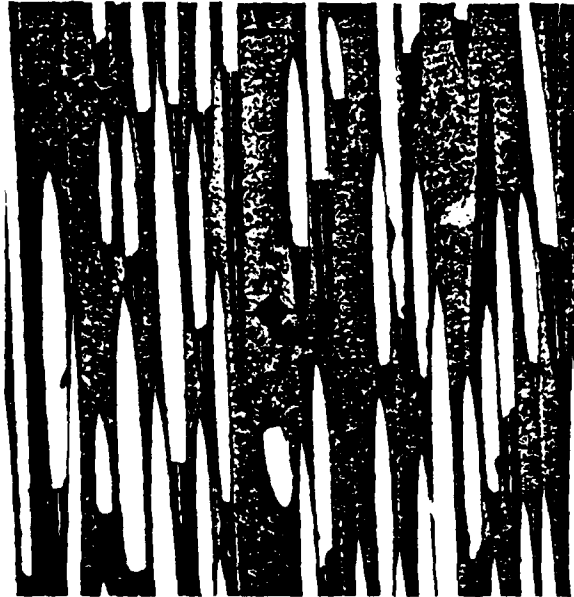


Fig. 11

SC84-28376

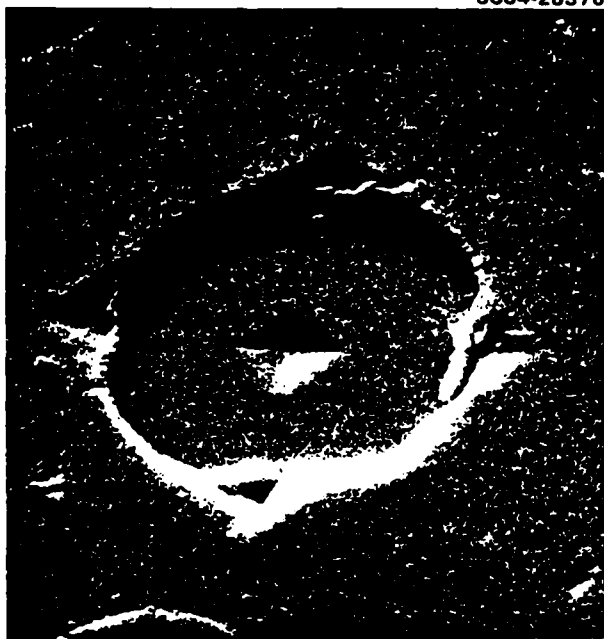


Fig. 10B

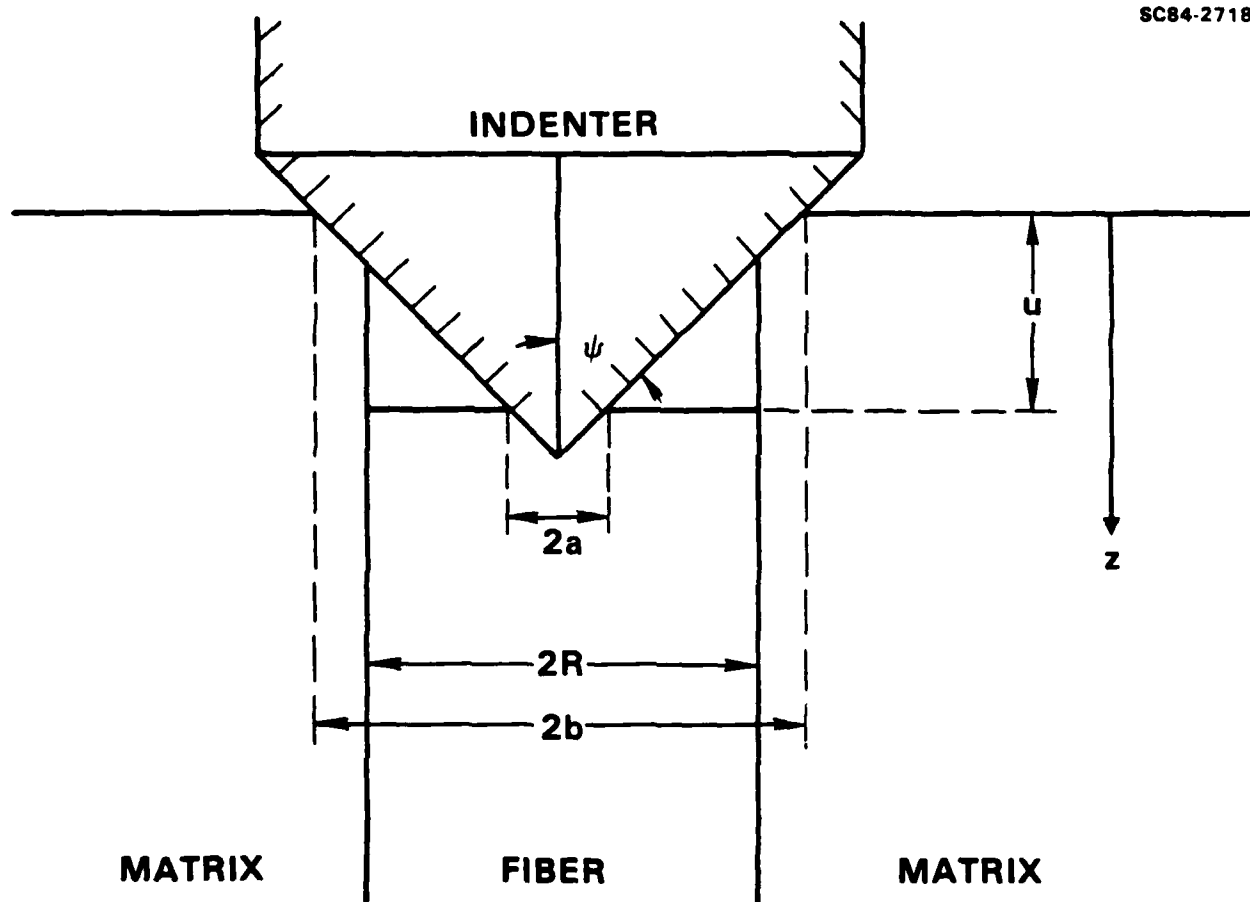
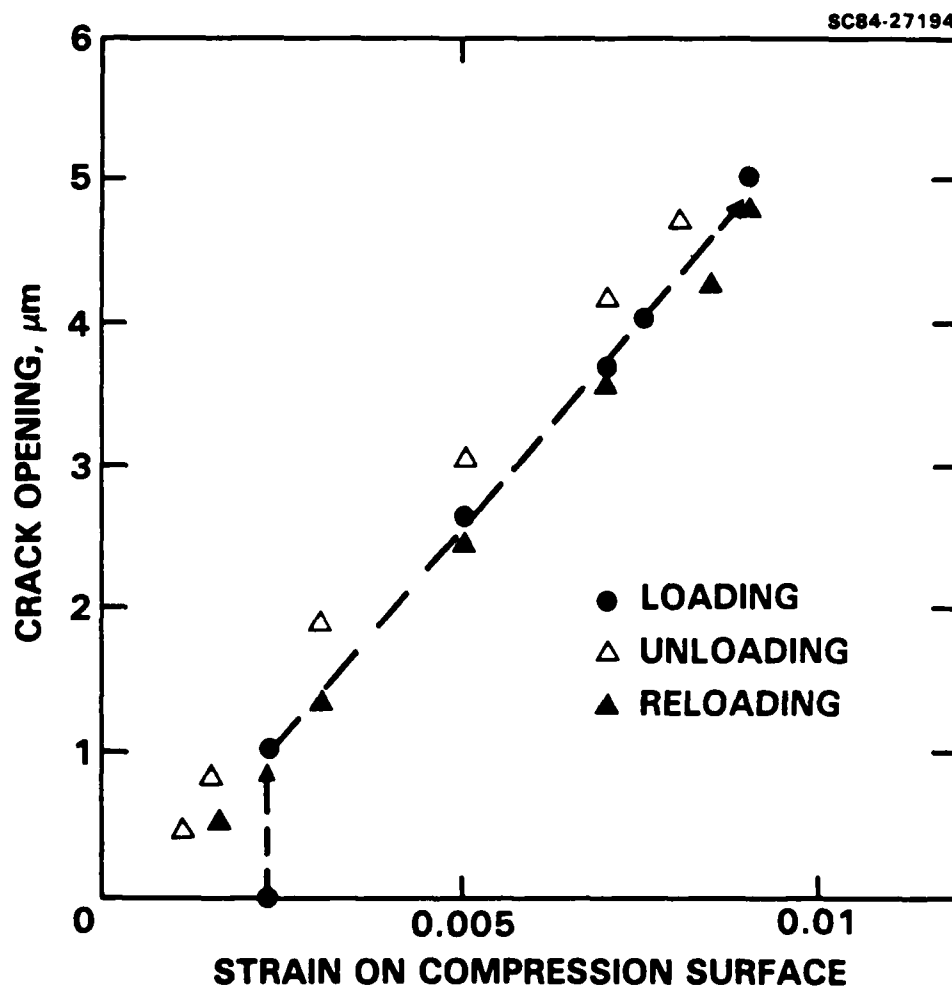


Fig. 10(a)



SC84-28375

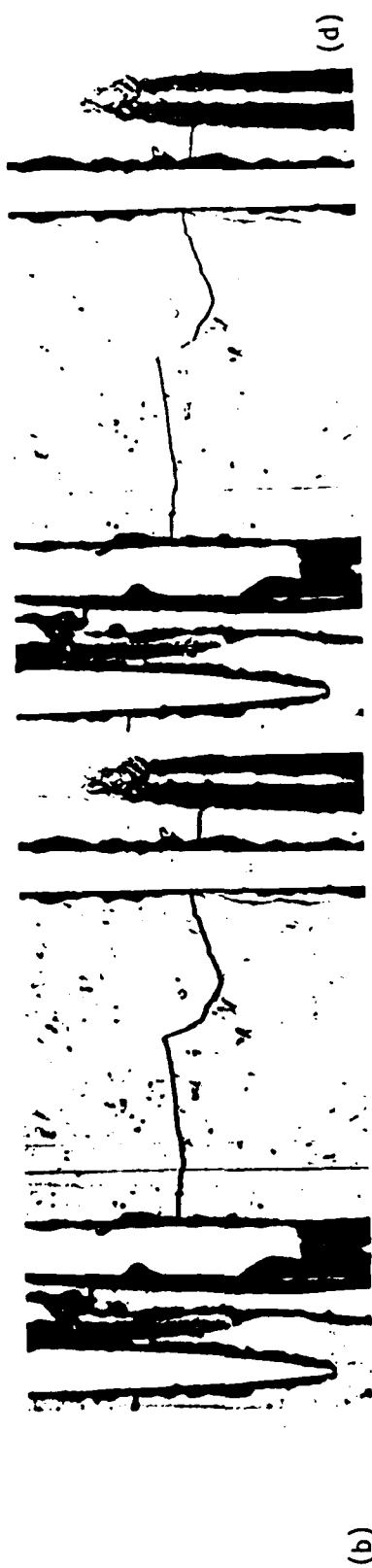
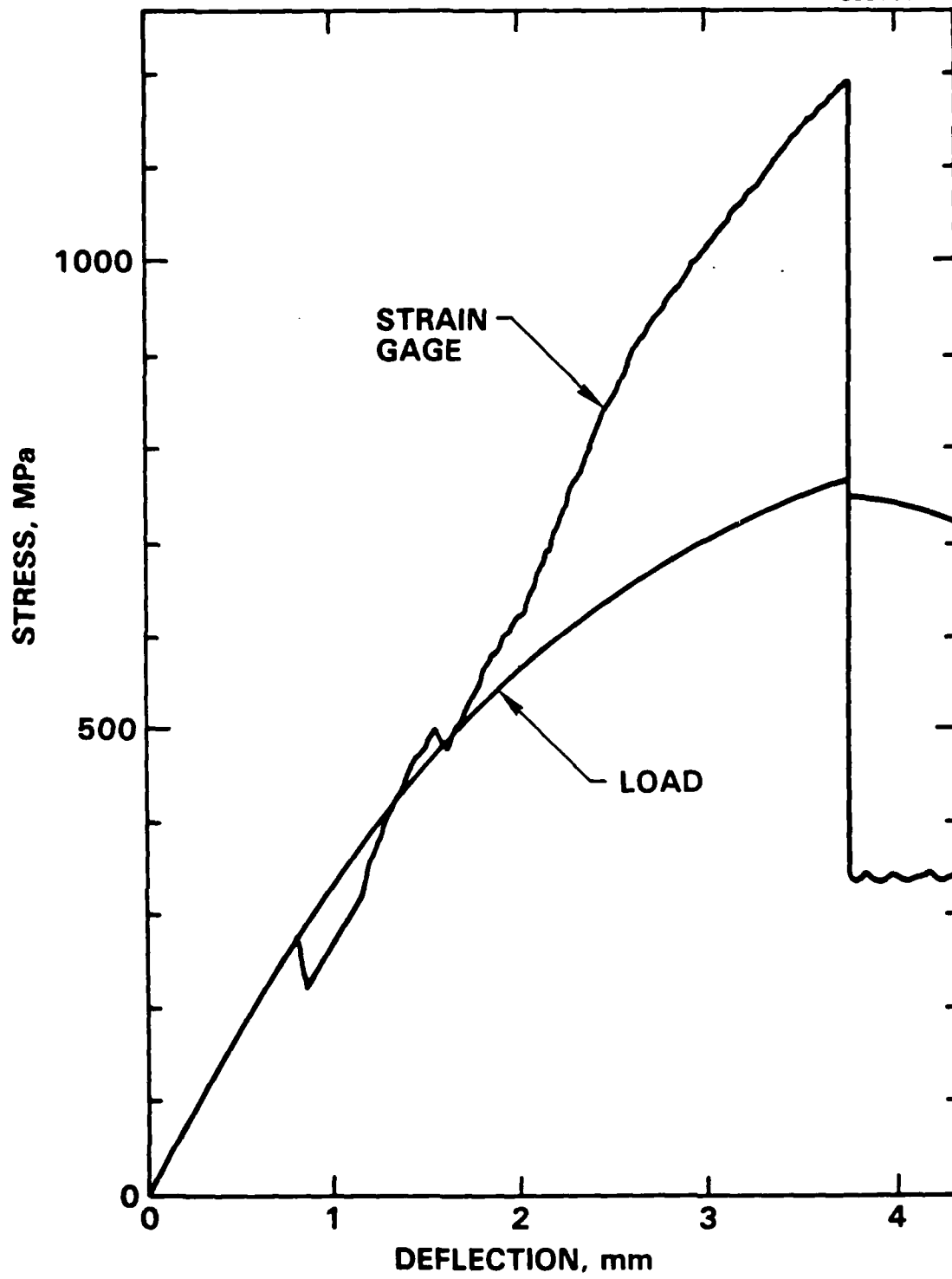


Fig. 8



$$p(x) = T(x) V_f \quad (1)$$

where x represents the position on the crack surface (Fig. 2b) and V_f is the volume fraction of fibers. The closure induced by the pressure $p(x)$ opposes the opening due to the applied stress σ_∞ . The influence of the applied stress on the crack tip stress intensity can be exactly evaluated by regarding the stresses as a uniform opening pressure, σ_∞ , acting along the crack surfaces. Therefore, the crack surfaces are subjected to net pressure $(\sigma_\infty - p(x))$, such that a composite stress intensity factor for a straight embedded crack in an infinite medium can be defined as;^{12,13}

$$K^L = 2(c/\pi)^{1/2} \int_0^1 [\sigma_\infty - p(X)](1 - X^2)^{-1/2} dX \quad (2)$$

where $X = x/c$. The corresponding equation for a penny crack is given in Appendix 2.

The stress intensity K^L characterizes the composite stress and strain fields in the region immediately ahead of the matrix crack. In this region, net relative displacements between the fibers and the matrix are not permitted. Consequently, the matrix and fiber strains must be compatible, whereupon the stresses exhibit the composite relationship

$$\sigma^M/E_m = \sigma_\infty/E_c \quad (3a)$$

where σ^M is the matrix stress and E_c is the composite modulus,

$$E_c = E_m V_m + E_f V_f$$

with E_m and E_f referring to the Young's modulus of the matrix and fibers, respectively and $V_m (\equiv 1 - V_f)$ the volume fraction of matrix. The matrix and composite stress intensities must scale with the stresses, such that

$$K^L = K^M E_c / E_m \quad (3b)$$

where K^M is the stress intensity factor in the matrix. In the absence of environmental effects the condition for equilibrium crack growth is given by setting K^M equal to the critical stress intensity factor, K_c^M , for the matrix. Equivalently, the criterion for crack growth can be expressed in terms of K^L ;

$$K^L = K_c^L \equiv K_c^M E_c / E_m \quad (4)$$

Thus, Eqs. (2) and (4) relate the matrix cracking to the applied stress σ_∞ .

Evaluation of K^L in Eq. (2) requires a separate calculation of the pressure distribution $p(x)$. Analysis of fiber pullout from the matrix (Appendix 1) reveals that the closure pressure is related to the crack opening at a given location:

$$p = 2[u\tau V_f^2 E_f (1 + \eta)/R]^{1/2} \quad (5)$$

where $\eta = E_f V_f / E_m V_m$, R is the fiber radius, and τ is the sliding frictional stress at the interface. However, the crack opening at a given position is determined by the entire distribution of surface tractions¹⁶

$$U(x) = \frac{4(1 - \nu^2)}{\pi E_c} \int_x^c \frac{s}{\sqrt{s^2 - x^2}} \int_0^s \frac{[\sigma_\infty - p(t)] dt}{\sqrt{s^2 - t^2}} ds \quad (6)$$

where ν is the Poisson's ratio of the composite. Therefore, analysis of matrix cracking by the stress intensity approach requires solution of Eqs. (5) and (6) to obtain the crack surface tractions, followed by evaluation of the integral in Eq. (2) and combination with Eq. (4).

3. STEADY STATE CRACKS

The intent of this section is to demonstrate that the energy balance and stress intensity approaches predict equivalent dependence of the stress for steady state crack growth, σ_0 , on microstructural parameters. The energy balance solution derives from the earlier analysis by Aveston et al., but is expressed in terms of incremental crack extension. The stress intensity approach has not been considered previously.

3.1 Energy Balance Analysis

The energy changes occurring in the specimen and loading system during an incremental crack extension define the crack growth behavior. These energy changes can be calculated by employing the hypothetical operation depicted in Fig. 3 to extend the crack by dc . A strip of material of width dc ahead of the crack (area AA'B'B) is removed, a cut is made in the matrix along CC', the matrix is allowed to relax causing the ends of the strip to displace, and the strip is attached at the mouth of the crack. When the cut is made in the matrix, the matrix must slide back over the fibers while the fibers also extend. When this occurs work, dU_s , is done against frictional forces, the strain energy in the matrix decreases by dU_m , the strain energy in the fibers increases by dU_f , and the potential energy of the loading system decreases by dU_L . These energy changes can be calculated from the results presented by Aveston et al.¹;

$$dU_s = [\sigma_\infty^3 R/6\tau E_f V_f^2 (1 + \eta)^2] dc \quad (7a)$$

$$dU_m = [\sigma_\infty^3 R \eta / 3\tau E_f V_f^2 (1 + \eta)^3] dc \quad (7b)$$

$$dU_f = [\sigma_\infty^3 R (3\eta + 1) / 6\tau E_f V_f^2 (1 + \eta)^3] dc \quad (7c)$$

$$dU_L = [\sigma_\infty^3 R / 2\tau E_f V_f^2 (1 + \eta)^2] dc \quad (7d)$$

The net energy change of the system resulting from the incremental crack extension is

$$dU = 2\Gamma_m V_m dc + dU_s + dU_f - dU_m - dU_L \quad (8)$$

where $2\Gamma_m = G_C^m = K_C^{M^2} (1 - \nu^2) / E_m$ is the fracture surface energy of the matrix. Setting $\sigma_\infty = \sigma_0$ at Griffith equilibrium ($dU/dc = 0$) and combining Eqs. (7) and (8) yields a crack extension stress:

$$\sigma_0 = \delta [(1 - \nu^2) K_C^{M^2} \tau E_f V_f^2 V_m (1 + \eta)^2 / E_m R]^{1/3} \quad (9)$$

where $\delta = 6^{1/3}$.

3.2 Stress Intensity Analysis

A simple dimensional analysis is used in this section to demonstrate that the crack extension stress obtained from stress intensity considerations exhibits the same form as Eq. (9). Specific numerical quantities for the steady-state crack will be obtained in the following section.

The stress system for a steady state crack is depicted in Fig. 4. As noted previously, the closure pressure exactly balances the applied loading in the region $x < c - c_0$ (i.e., the net crack surface tractions, $\sigma_\infty - p$, are zero). However, over the area $c - c_0 < x < c$, p is smaller than σ_∞ , such that net opening tractions exist. In this region $p(x)$ must vary smoothly between zero at $x = c$ (where the matrix/fiber slipping is zero) and σ_∞ at $x = c - c_0$, i.e.,

$$p = \sigma_\infty f(\rho) \quad \rho \leq 1 \quad (10)$$

where $\rho = r/c_0 = (c - x)/c_0$ and $f(\rho)$ is a function that varies between zero at $\rho = 0$ and unity at $\rho = 1$. Thus, for steady state cracks ($c \gg c_0$ and $(\sigma_\infty - p) = 0$ for $r > c_0$), Eq. (2) reduces to

$$\begin{aligned} K^L &= (2/\pi)^{1/2} \int_0^{c_0} [\sigma_\infty - p(r)] r^{-1/2} dr \\ &\equiv v \sigma_\infty c_0^{1/2} \end{aligned} \quad (11)$$

where v is a dimensionless constant ($v = (2/\pi)^{1/2} \int_0^1 [1 - f(\rho)] \rho^{1/2} d\rho$).

The length c_0 is evaluated by considering the crack opening displacements within the range $r < c_0$. For the steady state crack Eqs. (6) and (10)

reduce to

$$u(\rho) = \frac{2(1 - v^2) \sigma_{\infty} c_0}{\pi E_c} \int_0^{\rho} \frac{1}{\sqrt{\rho - \lambda}} \int_1^{\lambda} \frac{[1 - f(\phi)] d\phi}{\sqrt{\phi - \lambda}} d\lambda \quad (12)$$

where $\phi = t/c_0$ and $\lambda = s/c_0$. An alternative expression for $u(\rho)$ is obtained from Eqs. (5) and (10),

$$u(\rho) = \sigma_{\infty}^2 [f(\rho)]^2 R/4\tau V_f^2 E_f (1 + \eta) \quad (13)$$

Thus, equating Eqs. (12) and (13) yields

$$c_0 = w \sigma_{\infty} E_c R / \tau V_f^2 E_f (1 + \eta) (1 - v^2) \quad (14)$$

where w is another dimensionless constant

$$w = \pi [f(\rho)]^2 / 8 \left[\int_0^{\rho} \frac{1}{\sqrt{\rho - \lambda}} \int_1^{\lambda} \frac{[1 - f(\phi)] d\phi}{\sqrt{\phi - \lambda}} d\lambda \right] \quad (15)$$

The matrix cracking stress, σ_0 , is now obtained by evaluating K^L from Eqs. (11) and (14) and setting $\sigma_{\infty} = \sigma_0$ at $K^L = K_c^L \equiv K_c^M E_c / E_m$;

$$\sigma_0 = \delta' [(1 - v^2) K_c^M]^2 \tau E_f V_f^2 V_m (1 + \eta)^2 / E_m R]^{1/3} \quad (15)$$

where

$$\delta' = (w v^2)^{-1/3}.$$

Comparison of Eqs. (9) and (15) indicates that the energy balance and stress intensity analyses predict identical dependencies of matrix cracking stress on microstructural parameters.

4. SHORT CRACKS

Evaluation of K^L for short cracks requires explicit determination of the crack opening displacements from Eqs. (5) and (6). However, rigorous analytic solutions for $u(x)$ cannot be obtained. Even numerical solutions involving more simple $p(u)$ relations require iterative procedures.¹⁷ Nevertheless, considerable insight into the mechanics of crack growth can be obtained by adopting an analytical approximation for $u(x)$.

The approximation involves an assumption that, at small crack sizes, the crack profile does not differ greatly from that of a crack subject to uniform pressure. Then an analytical solution for $u(x)$ is obtained from Eq. (6), in terms of the net stress intensity factor K^L ;

$$u(x) = 2(1 - \nu^2)K^L c^{1/2} (1 - x^2/c^2)^{1/2} / E_c \pi^{1/2} \quad (16)$$

The actual pressure distribution is obtained by combining Eqs. (5) and (16)

$$p(x) = [\alpha K^L c^{1/2} (1 - x^2/c^2)^{1/2}]^{1/2} \quad (17a)$$

where

$$\alpha = 8(1 - \nu^2) \tau_f^2 E_f (1 + \eta) / E_c R \pi^{1/2} \quad (17b)$$

For $x \approx c$, Eq. (16) is an exact solution for the present problem (since displacements near the crack tip must be a unique function of K^L). However, it is clearly not appropriate at small x in large cracks, because as already noted the crack opening must asymptotically approach u_0 , whereas the opening in Eq. (16) is unbounded at large c . The limiting displacement is given by setting $p = \sigma_\infty$ in Eq. (5)

$$u_0 = \sigma_\infty^2 R / 4 \tau_f^2 E_f (1 + \eta) \quad , \quad (18)$$

and the corresponding transition crack length c_0 is given by Eq. (16) with $u = u_0$ and $x = 0$;

$$c_0 = \sigma_\infty^4 / \alpha^2 K^2 L^2 \quad . \quad (19)$$

Therefore, the displacement expressed by Eq. (16) is used only for cracks smaller than c_0 (i.e., $u < u_0$). For larger cracks an approximate limiting solution is obtained from a crack profile that is uniform ($u = u_0$) near the center ($x < c - c_0$) and governed by a pressure distribution in the near tip region ($x > c - c_0$) that is the same as for a crack of length c_0 . The final result will be shown to be insensitive to the exact value of crack length at which the crack opening is truncated.

With this approximation the stress intensity factor for $c < c_0$ is given by substituting Eq. (17a) into Eq. (2)

$$K^L = \Omega \sigma_c^{1/2} - (4\alpha/\pi)^{1/2} (K_c^L)^{1/2} c^{3/4} I \quad c < c_0, \quad (20a)$$

where $\Omega = \pi^{1/2}$ and

$$I = \int_0^1 (1 - x^2)^{-1/4} dx = 1.20. \quad (20b)$$

The mechanics of crack growth can be investigated by setting $K^L = K_c^L$ in Eq. (20a) and solving for σ_∞ to obtain an equilibrium-stress/crack-size function;

$$\sigma_\infty = K_c^L / \Omega c^{1/2} + [4\alpha K_c^L I^2 / \pi \Omega^2]^{1/2} c^{1/4} \quad (c < c_0) \quad (21)$$

This function can be conveniently expressed in normalized form,

$$\sigma/\sigma_m = (1/3)(c/c_m)^{-1/2} + (2/3)(c/c_m)^{1/4} \quad (c < c_0), \quad (22)$$

where

$$c_m = (\pi K_c^L / \alpha I^2)^{2/3} \quad (23a)$$

$$\sigma_m = (3/\Omega)(K_c^L)^2 \alpha I^2 / \pi)^{1/3} = 3K_c^L / \Omega c_m^{1/2}. \quad (23b)$$

Equation (23) provides a relation between normalized stress and crack length parameters, $S = \sigma/\sigma_m$ and $C = c/c_m$, without explicit reference to material and microstructural properties (these properties enter only in their influence on

the normalizing factors c_m and σ_m). Thus, the mechanics of crack growth may be examined independently of the specific composite system.

For $c > c_0$ the region of crack where $u = u_0$ does not contribute to the stress intensification at the crack tip. Therefore, for a straight crack, which maintains geometrical similarity as it extends, the stress intensity factor for $c > c_0$ is given by Eq. (20) with $c = c_0$. The corresponding equilibrium stress, σ_0 , which is independent of crack length, is given by Eqs. (19) and (21);

$$\sigma_0 = \sigma_\infty = [\alpha(K_c^L)^2 / \Omega(1 - 2I/\Omega\pi^{1/2})]^{1/3} \quad (24a)$$

which, with substitution from Eqs. (4) and (17b), can be expressed

$$\sigma_0 = \delta''[(1 - \nu^2)(K_c^M)^2 \tau E_f V_f^2 V_m (1 + \eta)^2 / E_m R]^{1/3} \quad (24b)$$

where

$$\delta'' = [8/\Omega\pi^{1/2}(1 - 2I/\Omega\pi^{1/2})]^{1/3} .$$

The relative values c_0/c_m and σ_0/σ_m are obtained from Eqs. (19), (22a), (22b) and (24a):

$$c_0/c_m = [I/\pi^{1/2}\Omega(1 - 2I/\pi^{1/2}\Omega)]^{4/3} = 1.88 \quad (25a)$$

$$\sigma_0/\sigma_m = [\Omega^2 \pi / I^2 (1 - 2I/\Omega\pi^{1/2})]^{1/3} / 3 = 1.02 . \quad (25b)$$

s, in the normalized form these stress and crack length parameters also are explicitly dependent upon material or microstructural properties.

The complete equilibrium-stress/crack-size function is plotted in Fig. 5 (solid curve). It is noted that the stress required to propagate a critical crack is almost independent of crack length (within about 2%) for cracks longer than about $c_m/3$. This defines the range of crack sizes for which steady state conditions pertain. The crack response in this region contrasts with the behavior of cracks in unreinforced brittle materials, where the strength decreases with $c^{-1/2}$. For cracks shorter than $\sim c_m/3$ the equilibrium stress increases, with a crack length dependence resembling that of a monolithic brittle material. It is also noted that, since the stress/crack-size function for $c < c_0$ is very flat in the vicinity of $c = c_0$, the curve in Fig. 5 is not sensitive to the use of the truncated form for the crack profile as an approximation to the true profile.

5. IMPLICATIONS AND DISCUSSION

One of the important results of the present analysis is the definition of the approximate crack dimensions over which the transition from short crack behavior to steady-state response occurs. The matrix cracking stress approaches steady-state value for crack lengths $\geq c_m/3$ (Fig. 5). The crack length c_m can be evaluated from Eq. (23a), in conjunction with Eq. (17b):

$$c_m = (\pi/4I^{4/3})[K_C^M E_m V_m^2(1 + \eta)R/\tau V_f^2 E_f(1 - \nu^2)]^{2/3}. \quad (26)$$

Values of c_m calculated for two composite systems in which the parameters of Eq. (26) are known with reasonable accuracy are shown in Table 1. For both composites, $c_m/3$ is several fiber spacings. Since the sizes of inherent flaws in brittle materials are usually about the same as microstructural dimensions, these results imply that the stress for matrix cracking in these composites is reduced by the further introduction of larger flaws during fabrication or in service (e.g., mechanical contact damage), or by the extension of pre-existing flaws in thermal shock or environmentally assisted slow crack growth. It is also noted that, with the continuum approximation adopted in Section 4, the analysis holds only for crack lengths larger than several fiber spacings, i.e., is not valid in the region where the $\sigma(c)$ curve in Fig 5 rises with decreasing c .

The crack size independence of the matrix cracking stress at $c \geq c_m/3$ verifies, in part, the earlier analysis of Aveston et al,¹ for it is now

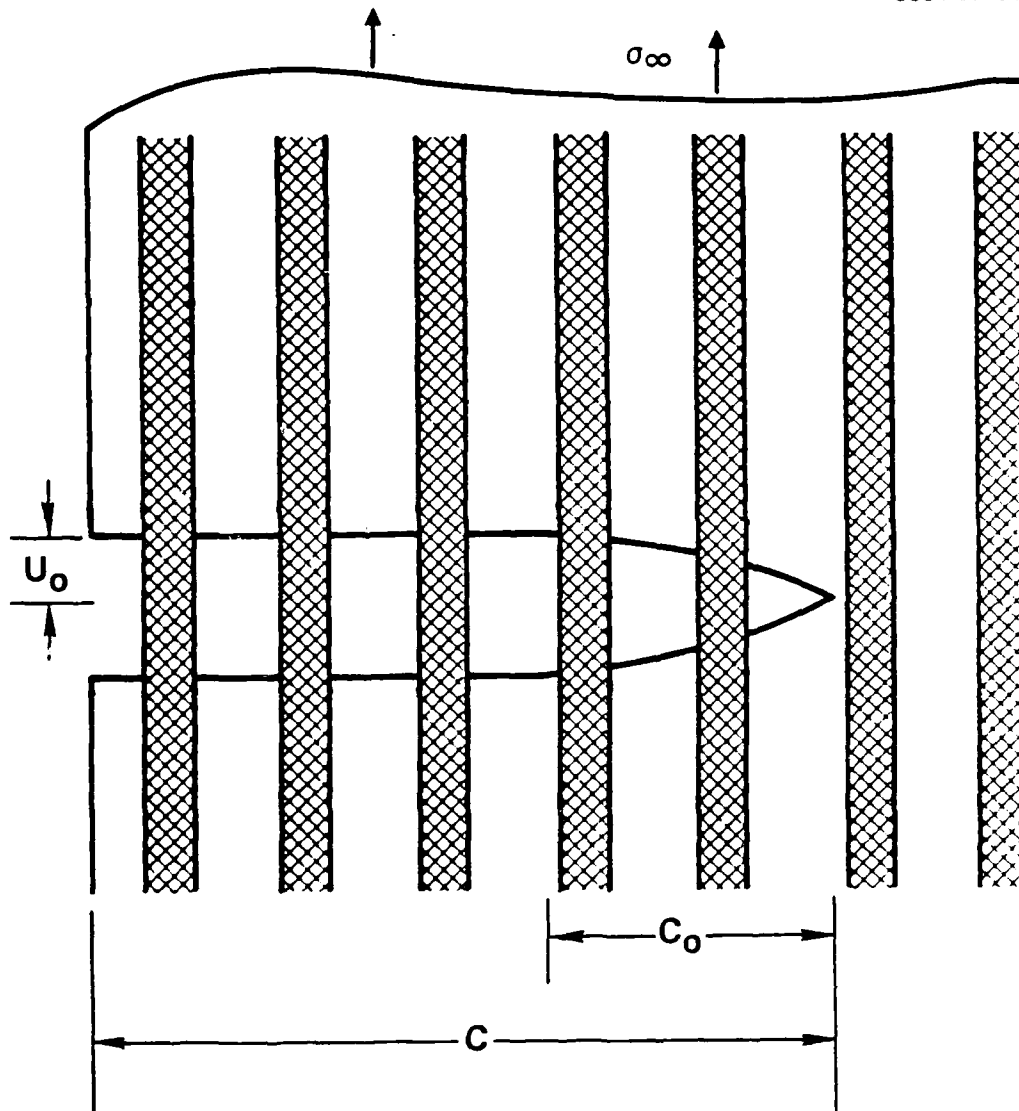


Fig. 1

FIGURE CAPTIONS

- g. 1 Schematic representation of a steady-state matrix crack in a fiber composite.
- g. 2 (A) and (B) Hypothetical operations used to evaluate the closure effect of the fibers in the stress intensity analysis.
- g. 3 Steady-state crack configuration used for energy balance analysis.
- ig. 4 Net surface tractions acting on steady-state crack.
- ig. 5 Equilibrium-stress/crack-size functions for matrix crack in composite and for a monolithic matrix.
- ig. 6 Analysis of fiber pullout mechanics.
- ig. 7 Equilibrium-stress/crack-size functions for penny crack.

Table 1
Fiber/Matrix

| | SiC/Glass Ceramic ^(a) | Carbon/Glass ^(b) |
|------------------------------|----------------------------------|-----------------------------|
| <u>Measured Properties</u> | | |
| K_C^M | 2 MPa·m ^{1/2} | 0.75 MPa·m ^{1/2} |
| E_f | 200 GPa | 380 GPa |
| E_m | 85 GPa | 70 GPa |
| V_f | 0.5 | 0.4 |
| R | 8 μ m | 8 μ m |
| τ | 2 MPa | 10 MPa |
| Matrix Cracking | | |
| Stress | 270 - 300 MPa | 340 MPa |
| <u>Calculated Properties</u> | | |
| c_m | 313 μ m | 68 μ m |
| σ_0 | 307 MPa | 361 MPa |

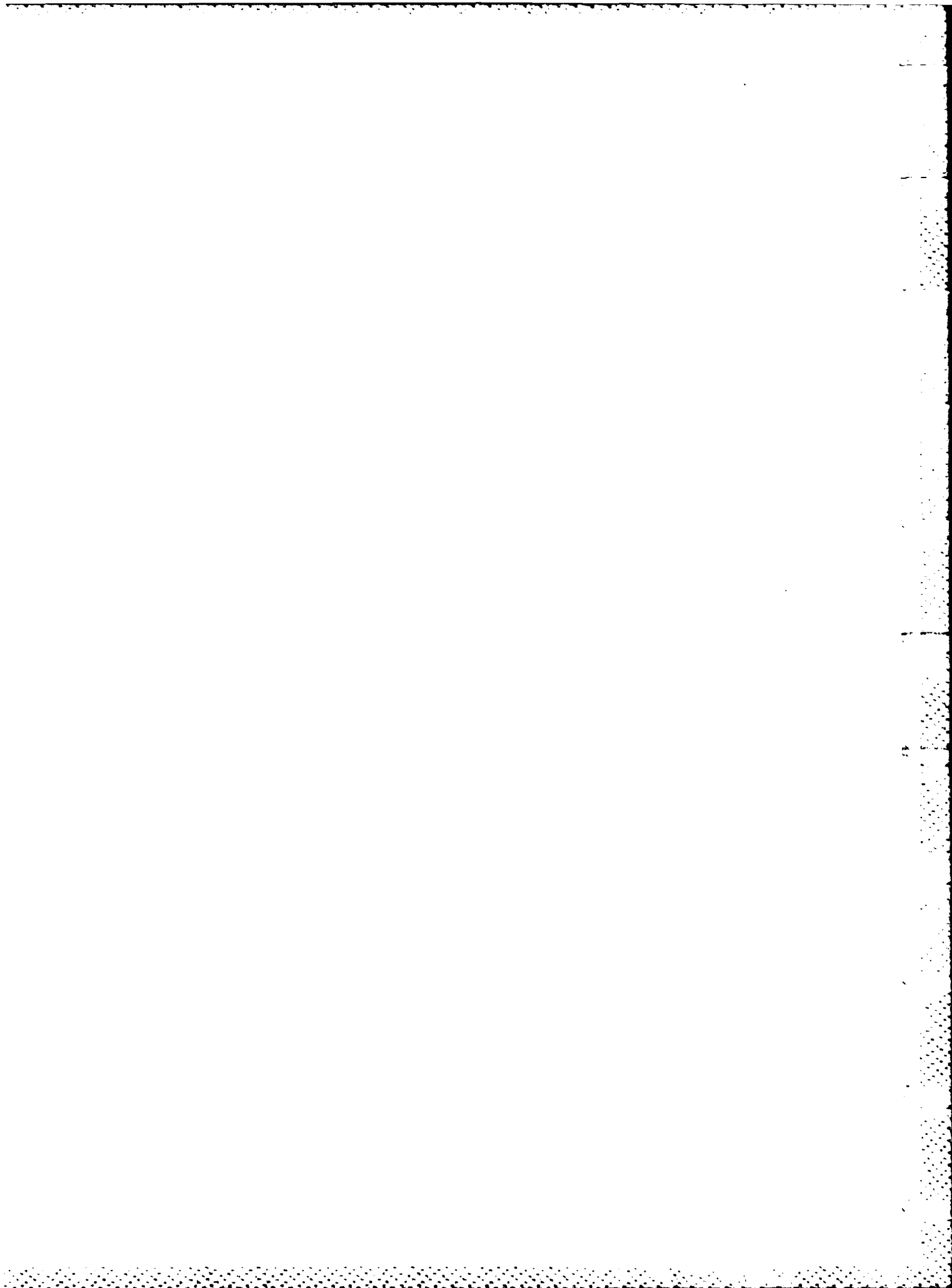
(a) Data from Refs. 10 and 11.

(b) Data from Refs. 7 to 10.

- i. B.J. Pletka and S.M. Wiederhorn; pp. 745-59 in Fracture Mechanics of Ceramics, Vol. 4. Edited by R.C. Bradt, D.P.H. Hasselman and F.F. Lange, Plenum, New York, 1978.
- j. I.N. Sneddon and M. Lowengrub, "Crack Problems in the Classical Theory of Elasticity," Wiley, New York, 1969.
- k. C. Atkinson, "An Iterative Scheme for Solving Problems Related to Cracks Opening Under a Displacement-Dependent Internal Stress," Int. J. Fract. 6[2] 193-197 (1970).

REFERENCES

1. J. Aveston, G.A. Cooper and A. Kelly, "Single and Multiple Fracture," pp. 15-26 in The Properties of Fiber Composites, Conference Proceedings, National Physical Laboratory, IPC Science and Technology Press Ltd. 1971.
2. M.A. Ali and F.J. Grimer, "Mechanical Properties of Glass Fiber Reinforced Gypsum," J. Mat. Sci. 4[5] 389-95 (1969).
3. A.J. Majumdar, "Glass Fiber Reinforced Cement and Gypsum Products," Proc. Roy Soc. A319 69-78 (1970).
4. R.C. deVekey and A.J. Majumdar, Mag. Concrete. Res. 20 229- (1968).
5. H.G. Allen, "Stiffness and Strength of Two Glass-Fiber Reinforced Cement Laminates," J. Comp. Mats. 5[2] 194-207 (1971).
6. J.P. Romualdi, U.S. Patent 3429094 (1969).
7. R.A.J. Sambell, A. Briggs, D.C. Phillips and D.H. Bowen, "Carbon Fiber Composites with Ceramic and Glass Matrices," J. Mat. Sci. 7[6] 676-681 (1972).
8. D.C. Phillips, "The Fracture Energy of Carbon-Fiber Reinforced Glass," J. Mat. Sci. 7[10] 1175-91 (1972).
9. J.J. Brennan and K.M. Prewo, "Silicon Carbide Reinforced Glass-Ceramic Matrix Composites Exhibiting High Strength and Toughness," J. Mat. Sci. 17[8] 2371-83 (1982).
10. K.M. Prewo and J.J. Brennan, "Silicon Carbide Yarn Reinforced Glass Matrix Composites," J. Mat. Sci. 17[4] 1201-6 (1982).
11. D.B. Marshall and A.G. Evans, "Failure Mechanisms in Ceramic-Fiber/ Ceramic-Matrix Composites," submitted to J. Amer. Ceram. Soc.
12. B.R. Lawn and T.R. Wilshaw, Fracture of Brittle Solids, Cambridge University Press, London, 1975.
13. G.C. Sih, Handbook of Stress Intensity Factors, Lehigh University, Bethlehem, 1973.
14. S.M. Wiederhorn; pp. 613-46 in Fracture Mechanics of Ceramics Vol. 2. Edited by R.C. Bradt, D.P.H. Hasselman and F.F. Lange, Plenum, New York, 1974.



factor) maintains geometrical similarity as the crack extends beyond c_0 , such that a steady-state condition exists. The corresponding region of a penny crack, on the other hand, does not maintain geometrical similarity. In this case the region that determines the stress intensity factor can be viewed as an annular crack around a cylindrical hole. At $c \approx c_0$ this configuration approaches a penny crack, whereas at large crack lengths $c \gg c_0$ it approaches an edge crack. Therefore, c_0 and σ_0 vary between these two limits as the crack grows. The relative values of σ_0 and c_0 for straight cracks and penny cracks are 0.97 and 0.87, respectively (Eqs. 19 and 24). Since the difference between the values of σ_0 for these two geometries is very small, calculations for intermediate configurations are not deemed necessary.

The complete equilibrium-stress/crack-size function for penny cracks is plotted in Fig. 7. The curve is almost the same as the corresponding result for straight cracks (Fig. 5).

APPENDIX 2: PENNY CRACKS

For a penny crack the stress intensity factor and crack opening relations (Eqs. 2 and 5) become^{13,16}

$$K^L = 2(c/\pi)^{1/2} \int_0^1 [\sigma_\infty - p(x)] x(1 - x^2)^{-1/2} dx \quad (A10)$$

$$u(x) = \frac{4(1 - \nu^2)}{\pi E} \int_x^c \frac{1}{\sqrt{s^2 - x^2}} \int_0^s \frac{[\sigma_\infty - p(t)] t dt}{\sqrt{s^2 - t^2}} ds \quad (A11)$$

These differ from the corresponding relations for straight cracks by the factors x and t within the integrals. In the limit of steady-state cracks these equations reduce to Eqs. (10) and (12) (i.e., the same result as for straight cracks). Therefore, the analysis of Section 3.2 holds for both crack configurations.

In the analysis for short cracks (Section 4) some numerical differences appear. The approximate crack profile, when expressed in the form of Eq. (16), pertains to both crack geometries. The stress intensity factor relation and all other equations in that section are also of the same form, except that $\Omega = 2/\pi^{1/2}$ and the dimensionless integral I (Eq. 20b) becomes

$$I = \int_0^1 x(1 - x^2)^{-1/4} dx = 2/3 \quad .$$

With these values we obtain $c_0 = c_m$ from Eq. (25a), and $\sigma_0 = \sigma_m$ from Eq. (25b).

For crack growth beyond c_0 an additional difference appears. For a straight crack, the region $c - c_0 < x < c$ (which determines the stress intensity

$$\delta/l = \pi R l \tau / A_m E_m \quad (A4)$$

$$(\delta + u)/l = T_f/E_f + \pi R l \tau / A_f E_f \quad (A5)$$

where $A_f = \pi R^2$ is the fiber cross-sectional area and A_m is the area of matrix per fiber. The requisite relation between T and u is then obtained from Eqs. (A1) to (A5). First, Eqs. (A1) to (A3) combine to give

$$T = 2 l \tau (1 + \eta) / R \quad (A6)$$

where $\eta = E_f V_f / E_m V_m$. Then Eqs. (A1), (A2), (A4) and (A5) combine to give

$$l^2 = u R E_f / \tau (1 + \eta) \quad (A7)$$

Finally, from Eqs. (A6) and (A7) we obtain

$$T = 2 [u E_f \tau (1 + \eta) / R]^{1/2} \quad (A8)$$

and, with Eq. (1),

$$\rho = 2 [u \tau V_f^2 E_f (1 + \eta) / R]^{1/2} \quad (A9)$$

APPENDIX 1: MECHANICS OF FIBER PULLOUT

The application of tractions T to the end of the fiber in Fig. 6 causes sliding between the matrix and fiber over a distance l , and allows the fiber to pull out of the matrix a distance u . For a purely frictional matrix-fiber bond, the sliding distance is determined by the length over which the interface shear stresses exceed the frictional stress τ . A relation between T and u is required for the stress intensity analysis.

The mechanics of fiber pullout can be conveniently analyzed by applying tractions T_m and T_f , equal and opposite to the stresses in the matrix and fibers, along the plane AA' at the end of the slipped region, and removing the section $A'C'C'A$ (Fig. 6b). If we neglect the effect of shear stresses above AA' in Fig. 6a (i.e., assume that the strains in the matrix and fiber are equal above AA') these tractions are related by

$$T_m/E_m = T_f/E_f \quad (A1)$$

Equations relating the stresses and displacements in Fig. 6b are obtained by considering the equilibrium of the matrix and fiber separately and also by calculating the extensions δ and $\delta + u$ of the matrix and fiber:

$$T_m A_m = 2\pi R l \tau \quad (A2)$$

$$T A_f = 2\pi R l \tau + T_f A_f \quad (A3)$$

which is not strongly influenced by τ . Increasing K_C^m increases both σ_0 and c_m . Thus, a maximum K_C^m could be dictated either by the fiber failure stress or by the requirement that c_m be less than pre-existing flaw sizes.

The preceding restrictions account for the brittle response observed in a number of fiber or whisker reinforced brittle systems, and place important bounds on the design of optimum microstructures. Furthermore, implicit in the ability to design materials and to interpret results within the context of the present analysis is the availability of methods for measuring τ , K_C^m and σ_0 . Developments pertinent to such measurement have been reported in recent studies.

Concluding Remarks

The principal implications of the present analysis concern the predicted transition to a crack length independent matrix cracking stress, σ_0 , for cracks longer than a characteristic length $\sim cm/3$, and the associated trends in matrix fracture. The matrix cracking stress (i.e., the first deviation from linearity in the stress strain curve) should be both damage tolerant and independent of specimen size, provided the characteristic length $cm/3$ is smaller than preexisting flaws in the matrix. In this sense ceramic matrix composites can be more like metals than ceramics in their tensile mechanical behavior.

The analysis indicates that the attainment of steady state cracking at high stress levels is likely to be restricted to a narrow range of microstructures. These restrictions arise from the requirements that cm be sufficiently small and that the fibers remain intact after a crack passes completely through the matrix (i.e., $\sigma_0 < \sigma_b V_f$, where σ_b is the bundle strength of the fibers in the presence of additional stresses due to frictional forces). Thus, uniaxially reinforced composites, in which V_f can be large, offer the potential for optimum properties (increasing V_f increases both σ_0 and $\sigma_b V_f$ and decreases cm). In multiaxially reinforced systems (such as 3-D or random whisker composites) the smaller volume fraction of fibers aligned in any direction limits the value of σ_0 that can be achieved without causing fiber failure and increases cm , making a crack-length-dependent matrix fracture stress more likely. The existence of optimum values of matrix toughness, K_c^m , and interfacial shear resistance, τ , can be inferred from the analysis. Increasing τ increases σ_0 and decreases cm , but a maximum acceptable increase is defined by the fiber failure stress, $\sigma_b V_f$,

results can be obtained by estimating the dimensionless constant, wv^2 , in Eq. (15) from the analysis of Section 4. Thus, from Eqs. (5) and (24b) we obtain $wv^2 = 2.21$ which yields a stress $\sim 20\%$ higher than that obtained from the energy balance analysis. This represents reasonable agreement in view of the simplifications which underlie the analyses (e.g., assumed crack profile, representation of frictional forces as tractions applied to the crack surfaces rather than distributed along the fibers).

Predicted values of the stress for matrix cracking (from Eq. 9) in the SiC/glass-ceramic and carbon/ glass composite systems are shown in Table 1. In both cases good agreement with experimentally measured values is evident. Hence, the predicted relation between the critical stress for matrix cracking and microstructural parameters appears to provide a basis for design of optimum microstructures. Specifically, the critical stress increases with the toughness of the matrix, the modulus and volume fraction of fibers, the frictional stress at the fiber/matrix interface, and decreasing fiber diameter. However, it should also be appreciated that, as the interface frictional resistance increases, the net tensile stress on the fibers ahead of the crack also tends to increase. This stress enhancement must eventually result in fiber failures ahead of the advancing matrix crack and a consequent change in the failure mode. An optimum frictional resistance is thus anticipated, coincident with the maximum matrix cracking stress that prohibits fiber failure. This aspect of the problem remains to be resolved.

possible to define a matrix cracking stress as an intrinsic property of the composite, as required for their explanation of the regularity of the multiple matrix cracking. Moreover, for steady state crack growth their analysis based on a comparison of the energy of the uncracked system and the energy after complete cracking is valid, and the result is equivalent to Eq. (9). However, their analysis differs in one important respect from the present work. They prescribed the matrix cracking strain ϵ_m as a characteristic of the matrix rather than the composite, and proposed that Eq. (9) applies only at small fiber diameters for which σ_0 exceeds the stress corresponding to ϵ_m . Such a restriction is not required in the present analysis which takes into account the crack length dependence of the strength of the unreinforced matrix. In fact, the reinforcing effect of the fibers can be inferred directly from Eq. (21). The first term on the right side represents the product of the strength of the unreinforced matrix ($K_C^M/\Omega c^{1/2}$) and the modulus ratio, E_c/E_m . This term is plotted, along with the matrix cracking stress for the composite, in Fig. 5. The difference between these two curves represents the reinforcing effect of the fibers for a composite with equal fiber and matrix moduli ($E_f = E_m$). For typical composites the fiber modulus is the larger, and the matrix cracking stress of the composite is always higher than the strength of the unreinforced matrix, for a given crack length. However, for composites with $E_f < E_m$ the relative strengths are dependent upon the crack length.

The energy balance and stress intensity analyses provide equivalent relations between the steady-state matrix cracking stress and microstructural parameters, as indicated in Section 3.2. A quantitative comparison of the two

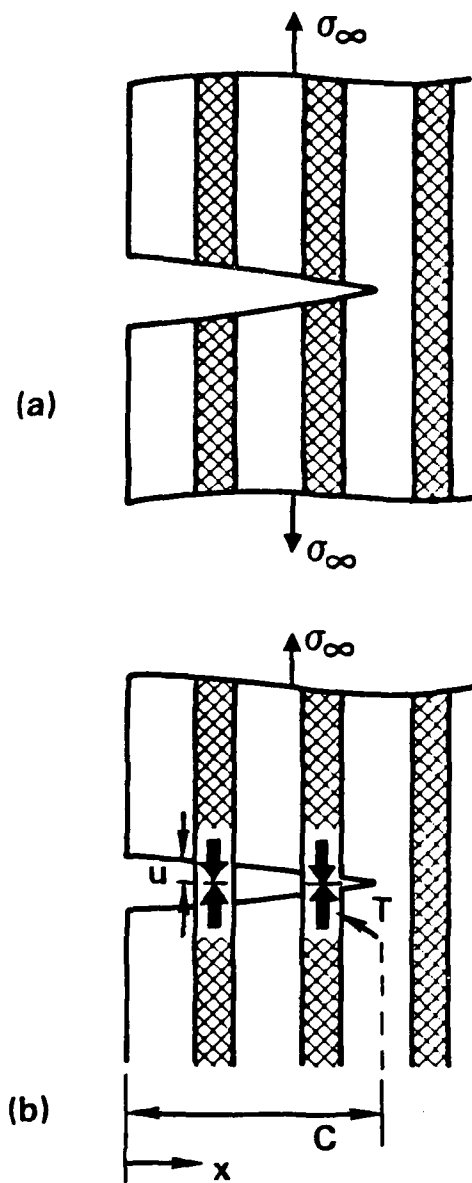


Fig. 2

SC84-27384

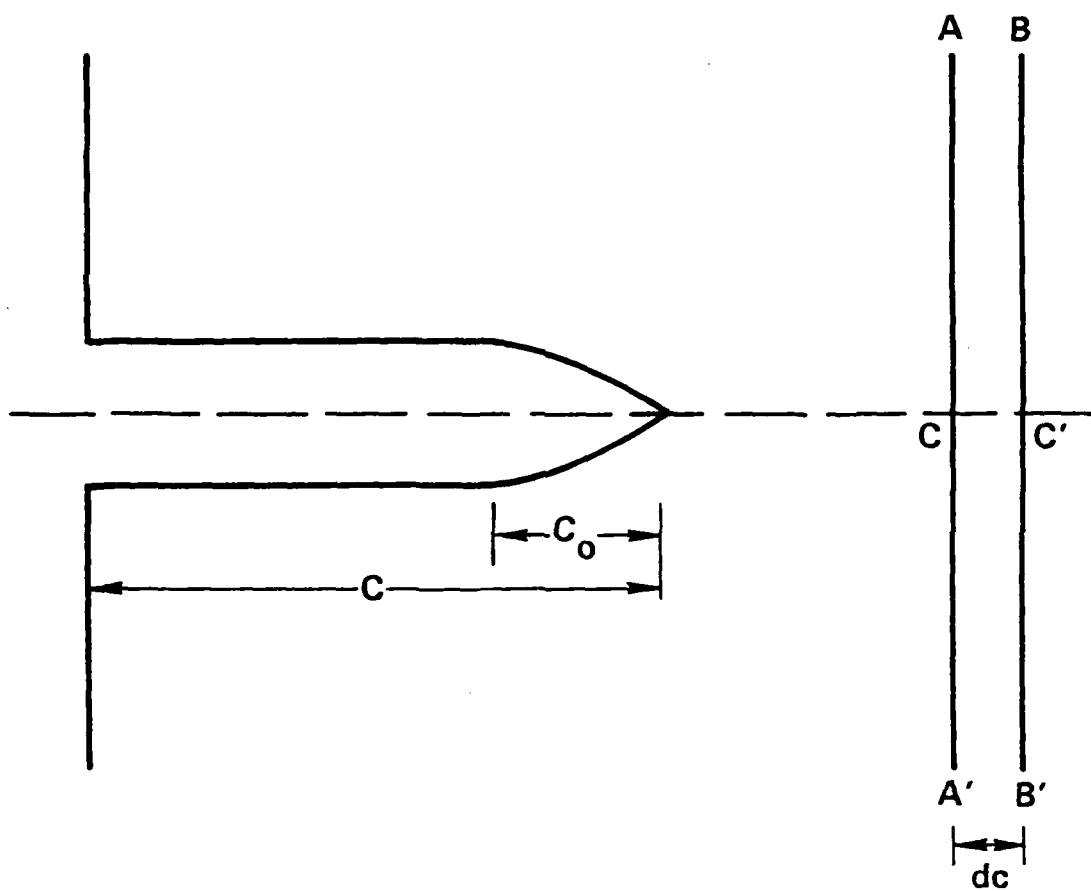


Fig. 3

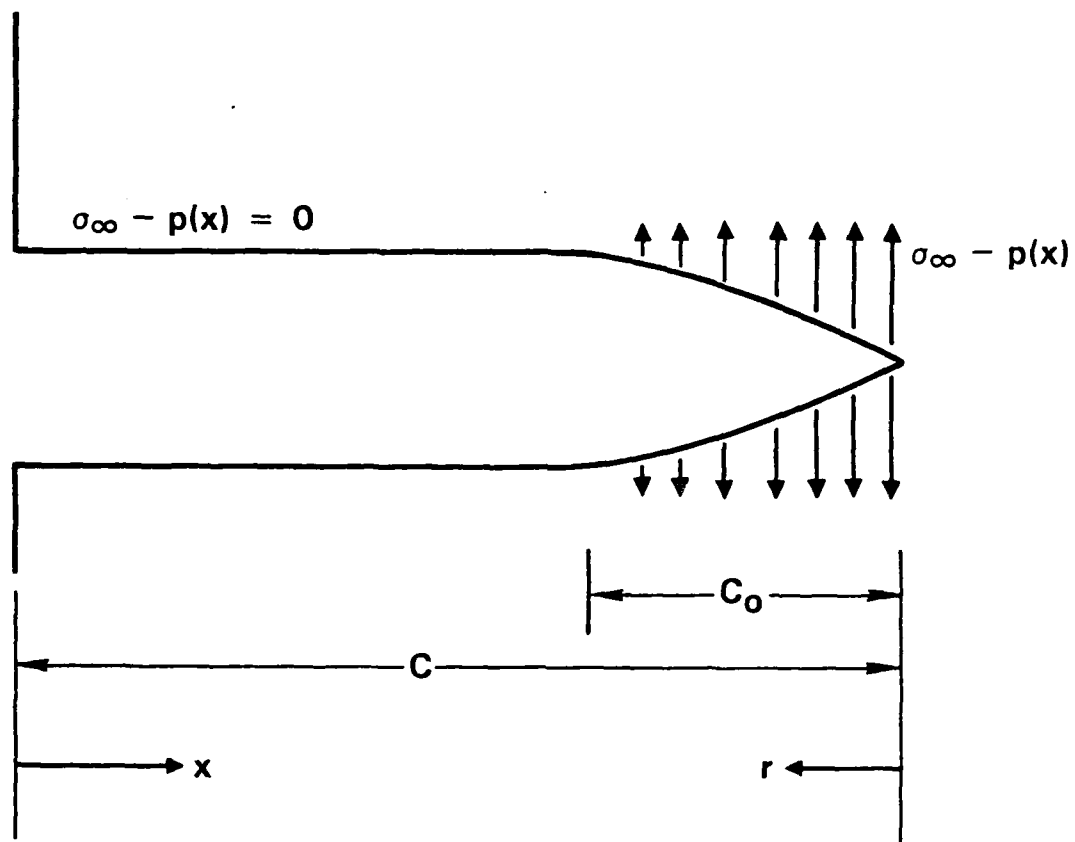


Fig. 4

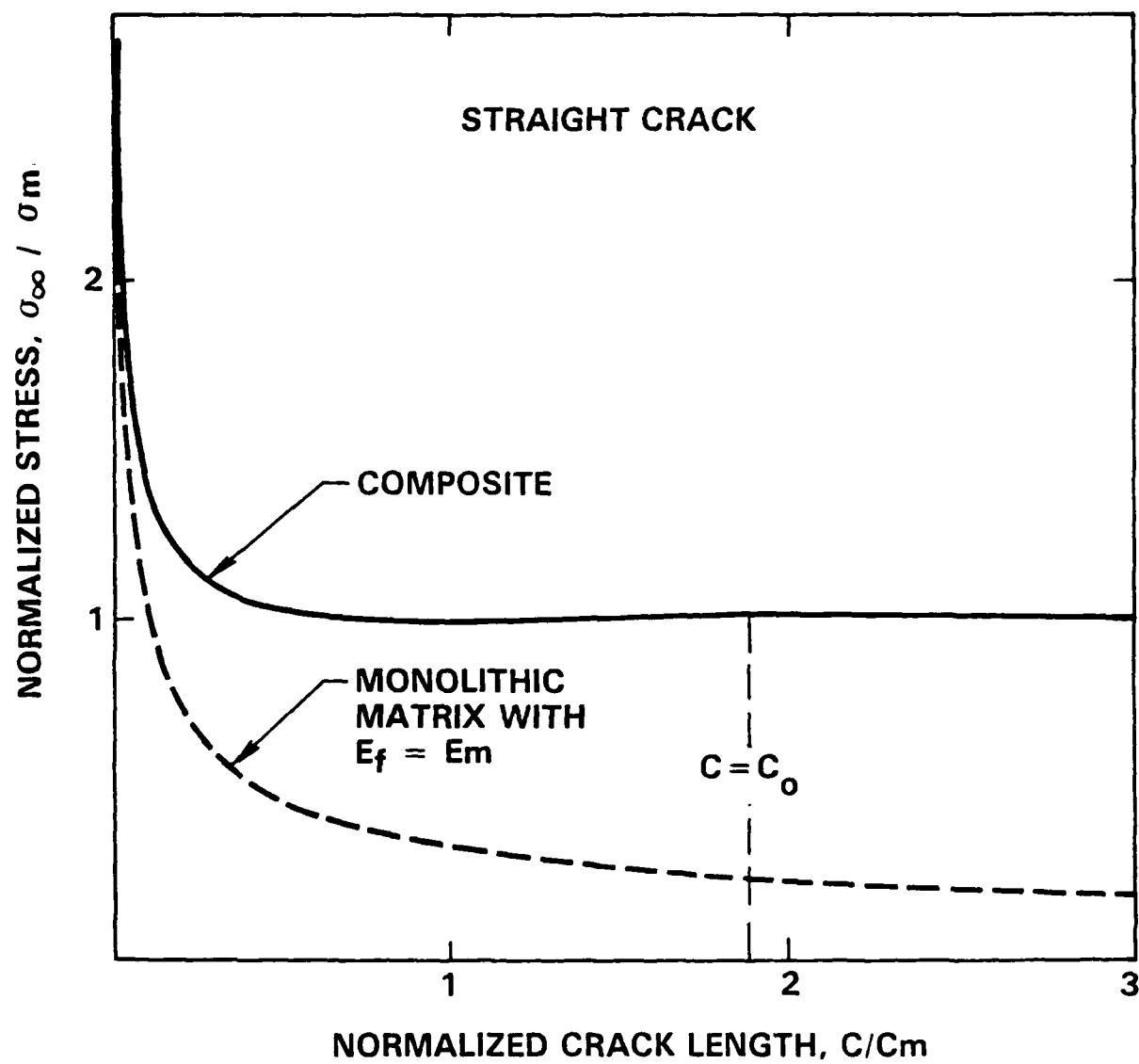


Fig. 5

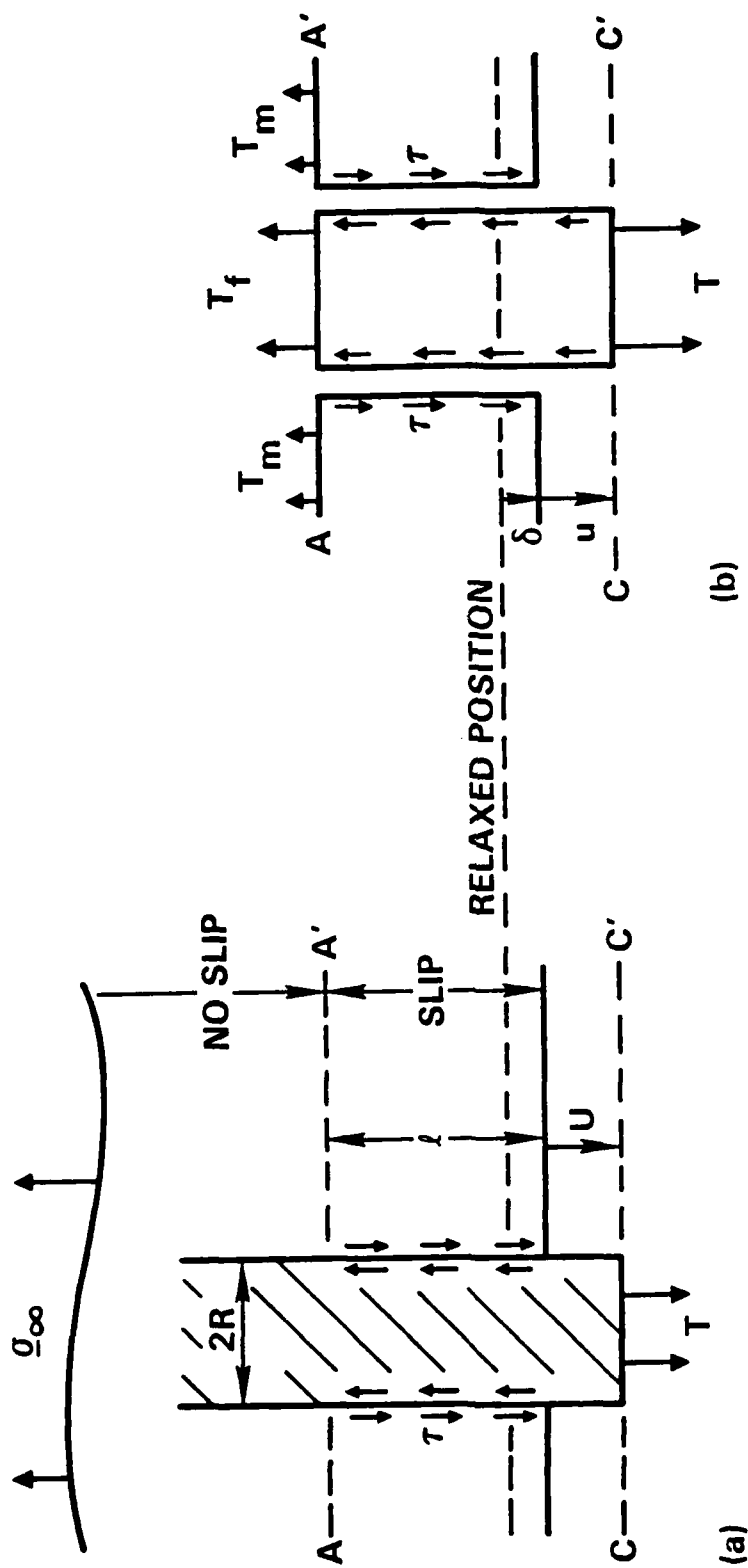


Fig. 6

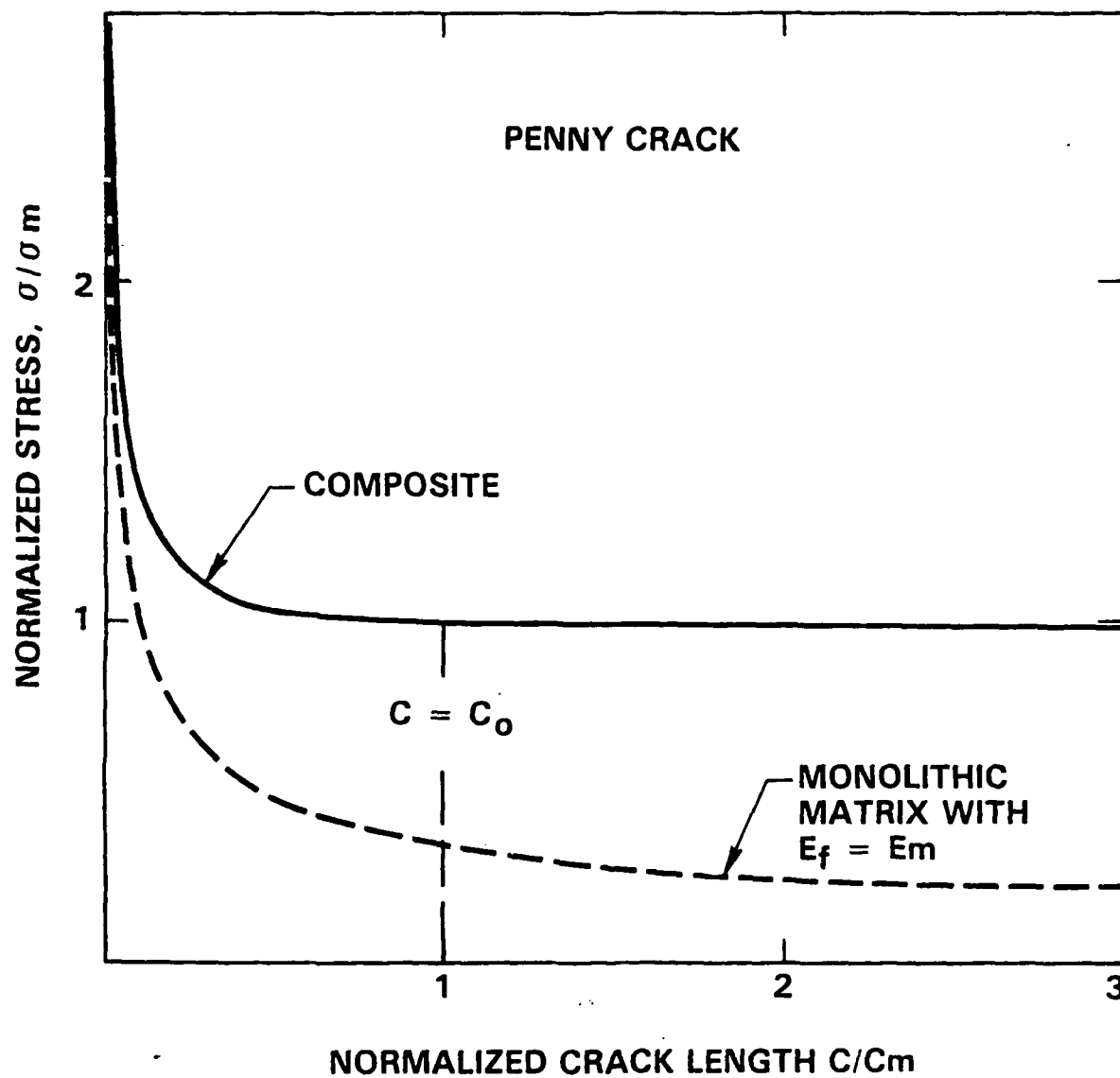
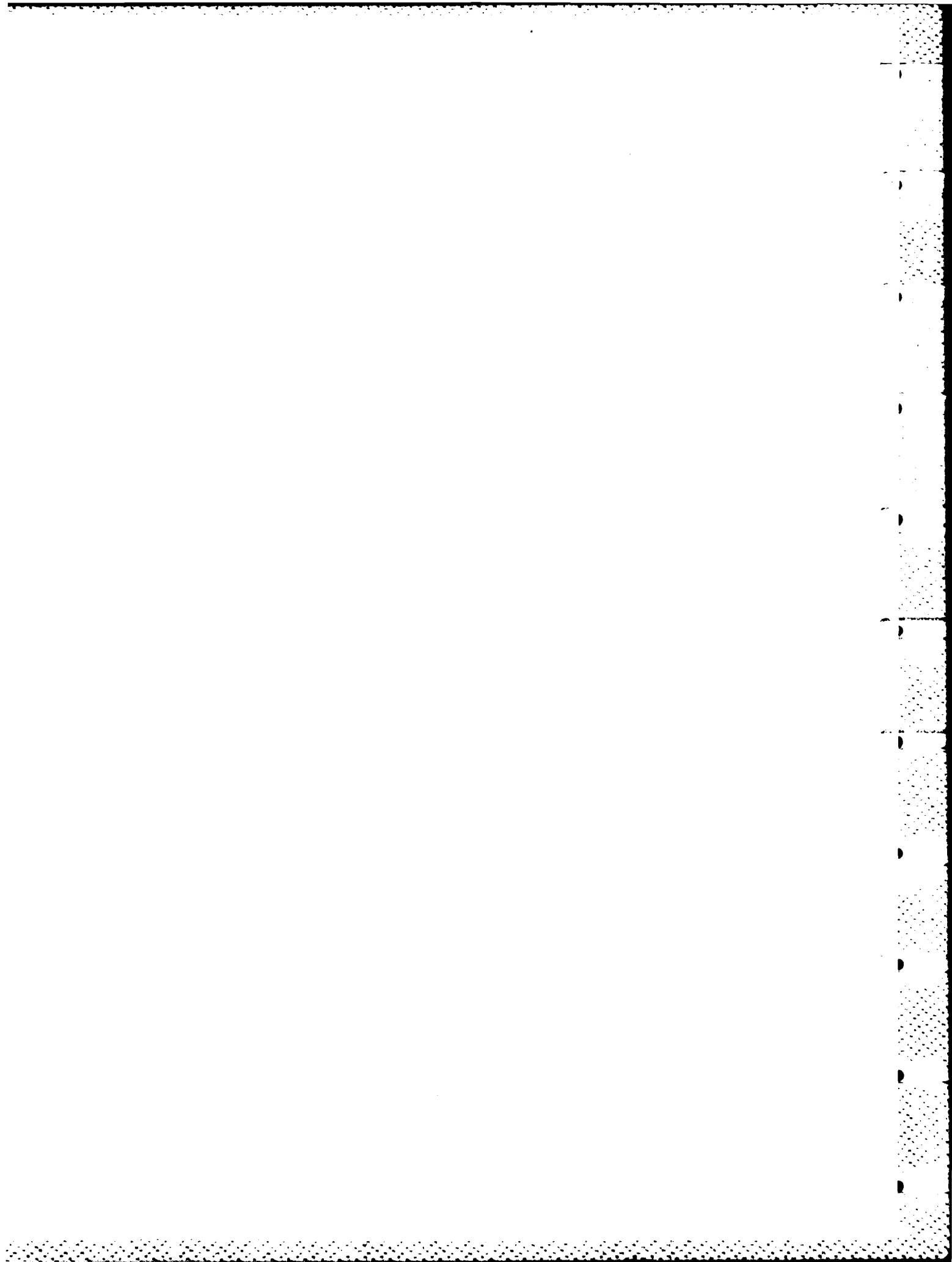


Fig. 7



CHAPTER V

ON THE MECHANICS OF FAILURE
IN CERAMIC/METAL BONDED SYSTEMS

A. G. Evans and M. Ruhle

ANTHONY G. EVANS* AND M. RÜHLE**

*Department of Materials Science and Mineral Engineering,
University of California, Berkeley, CA 94720

**Max Planck Institut für Metallforschung, Institut für
Werkstoffwissenschaften, Stuttgart, Federal Republic of Germany

ABSTRACT

Stress concentrations that develop in metal/ceramic bonded systems have been evaluated and shown to encourage crack propagation at, or near, the edge of bonded interfaces. Experimental indentation observations on Nb/Al₂O₃ confirm the existence of the predicted stress concentrations. In this system, failure was invariably observed to initiate in the ceramic, such that quasi-static cracks located at the interface exhibited crack blunting. However, substantial dynamic reductions in the crack growth resistance of the interface are inferred from fracture surface observations. Implications for the optimal strengths of ceramic/metal bonded systems are presented.

INTRODUCTION

The mechanical response of a system is governed by the stress distribution and by the fracture characteristics of each material constituent. Both aspects must be separately investigated before devising an approach for optimizing mechanical strength. Consequently, investigation of the mechanical behavior of ceramic/metal bonded systems requires consideration of the stress state, as dictated by the applied loads and the elastic and thermal expansion mismatch, as well as the individual fracture characteristics of the ceramic, metal and interface. The limited available research on ceramic/metal bonded systems indicates that fracture in the ceramic, adjacent to the interface, is a frequent failure mode (1,2). Interfaces with a greater fracture resistance than the ceramic thus appear to be attainable. Consequently, an issue of greater present concern is the state of stress associated with bonded systems. The intent of this article is to examine various problems associated with the growth of cracks at, or near, the interface in ceramic/metal bonded systems, as a basis for understanding mechanical strength.

The strength issues are illustrated by experiments conducted in the Al₂O₃/Nb system. This system has the attractive features that thermal expansion mismatch is minimized and that discrete interfaces can be achieved (3). However, mismatch in elastic modulus provides unique failure modes, typical of ceramic/metal bonded systems. In particular, failure frequently initiates at edges, due to substantial stress concentrations (4). Edge effects are thus afforded special emphasis.

The mechanical response of the system is probed using indentations placed at various sites adjacent to, and remote from, the interface. The indentation method has been selected because it simulates the fracture behavior induced by machining damage (5) and by inclusions (6) - two of the most deleterious defect types in high strength material systems (6).

EDGE EFFECTS

Stress Concentrations

When a mismatch exists in either thermal expansion or elastic modulus, edges and corners are major sources of failure. The basic nature of the edge problem is illustrated for the configuration depicted in fig. 1. When the metal strip has either a larger thermal expansion coefficient or a lower modulus than the matrix; the unconstrained metal develops a smaller lateral dimension than the ceramic (fig. 1b). Hence, to simulate the stress state in the bonded system, the unconstrained metal must be uniformly extended by the application of edge tractions (fig. 1c). Then, surface forces (equal in magnitude but opposite in sign) must be applied to the metal, in the bonded state, to achieve stress free conditions at the surface (fig. 1d). This latter step induces large normal and shear stresses near the edge, which typically act over a distance similar to the thickness, h , of the metal. Furthermore, the stresses are frequently singular (4).

In the presence of elastic mismatch, the stresses near the edge, induced by an applied stress σ_∞ , exhibit a singular form (4). For plane strain conditions, the edge stresses can be expressed as

$$\frac{\sigma_{ij}}{\sigma_\infty} = \left(\frac{h}{r}\right)^\gamma f(\alpha, \beta) \quad (1)$$

where

$$\alpha = \frac{(\mu_1/\mu_2)(1-\nu_2) - (1-\nu_1)}{(\mu_1/\mu_2)(1-\nu_2) + (1-\nu_1)}$$

$$\beta = \frac{(\mu_1/\mu_2)(1-2\nu_2) - (1-2\nu_1)}{2(\mu_1/\mu_2)(1-\nu_2) - 2(1-\nu_1)}$$

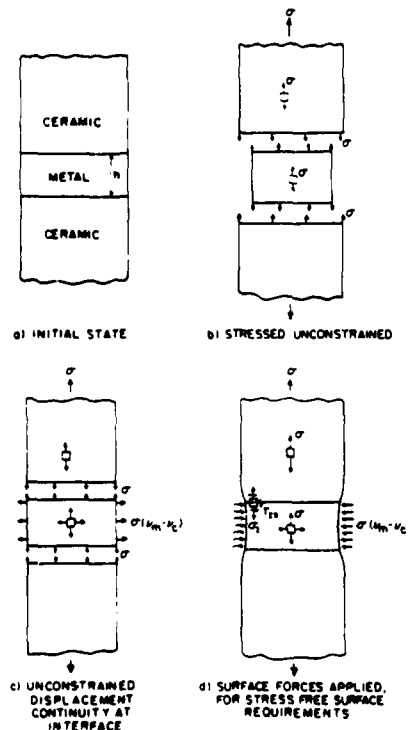


Fig. 1 - A schematic illustrating the development of interfacial stress concentrations due to elastic (or thermal expansion mismatch).

μ is the shear modulus, ν is Poisson's ratio, f is a function, γ is a coefficient (<1) and r is the distance from the edge, along the interface. Some typical results (4) are plotted in fig. 2. Very large tensile and shear stresses thus exist over small regions adjacent to the edge.

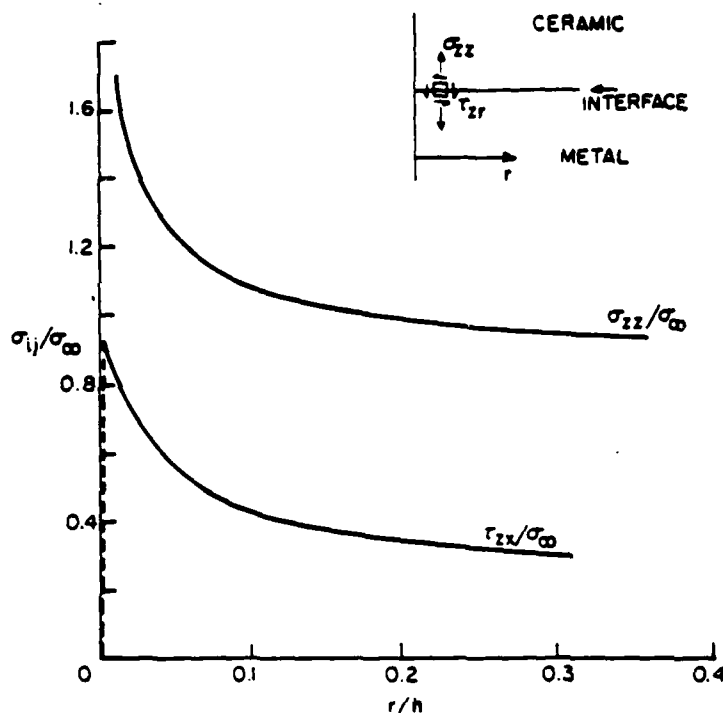


Fig. 2 - Stresses near a free surface at the interface between a bonded system for the condition $\mu_1/\mu_2 = 0.11$, $\nu_1 = \nu_2 = 1/2$ ($\alpha = -0.8$, $\beta = 0$) (4). The maximum shear stress occurs just beneath the surface.

Thermal expansion mismatch has a similar effect, by virtue of large residual stresses created near the edge. Specifically, if the elastic properties are the same for the metal and ceramic, the interface stresses are given for a bonded cylinder by (7);

$$\frac{\sigma_{ij}(1-\nu)}{E\Delta\alpha\Delta T} = \Omega(r/d) \quad (2)$$

where d is the diameter of the cylinder and the function Ω is plotted in fig. 3.

A mismatch in modulus generates interfacial tensile stresses σ_{zz} at the edge, irrespective of the sign of the mismatch and thus, invariably, enhances the propensity to fracture. Thermal expansion mismatch induces tensile stresses just outside the interface, within either the metal or the ceramic, depending upon the sign of the thermal expansion and the elastic mismatch. Generally, the metal has the larger thermal expansion coefficient and the expansion mismatch then induces σ_{zz} tensile stresses in the ceramic, adjacent to the interface, and encourages failure in the ceramic. Large shear stresses always exist along the interface, near the edge, in the presence of elastic or thermal mismatch. A substantial mode II contribution to edge failure should thus be anticipated in all situations.

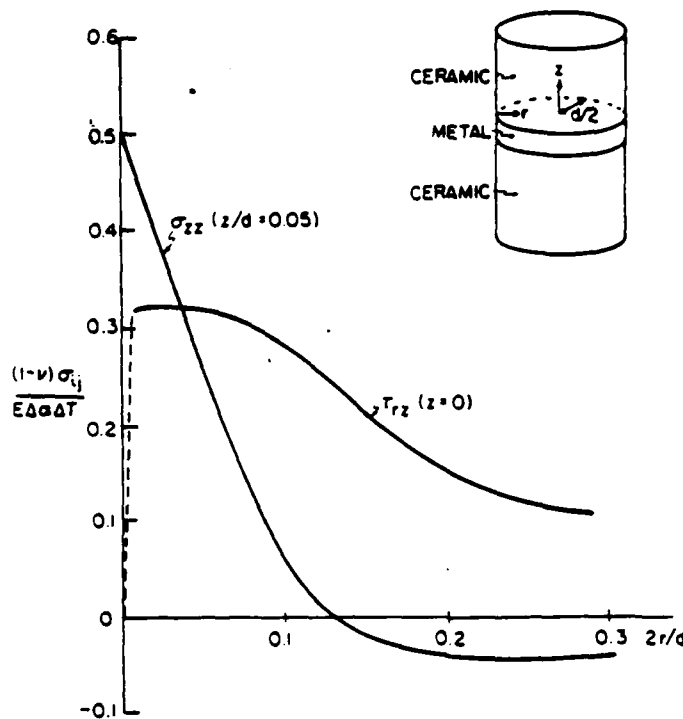


Fig. 3 - Stresses induced by a thermal expansion mismatch in a bonded cylinder. The shear stresses are at the interface, whereas the tensile stresses are in the ceramic close to the interface ($z/d = 0.05$). The normal stresses immediately at the interface are zero. The maximum shear stress occurs just beneath the interface.

Crack Propagation

The propagation of cracks from an edge along, or adjacent to, the interface is governed by the appropriate strain energy release rate (8,9). For example, the total strain energy release \mathcal{G} for an interface crack in the absence of thermal mismatch has the general form (10,11,12)

$$\mathcal{G} E_c / \sigma^2 a = g(\zeta, a/h) \quad (3)$$

where E_c is the composite modulus (12),

$$1/E_c = \left[\frac{1+\chi_1}{\mu_1} + \frac{1+\chi_2}{\mu_2} \right]$$

such that, for plane strain, $\chi = 3-4\nu$, the variable ζ is given by,

$$\zeta = \frac{\mu_1 + \chi_1 \mu_2}{\mu_2 + \chi_2 \mu_1}$$

and g is the function plotted in fig. 4. An approximate analytic expression for \mathcal{G} , deduced from fig. 4, is (10),

$$\mathcal{G} E_c / \sigma^2 a = \lambda_1 (h/a)^\phi + \lambda_2 \quad (4)$$

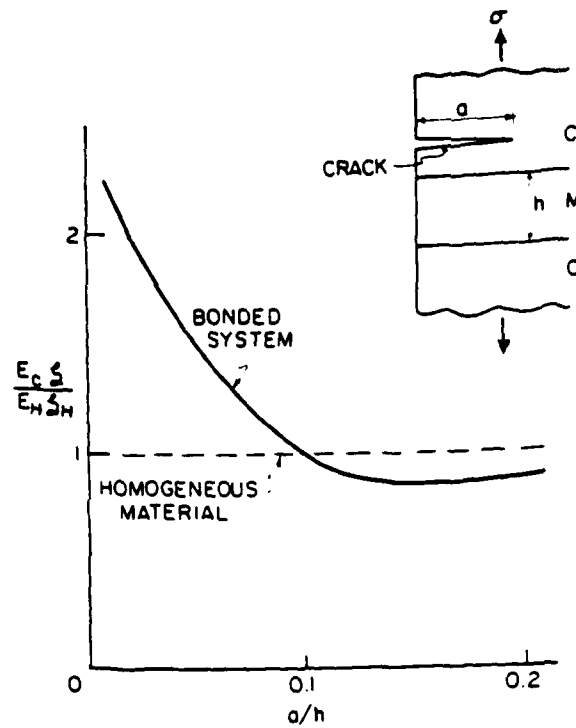


Fig. 4 - The variation in the normalized strain energy release for an interface crack.

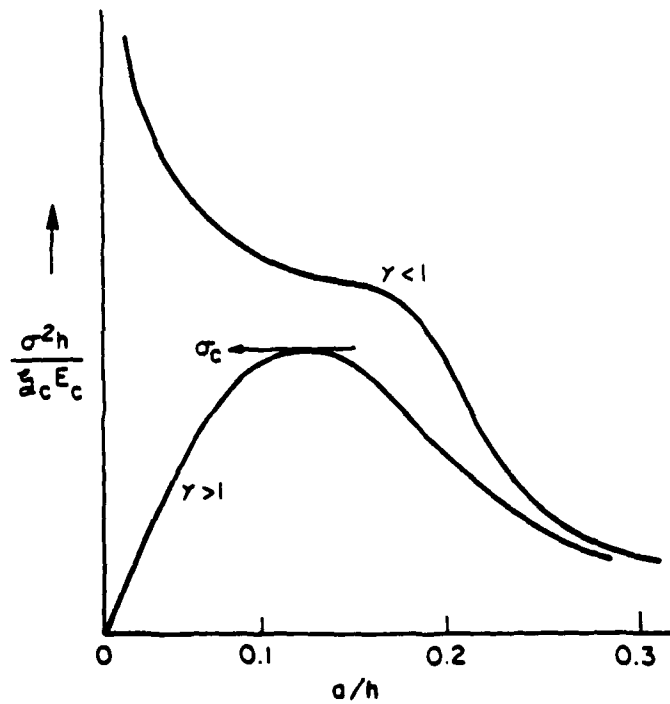


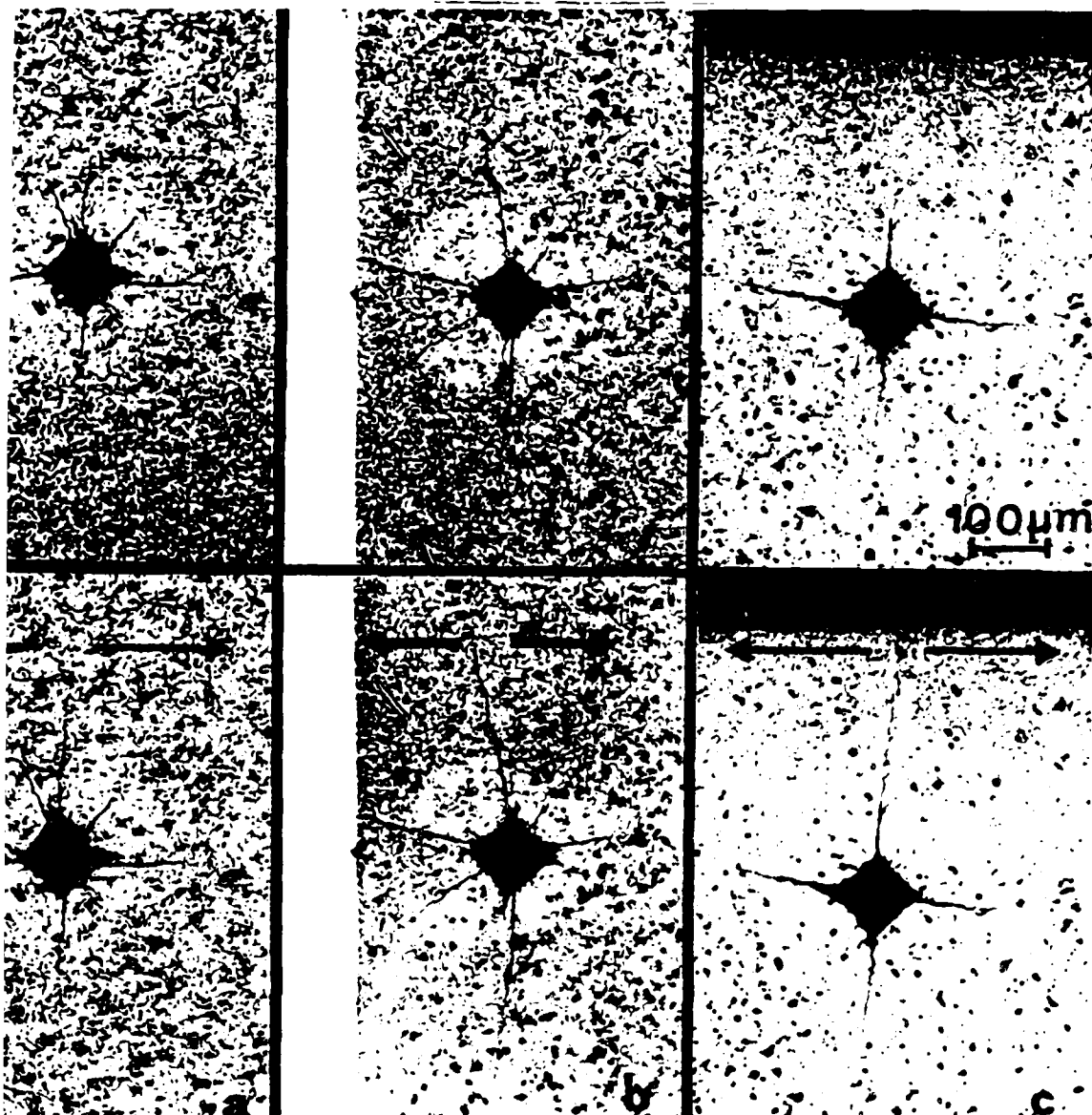
Fig. 5 - Trends in the interface crack growth stress within crack length for values of the singularity either smaller or larger than unity.

$\lambda_{1,2}$ are coefficients and ϕ is an exponent. When \mathcal{G} dictates crack at some critical level, \mathcal{G}_c (dictated by the lower value for either the ice or the ceramic), the equilibrium crack growth stress has the onless form

$$\sigma_{11}^2 / \mathcal{G}_c E_c = A(a/h) \quad (5)$$

λ is the function plotted in fig. 5. It is of interest to note that $\phi > 1$, the crack grows stably under increasing load and reaches an lity at a critical stress, σ_c , given by

$$\frac{\sigma_c^2 h}{E_c \mathcal{G}_c} = \frac{(\phi-1)^{1-1/\phi}}{\phi \lambda_1^{1/\phi} \lambda_2^{1-1/\phi}} \quad (6)$$



- Optical micrographs of indentation cracks before and after loading nominal stress of 80 MPa. (a) an indentation remote from the interface, (b) an indentation remote from the interface but close to the edge, (c) an indentation near the center, close to the interface.

AD-A151 978

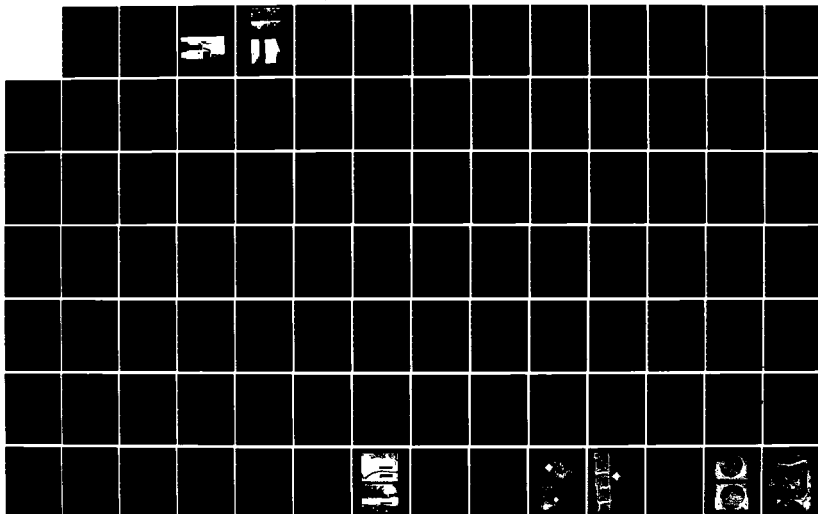
MECHANICAL ASPECTS OF INTERFACES AND SURFACES IN
CERAMIC CONTAINING SYSTEMS(U) CALIFORNIA UNIV BERKELEY
DEPT OF MATERIALS SCIENCE AND MINERA.

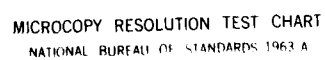
3/5

UNCLASSIFIED

A G EVANS ET AL. 14 DEC 84 N00014-81-K-0362 F/G 20/11

NL





MICROCOPY RESOLUTION TEST CHART
NATIONAL BUREAU OF STANDARDS 1963 A

The observed failure stress associated with edge flaws is dictated in this instance by the metal layer thickness, rather than the initial crack size (analogous to the behavior observed at indentations (5)). The metal layer thickness thus emerges as a preeminent fracture controlling parameter, consistent with practical experience (2).

An important limitation of the preceding analysis is the implicit assumption that all of the strain energy is available for crack propagation. Experience with delamination in polymer matrix composites (9) reveals that, frequently, the opening mode component, \mathcal{G}_I , is more important than the total \mathcal{G} . Such behavior is indicative of minimal coupling of the shear component of the strain energy release rate \mathcal{G}_{II} to the fracture mechanism. Consequently, since a substantial contribution to \mathcal{G} for interfacial edge cracks, derives from the shear stress (section 2.1), it is deemed improper to presume that the total \mathcal{G} is the pertinent crack driving force. Careful experimental studies of the respective influence of \mathcal{G}_I and \mathcal{G}_{II} on the growth of interface cracks are required before fully specifying an acceptable fracture criterion.

Thermal expansion mismatch imposes additional edge stresses that also contribute to \mathcal{G} (13). Computations of \mathcal{G} cracks have not yet been conducted. The relative influence of the elastic modulus and thermal expansion mismatch on the net crack driving force thus awaits further investigation. In this context it should also be recalled that strain energy release rates are not additive. Interaction terms must also be included, based on computations of \mathcal{G}_I and \mathcal{G}_{II} for each problem.

EXPERIMENTAL OBSERVATIONS

Test Procedures

Four point flexure specimens consisting of thin (~ 1 mm) strips of Nb, diffusion bonded to polycrystalline alumina, were prepared and carefully polished on the tensile surface. Vickers indentations were then placed at various locations with respect to the interface, but within the uniformly stressed regions of the flexure specimen (viz., between the inner loading rods) and the indentation cracks characterized by optical microscopy (fig. 6). Thereafter, the specimens were loaded to ~ 80 MPa and unloaded. Changes in the indentation crack lengths induced by the load were determined and related to local stress concentrations. Subsequently, the specimens were loaded to failure. Fracture origins were then identified and used to assess crack configurations at the failure instability.

Observations

Indentation cracks remote from the interface (fig. 6a) exhibited little extension, except at indentations close to an edge (fig. 6b). However, on the same specimen, indentation cracks placed adjacent to the interface experienced substantial growth (fig. 6c). The comparative extension provides a direct measure of the stress concentration factors, as described in the subsequent section. Maximal crack growth occurred at indentations placed near the interface, at the specimen edge.

Observations of cracks that terminate at the interface reveal slip band formation in the Nb and crack blunting (fig. 7a,b), indicative of appreciable ductility in the Nb adjacent to the interface. The large plastic stretch observed at other crack tips (fig. 7c) substantiates that the Nb can sustain extensive plastic strain. Yet, observations of the fracture surface, away from the initiation site, indicate that rapid crack propagation to failure has occurred at the interface, with no evidence of plastic deformation in the Nb (fig. 7c). This paradox appears to be explicable based on more detailed observations of fracture initiation sites. Indentation cracks that either

terminate at the interface, or grow stably to the interface during loading, invariably exhibit crack tip blunting and never initiate the final failure (fig. 8). Failure always initiates from cracks in the Al_2O_3 which becomes unstable while still contained within the ceramic (fig. 8). Further, unstable, growth of the crack then entails attraction of the crack to the interface, whereupon interface propagation occurs in a nominally brittle mode. These fracture characteristics are deemed to be consistent with a velocity sensitive σ_c for the interface crack, as discussed in the following section.

One final feature of the failure that merits consideration is the observation that indentations emplaced very close to the interface (fig. 9) result in low failure loads. An accompanying observation is the substantial residual openings exhibited by the indentation crack, and the extensive deformation of the Nb adjacent to the interface (fig. 9). These observations are shown to be consistent with the development of residual stress, due to the localized plastic deformation of the Nb, and the effects of the residual stresses on crack propagation in the Al_2O_3 .

metal

10 μm

interface

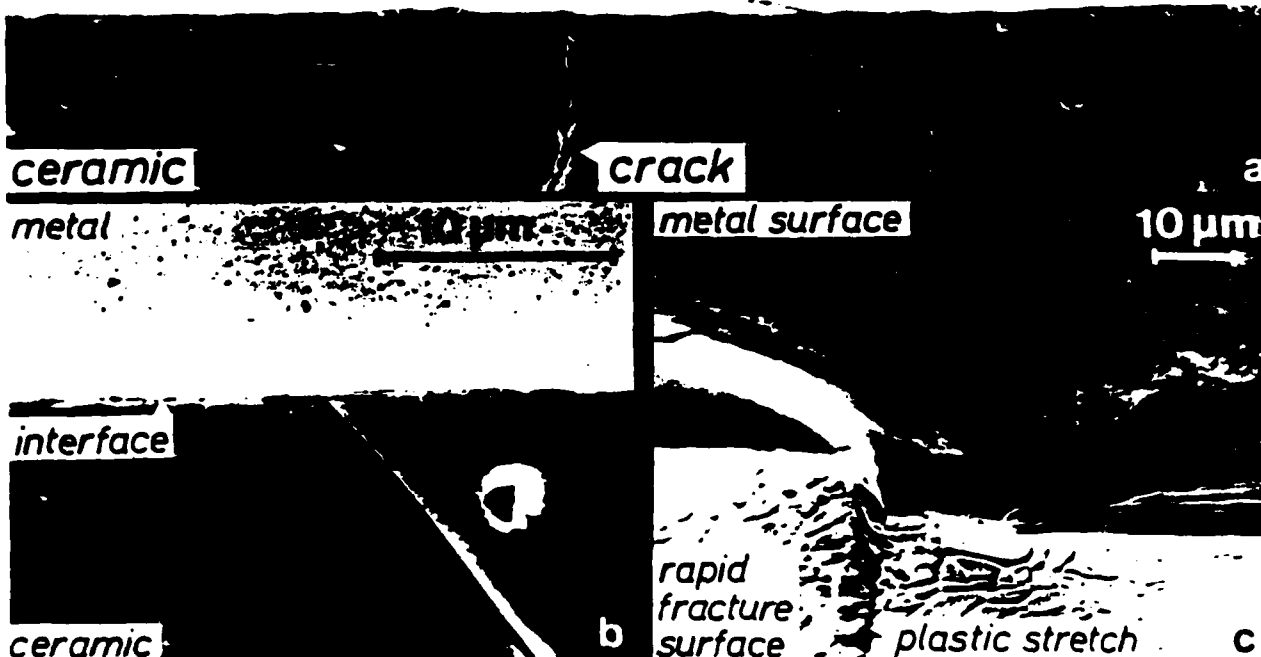


Fig. 7 - Crack tips at the interface showing near bands and crack tip blunting (a) crack normal to the interface (b) a crack inclined to the interface (c) the plastic stretch zone after removal of the ceramic by rapid fracture. The rapid fracture surface on fig. 7c indicates lines where the Al_2O_3 grain boundaries intersect the interface, but there is no evidence of plastic deformation at the interface away from the stretch zone.

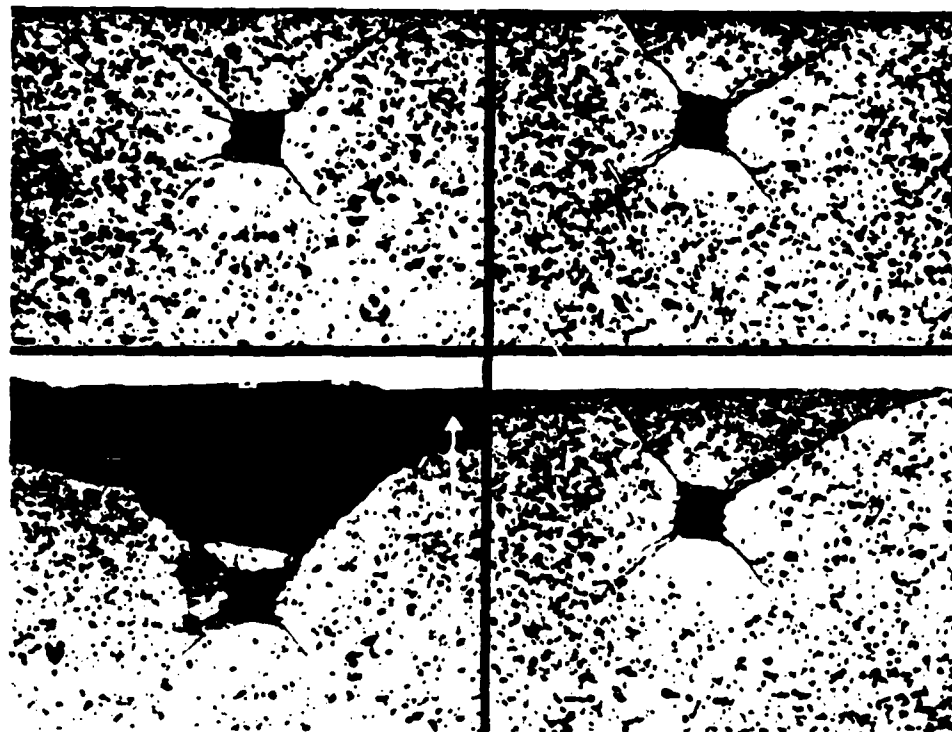


Fig. 8 - Two indentations on the same specimen but on opposite sides of the Nb layer. The indent which becomes unstable in the Al_2O_3 is the failure origin: (a) and (b). The indent with an initial crack tip at the interface does not cause failure: (c) and (d).

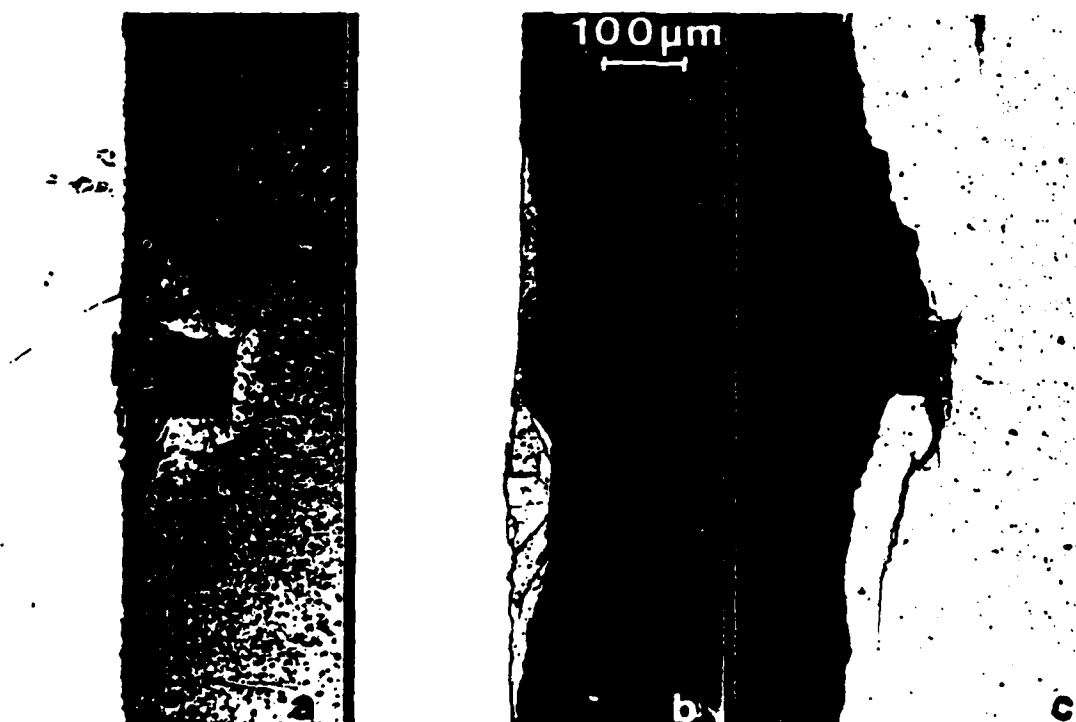


Fig. 9 - An indentation close to the interface causes premature failure. Note the substantial residual opening of the crack in the Al_2O_3 and the deformation of the Nb.

Analysis

The relative extensions of indentation cracks at various locations throughout the test specimens may be used to estimate stress distributions (Appendix I) using;

$$\sigma_1/\sigma_2 = (a_2/a_1)^{1/2} [(1-R_1^{3/2})/(1-R_2^{3/2})] \quad (A4)$$

This formula is only strictly valid for cracks in isotropic material and thus, has minimal utility for cracks very close to the interface. With this restriction, estimates of stress ratios from fig. 6 reveal that edge stresses within 100 m of the interface exceed the applied stress by ~ 1.6 , consistent with the calculations by Bogy (4).

DISCUSSION

Various experimental (14) and theoretical studies (15) of rapid crack propagation in b.c.c. metals have indicated that \mathcal{G} decreases rapidly with increase in crack velocity, due to the strong stress dependence of the dislocation velocity. Such behavior explains, for example, the existence of unstable brittle failure in steels, after initial crack tip plastic blunting (viz. in the upper transition range). A comparable rate dependence \mathcal{G}_c should be expected in the Nb, especially if appreciable amounts of oxygen are in solution near the interface. Furthermore similar rate dependent plasticity effects should be experienced by a crack tip located at the Nb/Al₂O₃ interface (albeit to a reduced extent, because of the constraint exerted by the non-deformable Al₂O₃). It is thus proposed that \mathcal{G} for the interface exhibits the crack velocity dependence depicted in fig. 10. At high crack velocities, plastic deformation of the Nb is essentially inhibited and \mathcal{G}_c for the interface, (\mathcal{G}_c^i), is smaller than that for the polycrystalline Al₂O₃ (\mathcal{G}_c^c). In this situation, \mathcal{G}_c^i is largely dictated by the interfacial energy associated with the interface structure, viz;

$$\mathcal{G}_c^i/\mathcal{G}_c^c \approx (\gamma_{Nb} + \gamma_{Al_2O_3} - \gamma_{int})^{1/2} \gamma_{Al_2O_3} \quad (7)$$

where the γ are surface energies and γ_{int} is the interface energy. At lower velocities, plastic zones can be activated by the crack tip stress field and the associated plastic work contributes to \mathcal{G}_c^i . A large increase in \mathcal{G} thus ensues, such that \mathcal{G}_c^i substantially exceeds \mathcal{G}_c^c (which is known to be insensitive to crack velocity (16)).

The preceding trends in \mathcal{G} for the composite system are fully consistent with the experimental observations. Specifically, stationary cracks at the interface invariably blunt (fig. 7) due to the large associated \mathcal{G}_c^i and have, consequently, never been observed as failure initiation sites (fig. 8). Failure always occurs from cracks which become unstable in the Al₂O₃. The rapidly moving crack, thus formed in the Al₂O₃, subsequently extends preferentially along the interface, where \mathcal{G}_c^i now exhibits its minimal value, due to the absence of plasticity in the Nb (fig. 8). Validation of this hypothesis, of course, requires crack growth studies as a function of velocity. However, the associated implication for the mechanical strength of the bonded system is that, for most situations, the interface fracture resistance \mathcal{G}_c^i is entirely adequate, viz., fracture is not limited by the interface. (Problems may arise at high loading rates, but such conditions are infrequently encountered).

Another important influence of plasticity in the metal concerns the development of residual stress. The presence either of machining damage or

of inclusions* in the ceramic immediately adjacent to the interface is likely to induce plasticity in the metal, comparable to that observed around the indentation depicted in fig. 9. Residual stresses of order, $4Y/3$, are thus to be anticipated (Appendix II) in the ceramic, where Y is the yield strength. The residual stresses superpose on the concentrated applied loads at the edges and cause premature failure. Such highly deleterious failure characteristics can be averted by avoiding near-interface defects of this type and/or by selecting a metal with a low yield strength.

CONCLUDING REMARKS

The indentation experiments reveal the sensitivity of the interfacial zone to the presence of defects in the adjacent ceramic by virtue of the large associated stress concentrations. The processing of high quality bonded systems thus requires that great care be exercised in the avoidance of defects in the interfacial zone, near the surface. Specifically, excessive inclusions or voids in this zone would be most damaging. Furthermore and perhaps, most importantly, machining damage in the ceramic near the interface (a phenomenon closely simulated by the indentation cracks (5)) would be extremely deleterious. Machining conditions thus demand careful control.

Several remarks concerning the influence of plasticity on the mechanical properties are also deemed worthy of consideration. Plasticity in the metal at low loading rates implies that interfacial cracks are likely to be susceptible to fatigue. Fatigue crack growth rates (da/dN vs. σ) should thus be measured, as well as fatigue crack initiation effects. Plastic deformation in the metal is also expected to induce complex behavior in notched specimens. In this context, it should be recalled that notched beam tests (e.g. Charpy tests) and J_{IC} tests in steels can yield opposite trends in failure load with microstructure, due to the difference in the scale of the plastic zone relative to the microstructural scale at which the fracture mechanisms operate (17).

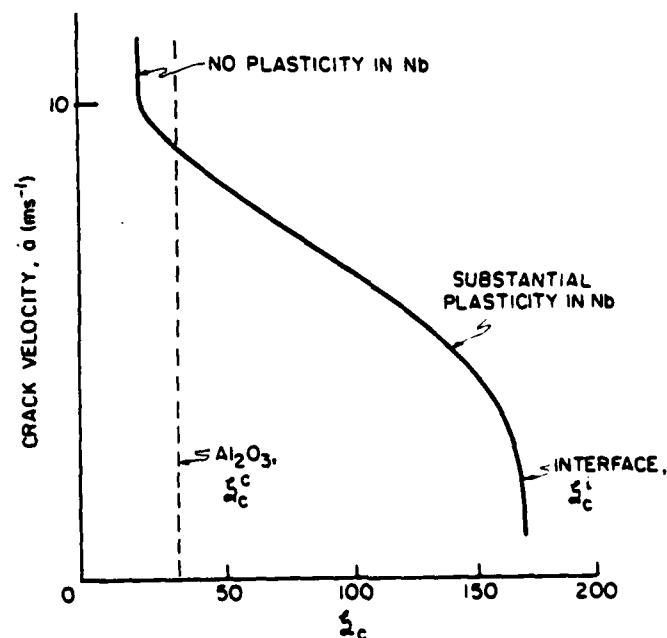


Fig. 10 - Postulated trends in K_{Ic} with crack velocity.

*Thermal expansion mismatch between the inclusion and the matrix induce matrix deformation that may exceed the yield strength of the metal; thereby causing residual stress.

APPENDIX I

Growth Characteristics of Indentation Cracks

An indentation crack of radius, a , contained in an isotropic body exhibits a stress intensity factor, K , given by (18);

$$K = C_1 \sigma a^{1/2} + C_2 a^{-3/2} \quad (A1)$$

where C_1 and C_2 are constants for a given indentation load and σ is the applied stress. Hence, the stress and crack length are related by;

$$\sigma = K_c / C_1 a^{1/2} - C_2 / C_1 a^2 \quad (A2)$$

However, K_c is also related to the initial crack radius, a_0 , at zero applied stress by, $K_c = C_2 a_0^{-3/2}$. Consequently, from eqn (A2), the stress is given by;

$$\sigma = \frac{K_c}{C_1 a^{1/2}} [1 - (a_0/a)^{3/2}] \quad (A3)$$

Furthermore, if similar indentations are placed at two different locations within an isotropic brittle solid the ratio of stresses developed at those sites is

$$\frac{\sigma_1}{\sigma_2} = \left(\frac{a_2}{a_1}\right)^{1/2} \left[\frac{1-R_1^{3/2}}{1-R_2^{3/2}} \right] \quad (A4)$$

where R is the crack length ratio, a_0/a . Stress variations within a body may thus be estimated from indentation crack length ratios, without requiring knowledge of either material parameters or geometric constants.

APPENDIX II

Residual Stress Effects

Residual stress effects and their influence on crack extension can be illustrated using the pressurized spherical cavity as an example (19). When two connected materials with different elastic and plastic properties are subject to internal pressure, such that the inner material is immune to plastic yielding, the outer material first experiences plastic deformation when the normal compression at the interface exceeds, $p = 2Y/3$, where Y is the yield strength. Further plastic deformation results in the radial stress distribution depicted in fig. 11, with a minimum occurring at the interface and a maximum at the elastic/plastic boundary in the outer material. Unloading requires that the elastic stress distribution be subtracted from the stress at peak pressure (fig. 11), resulting in the residual field depicted in fig. 11. The residual radial stress exhibits a peak tension at the interface.

However, for relatively low yield strength material, reverse yielding occurs and the peak residual tension is then (19), $\hat{\sigma}_R = 4Y/3$.

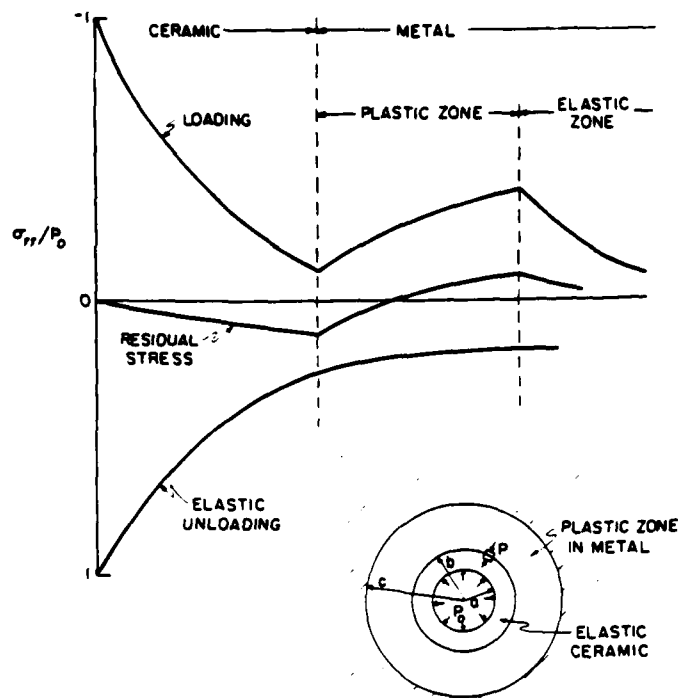


Fig. 11 - Residual stresses created by expansion of an elastic spherical shell into an elastic/plastic matrix.

REFERENCES

1. C. C. Berndt and R. McPherson, Surfaces and Interfaces in Ceramic and Ceramic/Metal Systems (Ed. J. A. Pask and A. G. Evans) Plenum, N.Y. (1981) p. 619.
2. M. E. Twentyman and P. Hancock, Surfaces and Interfaces in Ceramic and Ceramic/Metal Systems, *ibid.*, p. 535.
3. M. Florjanic, W. Mader, M. Ruhle and M. Turwitt, this volume.
4. D. G. Bogy, J. Appl. Mech. 42 (1975) 93.
5. D. B. Marshall, A. G. Evans, B. T. Khuri-Yakub, J. W. Tien and G. S. Kino, Proc. Roy. Soc. A385 (1983) 461.
6. A. G. Evans, J. Am. Ceram. Soc. 65 (1982) 127.
7. S. Timoshenko and J. N. Goodier, Theory of Elasticity, McGraw Hill (1951).
8. F. Erdogan and G. D. Gupta, Int. J. Solids and Structures, 7, (1971) 36.
9. T. K. O'Brien ASTM STP 775 (1982) p. 140.
10. S. Schmauder, M. Ruhle and A. G. Evans, to be published.
11. T. Suga, Ph.D. Thesis, Max Planck Institut fur Metallforschung, Stuttgart (1984).
12. A. Piva and E. Viola, Engng. Frac. Mech. 13 (1980) 143.
13. F. Erdogan, J. Appl. Mech. 32 (1965) 403.

14. H. Vehoff and P. Neumann, Acta Met. 28 (1980) 265.
15. L. B. Freund and J. W. Hutchinson, to be published.
16. R. L. Bertolotti, J. Am. Ceram. Soc. 57 (1974) 300.
17. R. O. Ritchie, B. Francis and W. L. Server, Met. Trans. 7a (1976) 831.
18. D. B. Marshall and B. R. Lawn, J. Am. Ceram. Soc. 63 (1980) 532.
20. R. Hill, Theory of Plasticity, Oxford Univ. Press (1950).

CHAPTER VI

RESIDUAL STRESSES IN METAL/CERAMIC METAL BONDED STRIPS

C. H. Hsueh and A. G. Evans

RESIDUAL STRESSES IN METAL/CERAMIC BONDED STRIPS

by

C. H. Hsueh and A. G. Evans

Department of Materials Science and Mineral Engineering

University of California, Berkeley, CA 94720

ABSTRACT

Residual stresses that develop during cooling of a metal/ceramic strip are calculated analytically. It is shown that the metal may behave elastically or plastically (with full or partial plasticity) depending on the mechanical properties, the thickness of the two constituents and the mismatch in thermal expansion. Residual stresses are also calculated for a sequence consisting of constrained undercooling, removal of the constraint and reheating. It is demonstrated that reheating, which results in elastic stress relaxation, may be used to eliminate the residual stress. The optimum undercooling and reheating conditions needed to produce a stress free strip, at the operational temperature, are calculated and specific results are presented for the Cu/Al₂O₃ system.

I. INTRODUCTION

A number of applications in microelectronics involve combinations of metal and ceramic constituents. These constituents are subject to residual stress due to thermal expansion mismatch. The stresses that develop depend on the configuration of the system. A metal cylinder imbedded in an infinite ceramic matrix has been previously analyzed¹, as appropriate for a conducting element in a microelectronics package.² A metal/ceramic strip, pertinent to a metallized substrate in hybrid power electronics,³ has also been analyzed,⁴ but only for a non-hardening metal. The present paper extends the stress analysis for the strip configuration to include work hardening and to identify the existence of an important partially plastic condition. Furthermore, a method of eliminating the residual stresses in the strip configuration is presented and analyzed.

Residual stress elimination can be achieved if the metal/ceramic strip is undercooled and reheated. Stress elimination is further facilitated if the strip is constrained from bending during cooling, allowed to undercool in the constrained state, and then reheated to the operational temperature. Judicious selection of the undercooling temperature permits the strip to be stress free at the operating temperature. The requisite undercooling is calculated in the present study.

The evolution of the residual stresses in the metal/ceramic strip is calculated, subject to the premise that bonding is conducted at elevated temperatures, where the longitudinal stresses are fully

the metal starts to yield in compression, initiating from the metal/ceramic interface. The optimum undercooling needed to straighten the strip and eliminate the residual stresses upon subsequent heating is predicted from the present study. Finally, a comparison of unconstrained with constrained cooling indicates that the curvature and the residual stresses that develop during the latter are significantly lower. The use of constraint is thus of general desirability with regard to the minimization of residual stresses in metal/ceramic strips.

boundary and the curvature of the strip, with the mismatch in thermal expansion, the mechanical properties and the thickness of the two constituents as variables. It is specifically demonstrated that, for a metal with a high work hardening rate, fully plastic deformation is suppressed, because of the stress redistribution caused by bending. It is also noted that, for a perfectly plastic metal, once the fully plastic condition has been achieved, the curvature and the stresses do not change with further cooling. Brittle fracture tendencies of the ceramic are thus reduced by using a non-hardening metal strip.

The calculations presented above refer to the stresses within the beam, away from the free ends, where the interface is stress free (i.e. no normal or shear stresses at the interface). At the ends, the requirement that the surfaces be stress free perturbs the stress field to a distance about three times the strip thickness.⁷ Within this region, shear stresses develop at the interface and exhibit a peak about one strip thickness away from the end. Large normal stresses also develop at the interface, which may be singular at the end. These end effects often result in debonding at the interface.

A constrained cooling procedure for the elimination of residual stress has also been analysed. During constrained cooling, the strip is prevented from bending and uniform tensile and compressive stresses develop in the metal and the ceramic, respectively. As the constraint is removed bending occurs due to the asymmetric stress. Upon reheating the curvature and the residual stresses initially reduce, as the strip becomes straight. However, further heating causes reverse bending and

1000C. It can be determined from the figure that undercooling of the strip by $\Delta T_c = -1044$ C and subsequent heating by $\Delta T_h = 44$ C would straighten the strip and eliminate the residual stresses. The critical cooling and reheating temperature needed to straighten the strip (Eqs. C4 and C5 are plotted in fig. 13 as functions of the relative metal thickness and work hardening rate. It is noted that the higher the work hardening rate, the lower the critical undercooling temperature, and hence, the higher critical reheat temperature (fig. 13).

It is also interesting to compare the residual stresses that develop in the strip with and without a cooling constraint (section 2). The comparison evaluated for a nonhardening metal ($H=0$) is plotted in Fig. 14 for $t_m/t_c = 1$. It is noted that both the curvature and the residual stresses at a specific undercooling are significantly lower when constraint is imposed. The imposition of constraint is thus of general desirability for the minimization of residual stress during undercooling and hence, inhibits the development of cracks, or other modes of damage.

4. CONCLUSIONS

A stress analysis has been conducted for a linear work hardening metal in a metal/ceramic strip. Stresses develop during cooling to room temperature, due to the different mechanical and thermal properties of the materials. This asymmetry results in bending and stress redistribution. The calculations illustrate trends in the stresses, the locations of the neutral axis and the elastic/plastic

axis ($x = t_n$), is zero. Residual stresses computed for the Cu/Al₂O₃ system are summarized in Figs. 8 and 9 for the case, $t_m/t_c = 1$ and $\Delta T_c = -1200^\circ\text{C}$. After constrained cooling, uniform tension and compression develop in the metal and ceramic, respectively (Fig. 8a). As the constraint is removed, bending occurs and the stress distributions are modified (Fig. 8b). Then, upon reheating, the residual stresses are initially reduced (Fig. 9a). However, further heating results in reverse bending and an increase in the residual stresses (Figs. 9b). Eventually, compressive yielding of the metal initiates from the metal/ceramic interface, such that partially (Fig. 9c) or fully (Fig. 9d) plastic conditions may develop.

The reheat temperature needed to straighten the strip and eliminate the residual stresses (eqn c3) is evaluated as a function of the relative metal thickness, t_m/t_c , and plotted for several cooling temperatures in fig. 10 (the essentially linear variation is attributed to the relative magnitude of the deformation parameters for Cu, for which $H \ll E_m$).

The variation of the curvature with the reheat temperature (for $t_m/t_c = 1$ and $\Delta T_c = -1200^\circ$) is plotted in Fig. 11. The regions of elastic, partially plastic and fully plastic response of the Cu are indicated. It is noted that the curvature and residual stress exhibit relatively large changes while the response is elastic. Conversely, quite small changes occur when the Cu becomes fully plastic.

An example of optimum undercooling is illustrated in Fig. 12, using a temperature difference between bonding and room temperature of

$$\sigma_m^h = E_m \left(c + \frac{x-t_n}{r} - \alpha_m \Delta T_h \right) \quad (16a)$$

$$(-t_m \leq x \leq -t_y)$$

$$\sigma_m^h = \left[c + \frac{x-t_n}{r} - \alpha_m \Delta T_h - \frac{\sigma_m^c + \sigma_y}{H} \right] \left[\frac{1}{E_m} + \frac{1}{H} \right]^{-1} \quad (16b)$$

$$(-t_y \leq x \leq 0)$$

where $-t_y$ is the position of the elastic/plastic boundary. Finally, for a fully plastic metal ($t_y = t_m$), eqn (16) reduces to,

$$\sigma_m^h = \left[c + \frac{x-t_n}{r} - \alpha_m \Delta T_h - \frac{\sigma_m^c + \sigma_y}{H} \right] \left[\frac{1}{E_m} + \frac{1}{H} \right]^{-1} \quad (17)$$

$$(-t_m \leq x \leq 0)$$

The total residual stresses are the sum of the cooling stresses and subsequent stresses due to loss of constraint and reheating, such that

$$\sigma_m = \sigma_m^c + \sigma_m^h \quad (18a)$$

$$\sigma_c = \sigma_c^c + \sigma_c^h \quad (18b)$$

The stresses are obtained subject to solutions for the constants: c , t_n and r (and t_y for partial yield). These constants can be solved (Appendix IID) by imposing the following boundary conditions (section 2). The sum of the bending stresses (terms involving $(x-t_n)/r$) is zero. The sum of the total stresses is zero. The stress at the elastic/plastic boundary ($x=-t_y$), equals $-\sigma_y$ (for partial yield only). Finally, the sum of the bending moments, with respect to the neutral

$$\epsilon^h = c + (x-t_n)/r \quad (-t_m \leq x \leq t_c) \quad (13)$$

where c is a constant (to be determined), t_n is the position of the neutral axis and r is the radius of curvature (r is positive when the metal is on the concave side).

The stresses σ_m^h and σ_c^h can be derived directly from the strains. In the linear elastic ceramic, the stress, σ_c^h , is directly related to the strains by

$$\sigma_c^h = E_c \left(c + \frac{x-t_n}{r} - \alpha_c \Delta T_h \right) \quad (0 \leq x \leq t_c) \quad (14)$$

In the metal, plastic strain may also be involved. Specifically, the metal may yield in compression during reverse bending. Furthermore, since the metal near the metal/ceramic interface is subject to the largest compressive stress, yield initiates at the interface ($x=0$). The relations between the stress and the strain that develop in the metal are thus formulated for three cases, depending on the material properties and the reheat temperature: elastic, partially plastic and fully plastic.

The elastic stresses are simply,

$$\sigma_m^h = E_m \left(c + \frac{x-t_n}{r} - \alpha_m \Delta T_h \right) \quad (-t_m \leq x \leq 0) \quad (15)$$

In the partially plastic case, the stresses may be deduced as (Appendix II),

$$\sigma_c^c t_c + \sigma_m^c t_m = 0 \quad (11)$$

the stresses become,

$$\sigma_m^c = \left[(\alpha_c - \alpha_m) \Delta T_c + \left(\frac{\sigma_y}{H} \right) \right] \left[\frac{1}{E_m} + \frac{t_m}{t_c} \frac{1}{E_c} + \frac{1}{H} \right]^{-1} \quad (12a)$$

$$\sigma_c^c = - \sigma_m^c t_m / t_c \quad (12b)$$

3.2 Relaxation and Heating

Removal of the constraint after undercooling induces bending, with the metal on the concave side of the strip (Fig. 7c). Subsequent heating relaxes the residual stresses, and reduces the curvature of the strip until the strip is straightened (Fig. 7d). Further heating then causes reverse bending and raises the residual stresses, such that the metal eventually yields in compression (Fig. 7e). Consequently, during heating the metal can either behave elastically, or be partially or fully plastic, depending on the material properties and the reheat temperature.

To evaluate the stresses that develop due to loss of constraint and reheating, the bending strains are regarded as being proportional to the distance from the neutral axis and inversely proportional to the radius of curvature.⁵ Then the strain, ϵ^h , becomes

σ^* (fig. 6a). However, overstraining followed by relaxation can appreciably reduce the final stress, because the stress relaxes elastically. By suitable choice of the overstraining stress σ^* , the final stress can be reduced to zero (fig. 6a).

A similar sequence obtains for the undercooling and reheating process (fig. 6b). The metal/ceramic strip is stress free at the bonding temperature. Elastic stress develops during initial cooling. Yielding of the metal then occurs and the stress increases at a diminished rate. Furthermore, by undercooling and reheating to room temperature, the residual stress can be eliminated (fig. 6b).

3.1 Constrained Cooling

The metal/ceramic strip is bonded at elevated temperature and then undercooled, with an external constraint imposed, over a temperature range ΔT_c (ΔT_c is negative), as depicted in Fig. 7a and b. During this step, bending is prohibited and the metal is amenable to plastic deformation. Uniform tensile, σ_m^c , and compressive, σ_c^c , stresses develop in the metal and the ceramic, respectively (for a metal with a larger thermal expansion coefficient than the ceramic). The cooling stresses, σ_m^c and σ_c^c , are determined, subject to strain uniformity within the strip, such that

$$\frac{\sigma_c^c}{E_c} + \alpha_c \Delta T_c = \frac{\sigma_m^c}{E_m} + \frac{\sigma_m^c - \sigma_y}{H} + \alpha_m \Delta T_c \quad (10)$$

Then, by noting that the total force on the system is zero, such that

fully plastic, it complies with the strains within the ceramic and the curvature does not alter with further decrease in the temperature.

Some trends in the stress distributions are plotted in fig. 5 for the elastic, partially plastic and fully plastic cases. It is evident from fig. 5b that while partial yielding conditions apply, the stress in the ceramic is relatively unaffected by the plasticity in the metal, being similar for $H=0$ (no work hardening) and $H = \infty$ (rapid work hardening). However, once fully plastic conditions develop, the plasticity of the metal exerts a profound influence on the stress in the ceramic (fig. 5c), as also apparent from the curvature (fig. 4). Most importantly, the maximum tensile stress in the ceramic is considerably smaller for the non hardening metal. Brittle fracture of the ceramic is thus suppressed by using a non hardening metal constituent. Finally, it is also noted that for a metal with high work hardening rate, fully plastic deformation is suppressed and the metal surface can yield in compression, because of the high compressive stress caused by bending (fig. 5d).

3. ELIMINATION OF RESIDUAL STRESSES

The procedure used for elimination of the residual stress by undercooling and reheating can be exemplified and simulated by considering a standard elastic/plastic material subject to a sequence of overstraining and relaxation (fig. 6). Upon straining, the stress increases linearly until yield, whereupon the stress increases at a reduced rate (dictated by the work hardening rate) to a final stress

conditions (Appendix I). However, for partial yield, analytic solutions of the four simultaneous equations (Eqs. 6 to 9) are too complex. Essential trends, are thus elucidated (Appendix I) for two limiting cases: $H = \infty$ (zero plastic strain) and $H = 0$ (perfect plasticity). Specific residual stresses are computed for the Cu/Al₂O₃ system (figs. 2 to 5) by substituting the constants: ϵ_0 , t_n , r and t_y into Eqs. (2), (4), and (5) and using the material parameters²: $E_m = 1.2 \times 10^5$ MPa, $E_c = 3.5 \times 10^5$ MPa, $\alpha_m = 17 \times 10^{-6} \text{C}^{-1}$, $\alpha_c = 6.5 \times 10^{-6} \text{C}^{-1}$ and $\sigma_y = 35$ MPa.

The conditions of temperature and thickness ratio that determine elastic, partially plastic and fully plastic behavior in the metal are summarized in Fig. 2. Note that the fully plastic condition is suppressed as the work hardening rate increases, or as the metal layer thickness increases. This trend can be appreciated by recognizing that bending generates compressive stresses on the metal surface, which reduce the tensile stresses induced by the thermal mismatch.

The locations of the neutral axis and the elastic/plastic boundary are plotted on fig3, as a function of the temperature change, $-\Delta T$. For a metal and ceramic of equal thickness, the neutral axis is observed to be always located within the ceramic, since the ceramic has the higher Young's modulus. Furthermore, for a metal with a high work hardening rate, note that the elastic/plastic boundary never reaches the metal surface and hence, conditions of partial plasticity always occur.

Trends in the curvature with the temperature change are shown in Fig. 4. For a perfectly plastic metal ($H=0$), once the metal becomes

$$\begin{aligned}
& \int_{-t_m}^{-t_y} E_m (x-t_n) r^{-1} \cdot dx + \int_{-t_y}^0 (x-t_n) \left[\left(\frac{1}{E_m} + \frac{1}{H} \right) r \right]^{-1} \cdot dx \\
& + \int_0^{t_c} E_c (x-t_n) r^{-1} \cdot dx = 0
\end{aligned} \tag{6}$$

The stress at the elastic/plastic boundary equals the yield strength (partial yield),

$$E_m [\epsilon_o - (t_y + t_n)/r] = \sigma_y \tag{7}$$

The net stress is zero,

$$\begin{aligned}
& \int_{-t_m}^{-t_y} E_m \epsilon_o dx + \int_{-t_y}^0 \left(\epsilon_o + \frac{\sigma_y}{H} \right) \left(\frac{1}{E_m} + \frac{1}{H} \right)^{-1} \cdot dx + \int_0^{t_c} E_c [\epsilon_o + (\alpha_m - \alpha_c) \Delta T] dx \\
& = 0
\end{aligned} \tag{8}$$

The sum of the bending moments with respect to the neutral axis ($x=t_n$) is zero,

$$\begin{aligned}
& \int_{-t_m}^{-t_y} E_m [\epsilon_o + (x-t_n)/r] (x-t_n) \cdot dx + \int_{-t_y}^0 [\epsilon_o + \sigma_y/H + (x-t_n)/r] (x-t_n) \\
& \left(\frac{1}{E_m} + \frac{1}{H} \right)^{-1} \cdot dx + \int_0^{t_c} E_c [\epsilon_o + (\alpha_m - \alpha_c) \Delta T + (x-t_n)/r] (x-t_n) \cdot dx \\
& = 0
\end{aligned} \tag{9}$$

General solutions can be obtained for both the elastic and fully plastic cases by evaluating the constants, ϵ_o , t_n , and r from the boundary

the Prandtl-Reuss relation.⁶ For the present geometry,

$$\epsilon_p = (\sigma_m - \sigma_y)/H \quad (3)$$

where H is the work hardening rate and σ_m is the stress in the metal. Hence, for fully plastic deformation of the metal,

$$\sigma_m = E_m \left(\epsilon_o + \frac{\sigma_y}{H} + \frac{x-t_n}{r} \right) \left(1 + \frac{E_m}{H} \right)^{-1} \quad (4)$$

whereas, for conditions of partial plasticity the stresses in the elastic region are

$$\sigma_m = E_m [\epsilon_o + (x - t_n)/r] \quad (-t_m \leq x \leq -t_y) \quad (5a)$$

while in the plastic region,

$$\sigma_m = E_m \left(\epsilon_o + \frac{\sigma_y}{H} + \frac{x-t_n}{r} \right) \left(1 + \frac{E_m}{H} \right)^{-1} \quad (-t_y \leq x \leq 0) \quad (5b)$$

where t_m is the thickness of the metal and $x = -t_y$ is the plane of the elastic/plastic boundary.

The stresses are contingent upon the magnitudes of the constants: ϵ_o , t_n and r (and t_y for partial yield), which can be determined from the following boundary conditions.* The sum of the bending stresses (terms involving $(x-t_n)/r$) is zero,

*Equations (6) to (9) are explicitly formulated for a metal subject to partial plasticity.

where t_n is the position of the neutral axis, r is the radius of curvature, and c is a constant.

The bending strains tend to reduce the stress in the metal. However, the reduction is appreciably larger at the metal surface than at the metal/ceramic interface. This behavior may induce partial yield in a strip adjacent to interface (fig. 1), i.e. when the effective stress in this region exceeds the yield strength. Three deformation characteristics of the metal must, therefore, be considered: elastic, fully plastic and partially plastic. These three conditions are evaluated in the subsequent analysis.

The stress, σ_c , in the linear elastic ceramic, can be invariably related to the strain by simply applying the relations,

$$\sigma_c = E_c(\epsilon - \alpha_c \Delta T) \quad (0 \leq x \leq t_c)$$

or,

$$\sigma_c = E_c[\epsilon_0 + (\alpha_m - \alpha_c)\Delta T] + E_c(x - t_n)/r \quad (2)$$

where t_c is the thickness and E_c is the Young's modulus of the ceramic, $\alpha_c \Delta T$ and $\alpha_m \Delta T$ are the thermal strains in the ceramic and metal respectively and ϵ_0 is a constant ($\epsilon_0 = c - \alpha_m \Delta T$).

In the metal, plastic strains may also be involved. The metal is assumed to satisfy the Von Mises criterion⁶, such that yield occurs when the effective stress equals the yield stress, σ_y . Furthermore, linear work hardening is assumed, whereupon the plastic strain, ϵ_p , satisfies

relaxed. Specific stresses and curvatures are calculated for the technologically important system: $\text{Cu}/\text{Al}_2\text{O}_3$. For purposes of stress elimination, the strip is constrained during cooling, whereupon spatially uniform stresses of opposite sign develop in the metal and ceramic. After cooling the constraint is released, bending occurs due to the asymmetric cooling stress, and spatially varying residual stresses result. Subsequent heating then straightens the strip and relaxes the residual stresses.

2. THE RESIDUAL STRESSES

The residual stresses are determined incrementally upon cooling by invoking the following analytic logic for each temperature decrement. The two constituents experience an unconstrained differential shrinkage, as depicted in Fig. 1. Uniform tensile and compressive stresses are then imposed on the metal and the ceramic, respectively, to achieve displacement compatibility, while the total forces still remain zero. Finally, bending is allowed to occur to balance the bending moment induced by the asymmetric stresses in the previous step. Naturally, these processes occur simultaneously in the actual strip.

The bending strains in both materials are prescribed, by bending theory, as being proportional to the distance from the neutral axis and inversely proportional to the radius of curvature.⁵ The strains, ϵ , in a strip can thus be expressed (fig. 1) by,

$$\epsilon = (x - t_n)/r + c \quad (1)$$

APPENDIX I

Stresses and Curvatures In a Ceramic/Metal Strip

The various bending conditions described in section 2 may be used to evaluate the bending constants t_n , ϵ , $1/r$ and t_y and hence, to determine the stresses. The essential results are summarized in the text.

For the elastic case, the bending constants subject to the requirement, $\sigma_m(x=0) \leq \sigma_y$, are

$$t_n = \frac{E_c t_c^2 - E_m t_m^2}{2(E_m t_m + E_c t_c)} \quad (A1)$$

$$\epsilon_o = \frac{E_c (\alpha_c - \alpha_m) \Delta T t_c}{E_m t_m + E_c t_c}$$

$$\frac{1}{r} = \frac{6E_m E_c t_m t_c (t_m + t_c) (\alpha_c - \alpha_m) \Delta T}{E_m^2 t_m^4 + E_c^2 t_c^4 + 2E_m E_c t_m t_c (2t_m^2 + 2t_c^2 + 3t_m t_c)}$$

Partial plasticity requires that $\sigma_m(x=0) > \sigma_y$ and $\sigma_m(x=-t_m) < \sigma_y$; whereupon, for a metal with a large work hardening rate ($H \approx \infty$),

$$t_n = \frac{E_c t_c^2 - E_m t_m^2}{2(E_m t_m + E_c t_c)}$$

$$\epsilon_o = \frac{1}{2r} \frac{E_c t_c (t_c + 2t_y) - E_m t_m (t_m - 2t_y)}{E_m t_m + E_c t_c} + \frac{\sigma_y}{E_m}$$

$$\frac{1}{r} = \frac{6E_m E_c t_m t_c (t_m + t_c) (\alpha_c - \alpha_m) \Delta T}{E_m^2 t_m^4 + E_c^2 t_c^4 + 2E_m E_c t_m t_c (2t_m^2 + 2t_c^2 + 3t_m t_c)}$$

$$t_y = \frac{\left\{ [E_m^2 t_m^4 + E_c^2 t_c^4 + 2E_m E_c t_m t_c (2t_m^2 + 2t_c^2 + 3t_m t_c)] \sigma_y + E_m E_c [E_c t_c^4 + E_m t_m^2 t_c (4t_m + 3t_c)] (\alpha_m - \alpha_c) \Delta T \right\}}{6E_m^2 E_c t_m t_c (t_m + t_c) (\alpha_m - \alpha_c) \Delta T} \quad (A2)$$

and for perfect metal plasticity ($H=0$),

$$t_n = \frac{1}{2} \frac{E_c t_c^2 - E_m (t_m^2 - t_y^2)}{E_m (t_m - t_y) + E_c t_c}$$

$$\epsilon_o = \frac{1}{2r} \frac{E_c t_c (t_c + 2t_y) - E_m (t_m - t_y)^2}{E_m (t_m - t_y) + E_c t_c}$$

$$\frac{1}{r} = 2 \frac{(E_m t_m + E_c t_c) \sigma_y + E_m E_c t_c (\alpha_m - \alpha_c) \Delta T}{E_m^2 (t_m - t_y)^2 - E_m E_c t_c (t_c + 2t_y)}$$

$$\begin{aligned} & [E_m^2 t_m^4 + E_c^2 t_c^4 + 2E_m E_c t_m t_c (2t_m^2 + 2t_c^2 + 3t_m t_c)] \sigma_y + [2t_y (E_m t_m + E_c t_c) \\ & - 3(E_m t_m^2 - E_c t_c^2)] E_m t_y^2 \sigma_y = E_m E_c (\alpha_m - \alpha_c) \Delta T [-t_c (E_c t_c^3 + 3E_m t_m^2 t_c + \\ & 4E_m t_m^3) + 6E_m t_m t_c t_y (t_m + t_c) - E_m t_c t_y^2 (2t_y + 3t_c)] \end{aligned} \quad (A3)$$

Finally for the fully plastic case ($\sigma_m(x=-t_m) > \sigma_y$)

$$t_n = \frac{1}{2} \frac{E_c t_c^2 - \left(\frac{1}{E_m} + \frac{1}{H}\right)^{-1} t_m^2}{\left(\frac{1}{E_m} + \frac{1}{H}\right)^{-1} t_m + E_c t_c}$$

$$\epsilon_o = - \frac{E_c t_c (\alpha_m - \alpha_c) \Delta T + \sigma_y \left(1 + \frac{H}{E_m}\right)^{-1} t_m}{\left(\frac{1}{E_m} + \frac{1}{H}\right)^{-1} t_m + E_c t_c}$$

$$\frac{1}{r} = \frac{6E_m E_c t_m t_c (t_m + t_c) \left(1 + \frac{E_m}{H}\right)^{-1} [(\alpha_c - \alpha_m) \Delta T + \frac{\sigma_y}{H}]}{\left(\frac{1}{E_m} + \frac{1}{H}\right)^{-2} t_m^4 + E_c^2 t_c^4 + 2E_m E_c t_m t_c \left(1 + \frac{E_m}{H}\right)^{-1} (2t_m^2 + 2t_c^2 + 3t_m t_c)}$$

(A4)

Note that, in the absence of work hardening ($H=0$) the curvature reduces to,

$$\frac{1}{r} = \frac{6t_m(t_m + t_c)\sigma_y}{E_c t_c^3}$$

and the stresses become;

$$\sigma_c = -\sigma_y \frac{t_m}{t_c} + \left(x - \frac{t_c}{2}\right) \cdot \frac{1}{r}$$

$$\sigma_m = \sigma_y$$

(A5)

The fully plastic solutions for a non-hardening material have previously been derived by Wittmer et al.⁴

APPENDIX II

Relations between stress and strain for reverse yielding in the metal

When the metal yields in compression upon reheating, the plastic strain, ϵ_p , is

$$\epsilon_p = (\sigma_m + \sigma_y)/H \quad (B1)$$

where σ_m is the total stress in the metal. The total strain that develops during this step is, $c + (x-t_n)/r$ (eqn 13), and the thermal strain is $\alpha_m \Delta T_h$. The reheat residual stress in the metal, σ_m^h , is thus;

$$\sigma_m^h = E_m \left[c + \frac{x-t_n}{r} - \alpha_m \Delta T_h - \frac{\sigma_m + \sigma_y}{H} \right] \quad (B2)$$

The total stress is the sum of the cooling and reheating stresses,

$$\sigma_m = \sigma_m^c + \sigma_m^h \quad (B3)$$

Hence, combination of eqns (B2) and (B3) gives,

$$\sigma_m = \left[c + \frac{x-t_n}{r} - \alpha_m \Delta T_h + \frac{\sigma_m^c}{E_m} - \frac{\sigma_y}{H} \right] \left[\frac{1}{E_m} + \frac{1}{H} \right]^{-1} \quad (B4)$$

Substitution of eqn (B4) into eqn (B2) then gives;

$$\sigma_m^h = \left[c + \frac{x-t_n}{r} - \alpha_m \Delta T_h - \frac{\sigma_m^c + \sigma_y}{H} \right] \left[\frac{1}{E_m} + \frac{1}{H} \right]^{-1} \quad (B5)$$

Appendix III

Stresses and Curvatures In a Constrained Metal/Ceramic Strip

The boundary conditions described in section 3 may be used to evaluate the bending and curvature terms that determine the stresses in a strip after constrained cooling. For elastic bending of the metal, upon loss of constraint and reheating, the constants can be explicitly determined as

$$\begin{aligned}
 t_n &= (E_c t_c^2 - E_m t_m^2) / 2(E_m t_m + E_c t_c) \\
 c &= (E_m \alpha_m t_m + E_c \alpha_c t_c) \Delta T_h / (E_m t_m + E_c t_c) \quad (C1) \\
 \frac{1}{r} &= \left[\sigma_m^c + \frac{E_m E_c t_c (\alpha_c - \alpha_m) \Delta T_h}{E_m t_m + E_c t_c} \right] \frac{6 t_m (t_m + t_c) (E_m t_m + E_c t_c)}{E_m^2 t_m^4 + E_c^2 t_c^4 + 2 E_m E_c t_m t_c (2 t_m^2 + 2 t_c^2 + 3 t_m t_c)}
 \end{aligned}$$

subject to the condition

$$\sigma_m (x=0) \geq - \sigma_y \quad (C2)$$

Note that the relation between the critical undercooling ΔT_c^* and reheating ΔT_h^* needed to produce a flat strip ($1/r = 0$), when the metal behaves elastically upon reheating, can be derived from eqn (C1) as

$$\Delta T_h^* = - \left[\Delta T_c^* + \frac{\sigma_y}{(\alpha_c - \alpha_m)H} \right] \left[1 - \frac{1}{1 + \frac{H}{E_m} + \frac{t_m}{t_c} \frac{H}{E_c}} \right] \quad (C3)$$

At this critical temperature, the strip is free from residual stress. It is noted that, since the stress relaxation is elastic, the reheating ΔT_h^* (eqn (C3)) is essentially the same as can be derived from section 3.1 (without removing the constraint). It is also possible to derive the critical undercooling ΔT_c^* and reheating ΔT_h^* associated with a given temperature difference, ΔT_o , between the bonding temperature and room temperature;

$$\Delta T_c^* = -(\Delta T_o + \Delta T_h^*) \quad (C4)$$

where

$$\Delta T_h^* = \left[\Delta T_o + \frac{\sigma_y}{(\alpha_m - \alpha_c)H} \right] \left[\frac{H}{E_m} + \frac{t_m}{t_c} \frac{H}{E_c} \right] \quad (C5)$$

For partial plasticity in the metal, the solutions are complex and can be determined from the four simultaneous equations:

$$\int_{-t_m}^{-t_y} E_m(x-t_n)/r \cdot dx + \int_{-t_y}^0 (x-t_n) \left[\left(\frac{1}{E_m} + \frac{1}{H} \right) r \right]^{-1} \cdot dx + \int_0^{t_c} E_c(x-t_n)/r \cdot dx = 0$$

$$\begin{aligned} \int_{-t_m}^{-t_y} E_m(c - \alpha_m \Delta T_h) dx + \int_{-t_y}^0 \left[c - \alpha_m \Delta T_h - \frac{\sigma_m^c + \sigma_y}{H} \right] \left[\frac{1}{E_m} + \frac{1}{H} \right]^{-1} dx \\ + \int_0^{t_c} E_c(c - \alpha_c \Delta T_h) dx = 0 \end{aligned}$$

$$\sigma_m^c + E_m \left[c - \frac{t_y + t_n}{r} - \alpha_m \Delta T_h \right] = -\sigma_y \quad (C6)$$

$$\begin{aligned} \int_{-t_m}^{-t_y} \left\{ \sigma_m^c + E_m \left[c + \frac{x-t_n}{r} - \alpha_m \Delta T_h \right] \right\} (x-t_n) dx \\ + \int_{-t_y}^0 \left[c + \frac{x-t_n}{r} - \alpha_m \Delta T_h + \frac{\sigma_m^c}{E_m} - \frac{\sigma_y}{H} \right] (x-t_n) \left[\frac{1}{E_m} + \frac{1}{H} \right]^{-1} dx \\ + \int_0^{t_c} \left\{ \sigma_c^c + E_c \left[c + \frac{x-t_n}{r} - \alpha_c \Delta T_h \right] \right\} (x-t_n) dx = 0 \end{aligned}$$

subject to the conditions

$$\sigma_m(x=0) \leq -\sigma_y \quad (C7)$$

$$\sigma_m(x=-t_m) \geq -\sigma_y$$

For complete plasticity in the metal, $\sigma_m(x=-t_m) \leq -\sigma_y$, specific solutions can be derived, as given by;

$$t_n = \frac{1}{2} \frac{E_c t_c^2 - \left(\frac{1}{E_m} + \frac{1}{H}\right)^{-1} t_m^2}{\left(\frac{1}{E_m} + \frac{1}{H}\right)^{-1} t_m + E_c t_c}$$

$$c = \frac{\left[\left(\frac{1}{E_m} + \frac{1}{H}\right)^{-1} \alpha_m t_m + E_c \alpha_c t_c\right] \Delta T_h + \left(\frac{1}{E_m} + \frac{1}{H}\right)^{-1} t_m \frac{\sigma_m^c + \sigma_y}{H}}{\left(\frac{1}{E_m} + \frac{1}{H}\right)^{-1} t_m + E_c t_c} \quad (C8)$$

$$\frac{1}{r} = \frac{\left\{ \left(\frac{1}{E_m} + \frac{1}{H}\right)^{-1} t_m \left(t_n + \frac{t_m}{2}\right) \left(c - \alpha_m \Delta T_h + \frac{\sigma_m^c}{E_m} - \frac{\sigma_y}{H}\right) + t_c \left(t_n - \frac{t_c}{2}\right) [\sigma_c^c + E_c (c - \alpha_c \Delta T_h)] \right\}}{\left(\frac{1}{E_m} + \frac{1}{H}\right)^{-1} t_m \left(\frac{t_m^2}{3} + t_n t_m + t_n^2\right) + E_c t_c \left(\frac{t_c^2}{3} - t_n t_c + t_n^2\right)}$$

The residual stresses are obtained by substitution of the constants, t_n , c , t_y and r into eqns (14) to (18).

References

1. C. H. Hsueh and A. G. Evans, submitted to J. Am. Ceram. Soc.
2. A. J. Blodgett, Jr., "Microelectronic Packaging," Scientific American, 249 (1) 86-96, July (1983).
3. Y. S. Sun and J. C. Driscoll, "A New Hybrid Power Technique Utilizing a Direct Copper to Ceramic Bond," IEEE Tran. El. Dev., ED-23 (8) 961-967 (1976).
4. M. Wittmer, C. R. Boer, P. Gudmundson and J. Carlsson, "Mechanical Properties of Liquid-Phase-Bonded Copper-Ceramic Substrates," J. Am. Ceram. Soc., 65 (3) 149-153 (1982).
5. S. Timoshenko and J. N. Goodier, "Theory of Elasticity," McGraw Hill (1951).
6. R. Hill, "The Mathematical Theory of Plasticity," Oxford, Clarendon Press (1950).
7. B. J. Aleck, "Thermal Stresses in a Rectangular Plate Clamped Along an Edge," J. Appl. Mech., 16 (2) 118-122 (1949).

Figure Captions

- Fig. 1 The metal and ceramic strips in the stress free initial condition. After cooling, the strips would exhibit unconstrained differential shrinkage. However, residual stresses allow displacement compatibility. Finally, bending stresses develop, to balance the bending moment.
- Fig. 2 The temperature regimes for elastic, partially plastic and fully plastic deformation of the Cu in a Cu/Al₂O₃ strip.
- Fig. 3 The position of the neutral axis and the elastic/plastic boundary of a Cu/Al₂O₃ strip as a function of the temperature change, $-\Delta T$, for $t_m/t_c = 1$.
- Fig. 4 The curvature of a Cu/Al₂O₃ strip as a function of the temperature change, $-\Delta T$, for $t_m/t_c = 1$.
- Fig. 5 The stress distribution within Cu/Al₂O₃ strips for three different deformation responses of the Cu: (a) elastic at $-\Delta T = 48.3^\circ\text{C}$, (b) partially plastic at $-\Delta T = 122^\circ\text{C}$ and (c) fully plastic for $H=0$ (perfect plasticity) at $-\Delta T = 227^\circ\text{C}$. Also shown (d) compressive yield occurring at the metal surface for $H \rightarrow \infty$ at $-\Delta T = 225^\circ\text{C}$, for $t_m/t_c = 1$.
- Fig. 6 A schematic showing reduction of stresses by (a) overstraining and relaxing and (b) undercooling and reheating, also showing the effects of work hardening rate.

Fig. 7. (a) The metal and the ceramic are bonded at high temperature.
 (b) Constraint is imposed on cooling to prevent bending:
 cooling temperature, ΔT_c .
 (c) Release of the constraint induces bending.
 (d) The strip is straightened by reheating.
 (e) Further heating results in reverse bending.

Fig. 8 Stress distributions within a Cu/Al₂O₃ strip for $t_m/t_c = 1$ and $\Delta T_c = -1200$ C showing (a) uniform tension and compression in the metal and the ceramic, respectively, after constrained cooling and (b) residual stresses modified by bending after removing the constraint.

Fig. 9 Stress distributions within a Cu/Al₂O₃ strip for $t_m/t_c = 1$ and $\Delta T_c = -1200$ C showing (a) that the residual stresses are reduced by heating to $\Delta T_h = 400$ C (b) reverse yielding occurs and increases the residual stresses at $\Delta T_h = 900$ C (c) partial yielding of the metal at $\Delta T_h = 1800$ C and (d) full plasticity of the metal at $\Delta T_h = 2250$ C.

Fig. 10 The critical heating temperature to straighten the strip as a function of the relative metal thickness for $\Delta T_c = -500$ C, -1000 C and -1200 C.

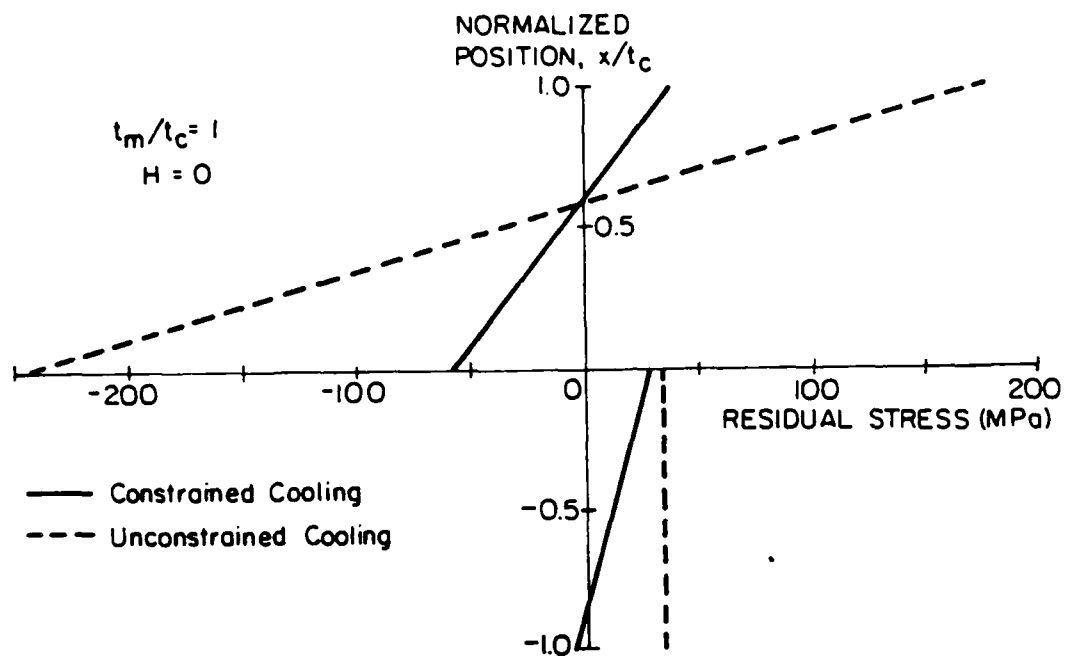
Fig. 11 The normalized curvature as a function of the reheating

temperature for $t_m/t_c = 1$ and $\Delta T_c = -1200\text{C}$. Also shown are the regions of elastic, partially plastic and fully plastic deformation response of the metal.

Fig. 12 The normalized curvature as a function of the undercooling temperature for $t_m/t_c = 1$. The temperature difference before cooling and after heating is 1000 C.

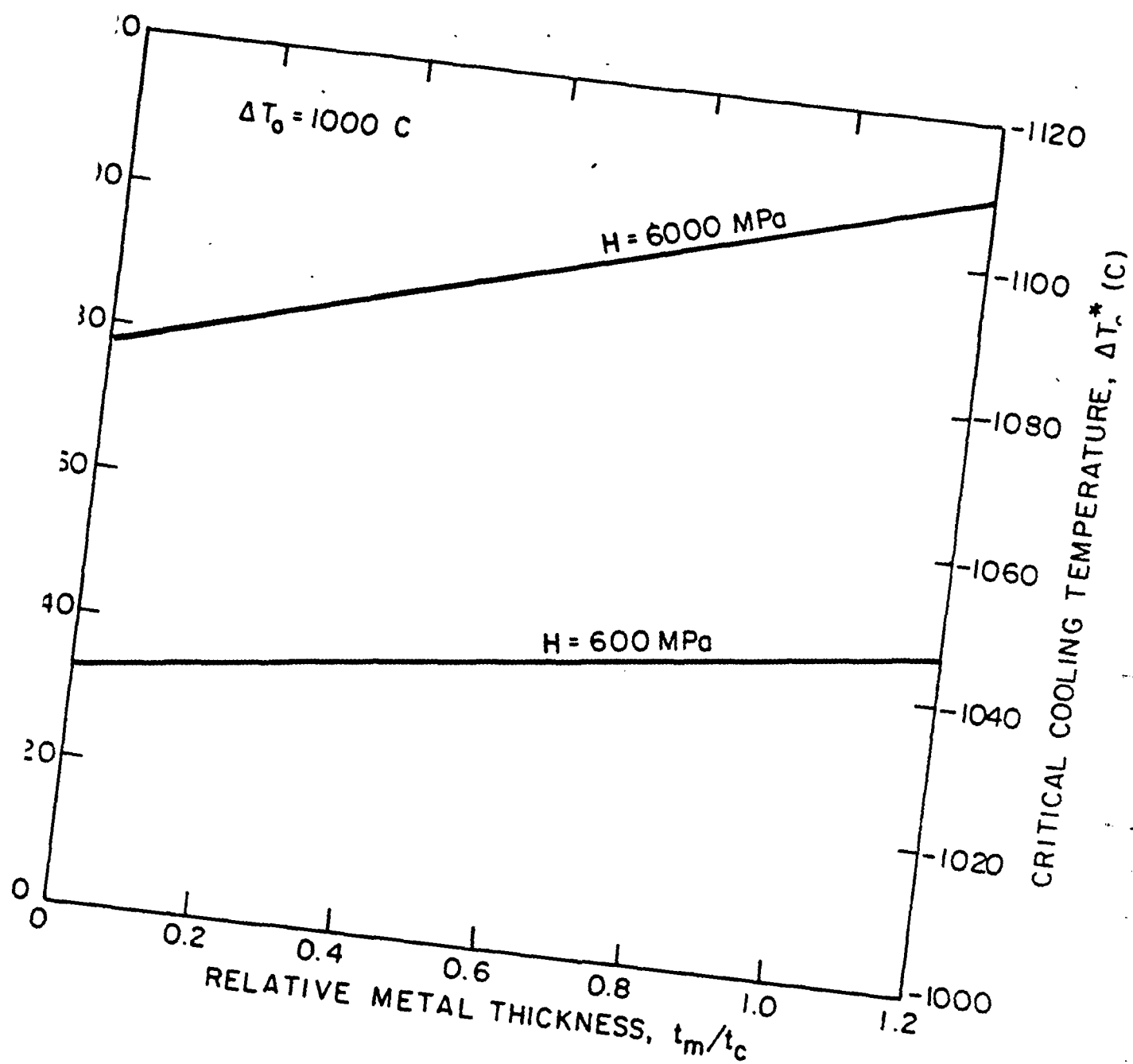
Fig. 13 The critical cooling and heating temperature to straighten the strip as a function of the metal thickness for the temperature difference between the bonding and the room temperature equals 1000 C, $H = 600\text{ MPa}$ and 6000 MPa .

Fig. 14 Stress distribution within a $\text{Cu}/\text{Al}_2\text{O}_3$ strip for $t_m/t_c = 1$, $H = 0$ for constrained and unconstrained cooling.



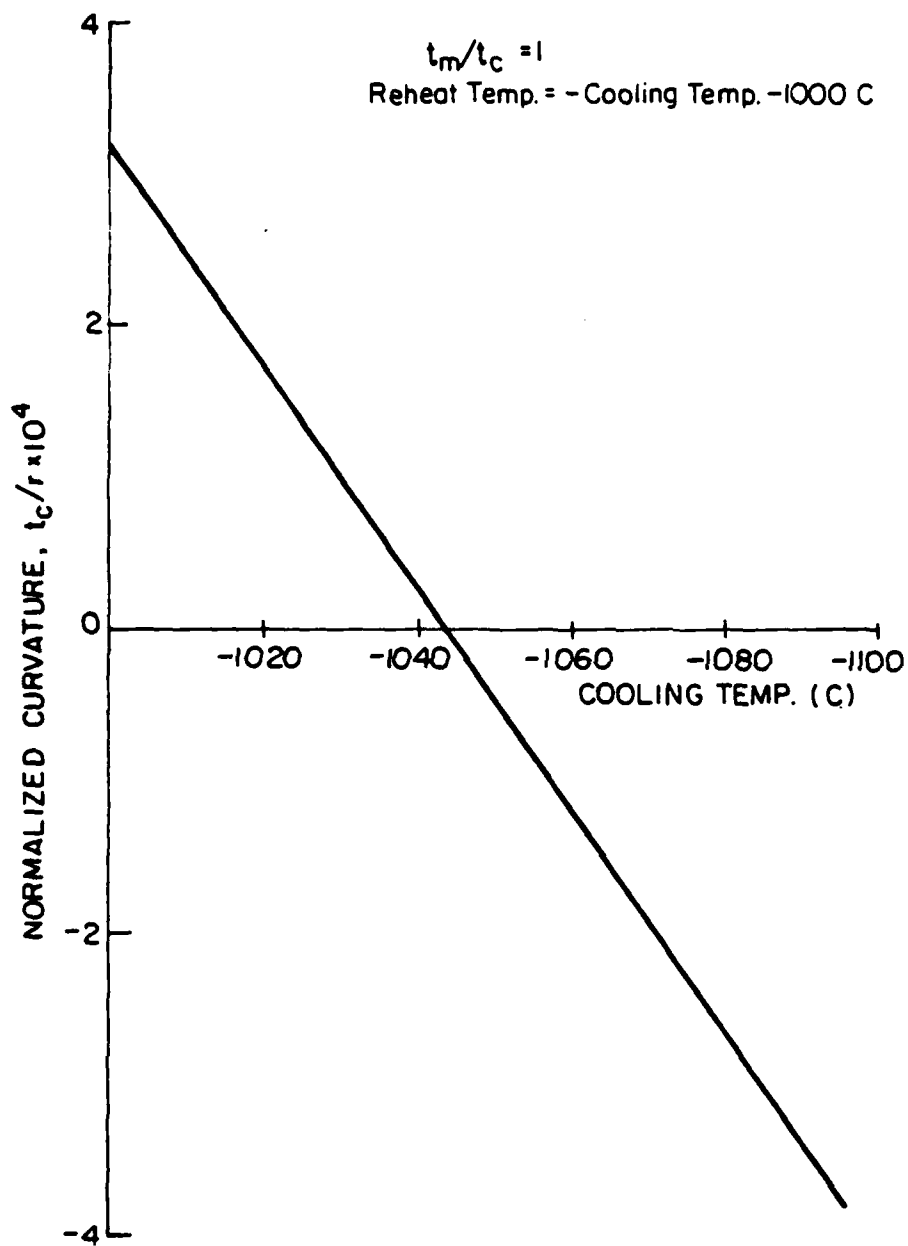
XBL 844-6898

Fig. 14



XBL 8411-605

Fig. 13



XBL 844-6897

Fig. 12

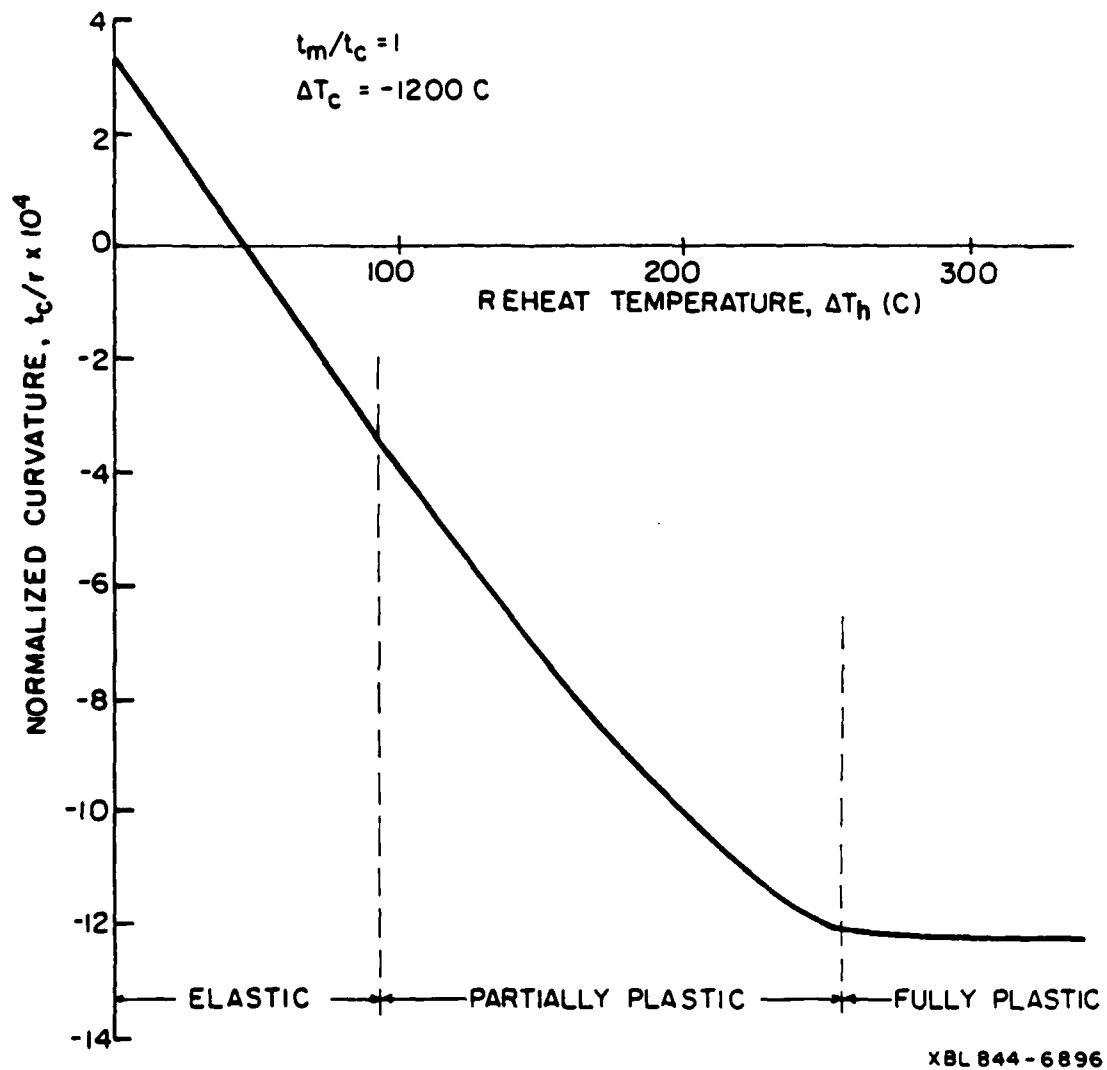


Fig. 11

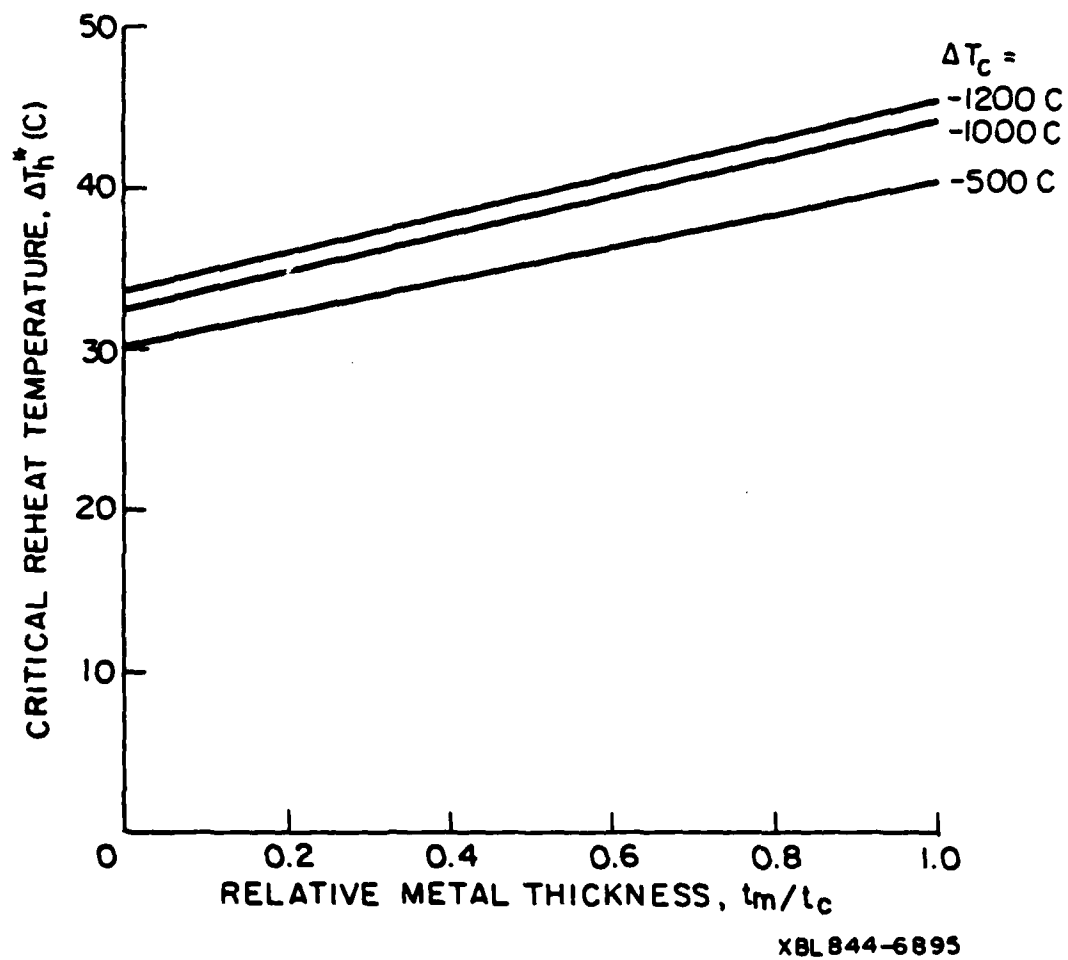
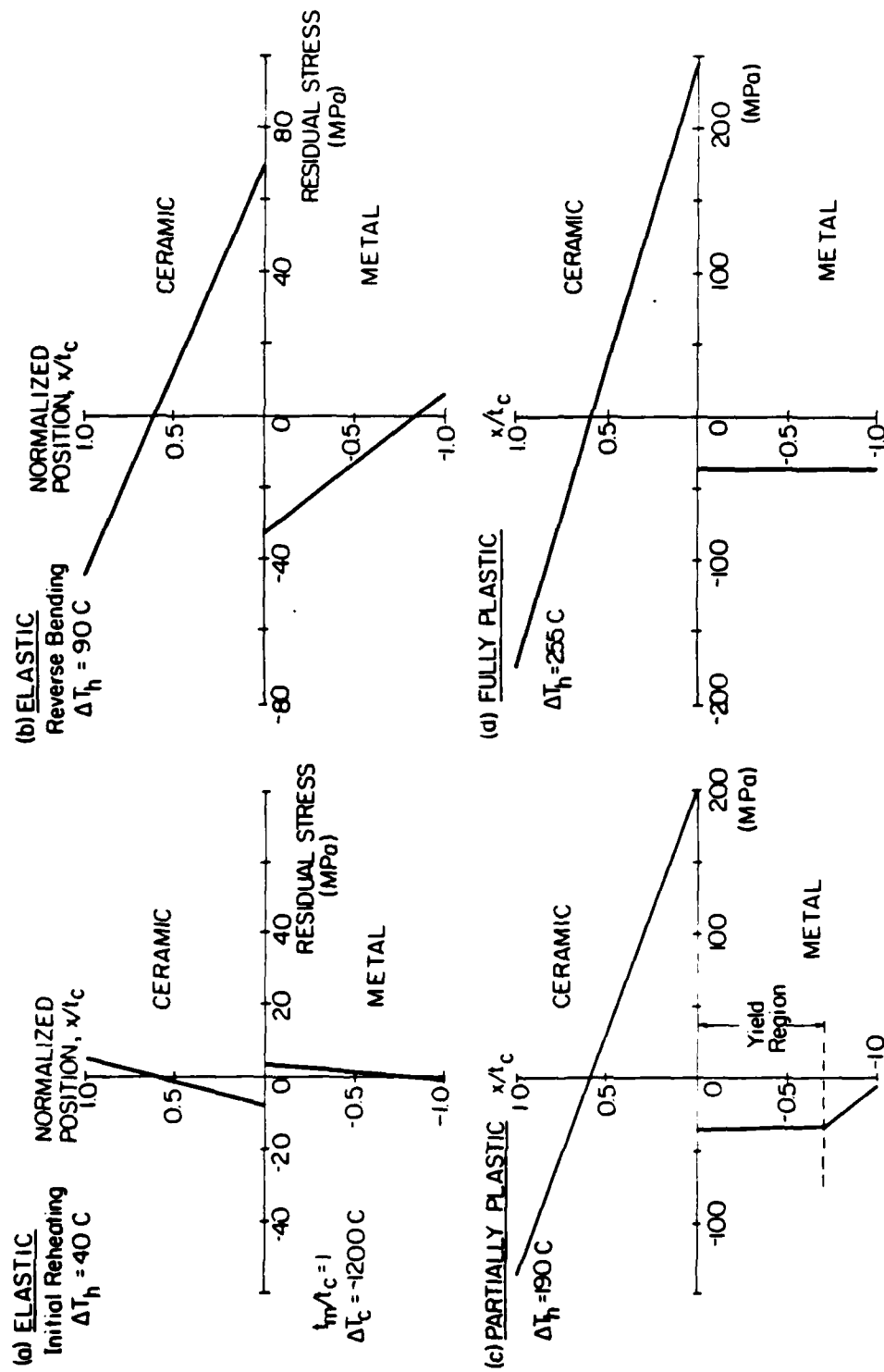
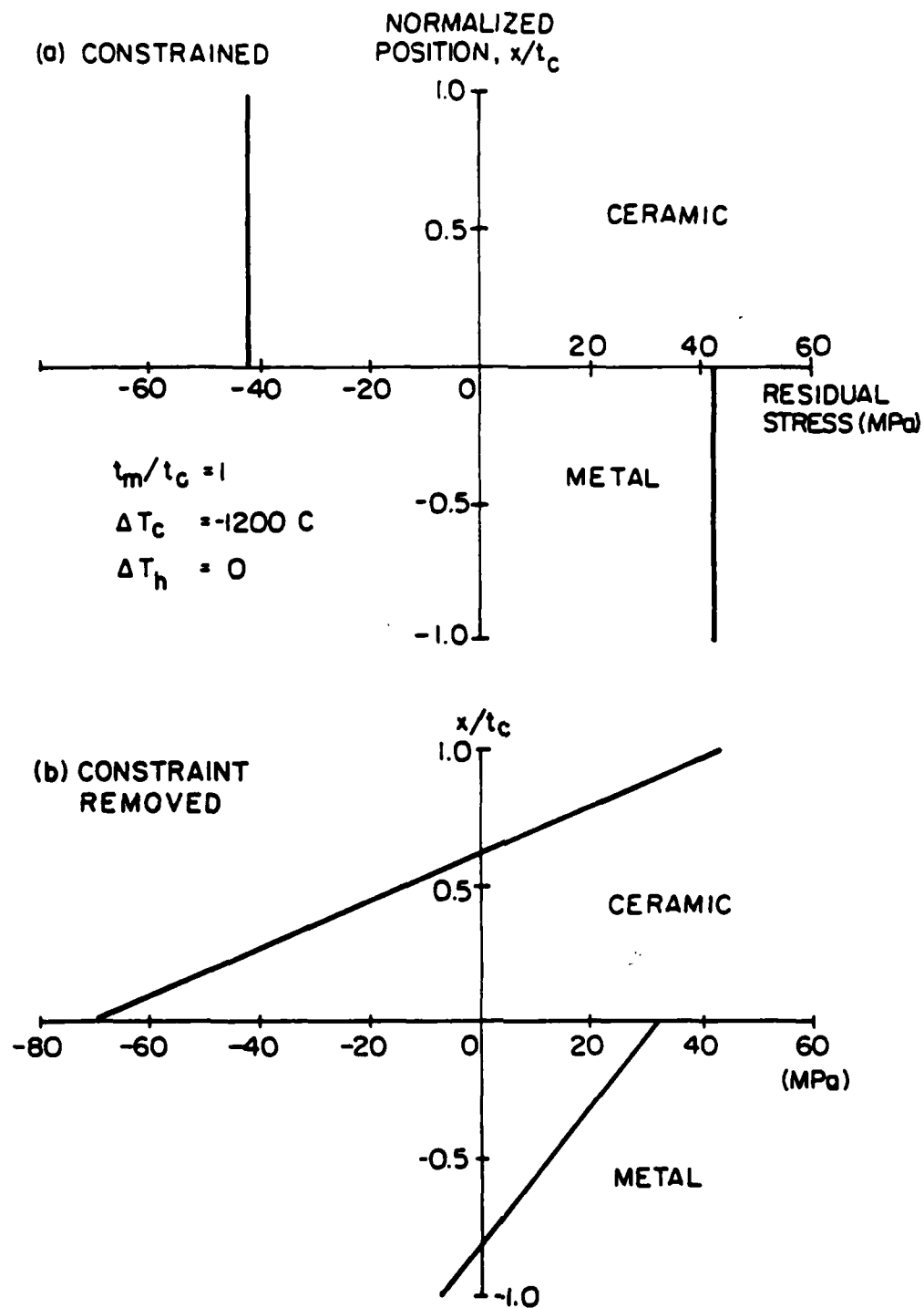


Fig. 10



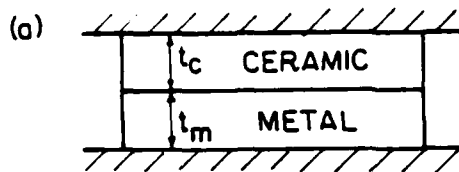
XL 844-6894

Fig. 9



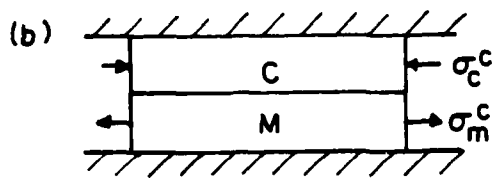
XBL844-6893

Fig. 8

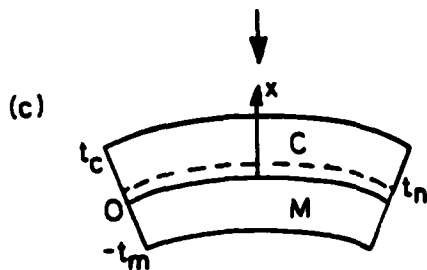


AT BONDING TEMPERATURE

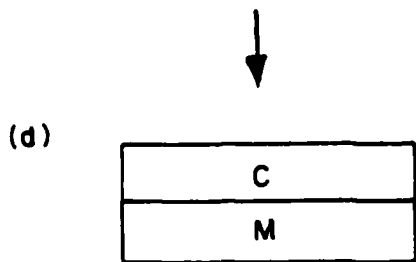
$\downarrow \Delta T_c (-)$



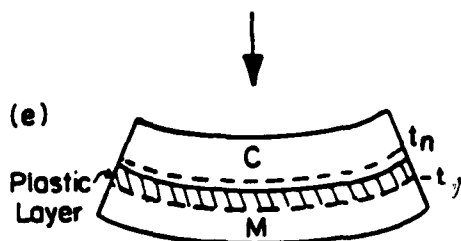
UNDERCOOLING WITH CONSTRAINT
(no bending)



RELEASE CONSTRAINT
(bending)



HEATING
(straightening)

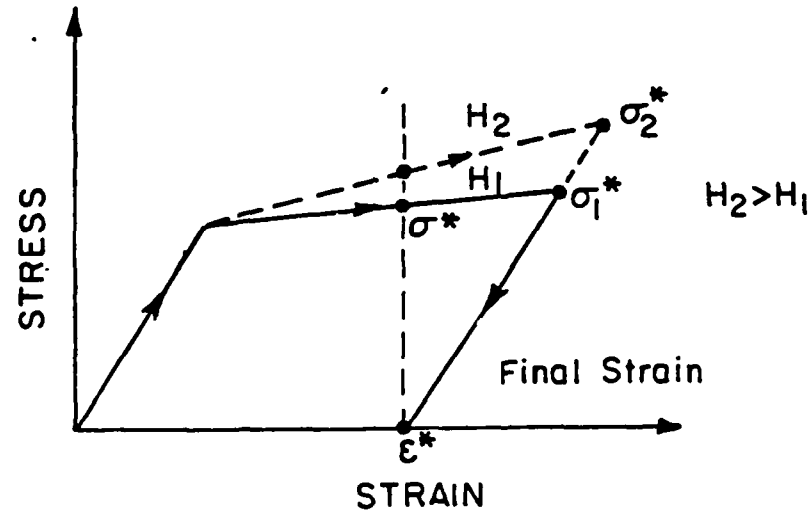


HEATING
(reverse bending)

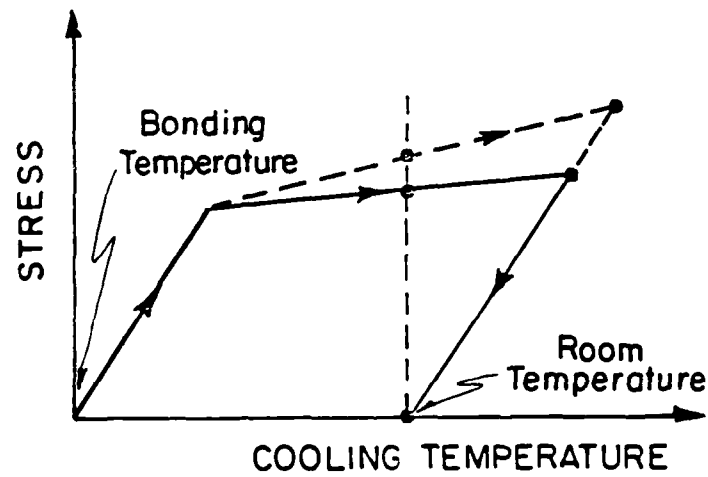
XBL 844-6892

Fig. 7

(a) OVERSTRAIN AND RELAXATION



(b) UNDERCOOLING AND REHEATING



XBL 8411-6055

Fig. 6

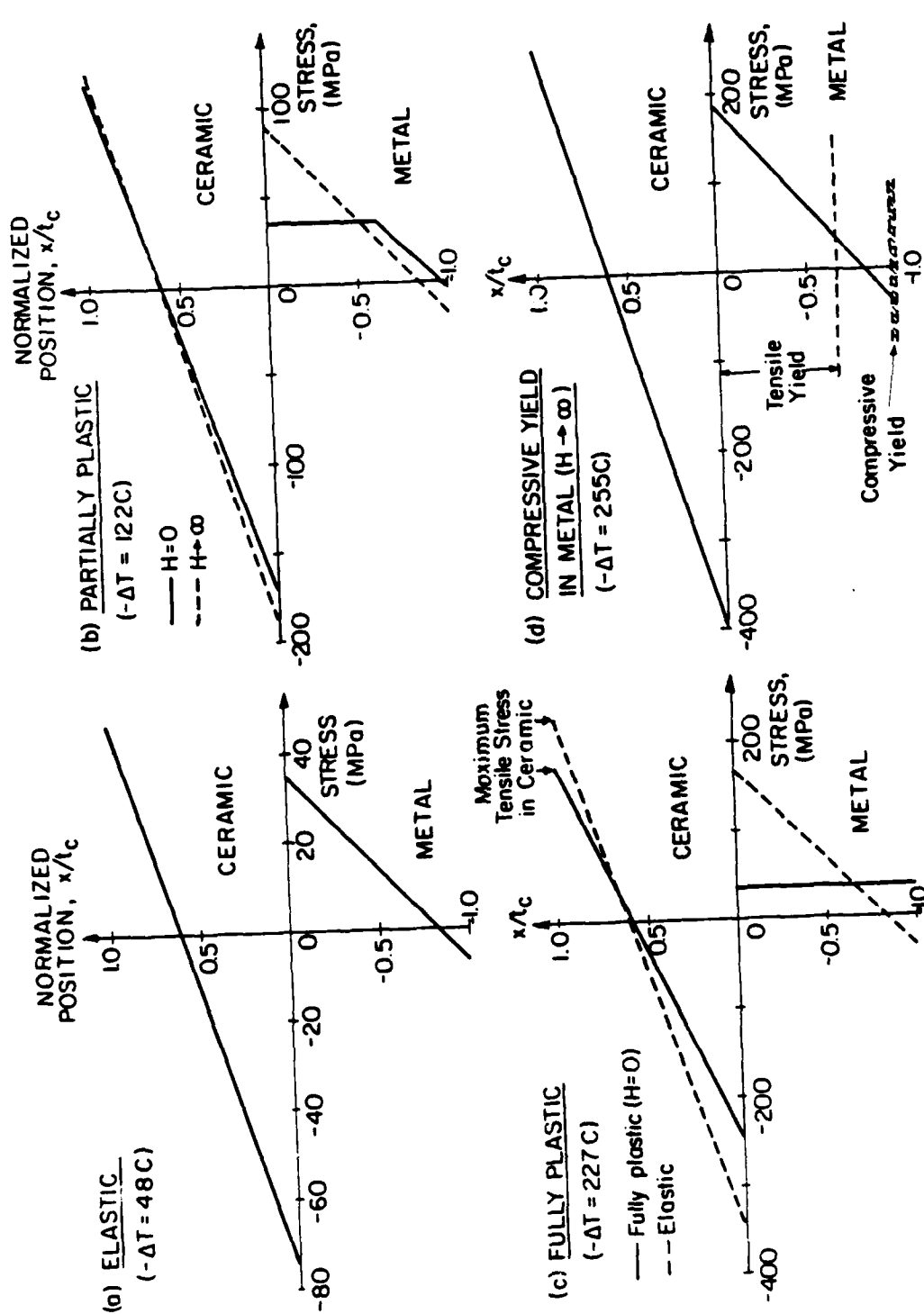
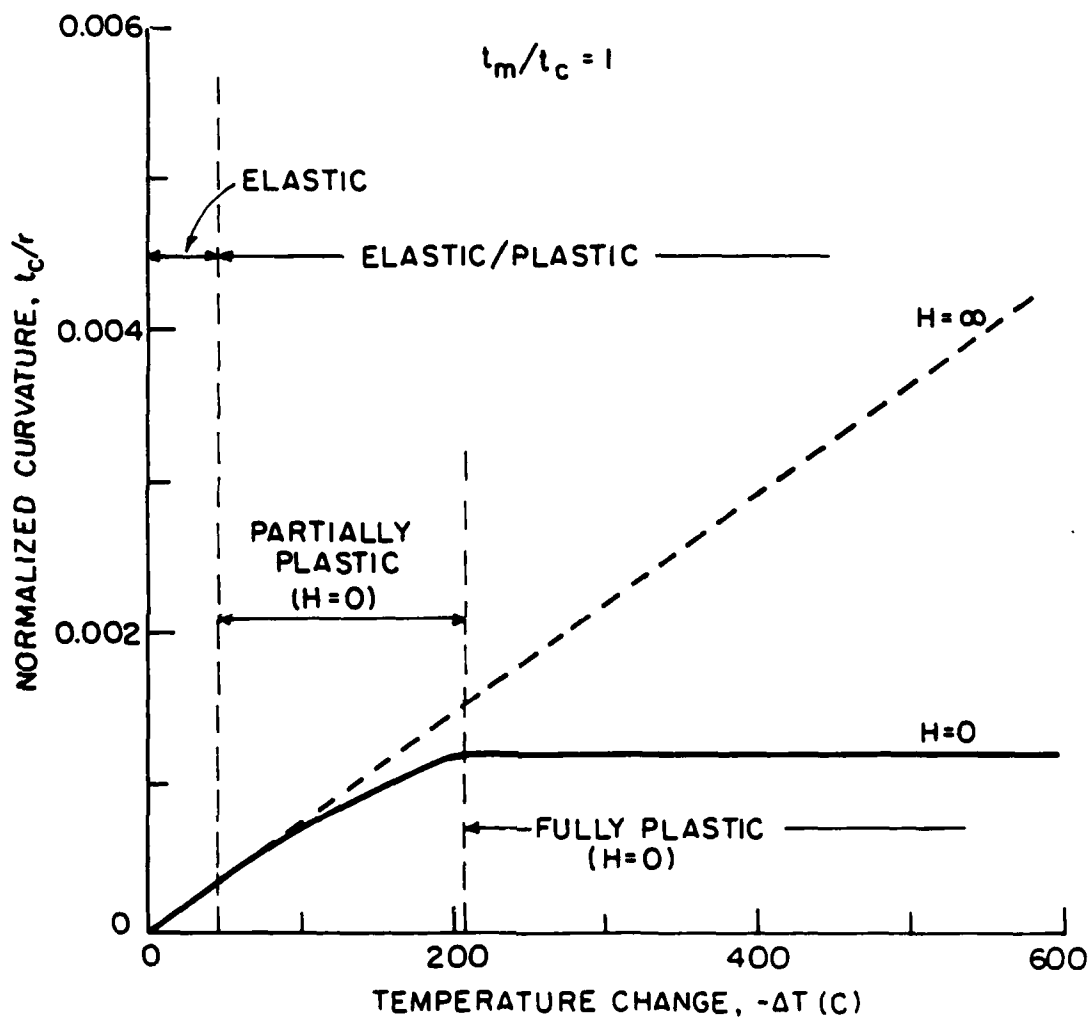
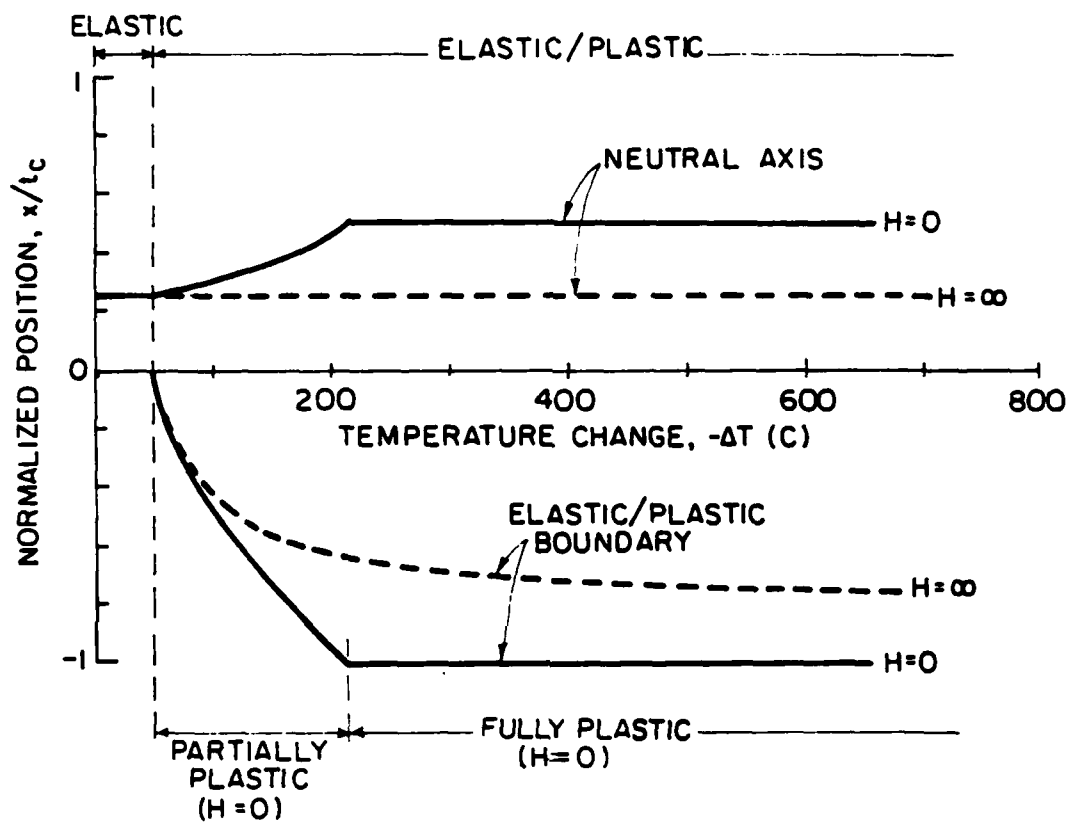


Fig. 5



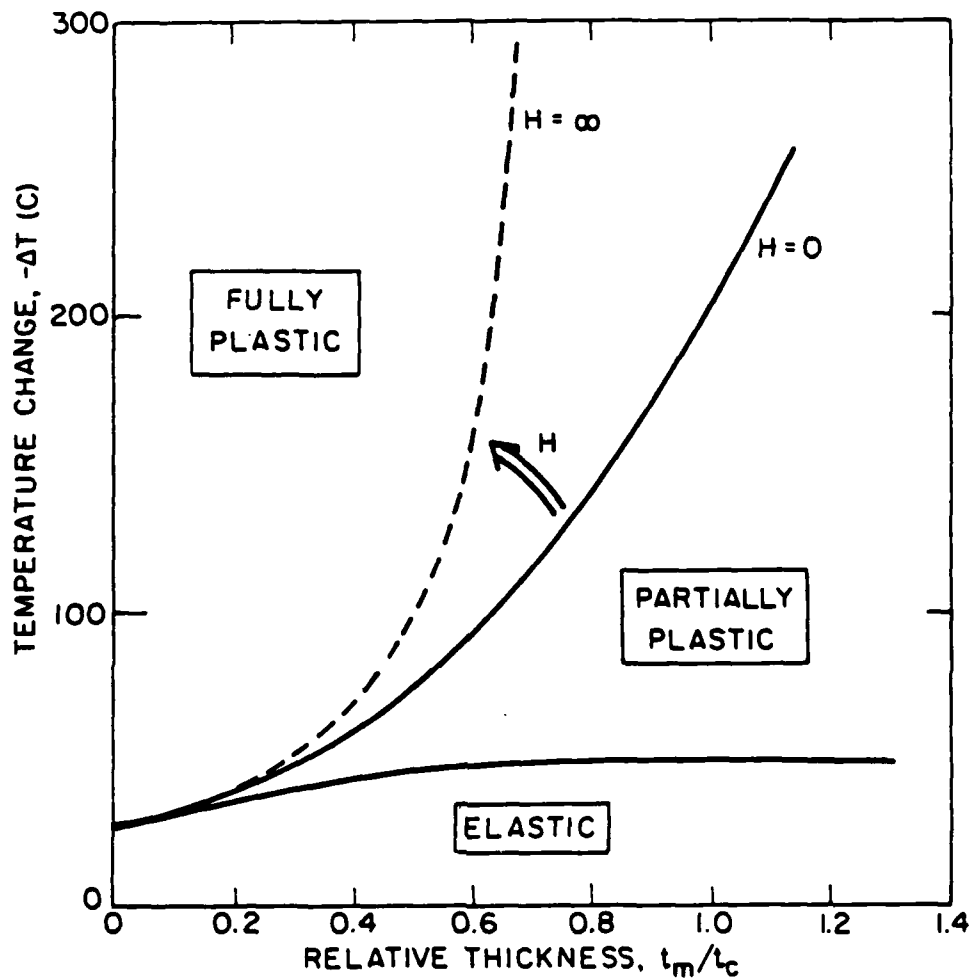
XBL844-6890

Fig. 4



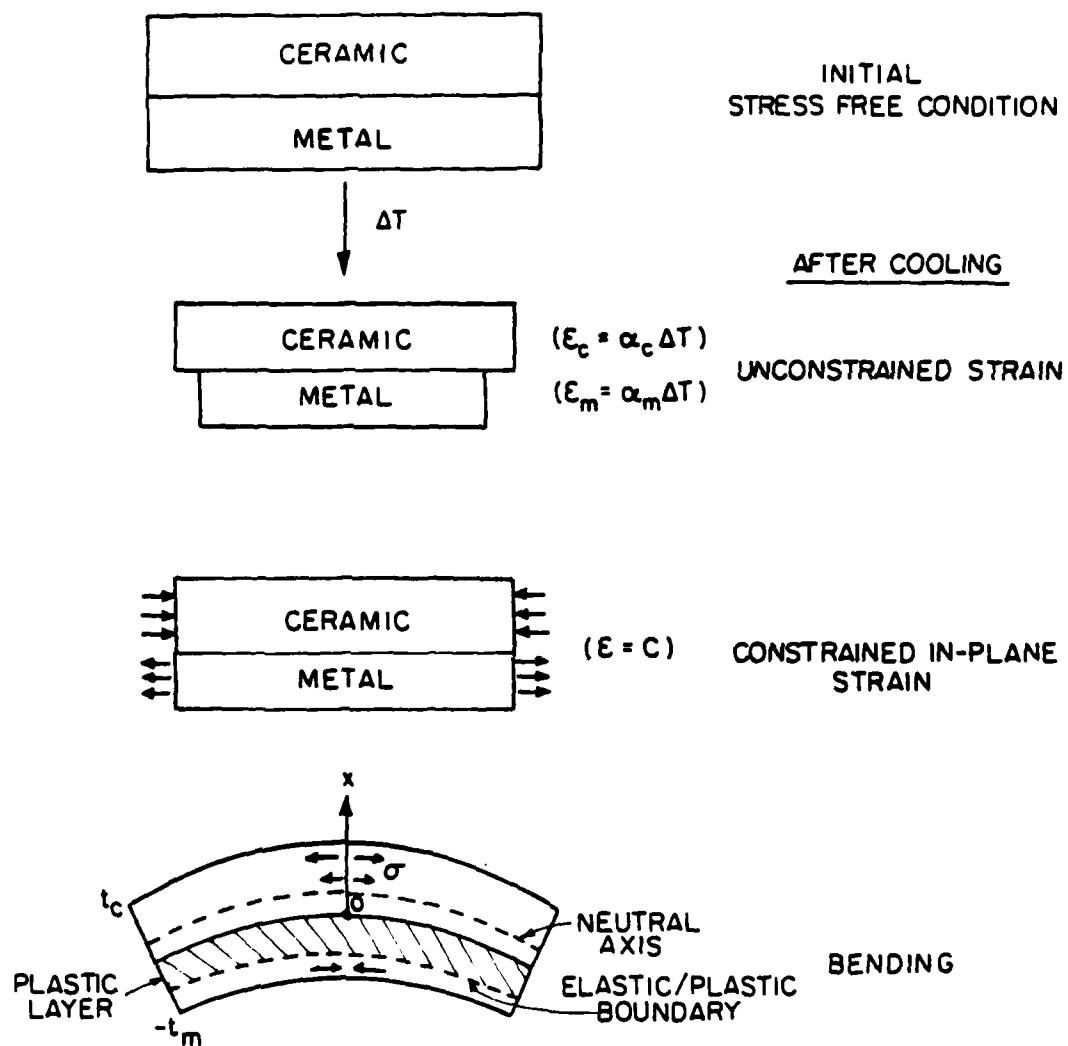
XBL 844-6889

Fig. 3



XBL 844-6888

Fig. 2



XBL 844- 6887

Fig. 1

CHAPTER VII

ON RESIDUAL STRESSES AND CRACKING
IN METAL/CERAMIC SYSTEMS FOR MICROELECTRONICS PACKAGING

C. H. Hsueh and A. G. Evans

ON RESIDUAL STRESSES AND CRACKING
IN METAL/CERAMIC SYSTEMS FOR
MICROELECTRONICS PACKAGING

by

C. H. Hsueh and A. G. Evans

Department of Materials Science and Mineral Engineering
University of California, Berkeley, CA 94720

ABSTRACT

Residual stresses that develop in a metal/ceramic system due to thermal expansion mismatch have been calculated for a work hardening metal. The calculations have been conducted for a cylindrical configuration, pertinent to certain microelectronics packaging systems. Experimental measurements of the stress have also been made on a Cu/cordierite ceramic system, using an indentation technique. It is shown that porosity in the metal can plastically expand and provide a mode of dilatational relaxation. Porosity in the metal thus emerges as an important stress relaxing mechanism.

I. INTRODUCTION

A number of applications in microelectronics involve combinations of metal and ceramic constituents. These constituents are typically subject to residual stress due to thermal expansion mismatch. The residual stresses may result in cracks, that impede the electrical performance of the device. The intent of this article is to evaluate the residual stresses that develop (for a sample configuration) and to examine the implications for cracking.

The metal constituent is generally amenable to plastic deformation and hence, the stress analysis is inherently an elastic/plastic problem. The residual stress is thus expected to exhibit dependence on the yield strength and work hardening coefficient, as well as the mismatch in thermal expansion. However, the specific influence of these material variables on the residual stress depends on the configuration of the system. For present purposes, a cylindrical geometry (fig. 1) is considered, as pertinent to the conduction element in a microelectronics package.¹

Residual stresses are calculated for the cylindrical configuration, subject to the premise that processing is conducted at elevated temperatures, where the stresses are fully relaxed. Stresses thus develop upon cooling due to thermal expansion mismatch. Specific stress amplitudes are computed using the material properties for the technologically significant system: copper/cordierite ceramic. The calculations include considerations of temperature dependent plastic properties and of the influence of porosity, especially in the metal

conducting element, on the residual stress.

The residual stress computations are compared with experimental measurements obtained for the copper/cordierite ceramic system. The localized residual stresses are determined using indentation techniques, with indentations placed in the ceramic, adjacent to the metal/ceramic interface (fig. 2). The plastic properties of the metal required for stress determination are also assessed using indentation methods.

Finally, the implications of the stress analysis for various modes of mechanical failure in the device are discussed. In particular, cracking of the ceramic, debonding of the interface and ductile fracture/fatigue of the metal are explored using specific failure criteria pertinent to each situation.

2. RESIDUAL STRESS ANALYSIS

2.1 The General Approach

The residual stresses are determined by the usual procedure of firstly allowing the two constituents to exhibit an unconstrained differential shrinkage, as depicted in fig. 3 (for a metal with a larger thermal expansion than the ceramic). Then, equal but opposite radial, σ_r , and axial, σ_z , tractions are placed around the metal and ceramic surfaces (fig. 3c) in order to restore displacement continuity at the interface. The tractions are subject to the requirement that the resultant average axial stress be zero since there is no external force on the system and furthermore, in the specific case of an infinite

ceramic matrix, the matrix-axial stress, $\sigma_z^c \rightarrow 0$.

The attainment of displacement continuity induces elastic strains in the ceramic matrix and both elastic and plastic strains in the metal cylinder. The induced strains in the metal cylinder consist of a dilatation and a shape change. The dilatation contributes stresses that depend primarily on the thermal mismatch strain, while the shape change induces stresses dictated largely by plastic flow stress. These two components are evident in the final solutions for the residual stresses.

The radial and tangential stresses in the infinite ceramic matrix, subject to interface tractions, σ , are given by,²

$$\begin{aligned}\sigma_r^c &= \sigma(a/r)^2 \\ \sigma_\theta^c &= -\sigma(a/r)^2\end{aligned}\tag{1}$$

where a is the cylinder radius and r is the distance from the axis of symmetry. The corresponding stresses in the metal are,²

$$\sigma_r^m = \sigma_\theta^m = \sigma\tag{2}$$

The interface, σ , and the longitudinal, σ_z , stresses are dictated by the boundary conditions and the thermal, elastic/plastic properties of the material. The present analysis examines the 'plane strain' condition⁺, pertinent to the stress away from the surface,

⁺This condition is sometimes referred to as the 'free end' condition.

wherein planes parallel to the surface remain planar after deformation (fig. 4). For this condition, a substantial axial stress exists in the metal cylinder.

The total strain within the elastic matrix is the sum of thermal and elastic strains, such that,

$$\begin{aligned}\epsilon_r^c &= \alpha_c \Delta T + \frac{(1+\nu_c)\sigma}{E_c} \left(\frac{a}{r}\right)^2 \\ \epsilon_\theta^c &= \alpha_c \Delta T - \frac{(1+\nu_c)\sigma}{E_c} \left(\frac{a}{r}\right)^2 \\ \epsilon_z^c &= \alpha_c \Delta T\end{aligned}\tag{3}$$

where α_c is the thermal expansion coefficient, ΔT is the temperature change, (ΔT is negative for cooling), E_c and ν_c are the Young's modulus and Poisson ratio respectively.

In the metal, plastic strains are also involved. These superpose on the thermal and elastic strains given by

$$\begin{aligned}\epsilon_r^{mt} &= \epsilon_\theta^{mt} = \epsilon_z^{mt} = \alpha_m \Delta T \\ \epsilon_r^{me} &= \epsilon_\theta^{me} = [(1-\nu_m)\sigma - \nu_m \sigma_z^m]/E_m \\ \epsilon_z^{me} &= [-2\nu_m \sigma + \sigma_z^m]/E_m\end{aligned}\tag{4}$$

The plastic strain is computed by assuming that the plastic deformation in the metal cylinder satisfies the Von Mises criterion,³

$$\sigma_e \equiv \frac{1}{\sqrt{2}} [(\sigma_r^m - \sigma_\theta^m)^2 + (\sigma_\theta^m - \sigma_z^m)^2 + (\sigma_z^m - \sigma_r^m)^2]^{1/2} \\ = \sigma_y \quad (5a)$$

where σ_e is the effective stress and σ_y is the yield stress, such that

$$\sigma_e = \sigma_z^m - \sigma \quad (5b)$$

Furthermore, linear work hardening is assumed, whereupon the plastic strain satisfies the Prandtl-Reuss relation,³

$$d\epsilon_{ij}^{mp} = \frac{3}{2} ' \sigma_{ij} d\sigma_e / \sigma_e H \quad (6)$$

where H is the slope of the work hardening curve and $' \sigma_{ij}$ are the deviatoric stresses:

$$' \sigma_{ij} = \sigma_{ij} - \frac{1}{3} \sigma_{kk} \delta_{ij} \quad (7)$$

In the present case

$$' \sigma_r^m = ' \sigma_\theta^m = \frac{1}{3} (\sigma - \sigma_z^m) \\ ' \sigma_z^m = \frac{2}{3} (\sigma_z^m - \sigma) \quad (8)$$

such that,

$$\begin{aligned} d\epsilon_r^{mp} &= d\epsilon_\theta^{mp} = - \frac{d(\sigma_z^m - \sigma)}{2H} \\ d\epsilon_z^{mp} &= \frac{d(\sigma_z^m - \sigma)}{H} \end{aligned} \quad (9)$$

The stresses can be determined from the strains, subject to the requirements that the displacements be continuous at the interface,

$$\begin{aligned} u_r^m &= u_r^c \quad (r=a) \\ u_z^m &= u_z^c \end{aligned} \quad (10a)$$

such that,

$$\begin{aligned} \epsilon_\theta^m &= \epsilon_\theta^c \quad (r=a) \\ \epsilon_z^m &= \epsilon_z^c \end{aligned} \quad (10b)$$

2.2 The Residual Stresses

The residual stresses can be readily evaluated from the preceding relations, subject to the requirement that the plastic strain ϵ^P , (after yielding initiates) increases monotonically with decrease in temperature, i.e.

$$d|\epsilon^P|/d(-\Delta T) \geq 0 \quad (11a)$$

or,

$$d(\sigma_z^m - \sigma - \sigma_y)/d(-\Delta T) \geq 0 \quad (11b)$$

For this case, the zero plastic strain condition can be referred directly to the yield stress at the current temperature, T. Consequently, integration of eqn (9) for a material with a temperature independent H, gives the plastic strains;

$$\epsilon_r^{mp}(T) = \epsilon_\theta^{mp}(T) = - [\sigma_z^m(T) - \sigma(T) - \sigma_y(T)]/2H \quad (12)$$

$$\epsilon_z^{mp}(T) = [\sigma_z^m(T) - \sigma(T) - \sigma_y(T)]/H$$

The stresses can now be obtained directly from eqns (3,4, 10 and 12) at temperature T, as;

$$\sigma(T) = \frac{-(\alpha_m - \alpha_c)\Delta T \left[\frac{(1+\nu_m)}{E_m} + \frac{3}{2H} \right] - \frac{(1-2\nu_m)}{2E_m} \frac{\sigma_y(T)}{H}}{\frac{(1-2\nu_m)(1+\nu_m)}{E_m^2} + \frac{3(1-2\nu_m)}{2E_m H} + \frac{(1+\nu_c)}{E_c} \left[\frac{1}{E_m} + \frac{1}{H} \right]} \quad (13)$$

$$\sigma_z^m(T) = \frac{-(\alpha_m - \alpha_c)\Delta T \left[\frac{(1+\nu_m)}{E_m} + \frac{3}{2H} + \frac{(1+\nu_c)}{E_c} \right] + \frac{\sigma_y(T)}{H} \left[\frac{1-2\nu_m}{E_m} + \frac{1+\nu_c}{E_c} \right]}{\frac{(1-2\nu_m)(1+\nu_m)}{E_m^2} + \frac{3(1-2\nu_m)}{2E_m H} + \frac{1+\nu_c}{E_c} \left[\frac{1}{E_m} + \frac{1}{H} \right]}$$

where σ_y is the yield strength at the current temperature, T. Terms that relate to the thermal stress $(\alpha_m - \alpha_c)\Delta T$ and to the plastic flow properties (σ_y, H) are evident.

The radial and tangential stresses can be obtained by substituting σ from eqn (13) into eqns (1) and (2). In the absence of work hardening (elastic/perfectly plastic material) the stresses reduce to,

$$\sigma = \frac{-3(\alpha_m - \alpha_c)\Delta T}{\frac{E_m}{3(1-2\nu_m)}} - \sigma_y \frac{1-2\nu_m}{E_m} + \frac{2(1+\nu_c)}{E_c} \quad (14)$$

$$\sigma_z^m = \frac{-3(\alpha_m - \alpha_c)\Delta T + 2\sigma_y \left[\frac{1-2\nu_m}{E_m} + \frac{1+\nu_c}{E_c} \right]}{\frac{3(1-2\nu_m)}{E_m} + \frac{2(1+\nu_c)}{E_c}}$$

Furthermore, if the temperature change is not large enough to induce plastic deformation of the metal, the stresses are given by the elastic solution,

$$\sigma = - \frac{E_m(\alpha_m - \alpha_c)\Delta T}{1-2\nu_m} \frac{E_c}{1+\nu_c} \bigg/ \left[\frac{E_c}{1+\nu_c} + \frac{E_m}{(1+\nu_m)(1-2\nu_m)} \right]$$

$$\sigma_z^m = - \frac{E_m(\alpha_m - \alpha_c)\Delta T}{1-2\nu_m} \left[\frac{E_c}{1+\nu_c} + \frac{E_m}{1+\nu_m} \right] \bigg/ \left[\frac{E_c}{1+\nu_c} + \frac{E_m}{(1+\nu_m)(1-2\nu_m)} \right] \quad (15)$$

This solution applies subject to the condition,

$$-\Delta T \leq \left[1 + \frac{E_c(1+\nu_m)(1-2\nu_m)}{E_m(1+\nu_c)} \right] \frac{\sigma_y}{E_m(\alpha_m - \alpha_c)} \equiv -\Delta T_c \quad (16)$$

The trends in residual stress with yield strength, at fixed ΔT , predicted by eqns (13), (14) and (15) are plotted in fig. 5. In the elastic range, the axial tension exceeds the interfacial stress, by an amount that depends on the relative elastic properties of the metal and ceramic,

$$\sigma_z^m / \sigma = 1 + (E_m / E_c) [(1+\nu_c) / (1+\nu_m)] \quad (17)$$

However, when yielding initiates (small σ_y or large $-\Delta T$), the stress difference diminishes due to plastic relaxation of the shape change (fig. 5). Ultimately, as $\sigma_y \rightarrow 0$ full plastic relaxation of the shape change occurs and for a perfectly plastic material (fig. 5b) the axial and interface stresses converge. The convergent stress σ^* is dictated by the dilatational component of the thermal mismatch, such that (for $H = 0$),

$$\sigma^* = -3(\alpha_m - \alpha_c)\Delta T / [3(1-2\nu_m)/E_m + 2(1+\nu_c)/E_c] \quad (18)$$

The corresponding trends in the residual stress for a material with a temperature independent yield strength are plotted in fig. 6. Yielding initiates at a critical temperature change, $-\Delta T_c$ (eqn 16). However, the stresses continue to increase with further decrease in temperature, due to the increase in dilatational mismatch. Also, note

that for materials that exhibit a large work hardening rate, H , the axial stress is enhanced and the interfacial stress reduced.

2.3 Some Effects of A Temperature Dependent Plastic Flow Stress

The preceding formulation of the residual stresses pertains, as noted above, provided that the metal exhibits continuous plastic straining upon cooling. Some conditions that satisfy and violate this requirement are schematically illustrated in fig. 7. A specific assessment is conducted for the copper/cordierite ceramic system by assuming a linear temperature dependence (fig. 8), with σ_y varying between zero at the bonding temperature and 110 MPa at room temperature. For this case, the stress difference, $\sigma_z^m - \sigma$, deduced from eqn (13) (with α_m replaced by α_m^*) satisfies the inequality $d(\sigma_z^m - \sigma - \sigma_y)/d(-\Delta T) \geq 0$ (fig. 9) at all temperatures. Consequently, for this material system, the residual stress formulae based on the current yield strength should be strictly applicable.

2.4 Effects of Porosity

The presence of porosity in the metal (see fig. 10) may modify the residual stress, by allowing dilatation of the metal, via plastic hole growth.⁵⁻⁷ This relaxation effect could be substantial for the present, cylindrical geometry, because of the relatively high mean stress.

Approximate account of the role of dilatation may be ascertained by invoking the solution for plastic hole growth in a non-hardening

material. Specifically, an isolated spherical pore with volume V subject to an effective remote strain rate, $\dot{\epsilon}_e$, exhibits a volume expansion rate, \dot{V} , given by⁶⁻⁷

$$\frac{\dot{V}}{V} = 0.85\dot{\epsilon}_e \exp \left[\frac{3\sigma_m}{2\sigma_y} \right] \quad (19)$$

Assessment of effects of porosity, based on eqn (19) can be achieved if an expression for the relaxation of the mean stress σ_m , by the pore expansion be incorporated into the analysis. This is attained, most simply, by replacing the expansion coefficient of the metal with an effective value α_m^* , that remains to be determined by further analysis. This approach assumes, of course, that the pores do not affect the yield criterion, based on the effective stress (eqn 5). With this premise, the means stress can be obtained from eqn (14) as;

$$\sigma_m = \frac{-9(\alpha_m^* - \alpha_c)\Delta T E_c + 2\sigma_y(1+\nu_c)}{6(1+\nu_c)} \quad (20)$$

The equivalent effective plastic strain is given by³

$$\epsilon_e^p \equiv \sqrt{2\epsilon_{ij}\epsilon_{ij}/3} = -(\alpha_m^* - \alpha_c)\Delta T \quad (21)$$

The plastic strain increment may thus be determined. For the simplified condition of a temperature independent α_m^* (see eqns (24b) and (25)).

$$d\epsilon_e^p = -(\alpha_m^* - \alpha_c)d\Delta T \quad (22)$$

nce, the pore expansion rates becomes;

$$\int_{V_0}^V \frac{dV}{V} = - \int_0^{\Delta T_b} 0.85(\alpha_m^* - \alpha_c) \exp \left[\frac{-9(\alpha_m^* - \alpha_c) \Delta T E_c}{4\sigma_y(1+\nu_c)} + \frac{1}{2} \right] d(\Delta T) \quad (23)$$

ere V_0 is the initial pore volume at the bonding temperature ($\Delta T=0$) and ΔT_b is the temperature change from the bonding temperature to room temperature.

Incorporating the temperature dependent yield characteristics of the metal phase (fig. 8), the total volume strain in the metal, θ , can be evaluated for non-interacting pores, as

$$\begin{aligned} \theta &\equiv f[V/V_0 - 1] \\ &= f \left[\exp \left\{ -1.4(\alpha_m^* - \alpha_c) \Delta T_b \exp \left[\frac{-9(\alpha_m^* - \alpha_c) E_c \Delta T_b}{4(1+\nu_c)\sigma_y} \right] \right\} - 1 \right] \end{aligned} \quad (24a)$$

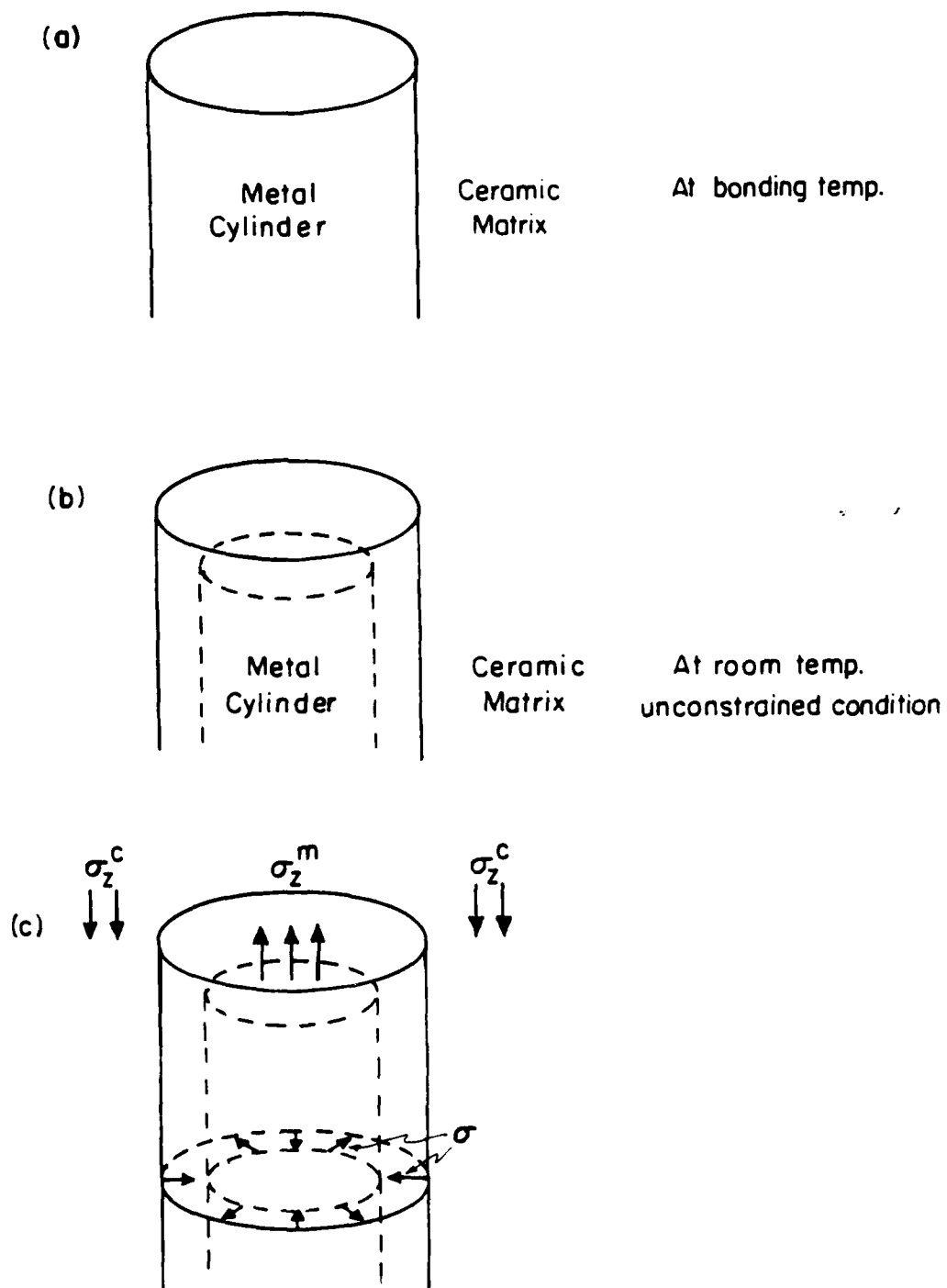
or

$$\theta \approx -1.4(\alpha_m^* - \alpha_c) \Delta T_b f \exp \left[\frac{-9(\alpha_m^* - \alpha_c) E_c \Delta T_b}{4(1+\nu_c)\sigma_y} \right] \quad (24b)$$

ere f is the volume fraction of initial porosity in the metal. The effective thermal expansion coefficient of the metal then becomes,[#]

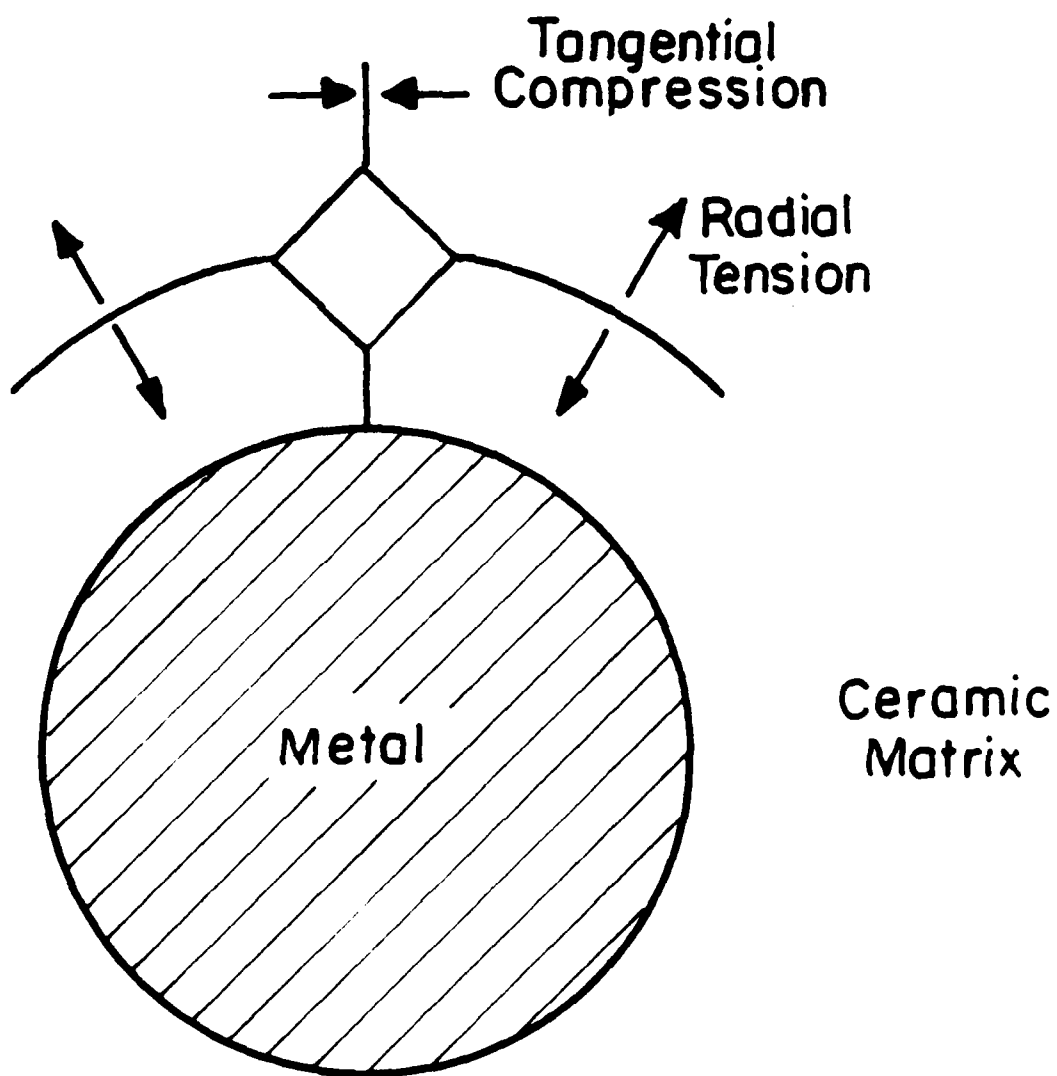
$$\alpha_m^* = \alpha_m + \theta/3\Delta T_b \quad (25)$$

ote that, with the linear approximation for the temperature dependence of the yield strength (fig. 8), $\sigma_y/\Delta T_b$ is constant and α_m^* is thus independent of temperature, consistent with our initial premise.



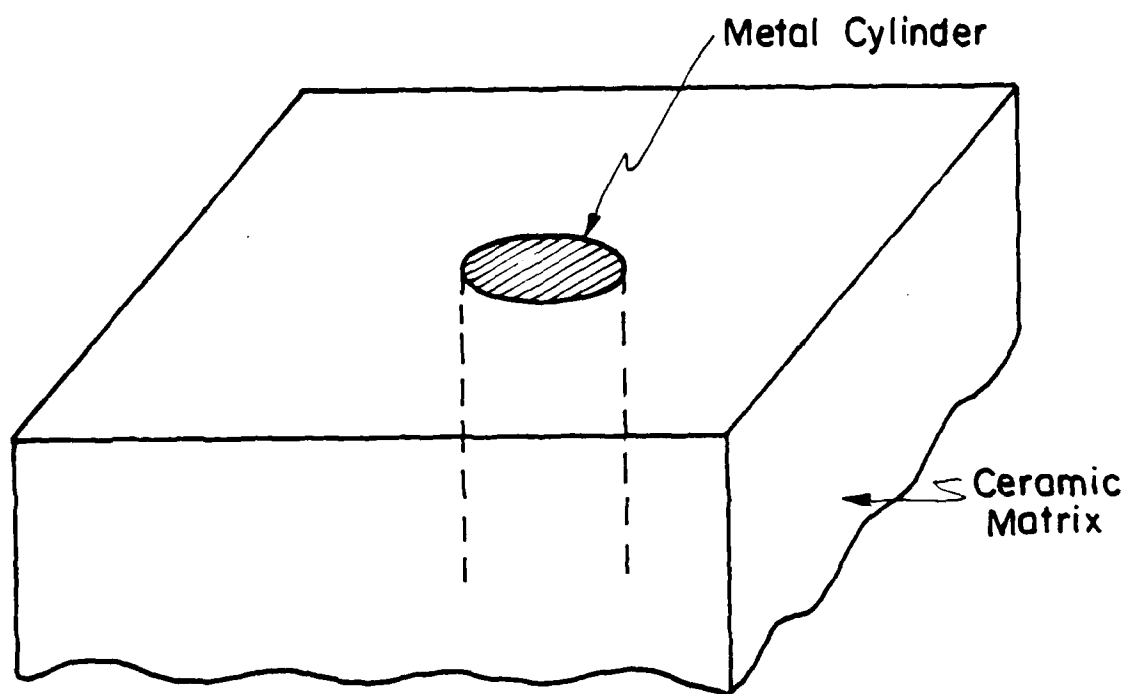
XBL 8312-6674

Fig. 3



XBL 8312-6673

Fig. 2



XBL8312-6672

Fig. 1

Fig. 16 Critical strain, ϵ_2^{cr} , for the onset of plastic flow localization in an infinite band perpendicular to the direction of maximum principal stress, σ_2^∞ , versus pore volume fraction in the band, f , for various stress triaxialities (see ref. 11).

plastic strain remains constant when $T \leq T_v$.

Fig. 8 Schematic showing the variation in yield strength with temperature (see ref. 4) and the linear approximation used in the present study (G is the shear modulus).

Fig. 9 The requirement $d(\sigma_z^m - \sigma - \sigma_y)/d(-\Delta T) \geq 0$ is satisfied for the copper/cordierite ceramic system when $\alpha_m^* > 3.5 \times 10^{-6} \text{ C}^{-1}$

Fig. 10 A scanning electron micrograph (with sample tilt 40°) of pores located on (a) a cracked interface, (b) a failure surface of Cu.

Fig. 11 The effective thermal expansion coefficient of copper, α_m^* , as a function of the initial volume fraction of pores, f .

Fig. 12 The stresses that develop in the Cu/cordierite ceramic system as a function of the temperature change, $-\Delta T$, assuming a linear approximation for the yield strength (see Fig. 8), using $\alpha_m^* = 17 \times 10^{-6} \text{ C}^{-1}$ and $\alpha_m^* = 4 \times 10^{-6} \text{ C}^{-1}$.

Fig. 13 Indentations emplaced (a) in the cordierite ceramic remote the copper, showing straight radial cracks; and adjacent to the copper, showing (b) normal and (c) longitudinal sections of Cu/cordierite ceramic.

Fig. 14 Stress-strain curves of copper alloys obtained from indentation tests.

Fig. 15 (a) Perfect bonding of metal/ceramic; and failure modes in metal/ceramic showing (b) interface decohesion (c) ductile failure of the metal.

Figure Captions

- Fig. 1 Geometry used for residual stress analysis: a metal cylinder in an infinite ceramic matrix.
- Fig. 2 A schematic illustrating the effect of residual stress on indentation cracks.
- Fig. 3 (a) The metal and ceramic bonded at high temperature.
(b) Unconstrained differential shrinkage at room temperature.
(c) The residual stresses that develop to allow displacement and stress continuity due to the expansion mismatch between the metal and ceramic.
- Fig. 4 At a sufficient distance from the free surface, a plane parallel to the free surface remains parallel during cooling and the axial stress in the infinite ceramic matrix, σ_z^c , is zero.
- Fig. 5 The interface stress, σ , and the axial stress in metal, σ_z^m , as a function of the yield stress of the metal, σ_y , for (a) elastic/plastic material (b) elastic/perfectly plastic material.
- Fig. 6 The interface stress, σ , and the axial stress in metal, σ_z^m , as a function of temperature for constant σ_y ; also shown are the effects of the work hardening rate, H .
- Fig. 7 A schematic illustrating stresses that satisfy (a and b) or violate (c) the requirement that the plastic strain increases monotonically with decrease in temperature. In (c) the

Table 1

The Physical Properties of the Cu and Cordierite Ceramic

| | E (Mpa) | ν | $\alpha (C^{-1})$ | H(MPa) |
|--------------------|-------------------|-------|---------------------|--------|
| Cu Alloy | 1.3×10^5 | 0.34 | 17×10^{-6} | 620 |
| Cordierite Ceramic | 1.3×10^5 | 0.25 | 2×10^{-6} | |

Table 2

The Plastic Strains Generated by Indentation

| Indenter Angle ϕ | 60° | 90° | 120° | 140° | 160° |
|-----------------------------|-----|------|------|------|------|
| Plastic Strain ϵ_p | 0.3 | 0.25 | 0.17 | 0.1 | 0.06 |

10. A. G. Atkins and D. Tabor, "Plastic Indentation in Metals with Cones," *J. Mech. Phys. Solids*, 13 (3) 149-164 (1965).
11. N. Ohno and J. W. Hutchinson, "Plastic Flow Localization due to Non-Uniform Void Distribution," *J. Mech. Phys. Solids*, 32 (1) 63-85 (1984).
12. C. H. Hsueh and A. G. Evans, "On Residual Stresses in Metal/Ceramic Bonded Strips: II. Elimination of the Residual Stress," to be published.

References

1. A. J. Blodgett, Jr., "Microelectronic Packaging," *Scientific American*, 249 (1) 86-96 (1983).
2. S. Timoshenko and J. N. Goodier, "Theory of Elasticity," McGraw Hill (1951).
3. R. Hill, "The Mathematical Theory of Plasticity," Oxford Clarendon Press, (1950)
4. A. G. Evans and T. G. Langdon, "Progress in Materials Science," 21 (3-4) 171-441 (1976).
5. F. A. McClintock, "A Criterion for Ductile Fracture by the Growth of Holes," *J. Appl. Mech.* 35 (2) 363-371 (1968).
6. J. R. Rice and D. M. Tracey, "On the Ductile Enlargement of Voids in Triaxial Stress Fields," *J. Mech. Phys. Solids*, 17 (3) 201-217 (1969).
7. B. Budiansky, J. W. Hutchinson and S. Slutsky, "Mechanics of Solids, The Rodney Hill 60th Anniversary Volume," Edited by H. G. Hopkins and M. J. Sewell, Pergamon Press, Oxford and New York, 13-45 (1982).
8. D. B. Marshall and B. R. Lawn, "Flaw Characteristics in Dynamic Fatigue: The Influence of Residual Contact Stresses," *J. Am. Ceram. Soc.*, 63 (9-10) 532-536 (1980).
9. F. P. Bowden and D. Tabor, "The Friction and Lubrication of Solids," Oxford, Clarendon Press, (1964).

triaxiality is relatively large in this case, $\sigma/\sigma_z \approx 0.67$, premature ductile rupture would be encouraged by local void clusters in the copper. A homogeneous distribution of initial porosity in the copper is evidently needed to inhibit local ductile rupture, while still permitting stress relaxation.

4. CONCLUSIONS

A stress analysis has been conducted for a linear work hardening metal cylinder embedded in an infinite ceramic matrix. The bond between the metal and ceramic is established at high temperature and stresses develop during cooling to room temperature. The calculations show that the stresses depend on the mismatch in thermal expansion, the elastic properties and the yield strength and work hardening rate of the metal. Experimental measurements of the surface stresses have also been made on a Cu/cordierite ceramic system, using an indentation technique. A comparison reveals that the calculated stresses in the plastic strain condition are appreciably larger than the measured surface stresses, indicating an important difference between the plane stress and plane strain residual stresses. However, it is also shown that porosity in the metal can plastically expand and permit substantial dilatational relaxation of the plane strain residual stresses. Conversely it is noted that pore clusters are capable of initiating ductile rupture, by means of a plastic instability, in the presence of appreciable triaxiality. A homogeneous distribution of porosity in the metal is thus needed.

the copper and cordierite ceramic to compute the 'plane strain' residual stresses, from the analysis presented in section 2. An interface residual stress, $\sigma = 1500$ MPa is obtained. This stress is substantially in excess of the measured stress ($\sigma = 130$ MPa), because the residual stresses have been measured on the surface, where plane stress conditions ($\sigma_z = 0$) apply. For plane stress the stresses are determined exclusively by the plastic flow stress, as confirmed by the similarity in the present measurements of the residual stress and the plastic flow stress (fig. 14). However, the 'plane strain' residual stress may also be appreciably less than the calculated stress of 1500 MPa, due to plastic dilatation of the pores in the copper (fig. 15). As estimated in section 2.4, porosity in excess of ~ 0.01 can reduce the residual stress by a factor of ~ 8 ; a reduction which coincidentally results in a stress similar to the measured stress. It is thus concluded that porosity in the copper should allow appreciable relaxation of the residual stress in the 'plane strain' region.

The residual stress can be further minimized by undercooling and then reheating the system.¹² The final stresses are the sum of eqn (13) (with ΔT as the undercooling temperature) and eqn (15) (with ΔT_h , the positive reheat temperature).

Initial porosity in the copper may also have the detrimental effect of inducing premature ductile rupture (fig. 15c). Void clusters are capable of initiating ductile rupture by means of a plastic instability.¹¹ The rupture strain depends on the initial fraction of voids and the triaxiality (fig. 16). Consequently, since the

3.2 Flow Stress of Metal

The flow stress of the metal cylinder can also be estimated using indentation techniques. In this instance, impressions are made with pyramidal indentors having various profiles, with included angle, ϕ . Then the flow stress σ_f is related to the load, P , and the indentation cross section, A , by⁹

$$\sigma_f \approx P/3A \quad (29)$$

while the corresponding plastic strains, ϵ_p , for each included angle, ϕ , are given in Table 2.¹⁰ Data obtained using included angles between 60° and 160° result in the flow stress trends summarized in fig. 14.

3.3 Mechanical Damage

Two primary modes of damage have been observed in the copper/cordierite ceramic sytem. Interface decohesion (fig. 15b) has been identified at a small fraction of normal and longitudinal sections. Ductile fracture of the copper has also been detected (fig. 15c) at various axial locations. These modes of damage are induced by the tensile residual stresses in the radial and axial directions, respectively. Appreciable porosity is also observed throughout the copper phase (fig. 10).

3.4 Remarks on Residual Stresses

The plastic flow properties of the copper measured at room temperature can be used in conjunction with the elastic properties of

$$K_c = \chi_* P(E/h)^{1/2} c_*^{-3/2} + \sigma_R \Omega c_*^{1/2} \quad (27)$$

where Ω is a coefficient that depends on the uniformity of the residual field (for a uniform field, $\Omega = 2/\sqrt{\pi}$). The residual stress, σ_R , can be related to the metal/ceramic interface stress, σ , by

$$\sigma_R = \sigma(r/a)^{-2} \quad (28)$$

Hence, by firstly evaluating K_c from indentations placed at locations remote from the metal (fig. 13a), the interface residual stress, σ , may be estimated from radial crack lengths measured at indentations placed at various radial positions, adjacent to the interface.

Inspection of cracking patterns around normal and longitudinal sections reveals (figs. (13b) and (13c)) that the circumferential or axial cracks are relatively enlarged, while the radially oriented cracks are suppressed. A condition of radial tension and circumferential compression is thus implied, consistent with the larger thermal expansion of the copper.

Determination of the toughness of the cordierite ceramic from remote indentations indicates that $K_c = 1.4 \text{ MPa}\sqrt{\text{m}}$. With this toughness, the interfacial residual tension can be determined from the radial crack lengths (as measured on the normal section) as,
 $\sigma = 130 \text{ MPa}$ ($\chi_* = 0.009$).

The trend in α_m^* with the initial volume fraction of pores, in a Cu/cordierite ceramic system, deduced from eqns (24a) and (25), is plotted in fig. 11. Note that, for $f > 0.01$, $\alpha_m^* \sim 4 \times 10^{-6} C^{-1}$.

Dilatational effects are thus capable of reducing the stress (fig. 12) by a substantial factor, ~ 8 , at relatively small initial porosity levels. Small amounts of porosity in the metal can thus cause appreciable stress relaxation, by acting as nuclei for plastic dilatation.

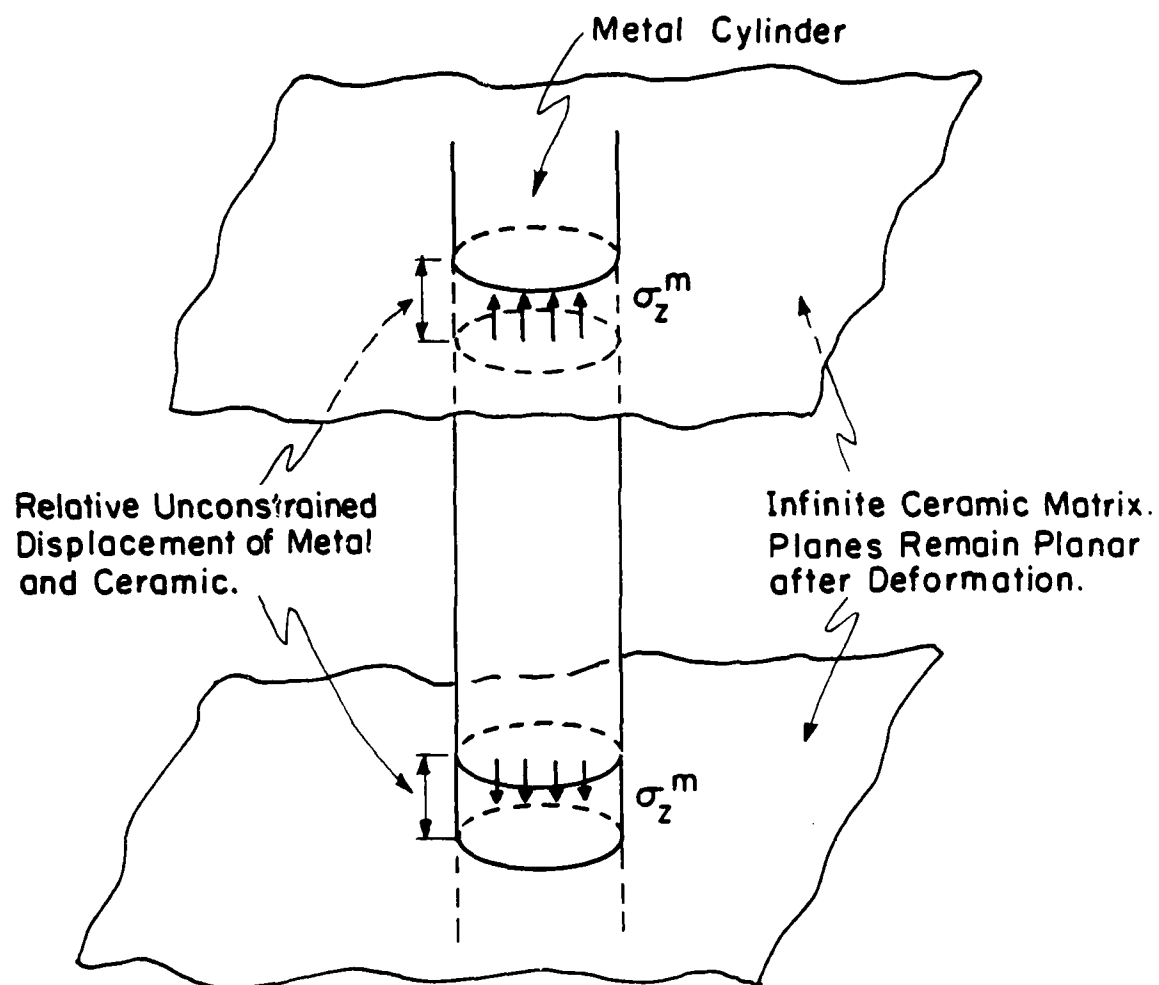
3. EXPERIMENTAL STUDIES

3.1 Residual Stresses

Residual stresses have been estimated for a copper/cordierite ceramic system, using an indentation technique. With this technique, small Vickers indentations are placed in the ceramic, adjacent to the metal/ceramic interface (fig. 13). Then, the relative extensions of the radial cracks provide information pertinent to the sign and magnitude of the residual stress. Specifically, in the absence of residual stress, indentation at a load, P , creates a radial crack of radius, c , related to the toughness of the ceramic, K_C , by;⁸

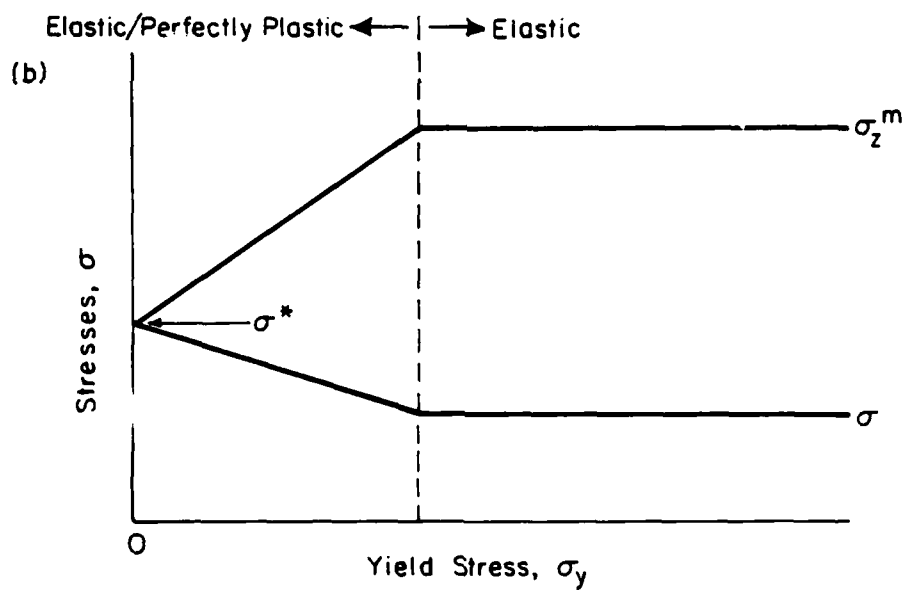
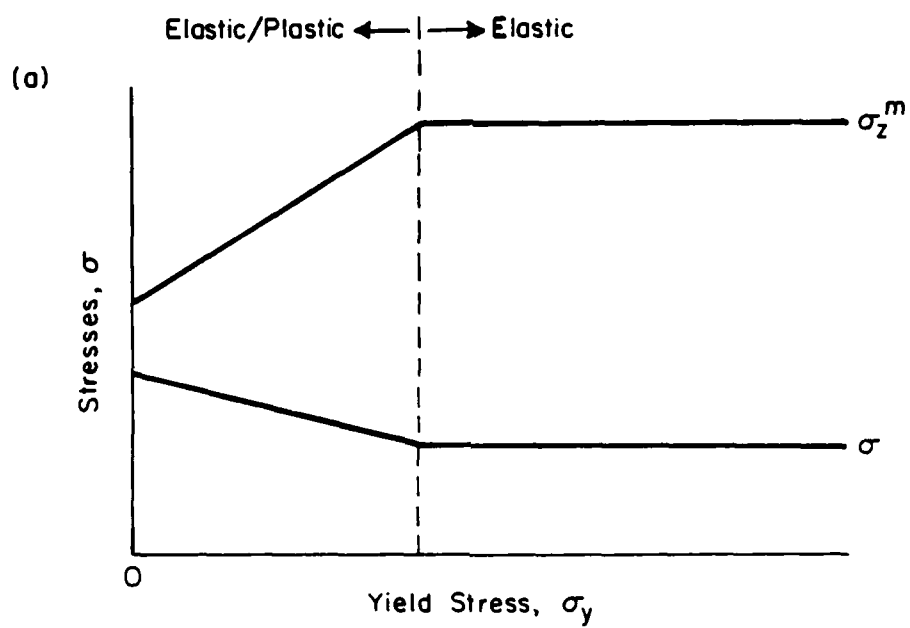
$$K_C = \chi P(E/h)^{1/2} c^{-3/2} \quad (26)$$

where E and h are the modulus and hardness of the ceramic and χ is a coefficient = 0.016. In the presence of residual stress, the crack length and geometry are modified, such that the residual stress, σ_R , and the crack radius, c_* , are related to the toughness by;



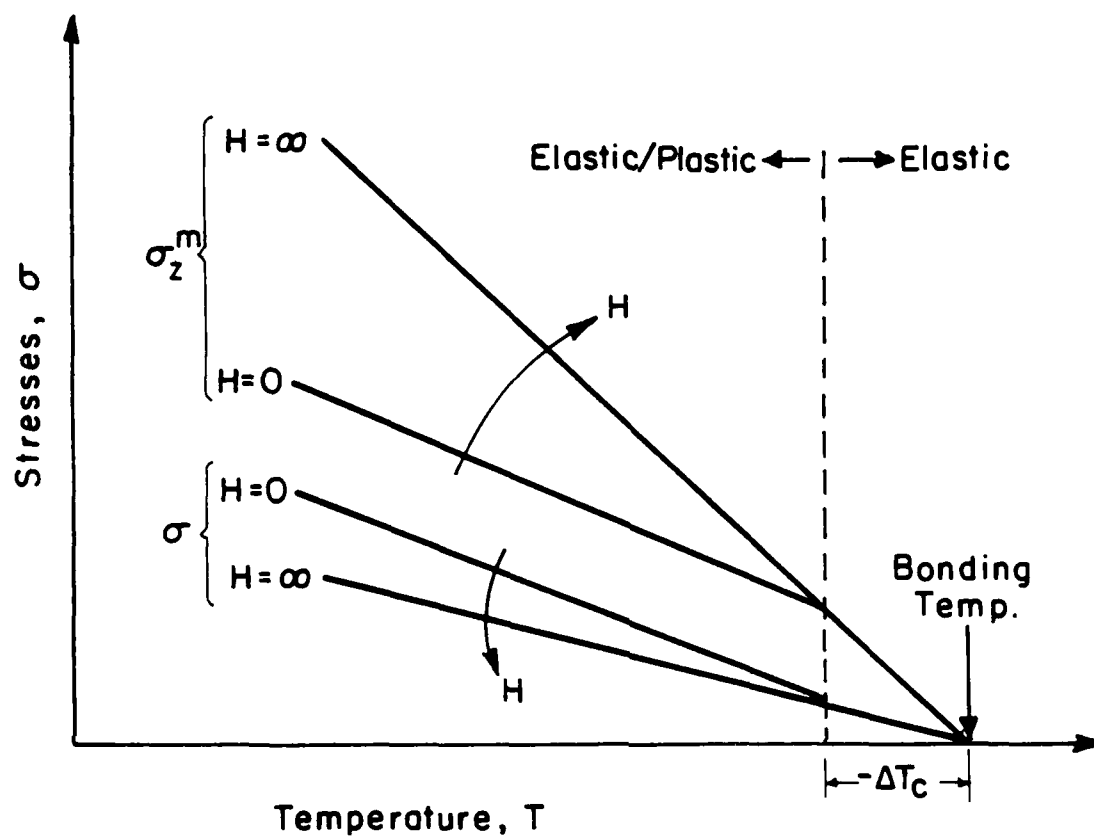
XBL8312-6675

Fig. 4



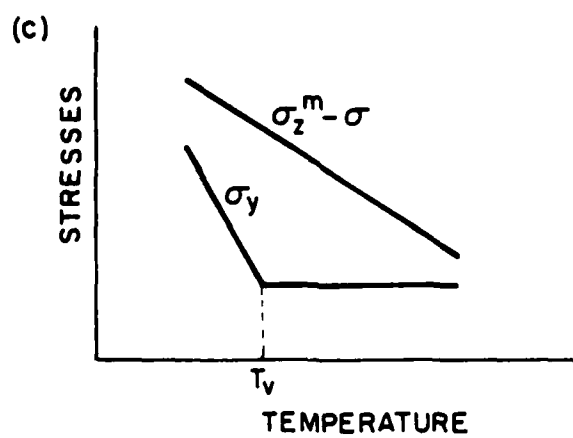
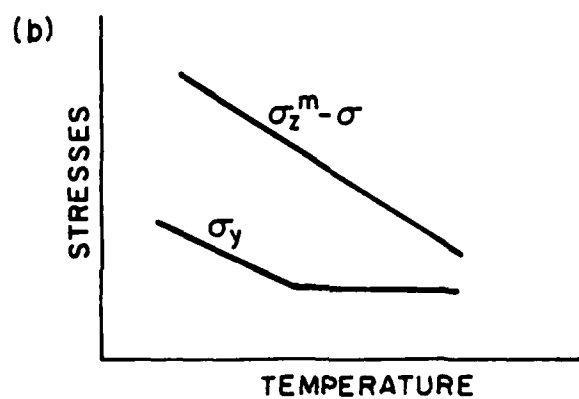
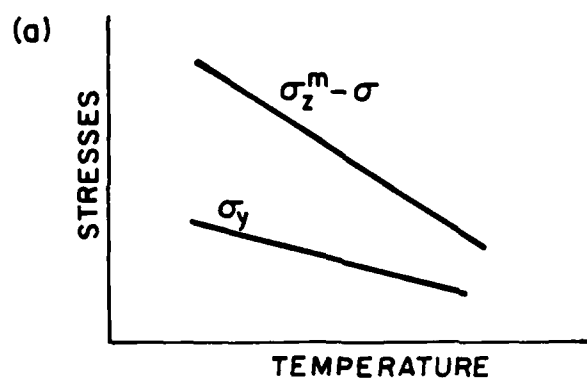
XBL 8312-6676

Fig. 5



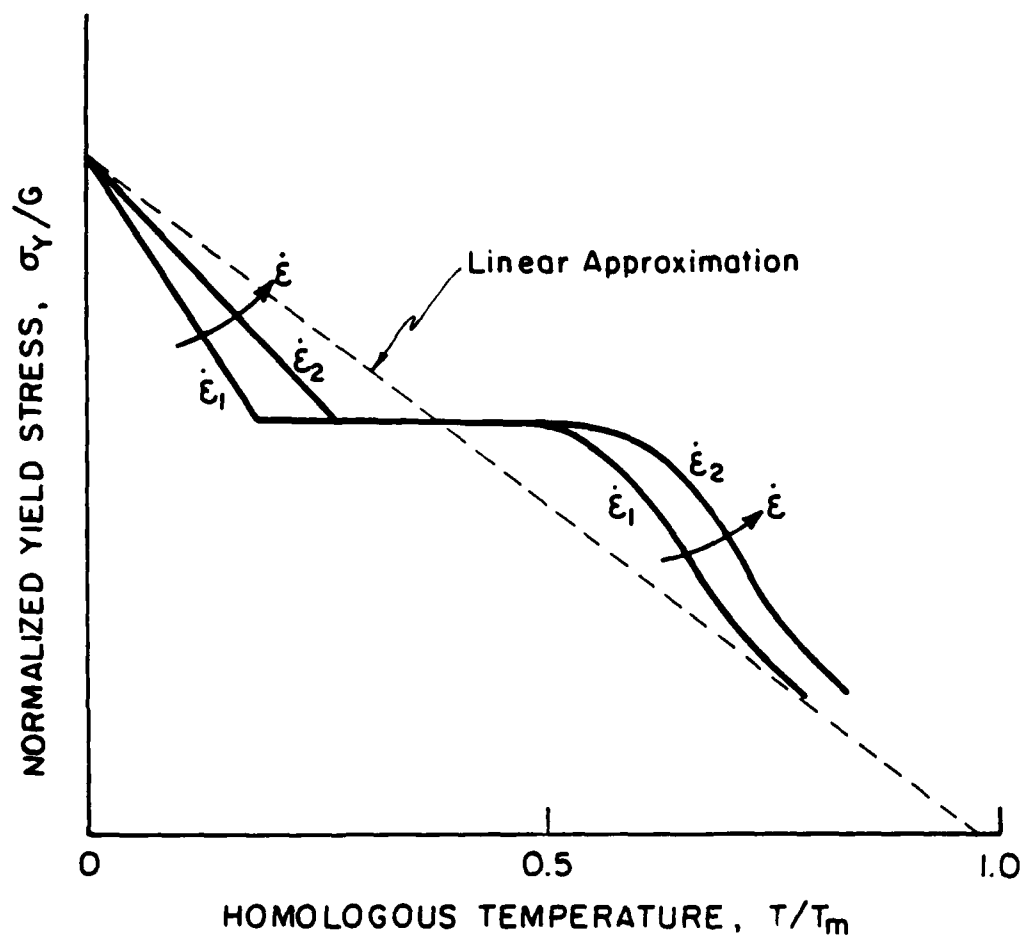
XBL 8312 - 6677

Fig. 6



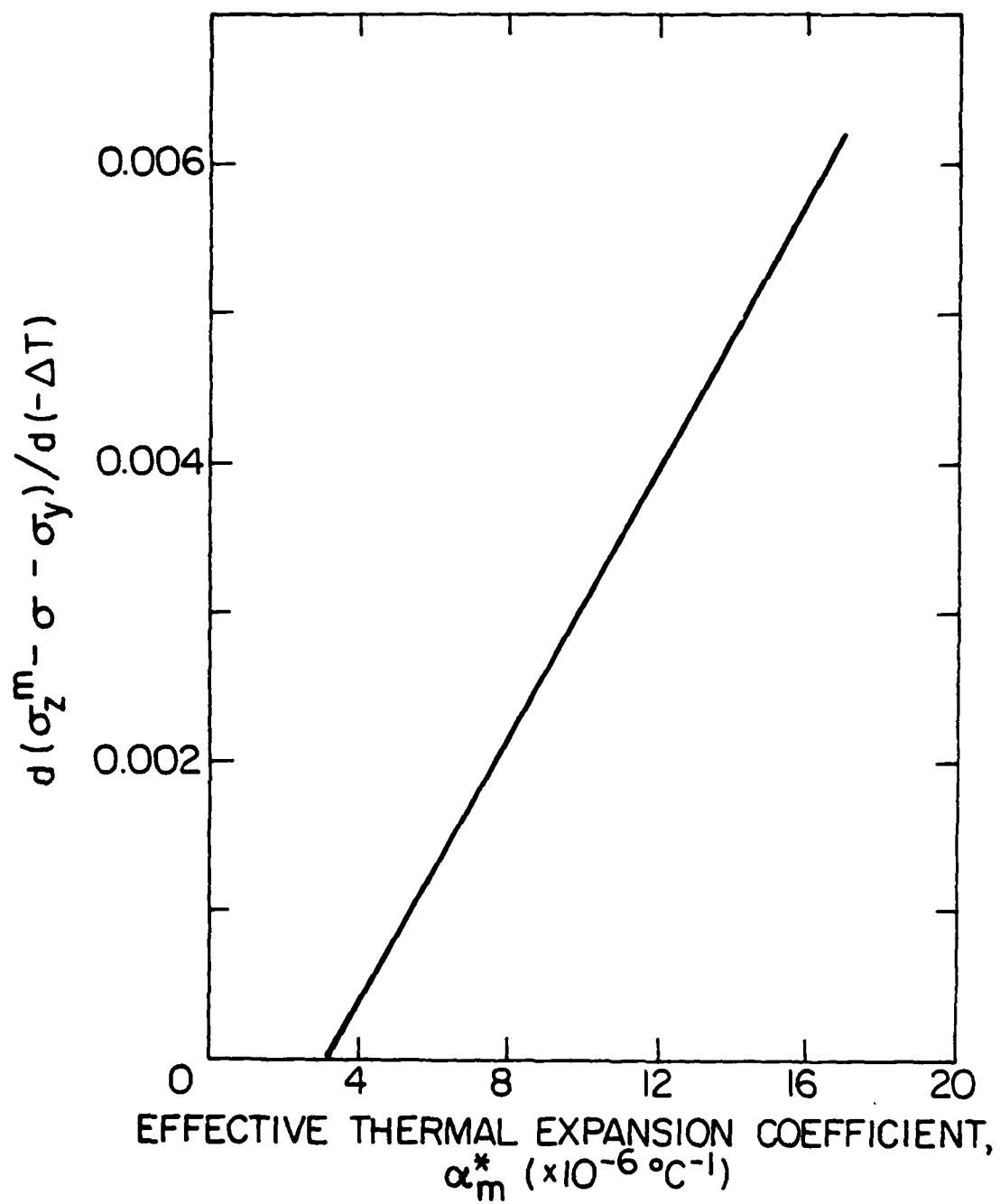
XBL 84 2-6608

Fig. 7



XBL 841-6505

Fig. 8



XBL 842-6609

Fig. 9

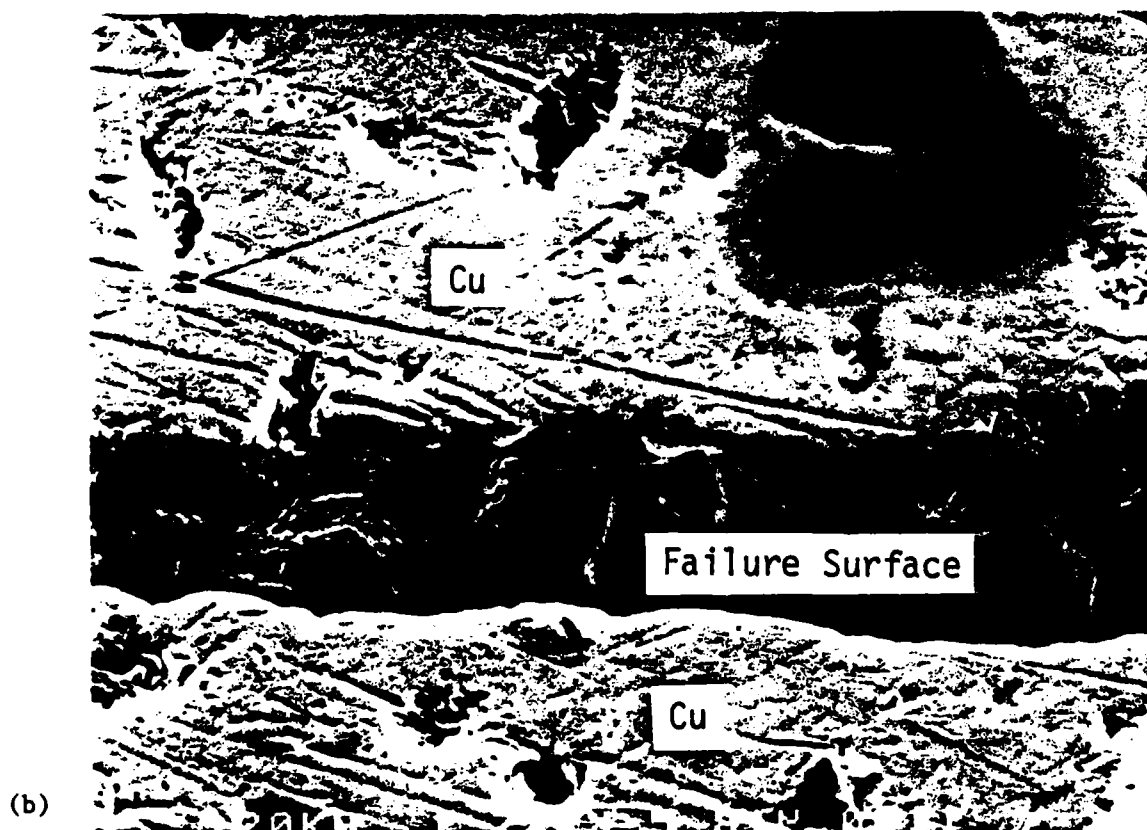
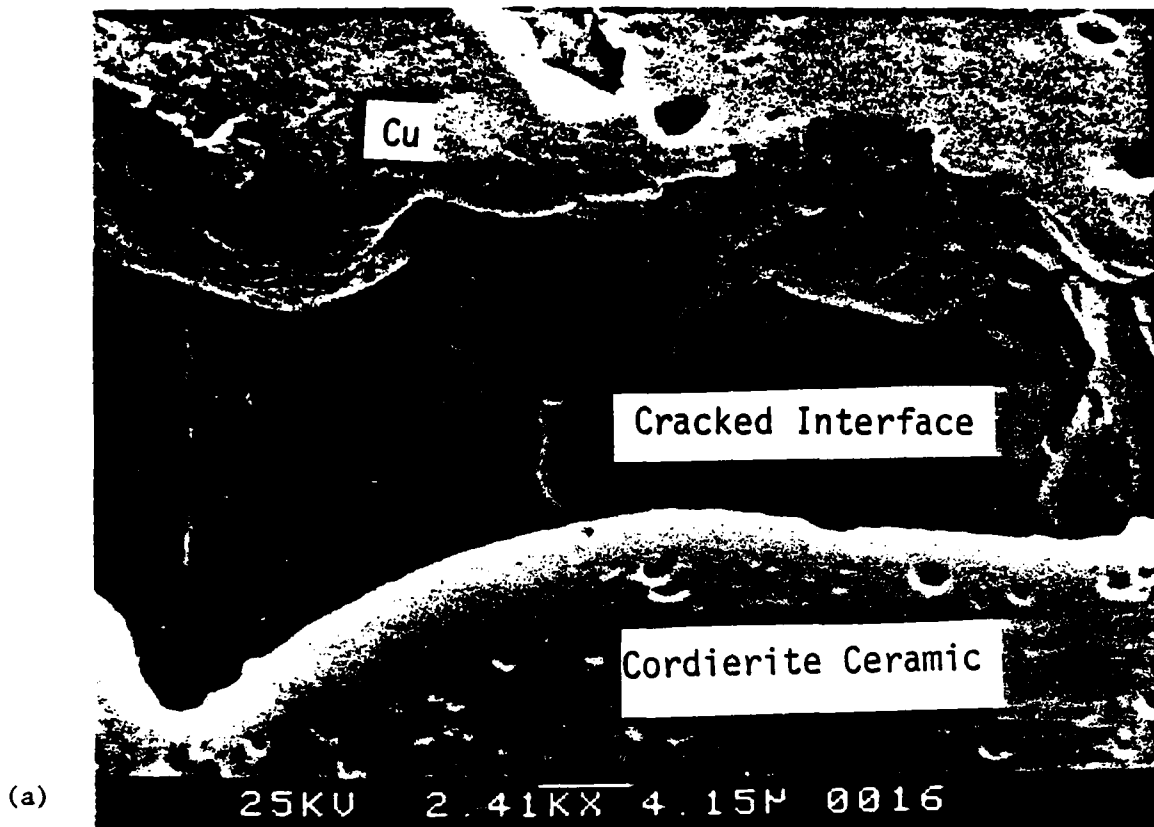
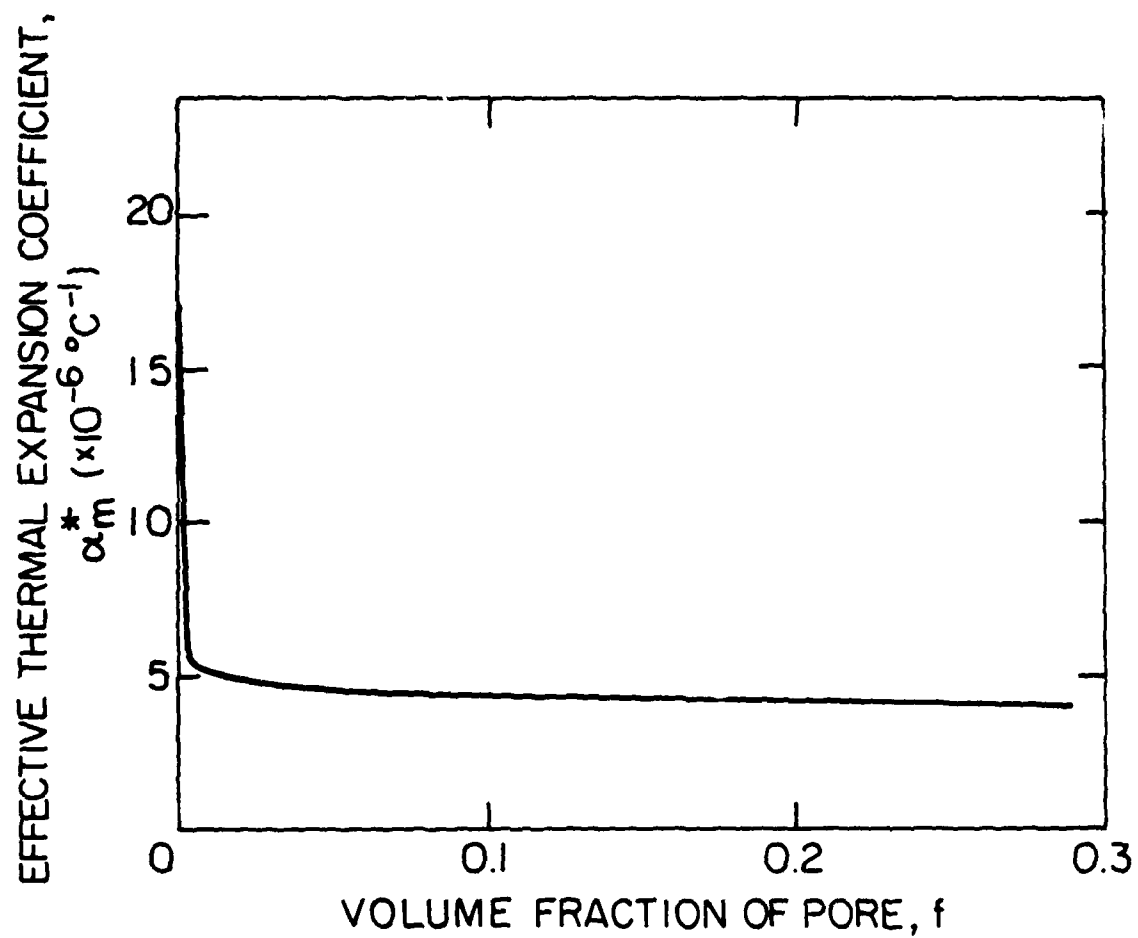
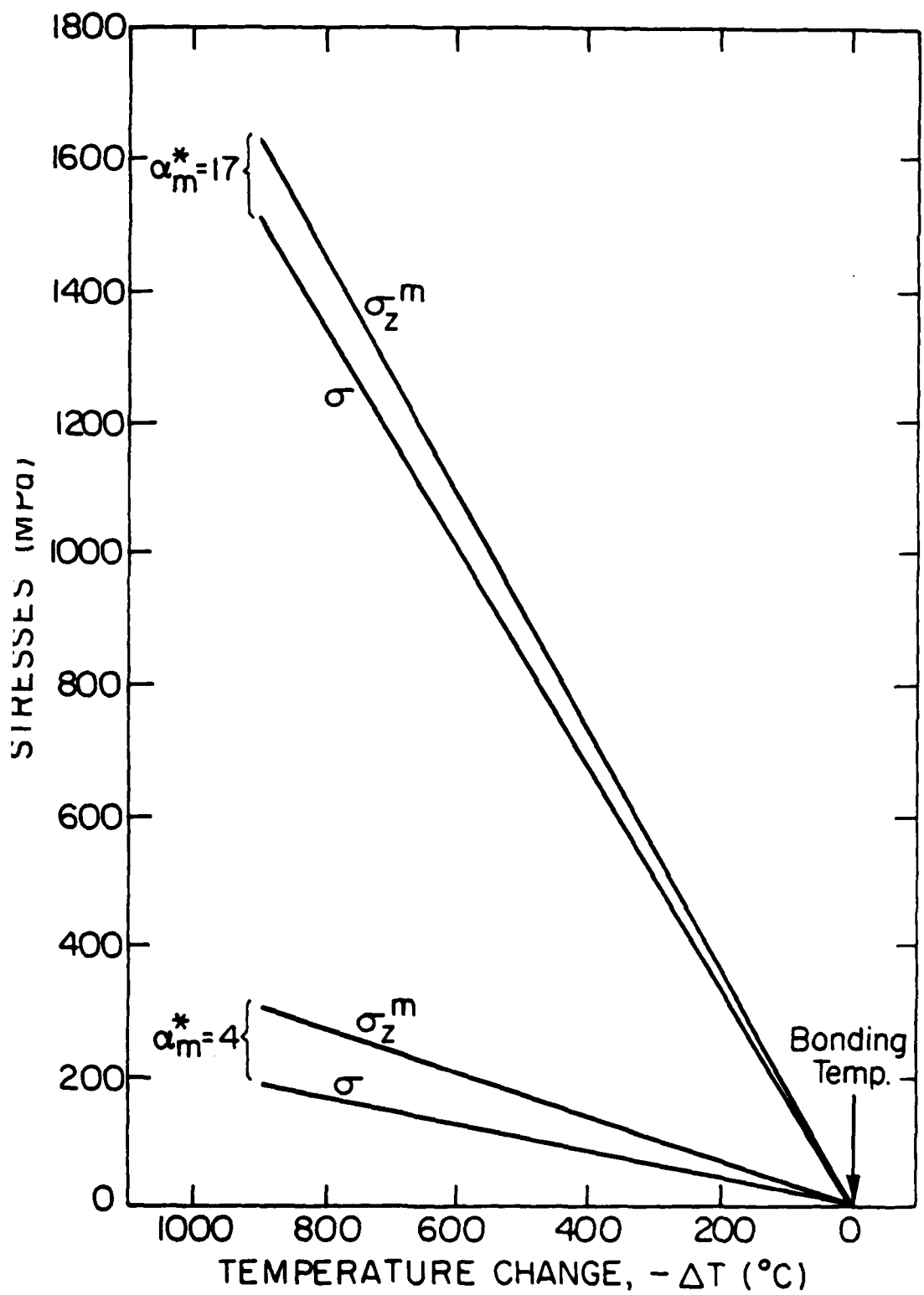


Fig. 10



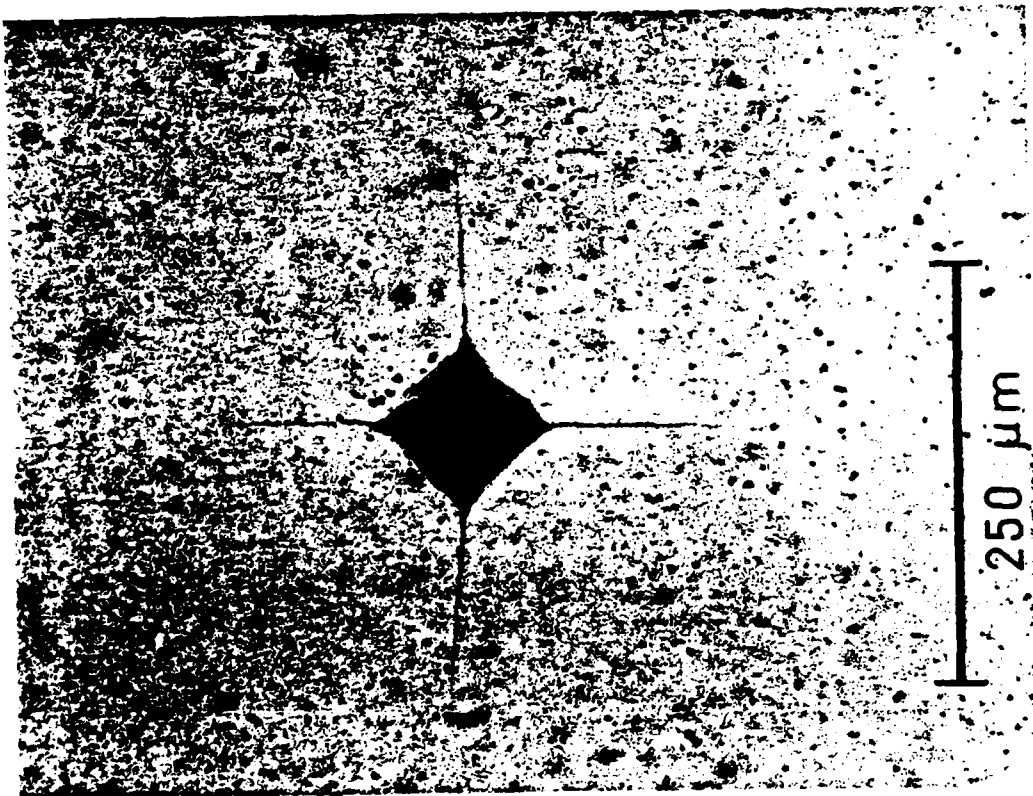
XBL 842-6610

Fig. 11

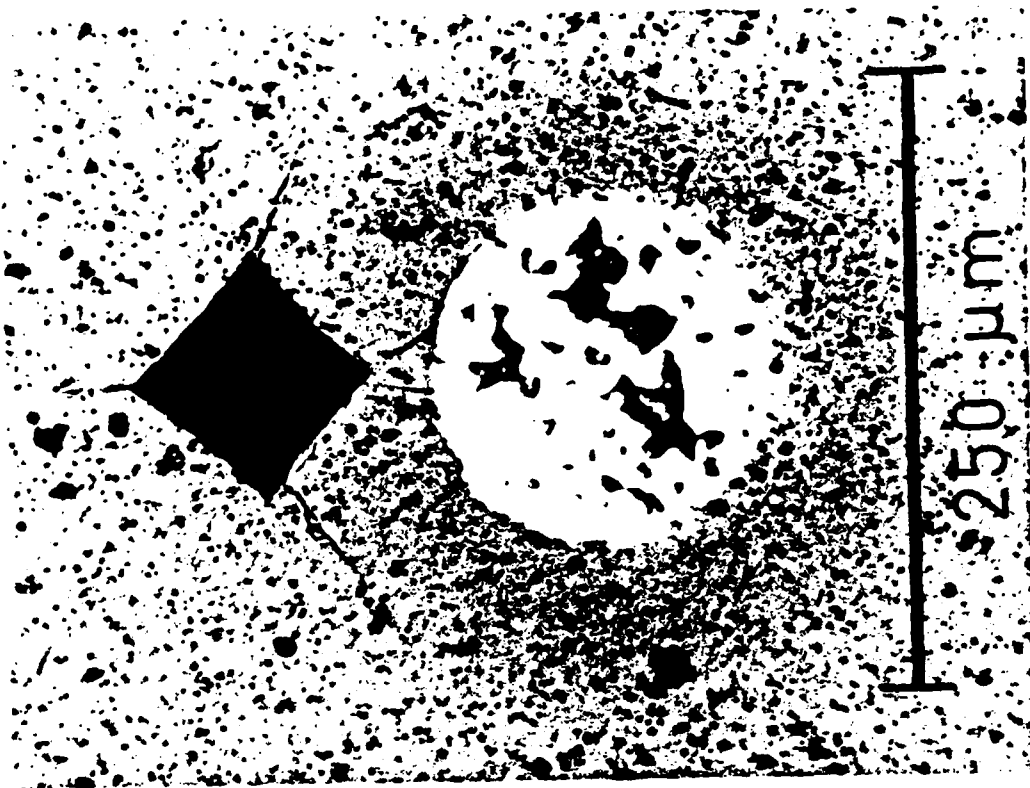


XBL 842 - 6611

Fig. 12



(a)



(b)

Fig. 13

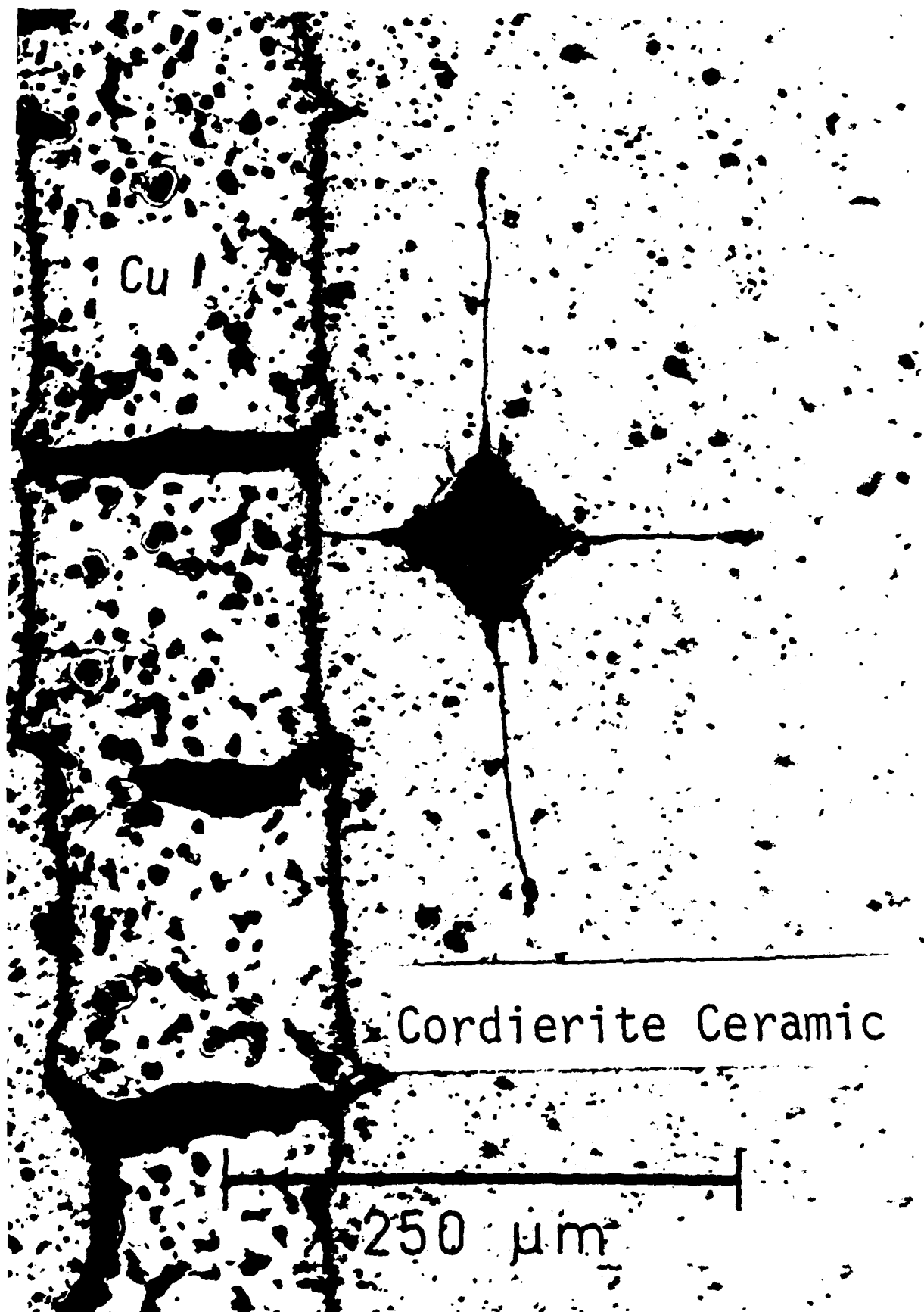
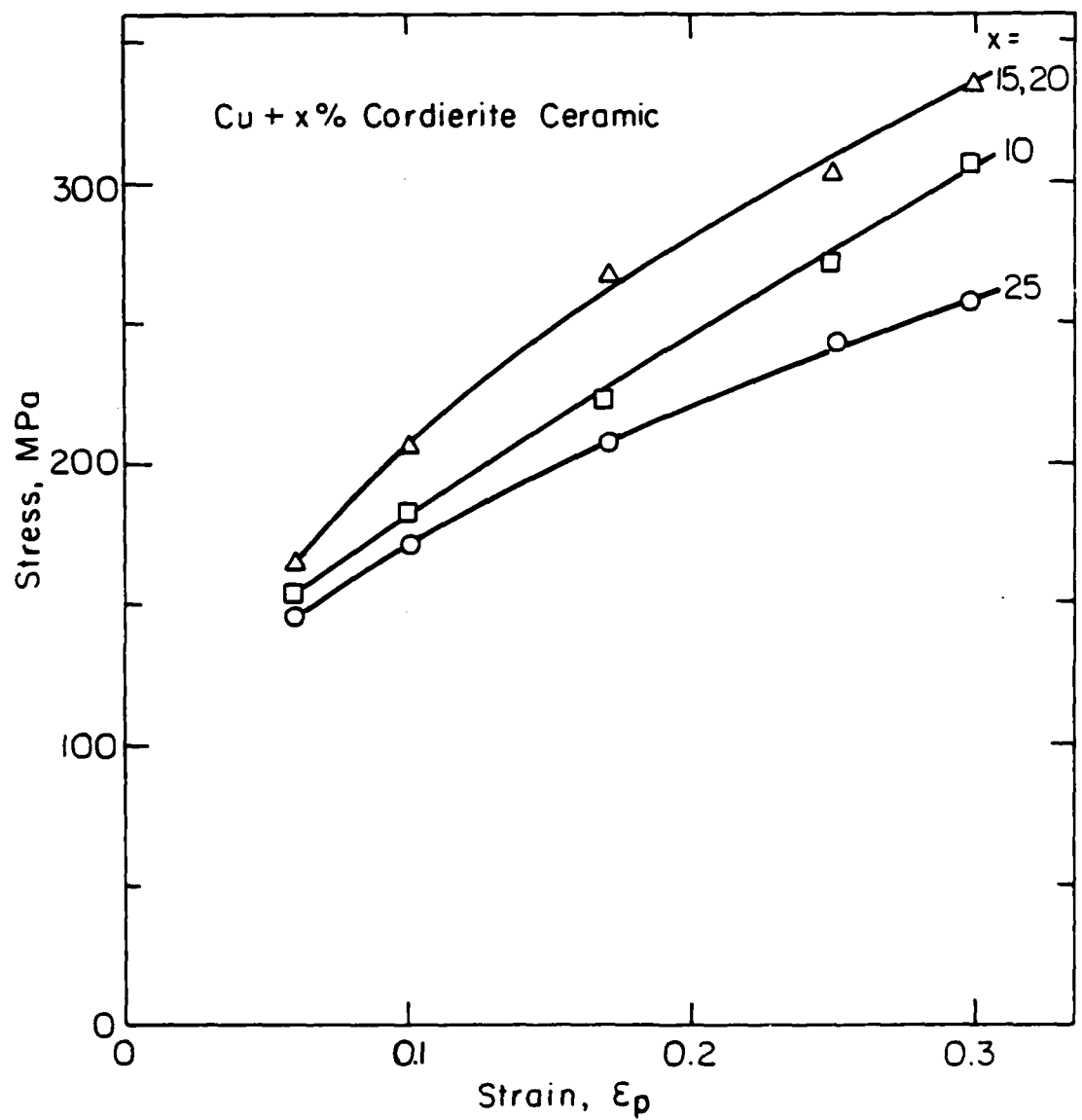


Fig. 13(c)



XBL6312-6678

Fig. 14

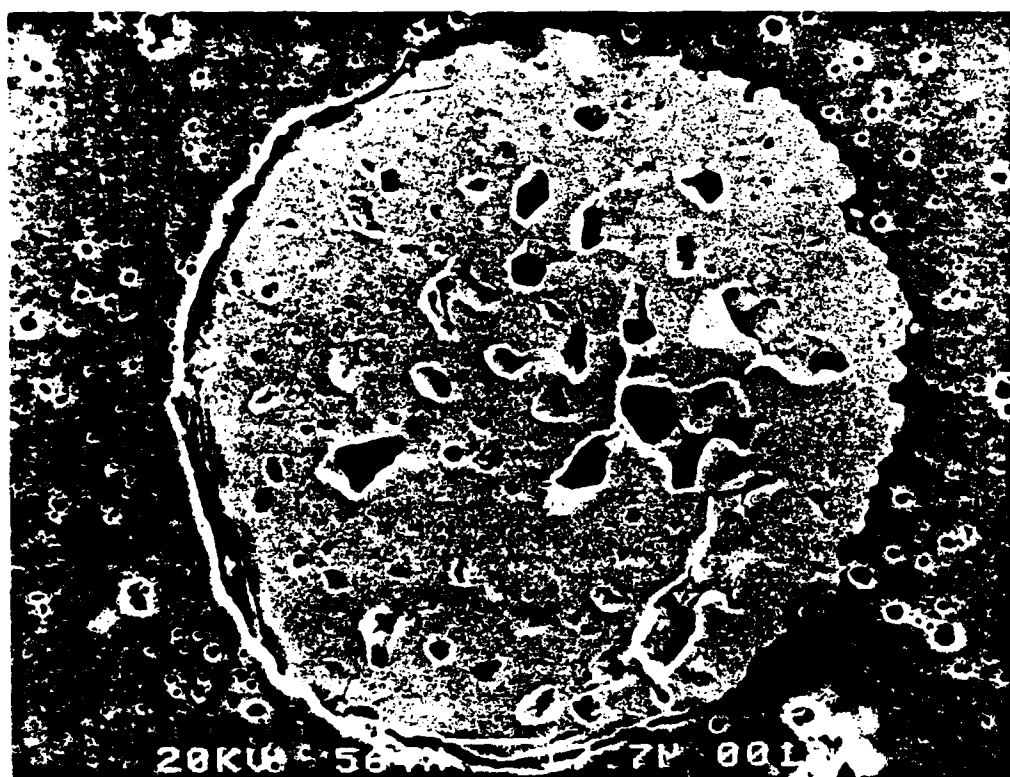
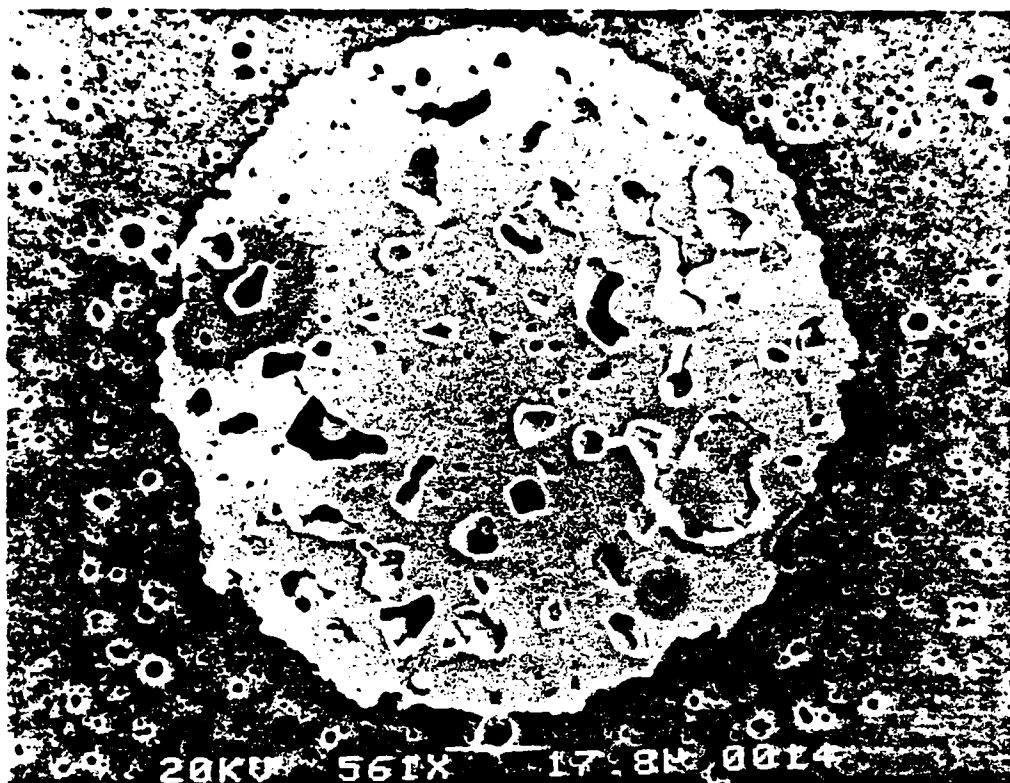


Fig. 15



Fig. 15(c)

AD-A151 978

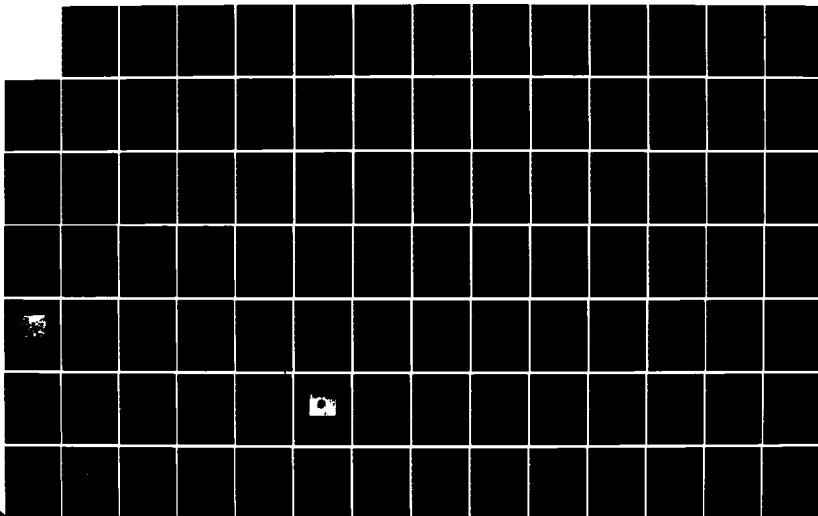
MECHANICAL ASPECTS OF INTERFACES AND SURFACES IN
CERAMIC CONTAINING SYSTEMS(U) CALIFORNIA UNIV BERKELEY
DEPT OF MATERIALS SCIENCE AND MINERA.

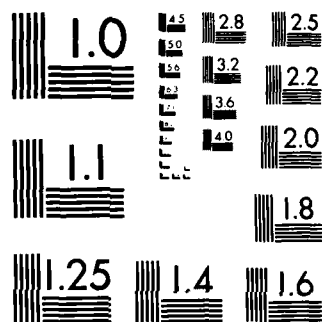
4/5

UNCLASSIFIED

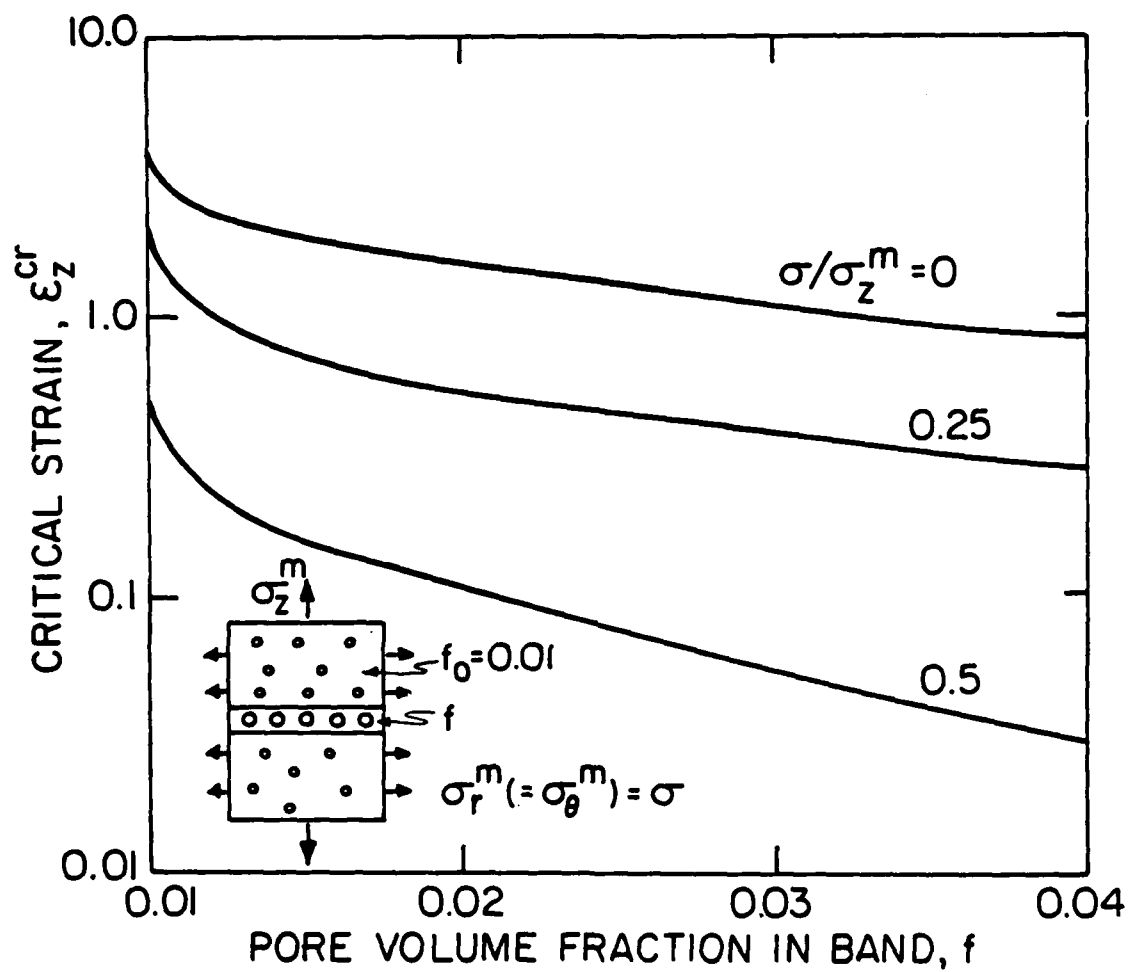
A G EVANS ET AL. 14 DEC 84 N00014-81-K-0362 F/G 20/11

NL





MICROCOPY RESOLUTION TEST CHART
NATIONAL BUREAU OF STANDARDS-1963-A



XBL 482-6612

Fig. 16

CHAPTER VIII

MECHANISMS OF TOUGHENING
IN RUBBER TOUGHENED POLYMERS

A. G. Evans, Z. B. Ahmad, D. G. Gilbert and P. W. R. Beaumont

MECHANISMS OF TOUGHENING IN
RUBBER TOUGHENED POLYMERS

A.G. Evans*, Z.B. Ahmad,
D.G. Gilbert and P.W.R. Beaumont

CUED/C/MATS/TR 108 (September 1984)

*University of California, Berkeley
Department of Materials Science

ABSTRACT

A method is presented whereby various potential contributions to the toughness of rubber toughened polymers can be quantified. The tendencies toward either synergism or additivity amongst mechanisms is emphasised for rubber stretching, cavitation and shear banding. The method reveals that specific experimental measurements of microstructural changes near a crack tip, in the crack wake, are needed to unequivocally ascertain the dominant toughening mechanisms.

1. INTRODUCTION

Substantial enhancement of toughness can be achieved by dispersing rubber precipitates within a polymer matrix. Various mechanisms have been proposed to account for this phenomenon. These include crack bridging by rubber precipitates intersected by the crack¹ and enhanced plastic deformation of the polymer matrix, induced by the precipitates². However, the manner in which the mechanisms combine, to determine the full toughness, has not been afforded detailed consideration. The intent of this article is to provide a rational basis for considering mechanism combinations.

The essential background for considering toughness is based on an appreciation that two general categories of toughening mechanism exist³. The first category includes processes that occur along the crack plane, such as crack bridging¹. These mechanisms exert a direct influence on the stress intensity factor, K , and on the local crack propagation resistance, K_C^I , of the material. The second category influences toughness by means of events occurring in a process zone^{3,4,5}, of width h (Fig.1), such as a phase transformation, plastic hole growth, etc. Mechanisms of this type result in a toughness that typically scales with the width of the process zone. Specifically, the enhancement in the critical J generally increases in direct proportion with the zone width³⁻⁵ (cf. eqns.25 and 31),

$$\Delta J_C = \beta h, \quad (1)$$

where β is a coefficient that depends on the characteristics of the non-linear mechanism that operates in the process zone. The process zone width, in turn, depends upon the magnitude of the net toughness, such that for plane strain conditions^{4,5},

$$h = \frac{E J_c g}{2 \sigma_y} , \quad (2)$$

where σ_y is the yield strength, E is Young's modulus and $g \approx 1/4$.
Noting that,

$$J_c = J_0 + \Delta J_c , \quad (3)$$

where J_0 is the fundamental toughness in the absence of a process zone, eqns. (1), (2) and (3) can be combined to give,

$$J_c = J_0 / [1 - \beta E / 4 \sigma_y^2] . \quad (4)$$

The final toughness J_c thus scales with the fundamental toughness, J_0 . Process zone effects are thus *multiplicative* and not additive. The importance of process zone scaling to the toughening of rubber toughened polymers is amply demonstrated in subsequent sections. Other examples of this type of toughness scaling in the literature include transformation toughening^{4,5} and various embrittlement phenomena.

2. GENERAL METHOD OF TOUGHENING ANALYSIS

The change in toughness induced by a specific mechanism can be formally treated by considering the energy changes that occur in each volume element of material as the crack translates through the system^{3,5,6}. For this purpose it is convenient to commence with a small element $dx dy$ of unit width that translates along a plane parallel to the crack plane, distance y from that plane (Fig.1). The energy change experienced by that element as it translates from $x = \infty$ to $x = -\infty$ dictates the contribution of the strip dy to the toughness. Specifically, the change in toughness due to energy changes in the strip is given by^{3,5,6},

$$dJ_c = U(y)dy, \quad (5a)$$

where $U(y)$ is the energy increase per unit area of plane associated with the transfer of the element dx from a region well in front of the crack to a region in the remote crack wake. Integration of this energy over the process zone width then gives the total change in toughness,

$$\Delta J_c = 2 \int_0^h U(y) dy. \quad (5b)$$

Furthermore, J associated with the applied loads, J_∞ , is related to J at the crack tip, J_ℓ , by,

$$J_\infty = J_\ell + 2 \int_0^h U(y) dy, \quad (6)$$

where

$$\Delta J = J_\infty - J_\ell.$$

Hence, the net toughness can be ascertained by equating J_ℓ to the fundamental toughness J_0 (i.e. the crack propagation resistance of the material at the crack tip) giving,

$$J_c = J_0 + 2 \int_0^h U(y) dy. \quad (7)$$

The energy density $U(y)$, in general, consists of contributions from residual strains in the wake (e.g. transformation^{4,5} or microcrack⁷ toughening), plastic work expended in the crack tip process zone and the energy of free surfaces (disbonds or microcracks) created by the crack tip stresses. The quantity $U(y)$ can be determined either from explicit thermodynamic considerations^{3,6} or from knowledge of the stress/strain curve of the material that translates through the process zone^{3,5}. The latter approach is generally more direct and less susceptible to ambiguity.

3. TOUGHENING MECHANISMS

The toughening mechanisms considered in this paper are based on several experimental observations of crack propagation in rubber toughened polymers which produce the effects summarised in Fig.2. Firstly, crack growth is generally accompanied by the development of a zone of 'whitened' material over the crack surfaces.² This zone is considered to contain void space (that affects light adsorption) in the form of either debonded or cavitated rubber precipitates. The creation of voids requires that *dilatation* be occurring within this zone (Fig.2), resulting in a toughening process similar to the effects of dilatation in transformation and microcrack toughening^{5,7}. Secondly, the non-linear stress/strain curves obtained in these materials are indicative of macroscopic plasticity. Furthermore, observations of shear bands between rubber precipitates in deformed material suggests that the deformation occurs heterogeneously. The *shear* deformation (Fig.2) constitutes an additional source of toughness, analogous to toughening by mechanical twinning³.

Specific calculations of the dilatational and shear band toughening are conducted in the following section, subject to certain conjectures regarding these processes. Debonding or cavitation of the rubber precipitates are assumed to be initiated by plastic flow, as the precipitates enter the crack tip plastic zone (Fig.1). The net dilatation is then presumed to be plasticity dominated, similar to plastic hole growth in ductile metals⁸. The material within the 'whitened' zone is thus treated as a porous plastic continuum, as reflected in the strain/strain characteristics of the material.

This simplification is deemed reasonable provided that the zone contains a large number of holes and shear bands. The formation of shear bands is assumed to occur in orientations aligned with the maximum shear strain within the crack tip field, such that each shear band provides the maximum possible contribution to the toughness. Assessment of the utility of this premise requires careful study of the process zone shear band orientation at the *instant* the shear bands initiate. Evidently, certain features of the models will require modification should these conjectures prove invalid.

The *dilatational* toughening is associated with the plastic work expended by the volume expansion of the porous plastic zone. Specifically, as each volume element approaches the crack tip, a non-linear volumetric expansion occurs in response to the mean stress (Figs.1,3). Furthermore, elastic unloading of the element occurs in the wake, behind the crack tip, as dictated by the bulk modulus of the porous material (Fig.3). The resultant hysteresis in the stress/strain curve, integrated over each strip, dy , in the plastic zone (Fig.1) determines the change in J induced by the dilatation, as expressed by eqn.(7). (Alternatively, the change in J can be considered to derive from the constraint exerted on the expanding plastic zone, which induces closure tractions on the crack surfaces⁴.)

The *shear* band toughening is provided by the plastic work involved in creating the shear band strain. This is manifest as a non-linear increase in the net *shear* strain with crack tip shear stress, followed by elastic unloading in the wake, and again, integration of the stress-strain hysteresis over the shear band zone determines the change in J .

It is important to note that the deviatoric and dilatational energy densities are *strictly* additive⁹. Hence, the change in the

critical energy release rate determined for the plastic dilatation and shear band components of toughening can be added together to obtain the total toughness induced by the zone associated toughening phenomena,

$$\Delta J_c = \Delta J_{pd} + \Delta J_{sb} \quad (8)$$

Furthermore, rubber stretching across the crack surfaces, by those precipitates intercepted by the crack, constitutes an additional contribution to the toughness. Specifically, since the contribution to toughening from plastic dilatation and shear bands both scale with the process zone size they are multiplicative with rubber bridging across the crack surface. Consequently, a synergistic combination of processes seems to determine the rubber toughening of polymers. This synergism distinguishes the substantial toughening that occurs in the presence of rubber from the modest influence of holes.

4. ANALYSIS OF TOUGHENING

4.1 Rubber Stretching

The contribution of rubber stretching to toughness, as demonstrated by Kunz et al.¹, can be deduced by evaluating the work done in stretching the rubber particles to failure, per unit area of fracture surface. This work is dissipated in those precipitates *intercepted* by the crack, and thus yields a change in toughness given by,

$$\Delta J_{rs} = \bar{\mu} f \langle R \rangle (\lambda_f^2 + 2/\lambda_f - 3) \quad , \quad (9)$$

where λ_f is the extension of the rubber precipitates at failure, $\bar{\mu}$ is the shear modulus of the rubber and $\langle R \rangle$ is the mean radius of the precipitates. This toughness change simply superposes on the toughness J_0 governed by the growth of the crack front through the

matrix containing rubber precipitates. Regarding the rubber precipitates as impenetrable obstacles (a requirement for operation of the rubber stretching mechanisms), J_0 should be of the order¹⁰,

$$J_0 = J^*(1 + f^\alpha) \quad (10)$$

where J^* is the matrix toughness, f is the volume fraction of rubber precipitates and α is a coefficient. Hence, the total toughness in the presence of rubber stretching is,

$$J_{rs} = \bar{u}f \langle k \rangle (\lambda_f^2 + 2/\lambda_f - 3) + J^*(1 + f^\alpha) \quad (11)$$

4.2 Plastic Dilatation

i) The volume change

The debonding (or cavitation) of the rubber precipitates allows plastic dilatation of the matrix, within the plastic zone, similar to plastic hole growth in ductile metals. The volume increase dV is especially prominent in regions of high mean stress, σ_m . This is evident from the solution for the growth rate of an isolated hole, in a plastic continuum⁸,

$$dV/V = 0.84 d\epsilon \exp[3\sigma_m/2\sigma_e] \quad (12)$$

where σ_e and ϵ are the equivalent stress and equivalent plastic strain, respectively. The existence of appreciable mean stress near the crack plane suggests that significant dilatation occurs around debonded rubber precipitates within the plastic zone (Fig.4). This dilatation attains a maximum as the crack front extends beyond the precipitate (Fig.4) and is essentially retained (except for elastic unloading) in the wake of the crack. The associated dilatational plastic work constitutes a source of toughness, as described in section 3. It is noted here that dilatation is expected to be much

more prominent in the crack tip zone, where the mean stress is relatively large, than in uniaxial tension. This issue is discussed in more detail in section 5.

The expansion of the matrix around precipitates contained in a strip dy , distance y from the crack plane (Fig.1), is evidently determined by the crack tip stress and plastic strain fields. For a material with a macroscopic stress-strain law,

$$\epsilon = \epsilon_y (\sigma/\sigma_y)^n, \quad (13)$$

where ϵ_y is the uniaxial yield strain, σ_y is the uniaxial yield stress, and n is the work hardening exponent, the stress and strain fields near the crack tip^{11,12} are given by[†],

$$\begin{aligned} \sigma_{ij} &= \sigma_y \left[\frac{J}{\sigma_y \epsilon_y I_n r} \right]^{1/(n+1)} \tilde{\sigma}_{ij}(\theta, n) \\ \epsilon_{ij} &= \epsilon_y \left[\frac{J}{\sigma_y \epsilon_y I_n r} \right]^{n/(n+1)} \tilde{\epsilon}_{ij}(\theta, n) \end{aligned} \quad (14)$$

where (r, θ) are the polar coordinates with respect to the crack tip, $\tilde{\sigma}_{ij}(\theta)$ and $\tilde{\epsilon}_{ij}(\theta)$ are dimensionless functions (see Fig.5) and I_n is a numerical coefficient ($I_n \approx 10\sqrt{0.13 + 1/n} - 4.8/n$). These stress and strain fields may be used in conjunction with eqn.(12) to predict the plastic dilatation of an isolated hole as a crack extends past the hole.

Hole growth is assumed to initiate at the elastic/plastic boundary where the plastic flow causes immediate debonding (or cavitation) of the rubber precipitate. For this case, the expansion of the hole is obtained from eqn.(12) as,

[†] When the plasticity is inhomogeneous, these stress and strain fields should be regarded as average values within near crack tip volume elements, viz. when the plastic strain is confined to shear bands, local variations in stress often occur around the bands.

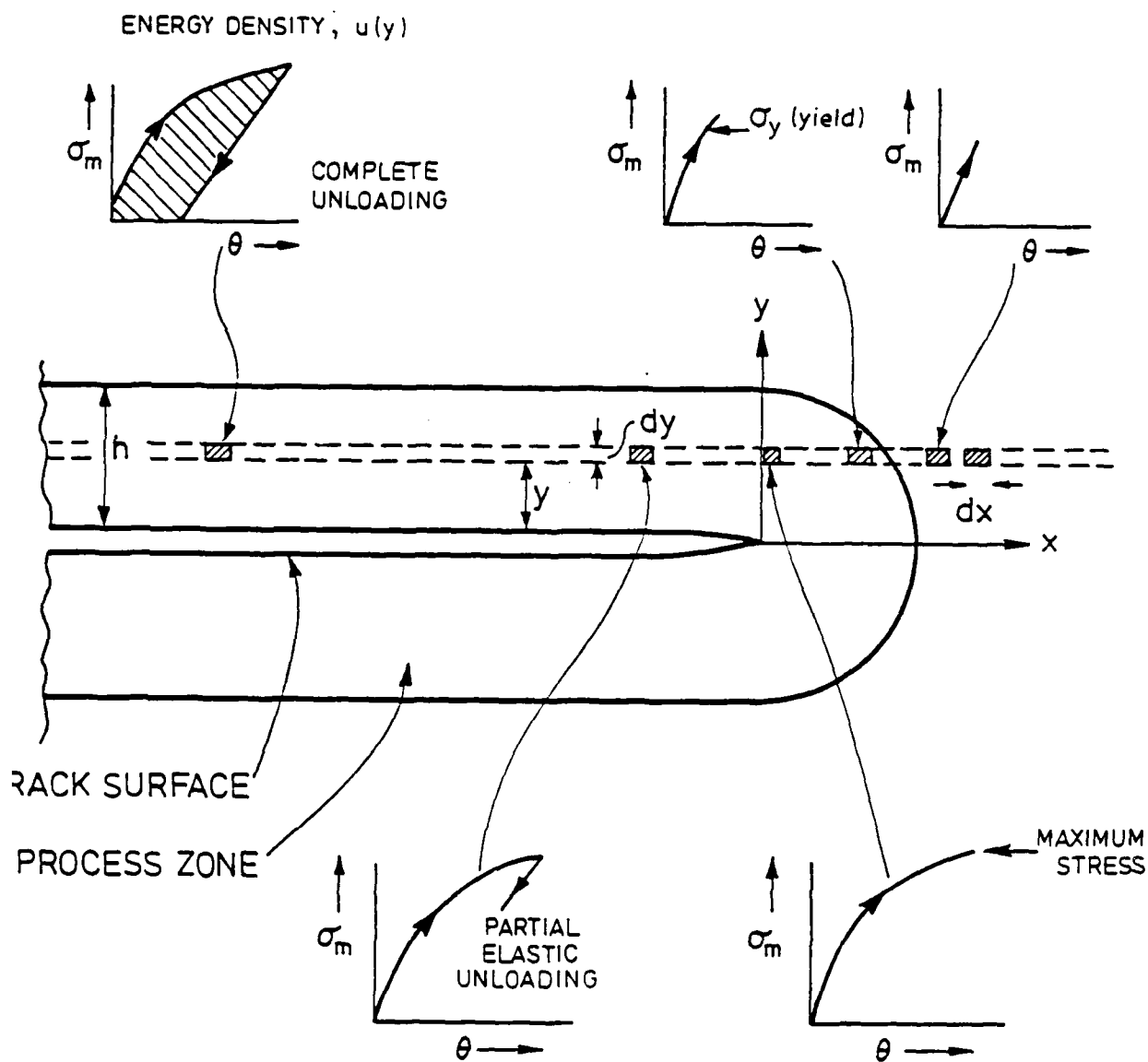


Fig. 1

FIGURE CAPTIONS

- Fig.1 A schematic illustrating the process zone and the stress/strain characteristics of an element $dx dy$ as it traverses across a strip dy within the zone.
- Fig.2 A schematic illustrating the proposed modes of deformation in rubber toughened polymers. Shear bands between precipitates provide a net shear strain to each loaded element, while debonding (perhaps initiated by the shear bands) results in dilatation. Both the shear and the dilatation contribute additively to the toughness.
- Fig.3 The variation in mean stress with volumetric strain for a material subject to plastic hole growth.
- Fig.4 A schematic illustrating the dilatation of a strip dy , due to plastic hole growth around debonded precipitates, as the strip passes through the crack tip process zone.
- Fig.5 A plot of the dimensionless crack tip field parameters $\tilde{\sigma}_{rr}$, $\tilde{\sigma}_{\theta\theta}$ and $\tilde{\sigma}_e$ for a material with a hardening exponent, $n = 5, 10, 20$ and 100 .
- Fig.6 The variation in hole volume V/V_0 with distance into the plastic zone, x/y , for various values of the dimensionless distance $\epsilon_y \sigma_y / J$: ϵ_y is the yield strain: $n = 10$.
- Fig.7 Trends in the peak hole volume, \hat{V}/V and in energy density $U(y)$ with normalised distance from the crack plane, $J/\sigma_y \epsilon_y$: $n = 10$.

TABLE II

Hole volume and energy density parameters

| Work hardening coefficient, n | ψ | q | ϕ | z |
|----------------------------------|--------|-----|--------|-----|
| 5 | 0.008 | 2.4 | 0.0009 | 3.3 |
| 10 | 0.01 | 2.3 | 0.0014 | 3.0 |
| 20 | 0.05 | 2.0 | 0.014 | 2.4 |
| 100 | 0.22 | 1.6 | 0.10 | 1.9 |

TABLE I

The values of \hat{x}, y at the peak hole volume

| <u>\hat{x}/y</u> | <u>n</u> |
|-------------------------------|-----------------------|
| 0.6 | 5 |
| 0.43 | 10 |
| 0.25 | 20 |
| 0.22 | 100 |

REFERENCES

1. S. Kunz, P.W.R. Beaumont and M.F. Ashby, Jnl. Mater. Sci., 15, (1980) 1109
2. A.J. Kinloch, S. J. Shaw, D.A. Tod and D.L. Hunston, Polymer, 24, (1983) 1341
3. A.G. Evans, Advances in Ceramics, in press
4. R.M. McMeeking and A.G. Evans, Jnl. Amer. Ceram. Soc., 65, (1982) 242
5. B. Budiansky, J. Hutchinson and J. Lambrapolous, Intl. Jnl. Solids and Structures, 19, (1983) 337
6. A.G. Evans and A.H. Heuer, Jnl. Amer. Ceram. Soc., 63 (1980) 241
7. A.G. Evans and K.T. Faber, Jnl. Amer. Ceram. Soc., 67 (1984) 256
8. J.R. Rice and D.M. Tracey, J. Mech. Phys. Solids, Vol. 17, (1969) 201
9. J.D. Eshelby, Proc. Roy. Soc. A241 (1957) 376
10. D.J. Green, Jnl. Amer. Ceram. Soc. 62 (1983) C4
11. J.R. Rice and G.F. Rosengren, J. Mech. Phys. Solids. 16 (1968) 1
12. J.W. Hutchinson, J. Mech. Phys. Solids, 16 (1968) 13
13. C.B. Bucknall, I.K. Partridge and M.U. Ward, Jnl. Mater. Sci., 19, (1984) 2064
14. C.J. Hooley, D.R. Moore, M. Whale and M.J. Williams, Plastics and Rubber Processing and Application, 1, (1981) 345
15. R.O. Ritchie, W.L. Server and R.A. Wulfoert, Met. Trans. 10A (1979) 1557
16. A.J. Kinloch (Private Communication)

applied herein to plastic dilatation (and elsewhere⁷ to micro-cracking). However, for this purpose, a basic relation between the mean stress and the volumetric strain is required, analogous to the expression (eqn.(12)) used to describe plastic hole growth.

6. CONCLUDING REMARKS

The analysis presented in this article provides a quantitative basis for assessing trends in toughness in rubber toughened polymers. However, comparison with experimental data is premature since many of the requisite microstructural parameters have not been independently measured. Further understanding of this phenomenon can be achieved, based on the concepts introduced herein, by measuring parameters such as the dilatation under triaxial tension, the shear band density in the process zone wake and the zone wake thickness. Such measurements can then be used in conjunction with eqns.(25) and (31) to provide a critical evaluation of the most important contributions to the toughness, for each material system.

ACKNOWLEDGEMENTS

One of us (A.G.E.) acknowledges the support of the Science and Engineering Research Council of Great Britain in the form of a Senior Visiting Scientist Fellowship. Z.B.A. is the recipient of the Cambridge Commonwealth Trust-Sime Darby Scholarship. D.G.G. is the recipient of an SERC research studentship.

zone wake is only a prerequisite for toughening when the crack tip advance mechanism remains invariant.

The expected role of dilatation in the toughening of rubber toughened polymers also requires further consideration. Uniaxial tests on several rubber toughened systems indicate that, in the absence of crazing, the dilatation is very small and essentially all of the deformation occurs by shear^{13,14}. However, it should not be inferred from these measurements that dilatation does not occur in the plastic zone near the crack tip, where the mean stress is substantially larger. In fact, the behaviour of ductile metals can be used as an effective analogy, to illustrate the importance of the mean stress. In uniaxial tests, significant void initiation and growth only begins after necking. Furthermore, the voids are confined to the necked region, where a triaxial state of stress develops. Hence, the dilatation is limited to the neck and is difficult to measure. By contrast, substantial void nucleation and growth occurs in the plastic zone around a crack, leading to the widely observed void coalescence (ductile dimple) mode of failure. Consequently, failure strains pertinent to the crack tip region can only be obtained by comparison with macroscopic data obtained in triaxial tests: uniaxial failure strain data substantially overestimate the peak strains experienced at the crack tip¹⁵. We conclude, therefore, that the role of dilatation in the toughening of rubber toughened polymers can only be directly assessed either from observations of debonding/cavitation¹⁶ in the crack tip region or from triaxial deformation experiments.

Finally it may be important to note that the considerable dilatation that accompanies crazing in certain systems (e.g. in HIPS) can be incorporated into the general dilatational toughening scheme,

between holes are quite restrictive. However, incorporating these effects into the analysis would require quite complex numerical computations. The assumption of homogeneous plasticity is not considered to be such a serious limitation, provided that the plastic zone is large enough (e.g. > 10 precipitate spacings) to permit the material behaviour within the zone to be adequately characterised by a macroscopic stress/strain law (eqn.(13)). Despite the above restrictions, it is hoped that the analysis provides physical insights regarding the dilatational component of toughening, capable of guiding further research on this topic.

Another feature of the analysis that requires elaboration is the 'steady-state' nature of the plastic dilatation and shear band toughening. The derived toughnesses *only* apply when the process zone extends appreciably into the crack wake^{4,5}. A loading zone contained ahead of the crack tip provides no toughening^{3,4,7}. The measured toughness thus depends on the manner in which the initial crack is introduced. Generally, the method of introduction of the sharp precrack (e.g. tapping with a razor blade) induces a process zone wake because the crack forms subject to $J = J_c$. Steady-state values of J_c then apply. However, cracks introduced by fatigue would not exhibit a fully developed wake. Subsequent propagation in the J_c test is then characterised by a J_R -curve^{4,7}, and the measured toughness is dictated by the instability length, as governed by the slope of the J_R -curve and the specimen geometry.

The preceding remarks should not be misconstrued to imply that a zone wake is always needed to induce toughness. Effects such as plastic crack tip blunting, which induce a change in the actual *mechanism* of crack tip advance (e.g. from brittle rupture to hole coalescence), provide toughness without a plastic zone wake. The

$$J_{sb} = \frac{J_o (1-f_b)}{1 - 2b\gamma_b f_b E/\tau_c} \quad (34)$$

The reduction due to the weakening effect of the shear bands in the crack plane thus appears in the numerator and the toughening due to the bands in the process zone appears in the denominator.

5. DISCUSSION

The framework for considering the toughness of rubber toughened polymers presented in the preceding sections is quite general and can accommodate any suggested mechanism. However, quantifying a proposed mechanism requires careful experimental evaluation of various microstructural features associated with that mechanism. Some of the important microstructural parameters have been elucidated for three prominent toughening mechanisms: rubber stretching, plastic dilation due to debonding or cavitation of the rubber particles, and shear banding between rubber particles. Insufficient data are available at present to permit confident statements regarding the dominant mechanisms. Furthermore, in view of the synergistic nature of toughening by rubber stretching, when occurring in conjunction with the other mechanisms, it seems unlikely that a single mechanism should be dominant.

The contribution to the toughening by plastic dilatation has been afforded primary attention in the specific analysis of toughening mechanisms, because the mechanism can be the most extensively analysed with available knowledge. Certain conjectures have still been required to obtain a final result and hence, some caution should be exercised before applying these results in a fully quantitative sense. In particular, neglect of the influence of the holes on the plastic crack tip stress field and of interactions

contains shear bands. Then, with the further restriction that no further deformation can occur within the band (after the initial formation), the change in toughness due to the shear bands becomes,

$$\Delta J_{sb} = 2\tau_c \int_0^h \gamma_b(y) f_b(y) dy \quad (30)$$

where h is the width of the shear band zone. Hence, even for this relatively restricted case, experimental details regarding $\gamma_b(y)$, $f_b(y)$, h and τ_c are needed before the role of this toughening mechanism can be assessed. Such experimental studies are strongly urged.

It is also noted that shear bands formed within the plane of the crack tend to reduce the local crack propagation resistance of the matrix, by weakening the material within the band. Hence, the increase in toughness represented by eqn.(30) will be partially offset by a reduced fundamental toughness. The net trend in toughness is illustrated for the simple case where γ_b and f_b are independent of y , whereupon eqn.(30) becomes,

$$\Delta J_{sb} = 2\tau_c \gamma_b f_b h \quad (31)$$

Noting that h is related to the critical stress (cf. eqn.(24)) by^{4,5}

$$h = \frac{bJ_{sb}E}{\tau_c^2} \quad (32)$$

where E is Young's modulus and b is a coefficient ≈ 0.2 , the change in toughness reduces to,

$$\Delta J_{sb} = \frac{2b\gamma_b f_b J_{sb} E}{\tau_c} \quad (33)$$

Hence, supposing that the fundamental toughness J_0 is reduced, due to the shear bands, to $\sim J_0(1-f_b)$ the net toughness becomes,

where J_0 is, again, the fundamental toughness. Consequently, if plastic dilatation and *rubber stretching* operate simultaneously, eqns. (11) and (26) may be combined to give a net toughness, J_c ,

$$J_c = \frac{J_0 [\mu f \langle R \rangle (\lambda_f^2 + 2/\lambda_f - 3) + J^* (1+f^\alpha)]}{(1-\Omega f)} \quad (27)$$

The synergistic effects of dilatation and stretching are thus evident by virtue of their emergence as the numerator and denominator of eqn. (27) respectively.

By contrast, the toughening in a *porous polymer* without rubber precipitates is appreciably smaller, because the pores degrade the fundamental toughness, by a factor⁷ of $\sim (1-f)$. The net toughness is thus,

$$J_c = \frac{J^* (1-f)}{(1-\Omega f)} \quad (28)$$

4.3 Shear Bands

An individual shear band formed between bonded or unbonded rubber precipitates, contained in a volume element dV , experiences a net shear strain γ_b . This strain occurs at some critical value of the shear stress, τ_c , imposed on the element boundaries. A zone of shear bands thus develops around the crack and the net energy change associated with shear band formation may induce toughening. The toughening can be deduced subject to the proviso that the shear band strain orients with the crack tip shear strain at the instant of formation, so that the work done on the element containing the shear band, as it forms, is simply,

$$dW = \tau_c \gamma_b f_b dV \quad (29)$$

where f_b is the volume fraction of material within the element that

$$U(y) = \phi f \epsilon_y^p \sigma_y^p \left(\frac{J}{\epsilon_y^p \sigma_y^p} \right)^z \quad (22)$$

where ϕ and z are coefficients that depend only on n (Table II).

The change in toughness, deduced from eqn. (7), is thus,

$$\begin{aligned} \Delta J_{pd} &= 2\phi f \sigma_y^p \epsilon_y^p \left[\frac{J_{pd}}{\sigma_y^p \epsilon_y^p} \right]^z \int_l^h y^{-z} dy \\ &= \frac{2\phi f \sigma_y^p \epsilon_y^p}{(1-z)} \left[\frac{J_{pd}}{\sigma_y^p \epsilon_y^p} \right]^z (h^{1-z} - l^{1-z}) \end{aligned} \quad (23)$$

where h is the plastic zone width and l is the precipitate spacing. However, h is related to J by¹¹

$$h = g(n) J_{pd} / \epsilon_y^p \sigma_y^p \quad (24)$$

where $g(n)$ is a coefficient of order $1/4$, determined by n ¹¹.

The change in toughness thus becomes, for $z > 1$ (Table I),

$$\begin{aligned} \Delta J_{pd} &= \frac{2\phi f J_{pd}}{(z-1)g^{z-1}} \left(\frac{h}{l} \right)^{z-1} \left[1 - \left(\frac{l}{h} \right)^{z-1} \right] \\ &= \Omega f J_{pd} \end{aligned} \quad (25)$$

Recall that the quantities ϕ , g and z are determined only by the work hardening coefficient, whereas h depends on the yield strength (eqn. 24). Thus, the toughness appears to depend both on the yield strength of the system and the work hardening coefficient. However, incorporation of interaction effects between voids and of the effect of the voids on the stress field within the plastic zone will undoubtedly modify the predicted dependence on σ_y .

The change in toughness is related to the net toughness by

$$\begin{aligned} J_{pd} &= J_o + \Delta J_{pd} \\ &= J_o / (1 - \Omega f) \end{aligned} \quad (26)$$

$$\ln(\hat{V}/V_0) = \psi \epsilon_y \left(\frac{J}{\epsilon_y \sigma_y} \right)^q \quad (18)$$

where ψ and q are functions of the work hardening coefficient, as listed in Table II.

ii) The toughening

The change in toughness induced by plastic dilatation can be estimated from the above solution for the expansion of an isolated hole if interaction effects between holes are neglected. With this simplification, the volumetric strain $d\theta$ experienced by each volume element of material, containing a volume fraction f of rubber precipitates is simply

$$d\theta = f dV/V \quad (19)$$

The hysteresis in the stress/strain curve (Fig.3), if the small elastic recovery due to unloading in the wake is neglected, gives an energy density,

$$\begin{aligned} U(y) &\equiv \int \sigma_m d\theta \\ &= f \int_{V_0}^{\hat{V}} \sigma_m dV/V \end{aligned} \quad (20)$$

Hence, inserting dV/V from eqn.(12), the energy density becomes,

$$U(y) = 0.84 f \int_{\epsilon_y^p}^{\hat{\epsilon}} \sigma_m \exp\left(\frac{2\sigma_m}{3\sigma_e}\right) d\epsilon \quad (21)$$

where ϵ_y^p is the yield strain and $\hat{\epsilon}$ is the stress at the peak hole volume, \hat{V} . Adopting the further simplification that the holes do not affect the stress field in the plastic zone, inserting the stresses from eqn.(14) and integrating yields the results plotted in Fig.7. These results may be expressed in the form

$$\int_{V_0}^V \frac{dV}{V} = 0.84 \int_{\epsilon_y}^{\epsilon} \exp\left(\frac{2\sigma_m}{3\sigma_e}\right) d\epsilon, \quad (15)$$

where V_0 is the initial hole volume. Integration of eqn.(15) for a material with low work hardening rate, typical of most rubber toughened polymers, i.e. $n \gg 1$, gives

$$\ln\left(\frac{V}{V_0}\right) = 0.84 \epsilon_y \left(\frac{\sigma_e}{\sigma_y}\right)^n \left[1 + \frac{3\sigma_m}{2(n-1)\sigma_e} \right] \exp\left(\frac{3\sigma_m}{2\sigma_e}\right) - \left[1 + \frac{3\sigma_m^*}{2(n-1)\sigma_y} \right] \exp\left(\frac{3\sigma_m^*}{2\sigma_y}\right) \quad (16)$$

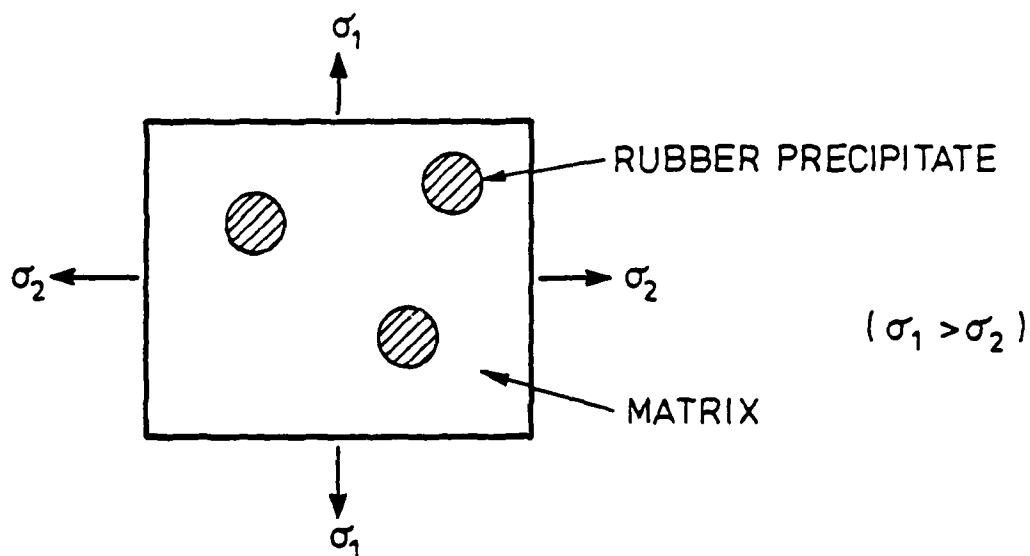
where σ_m^* is the mean stress at the elastic/plastic boundary.

Substituting the stresses from eqn.(14), the hole growth becomes,

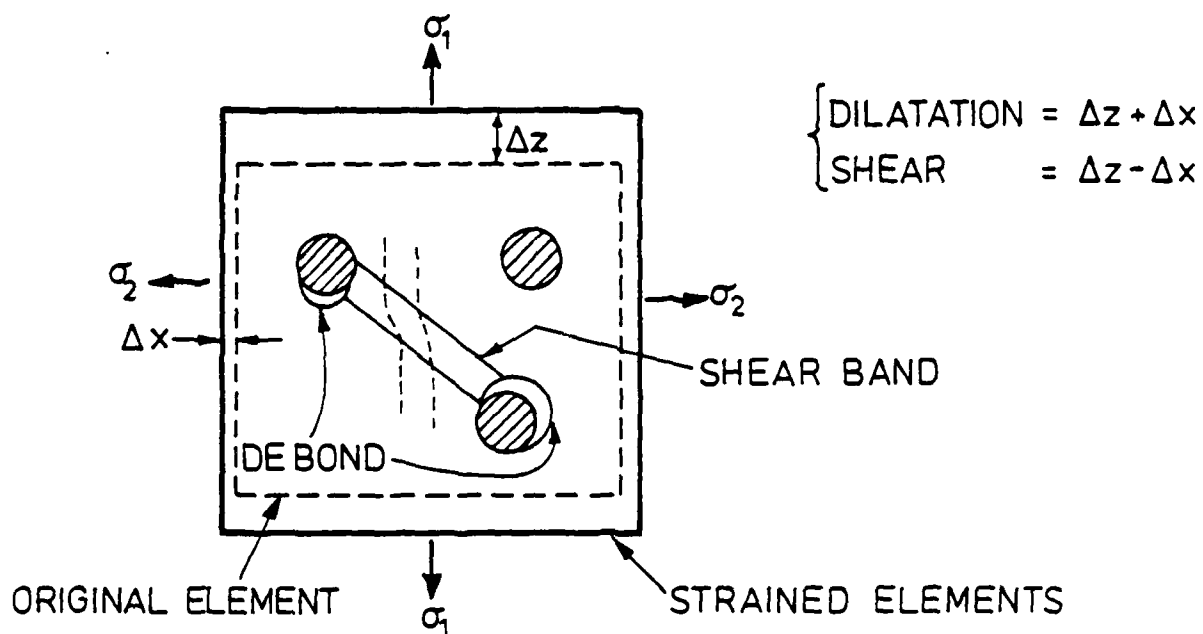
$$\ln\left(\frac{V}{V_0}\right) = 0.84 \epsilon_y \left(\frac{J}{I_n \epsilon_y \sigma_y}\right)^{n/(n+1)} \left[\frac{\bar{\sigma}_e^n}{(1+(x/y)^2)^{n/2(n+1)}} \left[1 + \frac{3(\bar{\sigma}_{rr} + \bar{\sigma}_{\theta\theta})}{4(n-1)\bar{\sigma}_e} \right] \times \right. \\ \left. \exp\left(\frac{3(\bar{\sigma}_{rr} + \bar{\sigma}_{\theta\theta})}{4\bar{\sigma}_e}\right) - \frac{1}{(1+(x^*/y)^2)^{n/2(n+1)}} \left[1 + \frac{3(\bar{\sigma}_{rr}^* + \bar{\sigma}_{\theta\theta}^*)}{4(n-1)} \right] \exp\left(\frac{3(\bar{\sigma}_{rr}^* + \bar{\sigma}_{\theta\theta}^*)}{4}\right) \right] \quad (17)$$

where * refers to the values of the parameters at the elastic/plastic boundary and x is the distance from the crack tip (Fig.1). The volume expansion can be evaluated from eqn.(17) for specific values of the work hardening exponent. The plastic zone shape can be determined from Rice and Rosengren¹¹, and the magnitude of the parameters at the elastic/plastic boundary may be deduced from Hutchinson¹². With these parameters, V/V_0 can be determined for various values of the dimensionless variable, $J/\epsilon_y \sigma_y$, as plotted in Fig.6.

The hole volume reaches a maximum \hat{V} at the x/y listed in Table I, such that (Fig.7),



Elastic Strain Outside Process Zone



Non-Linear Dilatation and Shear within Process Zone

Fig. 2

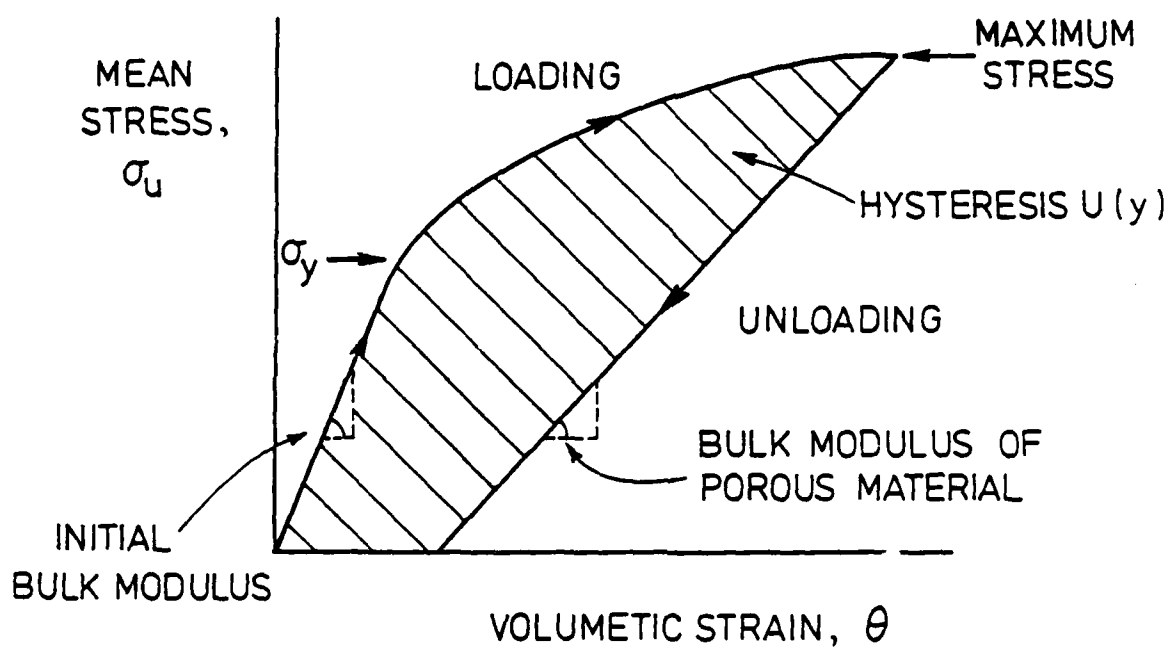


Fig. 3

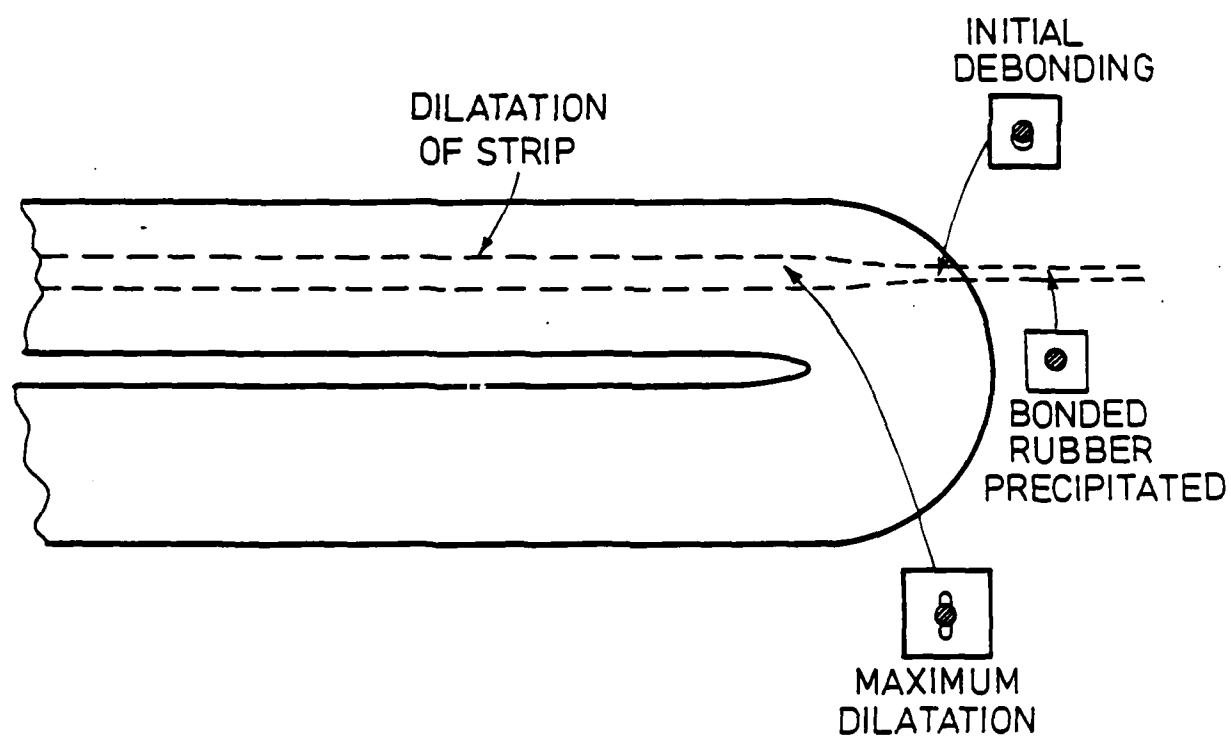
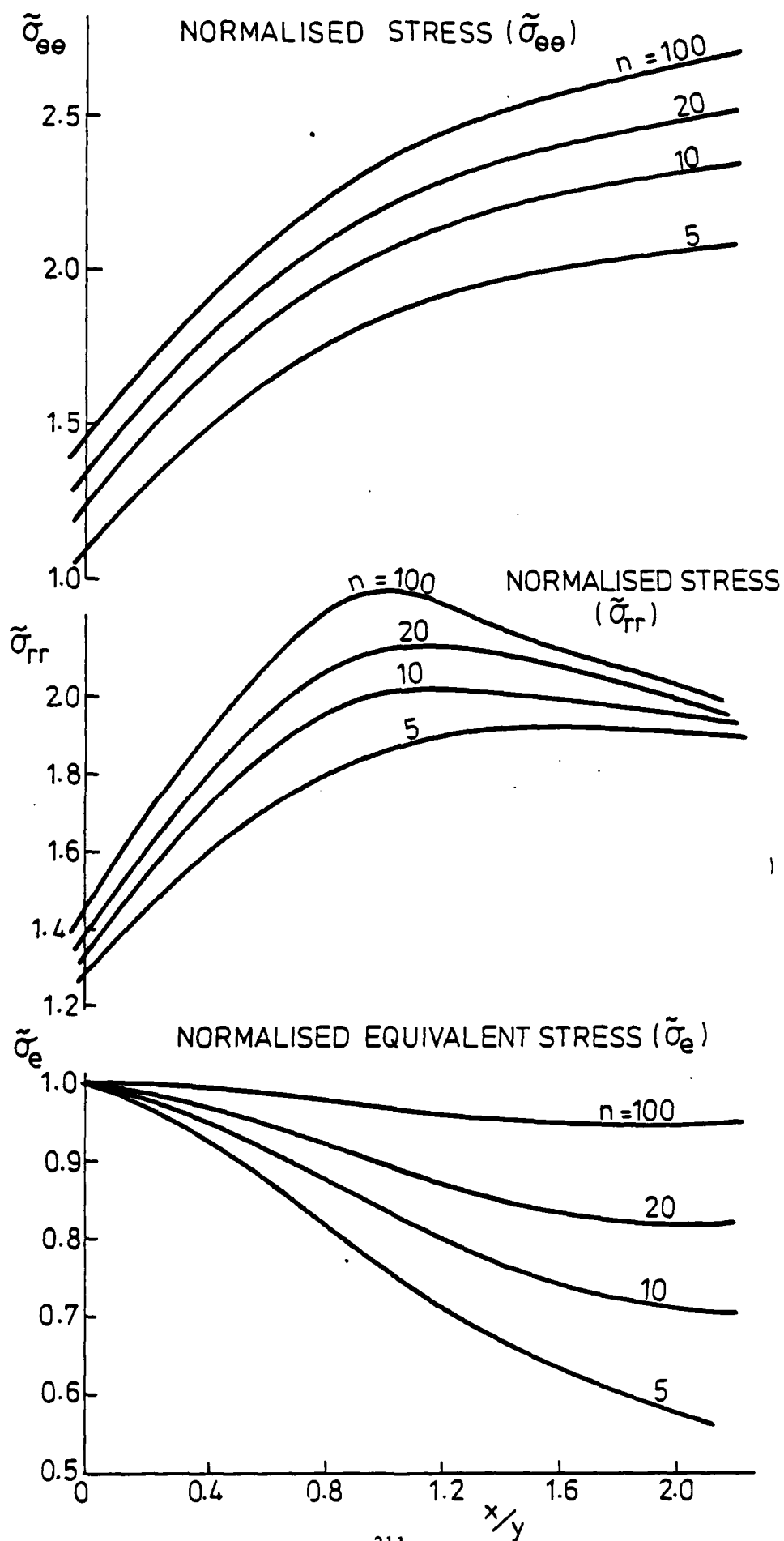


Fig. 4



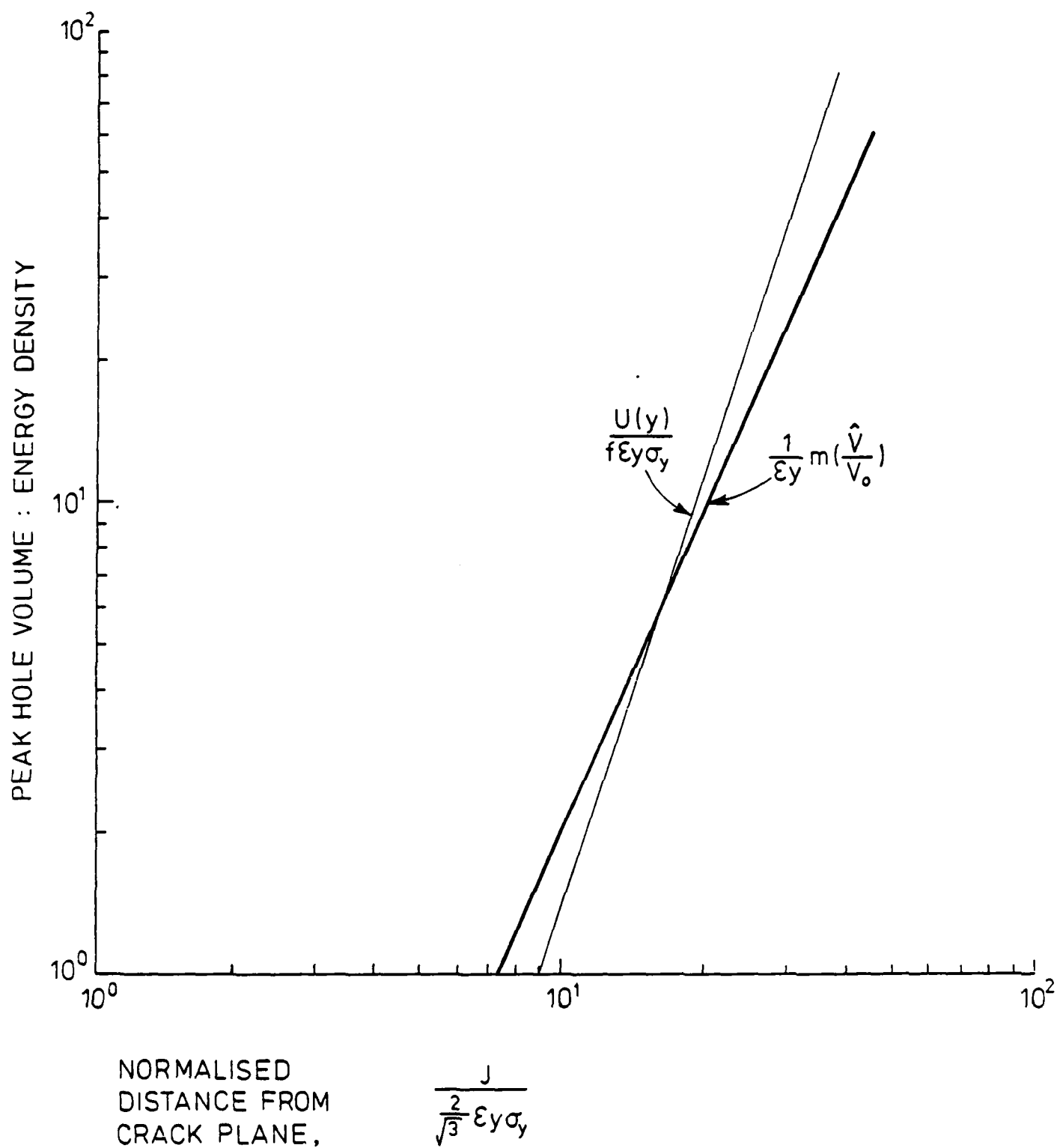


Fig. 7

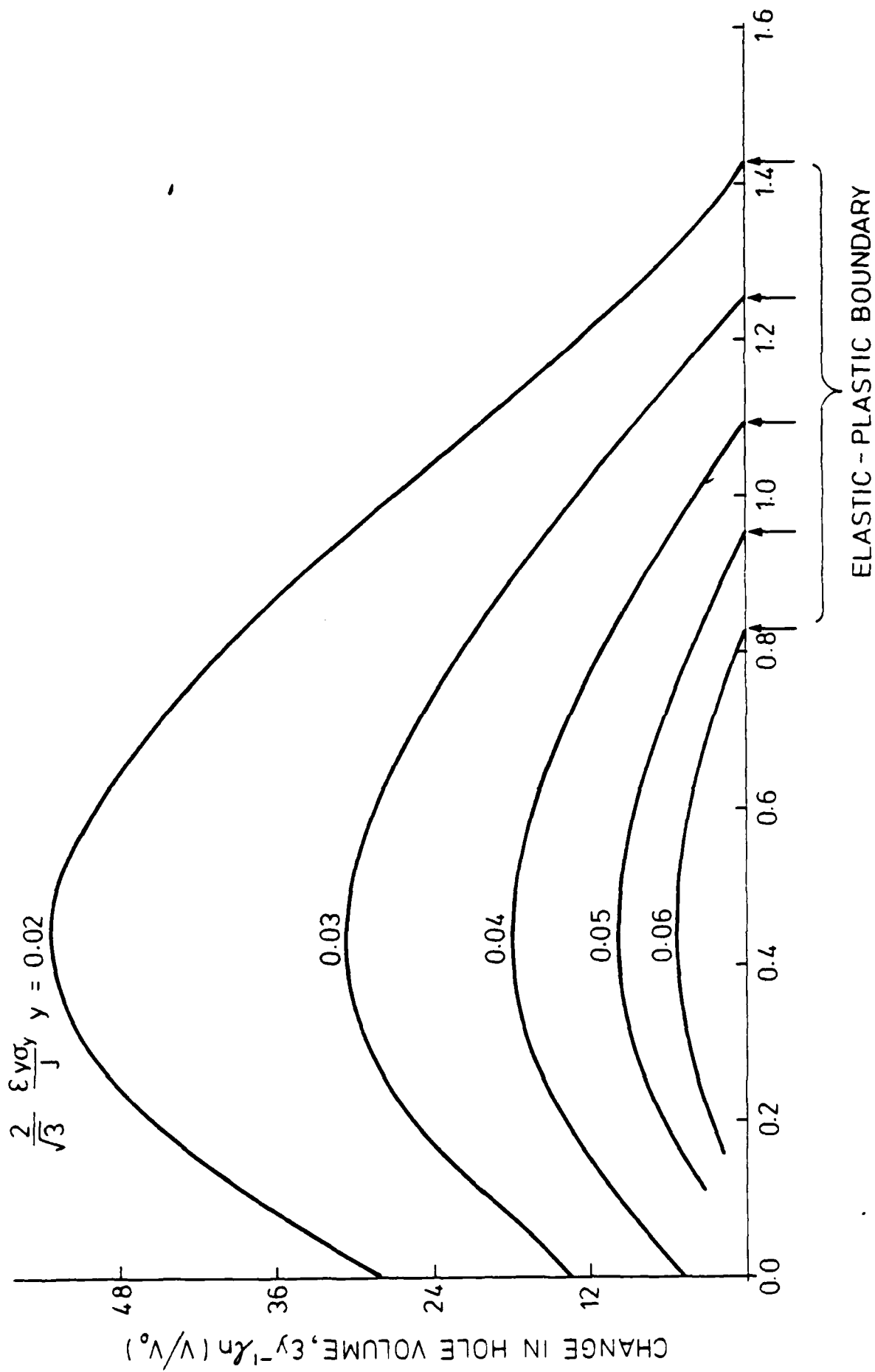


Fig. 6 POSITION RELATIVE TO CRACK TIP x/y

CHAPTER IX

ON THE TOUGHNESS OF PARTICULATE FILLED POLYMERS

A. G. Evans, S. Williams and P. W. R. Beaumont

ON THE TOUGHNESS OF PARTICULATE
FILLED POLYMERS

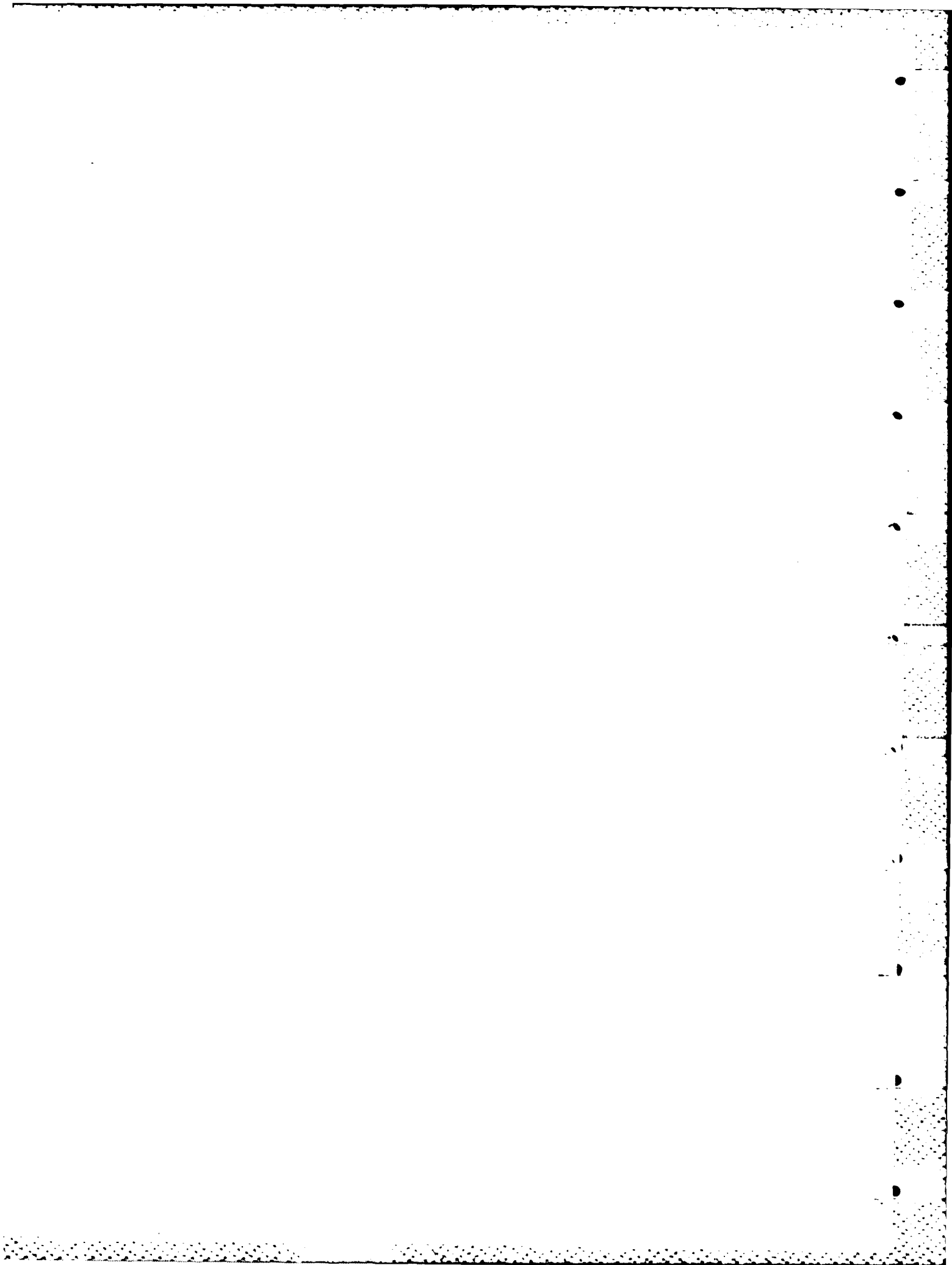
A G Evans*, S Williams and
P W R Beaumont

CUED/C/MATS/TR109 (October, 1984)

*Department of Materials Science and Mineral Engineering
University of California, Berkeley, Ca 94720

ABSTRACT

An approach for predicting trends in the toughness of particulate filled polymers has been presented. The approach is based on independent knowledge of the constitutive law that describes the non-linear behavior in the process zone. An idealized law is used to demonstrate expected trends with particulate volume fraction and size. The trends are correlated with experimental data. Some discussion of the non-linear process zone mechanisms, such as debonding and microcracking, is presented as a basis for developing more realistic constitutive laws and hence, providing superior predictions of toughness.



1. INTRODUCTION

The toughness of polymeric solids can be enhanced by the incorporation of glass, or other hard second phases.^{1,2,3} The toughening has been attributed to a number of different mechanisms, such as crack bowing, debonding and microcracking. The present article attempts an interpretation predicated on the recent observation³ that substantial debonding of the second phase occurs around the crack tip and hence, that the toughening relates in some manner to the extent of debonding.

Debonding results in a non-linear stress-strain curve and a reduced secant modulus^{3,4} as depicted in fig. 1. Representation of this deformation behavior by a constitutive law allows computation of the toughness, without detailed knowledge of the associated microstructural processes.^{5,6} Specifically, during initial propagation of a sharp pre-crack, a frontal process zone develops as the load is applied and material elements within the process zone experience monotonic straining (fig. 2). For this condition, J is generally path independent⁵ and thus, J_{∞} , determined on a contour remote from the crack tip (in the elastic zone for small scale yielding) and J_t for a contour in the immediate vicinity of the crack tip (fig. 2) are equal:

$$J_{\infty} = J_t \quad (1)$$

The stress intensity factors are thus related by:

$$K_{\infty}^2/E = K_t^2/E_T, \quad (2)$$

where E is Young's modulus and E_T is the tangent modulus of material

elements at the crack tip. Consequently, since $E_T < E$ (fig. 1), $K_t < K_\infty$, and hence, the crack tip stresses are reduced in the presence of the debond process zone. However, the reduced stress does not necessarily coincide with an enhanced toughness, because the debonding process degrades the material in the process zone ahead of the crack.⁶ Countervailing influences thus operate within a frontal process zone.

Propagation of the crack into the debond zone results in a process zone wake (fig. 3), because the stress-strain relation is non-reversible (fig. 1). In the presence of a steady-state wake (fig. 3), the energy density associated with a contour passing through the wake differs from that for a crack tip contour, such that:⁵

$$J_\infty = J_t + 2 \int_0^h U(y) dy, \quad (3)$$

where h is the width of the debond zone (fig. 3) and $U(y)$ is the residual energy density in a strip dy in the remote wake. The energy density $U(y)$ is simply the area under the stress-strain curve given in fig. 1. The change in J induced by the wake is, in fact, a direct measure of the hysteresis in the stress-strain curve, because material elements that traverse from the front of the crack to the remote wake (viz. the energy change brought about by crack advance) are exposed to a complete stress-strain cycle (fig. 3).

Computations of the stress-strain hysteresis in the debond process zone can be used to predict the change in J_t . The increase in toughness can then be determined by equating J_t to the local crack propagation resistance of the debonded material. The computations are strictly valid when the components of the stress tensor are consistent

with a path independent J for the frontal zone. Such conditions are assumed to be approximately valid for the polymer systems of present interest.

The analysis presented in this article is based on the stress-strain characteristics of the material, as outlined above. However, some consideration is first given to the debonding and deformation mechanisms that determine the observed stress-strain relations.

2. NON-LINEAR STRESS-STRAIN RELATIONS FOR FILLED POLYMERS

Recent studies have revealed that the onset of non-linearity in the stress-strain curve for filled polymers coincides with the debonding of the second phase.^{3,4} Debonding presumably occurs when the applied strain at the interface overcomes both the initial thermal contraction mismatch strain and the decohesion strain. For a relatively rigid second phase, such as glass, the principal strain concentration in the polymer occurs in the regions between closely spaced particles (fig. 4). Specifically, since nearly all of the strain is accommodated by the polymer, a uniaxial applied strain ϵ_∞ is magnified in the region between the particles by:

$$\epsilon/\epsilon_\infty \approx (1-2R/l)^{-1} \quad , \quad (1)$$

where l is the centre-to-centre spacing between particles and R is the sphere radius. For example, strain concentrations in the range 4 - 10 frequently occur in materials with a volume loading of ~ 0.3 . Such strains are well into the non-linear deformation response regime of the matrix (fig. 1).⁴ It seems reasonable, therefore, to regard debonding as a phenomenon that occurs primarily in regions between closely spaced

particles and, furthermore, that appreciable permanent deformation of the intervening matrix occurs after debonding. Plastic deformation of the debonded matrix (analogous to plastic hole growth⁷) should result in permanent debonding and hence, the presence of residually debonded particles. A concomittent dilatation is expected in the process zone wake.

Experimental observations substantiate that debonding predominates in the region between particles⁴ (fig. 5). Furthermore, evidence of optical interference in the wake⁴ is consistent with the presence of residual debonding. It is thus concluded that the non-linear loading features of the stress-strain curve (such as the tangent modulus) are dominated by matrix plasticity between debonded closely spaced particles; whereas the unloading (secant) modulus is governed by the elasticity of the composite containing debonded particles.

Micro-cracking or crazing of the matrix may constitute an alternative non-linear deformation mechanism. In this instance, the residual misfit strain due to differential shrinkage between the matrix and the particles results in residual tangential tensile stresses. Consequently, since the applied load imposes additional tangential tensile stresses, the potential for matrix microcracking between particles is readily visualized. Such microcracks would relieve the residual stress and be subject to residual opening.⁶ Hence, non-linear behavior accompanied by permanent dilatation and a reduced secant modulus would, again, be expected.

The observed stress-strain characteristics of particulate filled polymers are thus qualitatively explicable in terms either of enhanced plasticity of the matrix between debonded particles or of microcracking

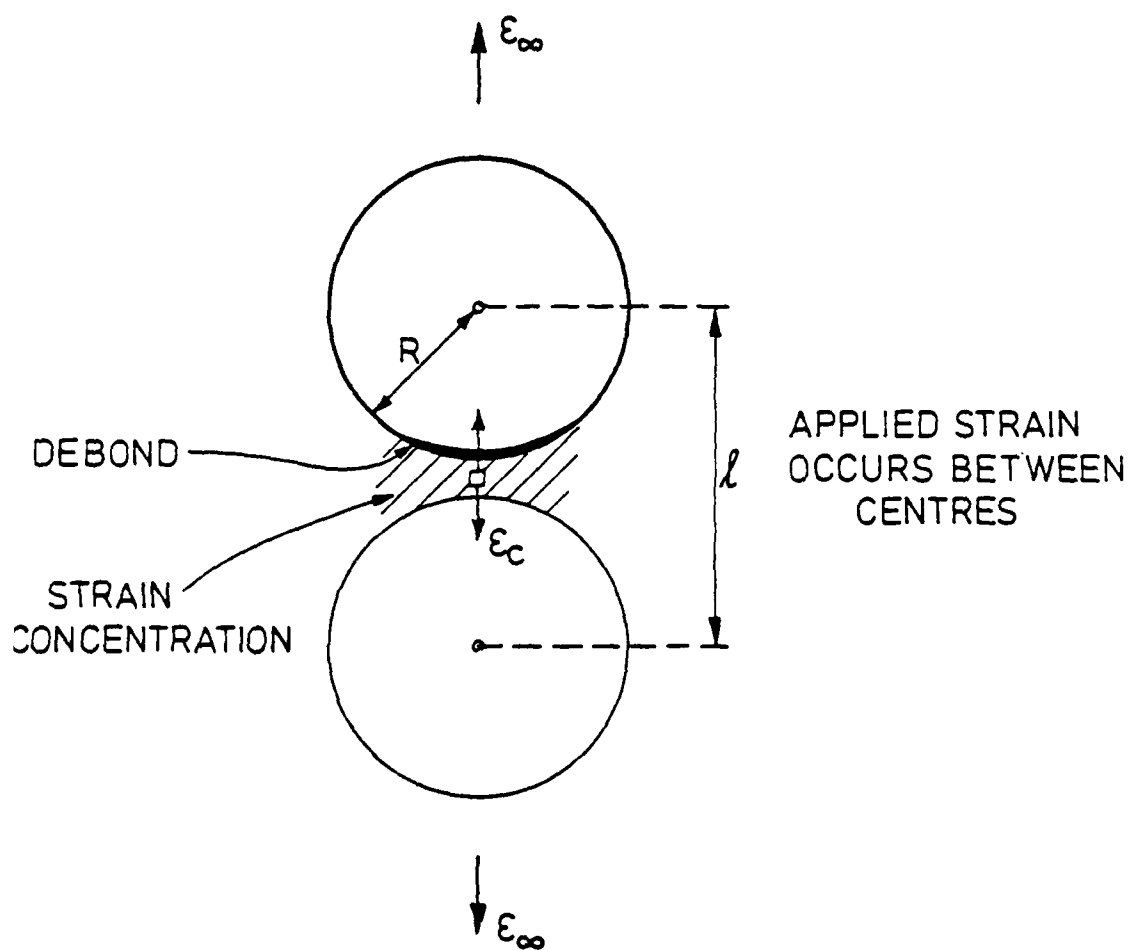


Fig. 4

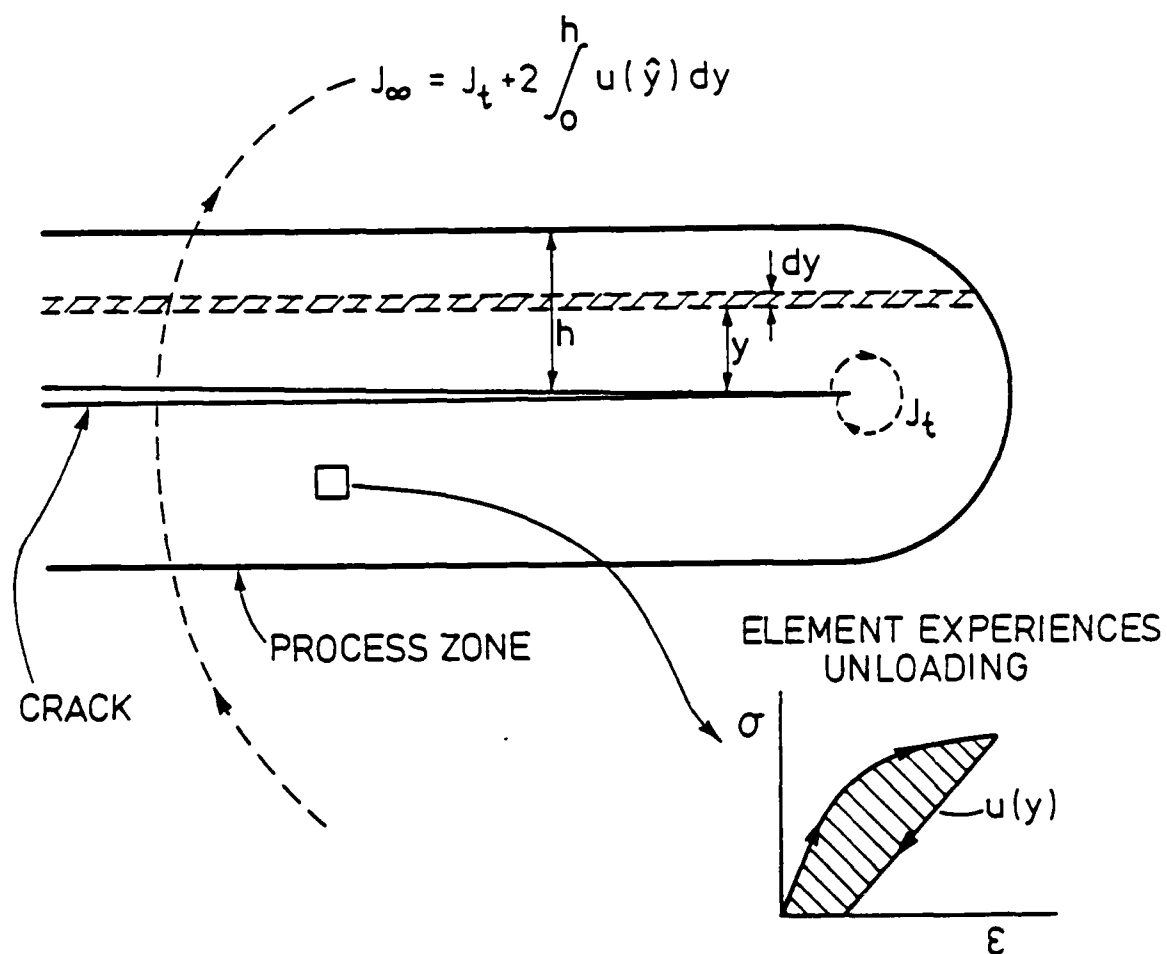


Fig. 3

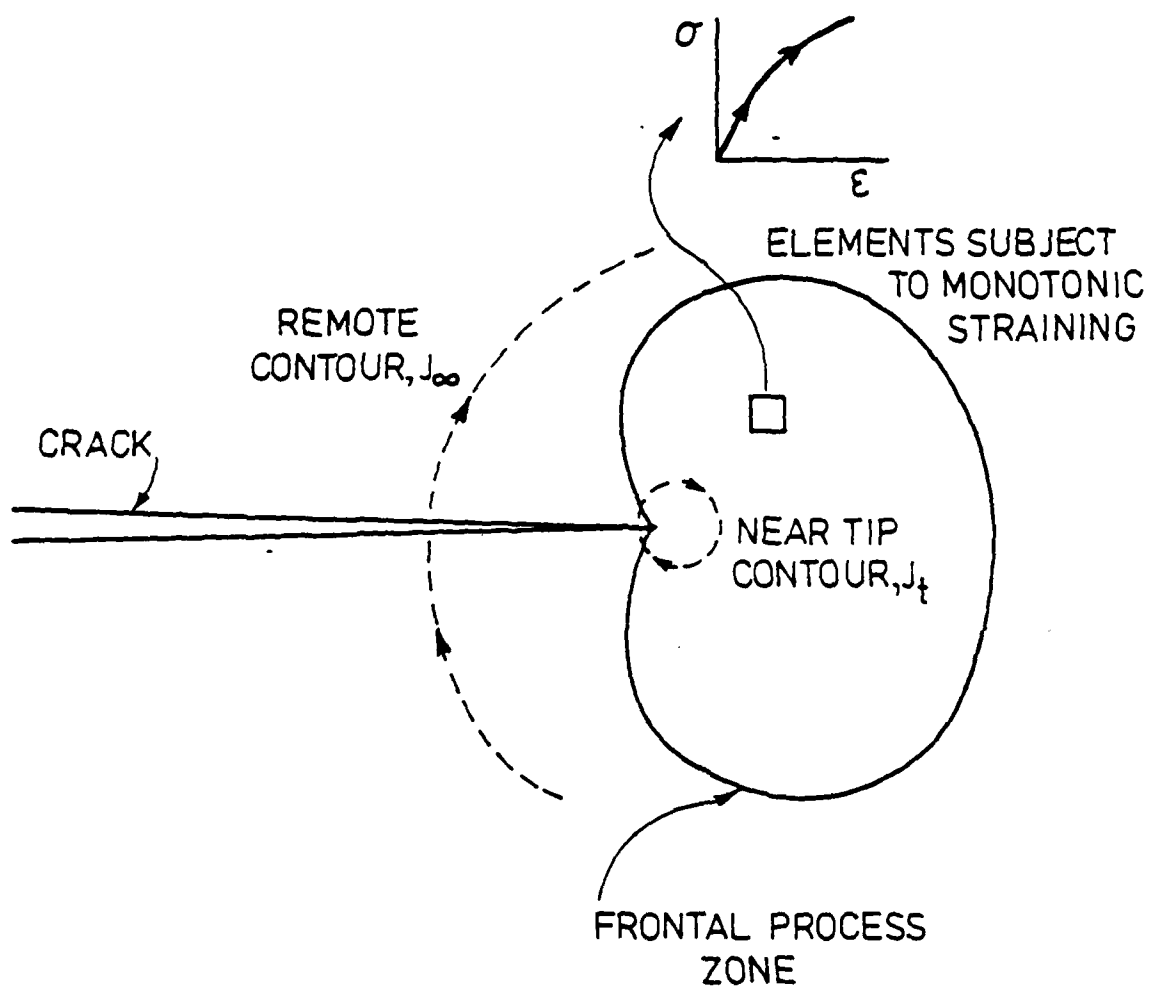


Fig. 2

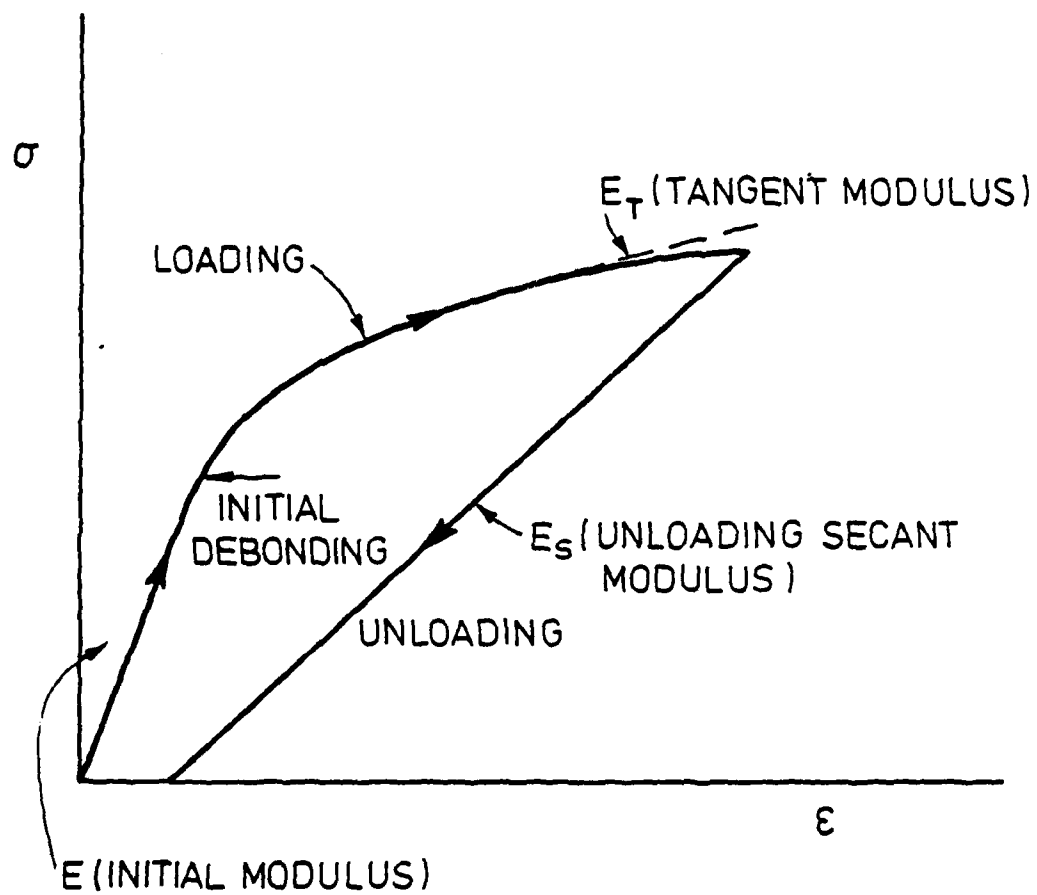


Fig.1

FIGURE CAPTIONS

- Fig. 1 A non-linear stress-strain curve typical of a particulate filled polymer.
- Fig. 2 A frontal process zone with an associated stress-strain curve for elements within the zone; also shown are two J contours.
- Fig. 3 An extended process zone indicating the hysteresis in the stress strain curve for material elements in the wake.
- Fig. 4 The strain concentration between closely spaced particulates and the associated interface debonding.
- Fig. 5 A micrograph illustrating debonding between closely spaced particulates in the crack tip process zone.
- Fig. 6 A comparison of trends in toughness predicted from the present analysis with experimental data. The toughness of the system with 10% of 40 μm radius spheres is taken as the reference.

REFERENCES

1. R. E. Lavengood, L. Nicolaus and M. Narkio, J. Appl. Pol. Sci. 7 (1972) 1443.
2. J. C. Mallick, L. J. Broutman, Mat. Sci. Eng. 18 (1975) 63.
3. S. Williams, Ph.D. Thesis, U. Cambridge (1982) 'Toughening Mechanisms in Particulate Filled Brittle Matrix'.
4. A. B. Owen, Ph.D. Thesis, U. Cambridge (1979), 'Fracture Toughness of Brittle Matrix Particulate Composites.'
5. B. Budiansky, J. W. Hutchinson and J. Lambropoulos, Int. J. Solids and Structures, 19 (1983) 337.
6. A. G. Evans and K. T. Faber, J. Am. Ceram. Soc., 67 (1984) 256.
7. A. G. Evans, Z. Ahmad, D. Gilbert and P. W. R. Beaumont, Acta Met, to be published.
8. J. R. Rice and G. F. Rosengren, Jnl. Mech. Phys. Solids 16 (1968) 1.
9. J. W. Hutchinson, Jnl. Mech. Phys. Solids 16 (1968) 13.
10. A. G. Evans, Phil. Mag. 26 (1972) 1327.

TABLE I

EXPERIMENTAL DATA FOR GLASS SPHERE FILLED EPOXY⁴

($\dot{\gamma} = 0.2 \text{ mm min}^{-1}$)

SYSTEM I

$\langle R \rangle \approx 30 \text{ } \mu\text{m}$

| f | σ_y (MPa) | E (GPa) | J_{IC} (Jm ⁻²) | h (μm) |
|-----|------------------|-----------|------------------------------|-----------------------|
| 0.1 | 40 | 3.5 | 430 | 240 |
| 0.2 | 35 | 4.5 | 510 | 470 |
| 0.3 | 25 | 5.5 | 590 | 1290 |

SYSTEM II

$\langle R \rangle \approx 13 \text{ } \mu\text{m}$

| f | σ_y (MPa) | E (GPa) | J_{IC} (Jm ⁻²) | h (μm) |
|-----|------------------|-----------|------------------------------|-----------------------|
| 0.1 | 40 | 3.5 | 550 | 300 |
| 0.2 | 35 | 4.5 | 690 | 630 |
| 0.3 | 25 | 5.5 | 900 | 2000 |

Measured h ($f = 0.25$, $\langle R \rangle = 30 \text{ } \mu\text{m}$) = $600 \text{ } \mu\text{m}$.⁴

5. CONCLUDING REMARKS

A method of relating the toughness of a particulate filled polymer to an independently determined stress-strain curve for the composite has been demonstrated, using an idealized constitutive law. The analysis illustrates trends in particulate volume fraction and size and seems to predict behavior consistent with measured trends.

Further understanding of particulate toughening based on the present concepts requires a superior characterization of the non-linear behavior in the process zone, based on micromechanics models of the debonding, microcracking and plasticity. More realistic constitutive laws can then be derived and used in a quantitative mode to predict trends in toughness. It would also be expedient to obtain direct measurements of the process zone width in the crack wake. Such determinations would constitute a superior measure of the utility of the present approach, as well as providing an independent assessment of the deformation characteristics within the process zone.

formula (eqn 15), subject to the availability of independent determinations of the zone height, h . Such determinations have not been conducted, except in one instance⁴ (table I). In lieu of direct determinations of h , estimates may be obtained from eqn (16), provided that trends in modulus and yield strength are independently determined. Appropriate data are available for a glass filled epoxy (table I). Note that, in the one instance for which h has been independently measured, the agreement with the value predicted from eqn (18) is relatively good. The toughness may be deduced from these data by combining eqns (15) and (16) to give;

$$J_c^\infty/J_c^0 = 1 - f + 0.8 \ln \left[\frac{EJ_c^\infty}{4\sigma_y^2 R} \right] \quad (18)$$

Before proceeding with the prediction, the choice of the reference toughness, J_c^0 , must be considered. It is inappropriate to select the toughness of the unfilled polymer because, in the absence of particulates, alternative inelastic toughening mechanisms (e.g. craze growth) are activated. Predictions afforded by eqn (18) only pertain when the same inelastic process zone mechanisms operate. The application of eqn (18) must, therefore, be restricted to the prediction of trends in toughness amongst particulate-filled systems. Consequently, one particulate system is used as a reference and the relative behavior of the other systems is determined. The reference system selected is the material containing 10% (by volume) of the larger ($R \geq 30 \mu m$) glass spheres. The toughnesses relative to this system are predicted from eqn (18) and plotted in fig. 6. A comparison with the measured toughnesses (fig. 6) indicates good consistency for both particle radii. The approach thus appears to have merit and warrants further investigation.

$n \approx 0.2$. With this choice for n , the upper bound toughness becomes:

$$J_c^\infty = J_c^0 \left[1 - f + 0.8 \ln(h/R) \right]. \quad (15)$$

where the zone width, h , can be approximately related to the yield strength, via the plane strain relation:⁸

$$h \approx \left[\frac{E J_c^\infty}{\sigma_y^2} \right] g(n) \quad (16)$$

where $g \approx 1/4$ for $n = 0.2$.

A more complete solution for the steady state toughening can be obtained from eqn (10) as;

$$J_c^\infty = J_c^0 \left\{ 1 - f + \frac{2^{n+2}}{(n+1)I_n} \ln(h/R) - \frac{2^{n+1}}{4} (n+1) \frac{\sigma_y J_c^0}{I_n E_s} \left[\frac{J_c^0}{\sigma_y I_n R} \right]^{(n-1)/(n+1)} \right\} \quad (17a)$$

which for $n = 0.2$ becomes:

$$J_c^\infty = J_c^0 \left[1 - f + 0.8 \ln(h/R) - 0.06 \frac{\sigma_y J_c^0}{E_s} \left(\frac{J_c^0}{\sigma_y R} \right)^{2/3} \right]. \quad (17b)$$

The specific dependence of J_c^∞ on h/R contained in the preceding formulas can be directly attributed to the selected form of the constitutive law (eqn 5). More realistic constitutive laws would undoubtedly yield a different functional dependence.^{5,6,7} However, the general trends should be unaffected.

4. COMPARISON WITH EXPERIMENT

Trends in the toughness with the volume fraction and size of particulates can be most expediently predicted using the upper bound

most convenient estimate for further analysis.

3.3 The Toughness

(i) Initial growth

The fracture toughness for initial growth of the crack, with a frontal process zone is simply obtained by equating J_t in eqn (1) to J_c^l in eqn (12) giving:

$$J_c^\infty \approx J_c^0 (1-f) . \quad (13)$$

The toughness is thus predicted to be slightly reduced, due to the degradation of the material by debonding. However, as noted above, the degradation is not likely to be as substantial as that given by eqn (12). Hence, circumstances could be envisaged wherein the reduced near tip stresses (eqn (2)), allow a small increase in toughness. Nevertheless, the effect should be small and, for all practical purposes, it is concluded that initial growth occurs at a toughness similar to that of the unreinforced matrix.

(ii) Steady state growth

When the crack has extended substantially into the debond process zone, the crack growth resistance approaches the steady-state solution. The upper bound toughness is deduced by obtaining J_∞ from eqns (3) and (11) and equating J_t to J_c^l (eqn (12)) to give:

$$\hat{J}_c^\infty = J_c^0 \left[1 - f + \frac{2^{n+2}}{(n+1)} \frac{\ln[h/R]}{I_n} \right] . \quad (14)$$

Typically, for filled polymers the work hardening rate is low,^{3,4}

An upper bound energy (that neglects the recovery of elastic energy on unloading) is thus:

$$\hat{U} \approx \frac{2^{n+1}}{(n+1)} \frac{J}{I_n} \ln \left(\frac{h}{R} \right). \quad (11)$$

The magnitude of J now requires further consideration. As evident from eqn (3), J varies within the zone from J_t to J_∞ , due to the presence of the wake. However, since the deformation closest to the crack plane has the maximum influence on the net energy ($U(y) \rightarrow \infty$ as $y \rightarrow 0$, eqn (9)), J_t is selected for present purposes.

3.2 Material Degradation

The presence of debonding in the process zone degrades the local crack propagation resistance of the material, because cracks deflect into the debonded material at the poles of the particles. If debonding occurs at all particles immediately ahead of the crack tip, the area fraction of debonded material along the crack plane will be of the order of the volume fraction, f , of particles. Debonding represents a loss of section and hence, the simplest expression for the toughness degradation is:⁶

$$J_C^l = J_C^0 (1-f), \quad (12)$$

where J_C^l is the degraded fracture resistance and J_C^0 is the reference fracture resistance of the matrix.

The degradation will not normally be as large as that determined by eqn (12) because some particles may not debond and a local toughening due to crack bowing¹⁰ may then occur. Nevertheless, eqn (12) is used as the

element within a strip, dy , distance y from the crack plane. The present choice of ϵ_* is predicated upon the non-linear solution for the principal strains in a crack tip field. For the present, idealised stress-strain law, the inelastic strains are;^{8,9}

$$\epsilon_{ij} = \left[\frac{J}{I_n \sigma_y r} \right]^{1/(n+1)} \tilde{\epsilon}_{ij}(\theta) \quad (7)$$

where r is the distance from the crack tip, $I_n \approx 10\sqrt{0.13+n} - 4.8n$, and $\tilde{\epsilon}(\theta)$ is the non-dimensional parameter given in ref. 9. Hence, the peak inelastic strain on the y plane becomes:

$$\epsilon_* \approx 2 \left[\frac{J}{I_n \sigma_y y} \right]^{1/(n+1)} \quad (8)$$

The energy density is thus:

$$U(y) = \frac{2^{n+1}}{(n+1)} \frac{J}{I_n} \left[\frac{1}{y} - \frac{(n+1)}{2y} \left(\frac{\sigma_y}{E_s} \right) \left(\frac{J}{\sigma_y I_n y} \right)^{(n-1)/(n+1)} \right], \quad (9)$$

and the net energy in the wake is:

$$U \equiv \int_{r_0}^h U(y) dy \\ = \frac{2^{n+1}}{n+1} \frac{J}{I_n} \left[\ln \left(\frac{h}{r_0} \right) - \frac{(n+1)}{4} \left(\frac{\sigma_y}{E_s} \right) \left(\frac{J}{\sigma_y I_n} \right)^{(n-1)/(n+1)} \left[\frac{1}{r_0^{(n-1)/(n+1)}} - \frac{1}{h^{(n-1)/(n+1)}} \right] \right] \quad (10)$$

where r_0 is the minimum distance from the crack plane at which the matrix between debonded particles experiences permanent deformation or microcracking. This distance should be of the order of the particle radius, because a crack typically deflects around one pole of the particle, leaving the deformed matrix at the opposite pole, in the wake.

between particles. Specific distinction between these processes is not attempted in the subsequent analysis.

3. THE FRACTURE TOUGHNESS

3.1 The Energy Density in the Wake

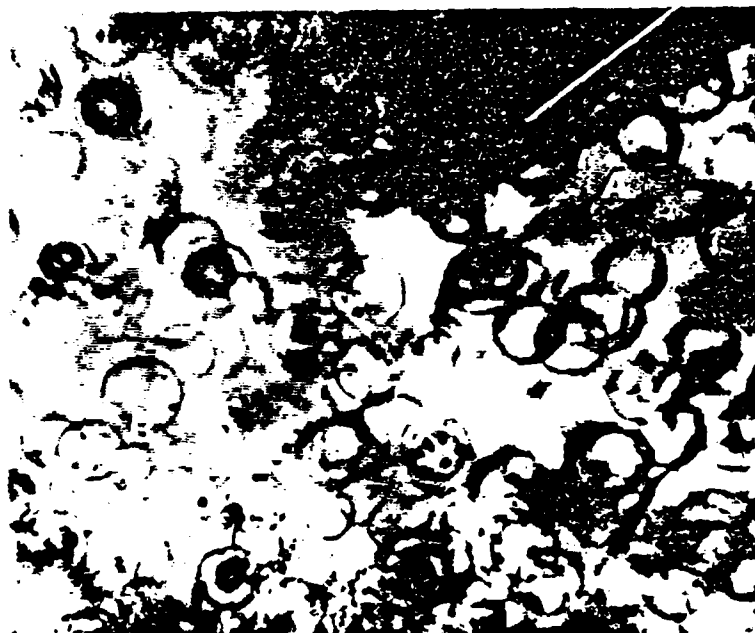
The energy density and hence, the toughness, may be computed from the hysteresis in the stress-strain curve provided that an appropriate constitutive law can be specified. For simplicity, the loading curves pertinent to both the shear and dilatational deformation of the particulate filled polymers are assumed to exhibit a common form, suggested by the uniaxial stress, strain curve, viz.,

$$\sigma_{ij} = \sigma_y (\epsilon_{ij})^n \quad (5)$$

where ϵ_{ij} is the inelastic strain, σ_y is the uniaxial yield strength, and n is a unique hardening coefficient. Unloading is assumed to be linear, with a secant modulus, E_s . With this idealization, many of the complexities of the toughening analysis⁵⁻⁷ are eliminated, while still providing a useful perspective on trends in toughness with microstructure. The energy density based on eqn (5) has the form

$$\begin{aligned} U(y) &\equiv \int \sigma_{ij} d\epsilon_{ij} \\ &\approx \frac{\sigma_y}{(n+1)} \epsilon_*^{n+1} - \frac{\sigma_y^2 \epsilon_*^{2n}}{2E_s} \\ &= \frac{\sigma_y \epsilon_*^{n+1}}{(n+1)} \left[1 - \frac{\sigma_y \epsilon_*^{n-1} (n+1)}{2E_s} \right] \end{aligned} \quad (6)$$

where ϵ_* is the maximum inelastic strain experienced by a material



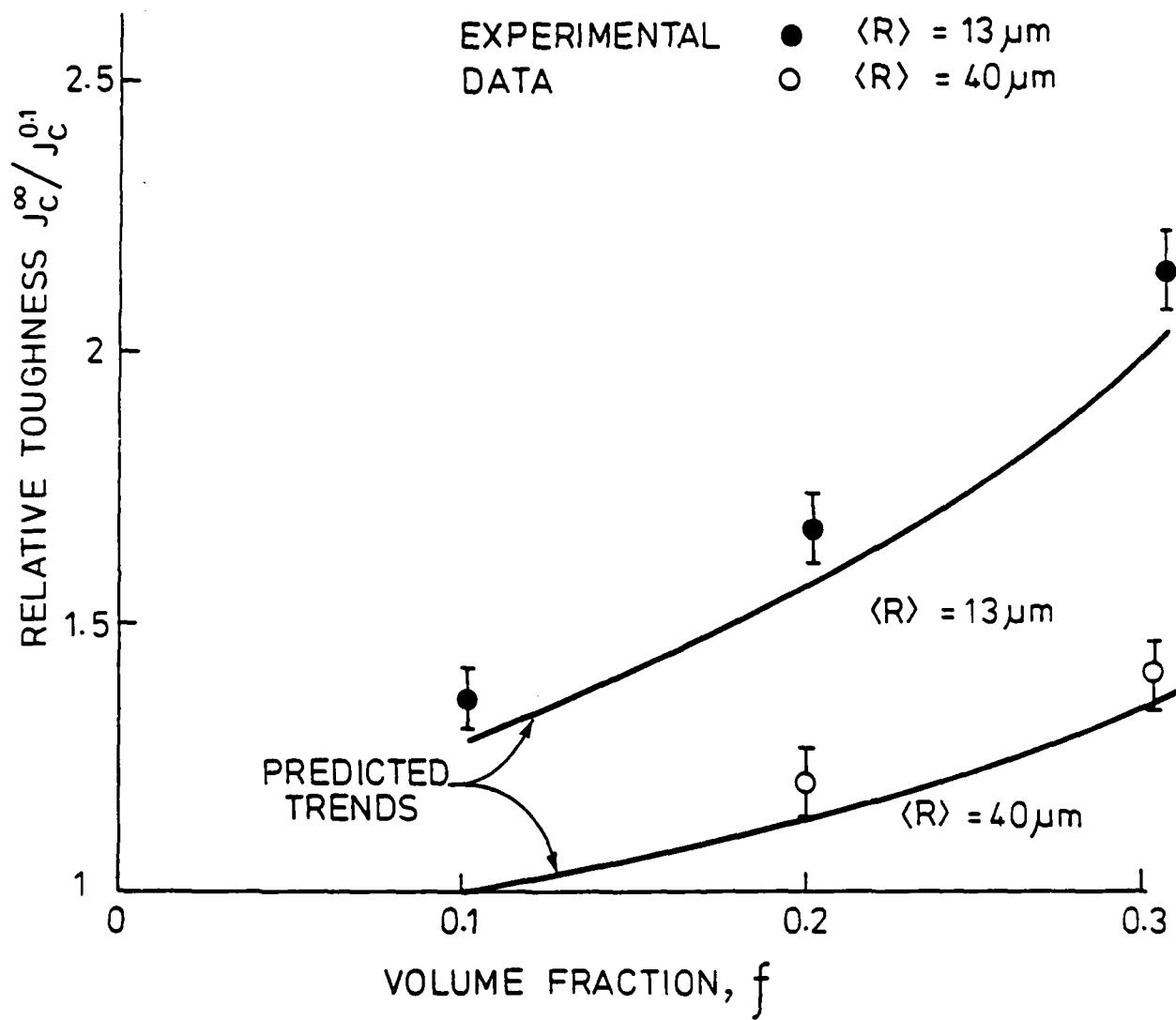


Fig. 6

CHAPTER X

A COMPUTER-GENERATED SIMULATION OF
WATER DROP IMPACT DAMAGE

E. D. Case and A. G. Evans

A Computer-Generated Simulation of

Water Drop Impact Damage

by

E. D. Case and A. G. Evans

Department of Materials Science and Mineral Engineering

University of California

Berkeley, CA 94720

Abstract

A computer simulation is presented for the water drop impact damage process. The simulation first assigns initial flaw positions and lengths on a surface. These precursor flaws are then liable to activation by an impact-generated stress pulse. The crack growth and arrest equations involve the crack incubation time, thereby including crack inertial effects in the analysis. The graphical features of the simulation are demonstrated, as well as the agreement between experimental data and the simulation.

1. INTRODUCTION

The impact of high velocity* water drops or jets on the surface of brittle materials produces an annular damage ring above a damage threshold.¹⁻³ The damage, which typically comprises several hundred circumferential cracks (fig. 1), exerts a major influence on the optical properties of the material.³⁻⁵ The stochastic nature of brittle fracture suggests that it will not be possible for a model to exactly reproduce the details of crack length and position for a given impact event. Rather, the model should predict the correct spatial and length distributions for the crack array. Predictions of the influence of material properties on optical transmission could then be addressed. This paper describes a recently developed computer simulation that provides both statistical and graphical information on a calculated crack array. The simulation is based on a prior simulation developed by Van der Zwaag and Field.⁶ However, the present simulation differs in both intent and in the details of the crack growth and arrest criteria, as described below.

* Depending on the material, the impact damage threshold velocity, v_{ft} , typically lies in the range $150 \text{ ms}^{-1} \leq v_{ft} \leq 1000 \text{ ms}^{-1}$.

2. IMPACT SIMULATION

The simulation introduces a statistical array of pre-existent small cracks into the surface of the solid. A stress pulse, characteristic of the impact induced Rayleigh wave⁷⁻⁹, is then imposed onto the surface and allowed to propagate radially outward from the impact center. The stress pulse activates crack growth in accord with an initiation criterion and permits crack arrest subject to an arrest criterion. The product of the simulation is thus an array of relatively large impact activated cracks centered around the impact site (see fig. 5).

A relatively large number of initial flaws, N , typically between 100 and 1000 is used for the present simulation. This number is appreciably larger than that used in the prior study (20-40). Each initial flaw, of radius a , is selected from a Weibull distribution,¹⁰

$$f(a) = \frac{m}{p_1} \left(\frac{a-p_2}{p_1} \right)^{m-1} \exp \left[- \left(\frac{a-p_2}{p_1} \right)^m \right] \quad (1)$$

This distribution has been selected, not only for its versatility, but also because it has been established as the extreme value distribution that most closely describes the large flaw size extreme in brittle solids.¹¹

Flaw positions are assigned randomly over an annular sector, bounded by polar angles θ_{\min} and θ_{\max} , at radial distances $a \leq r \leq b$ (figure 3). The flaw positions are subject to the spatial limits r_{\max} (Appendix) which prescribes the maximum radial distance at which cracks are likely to be activated by the stress pulse.

The stress pulse imposed on this crack array has an initial amplitude, σ_0 , given by;⁶

$$\sigma_0 = \beta z v \quad (2)$$

where z is the acoustic impedance of the drop, v is its velocity and β is a constant of order unity. The pulse is allowed to attenuate as it propagates. For present purposes, an experimental attenuation is used,¹²

$$\sigma(r) = \sigma_0 [\exp -\alpha(r-r_0)^{1/2}] \quad (3)$$

where α is the surface acoustic wave attenuation coefficient and r_0 is the radial distance from which the stress is launched (Appendix). This form is characteristic of material attenuation, due to scattering by grains, surface cracks, etc. An alternative choice, $\sigma \sim r^{-1/2}$, would be more pertinent if geometric spreading were the predominant attenuation mechanism. The stress pulse is assumed to be rectangular with an initial duration Δt (a position dependent duration can be readily incorporated, as required).

When the propagating stress pulse reaches one of the surface cracks, the quasi-static stress intensity factor¹³

$$K_I^S = 1.1(2/\sqrt{\pi})\sigma \sqrt{a} \quad (4)$$

is first compared with the material toughness K_{IC} . When $K_I \leq K_{IC}$, crack growth is prohibited. However, cracks subject to the condition $K_I > K_{IC}$ are considered liable to propagation. In the prior simulation⁶, crack growth was invariably considered to occur when $K_I > K_{IC}$ and to arrest when the stress pulse had propagated past the crack plane. Additional considerations are invoked in the present simulation, based on a previous recognition¹⁴ that inertial effects are likely to be important, especially with regard to crack extension after

the stress pulse has passed the crack plane. Specifically, three temporal regimes are considered: an incubation time τ , a crack acceleration phase, $\tau < t < \Delta t$,¹⁴⁻¹⁷ and a crack deceleration phase, $t > \Delta t$. The incubation time is the time interval between the instant the stress wave intercepts the crack and the instant the crack growth begins.^{15,16} Consequently, if $\tau > \Delta t$, the crack does not grow. When $t < \Delta t$, the changes in crack length, a_1 and a_2 , that occur during the acceleration and deceleration phases, respectively, are given by¹⁴

$$\Delta a_1 = v_r \tau (p_0 - 1 - \ln(p_0)) \quad (5a)$$

and

$$\Delta a_2 = \frac{v_r \tau}{4} \left[(1+p_0)^2 - 4 - \frac{2\gamma}{(1-\gamma)^2} + \ln \left(\frac{1+\gamma}{1-\gamma} \right) \right] \quad (5b)$$

where v_r is the Rayleigh wave velocity for the material, p_0 is $\Delta t/\tau$ and γ is $(p_0 - 1)/(p_0 + 1)$. The incubation time τ is in turn given by

$$\tau = \frac{\pi}{4} \left[\frac{K_c (1-\nu^2)}{v_r \sigma^2} \right]$$

where ν is the Poisson's ratio of the material (1).

The preceding crack growth relations (equations 5) are sequentially applied to each flaw in the initial flaw population that satisfies $K_I > K_{IC}$. For simplicity, crack interaction is neglected in this preliminary simulation. The program thereby provides a statistical analysis of the final crack population for non-interacting cracks, along with a graphical output of the final crack length and position (see fig. 5). The graphical capabilities allow a rapid appraisal of results, and aid in the iterative refinement of the

simulation.

3. RESULTS AND DISCUSSION

Two applications of the impact simulation are presented. First, the capabilities of the program to examine graphical changes in the crack field resulting from the temporal spreading and attenuation of the applied stress pulse are presented. Then, the spatial distribution of cracks in the simulated damage field is compared with that observed in photomicrographs of impact damage.

As an example of the graphical features of the simulation, the affect of changing the attenuation and temporal spreading of the initial stress pulse can be readily explored. Schematics of the evolution of a rectangular stress pulse for a non-attenuating constant duration pulse, an attenuating constant duration pulse, and a pulse with both attenuation and a linearly increasing duration are presented in fig. 4. A sequence of computer-generated plots that demonstrate the affects of such changes is presented in fig. 5 using axes that are arbitrary, but constant throughout the sequence. A crack array is computed for the case of no attenuation and no temporal spreading of the pulse, so that the initial and final pulse durations are both Δt . The corresponding array induced by a constant pulse duration Δt (no temporal spreading), but stress amplitude attenuated (equation 2) such that at a radial distance $r = 100$, the pulse amplitude is reduced by 10^2 is depicted by fig. 5b. Note that the spatial extent of the crack field in the attenuated case (figure 5b) is much reduced with respect to the non-attenuated case (figure 5a). Trends associated with the linear spreading of the pulse duration from an initial value of Δt to final values of $3\Delta t$ (figure 5c) and $9\Delta t$ (figure 5d) indicate that the

crack lengths become progressively longer as the pulse duration increases.

The spatial distribution of impact damage cracks is now examined in the context of recent research³. This research has shown that an exponential distribution of the form

$$f(\eta) = \exp[-\lambda\eta] \quad (7)$$

describes the crack number density for water drop induced damage. A single value of the scaling parameter, λ , adequately describes the crack distributions for several materials and for damage induced by two different laboratory techniques (water jet and water drop impact). The analysis entails mapping the inner and outer radii of the damage annulus (r_{\min} and r_{\max} , respectively) into a transformed coordinate system η such that $r_{\min} \rightarrow \eta_{\min}$, $r_{\max} \rightarrow \eta_{\max}$.

For twelve polycrystalline specimens representing seven different materials (ZnS , $3\text{Al}_2\text{O}_3$, 2GeO_2 , $3\text{Al}_2\text{O}_3 \cdot 2\text{SiO}_2$, MgF , MgO , Si_3N_4 , and ZnSe) the following relation yields a satisfactory fit* to the crack number density data (figure 6)

$$\lambda = 3.49/\eta_{\max} \quad (8)$$

These results thus form a quantitative basis for comparing the simulated impact damage to the actual impact damage. On this basis the crack number density obtained from the computer simulation (fig. 7) agrees favorably with experimental results. In order to perform this

*For each of the twelve polycrystalline materials, the significance levels α (obtained from a chi-squared "goodness of fit" test) are at the 0.25 level in most cases, and are ≥ 0.10 in all cases.³

comparison in a statistically meaningful way, the experimental data and the simulation data were sampled in the same way. For the actual damage, the crack population was sampled by superposing a polar grid upon optical micrographs of the damage field, followed by location of the radial position of each crack that intersects a grid line (figure 8). A subroutine included in the damage simulation sampled the calculated crack array in an identical fashion. Subsequent to the crack sampling, the data set obtained from the micrographs and the data set resulting from the simulation were analysed by the same statistical program.

4. CONCLUSIONS

A simulation of the water drop impact damage process has been developed which incorporates both graphical and statistical capabilities. The graphical facility allows rapid assessment of the simulation results, while the statistical facility provides a tool for analysing some of the details of the crack distributions.

The present computer simulation of water drop impact damage will be extended and refined by a number of program changes. For example, the simple rectangular stress pulse profile will subsequently be replaced by stress pulse profiles that evolve according to analytical^{19,26} and numerical^{21,22} predictions. A variety of surface stress wave attenuation mechanisms and functional forms will be considered, including geometrical spreading^{6,9}, "leaky" surface modes^{23,24}, temperature-dependent phonon scattering^{25,26}, and scattering from grains¹², surface irregularities²³, and from localized defects such as pre-existing cracks.²⁷⁻²⁹

Acknowledgments

This work was supported by the Office of Naval Research under
Contract No. N00014-81-K-0362.

APPENDIX

DERIVATIONS OF OUTER BOUND FOR SIMULATION

At a radial distance r_{\max} the amplitude of the stress pulse has sufficiently attenuated that crack extension can no longer occur. It is important to make a prior estimate of r_{\max} to avoid inclusion of a substantial number of inactive cracks at $r > r_{\max}$ and hence, to avert an inefficient simulation. An upper bound estimate of r_{\max} , referred to as r_{bound} , can be obtained from the critical stress intensity, K_{IC} , the maximum flaw length, a_{\max} , and the form of the surface wave attenuation. If K_{IC} is considered constant over the modeled region, then for a given flaw population, the flaw of length a_{\max} will not extend at a stress $< \sigma_b$ given by

$$\sigma_b = \frac{K_{IC}}{2(a_{\max})^{1/2}} \quad (A1)$$

The stress amplitude, σ , at radial distance r is

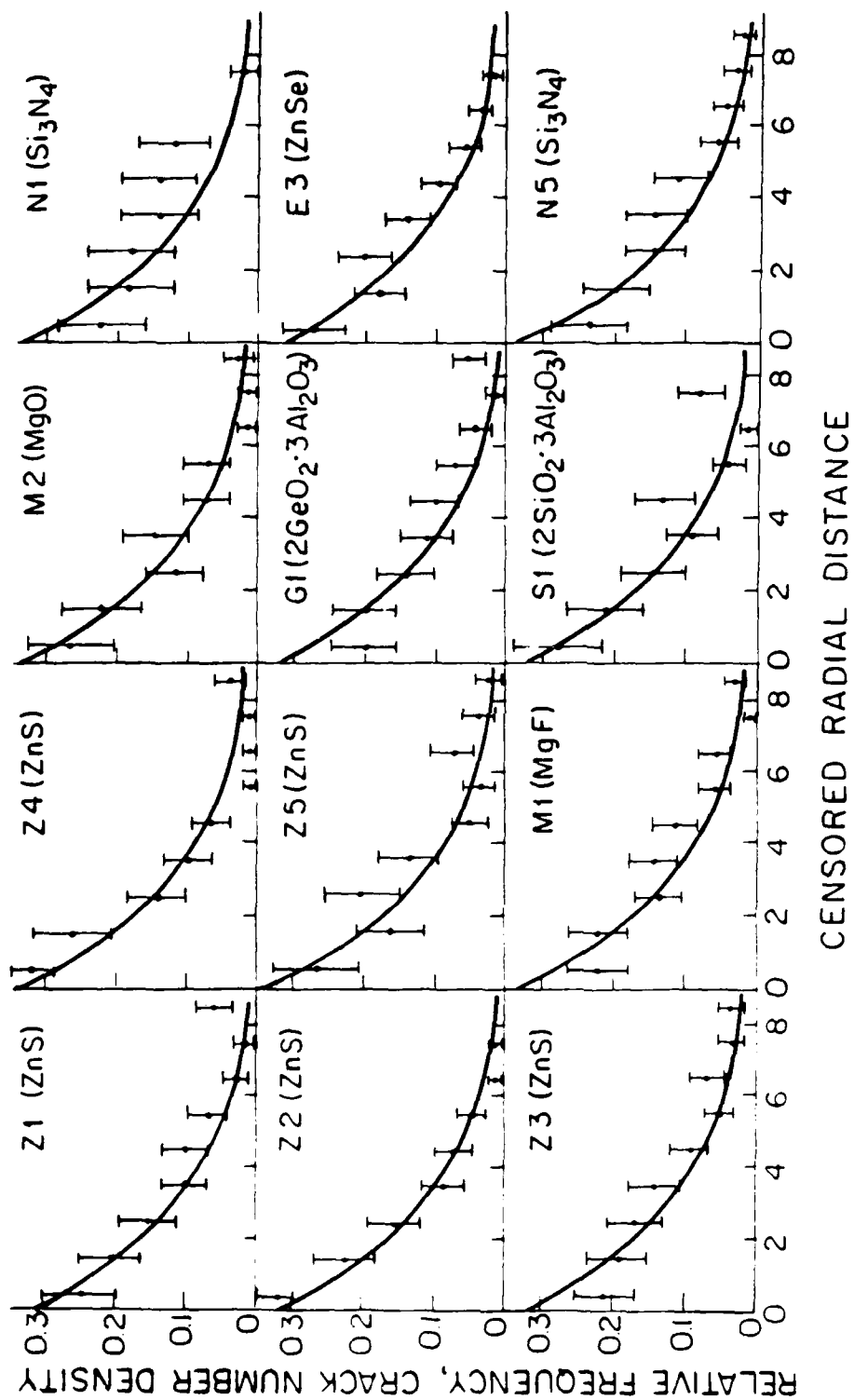
$$\sigma = \sigma_0 \exp[-\alpha(r-r_0)] \quad (A2)$$

where r_0 is the radial distance from which the stress wave is launched. The inclusion of r_0 in equation (A2) acknowledges that the stress waves (produced by the impact event) separate from the expanding contact zone of the drop only after some small radial distance, r_0 , has then traversed^{20,21}. To a first approximation, r_0 may be approximated by r_{\min} , the inner radius of the damage annulus³⁰. Thus the stress amplitude at r_{bound} is

$$\sigma_b = \sigma_0 \exp[-\alpha(r_{\text{bound}}-r_{\min})] \quad (A3)$$

Hence, from equations (A1) and (A3)

Fig. 6



XBL 839-6327A

Fig. 5d

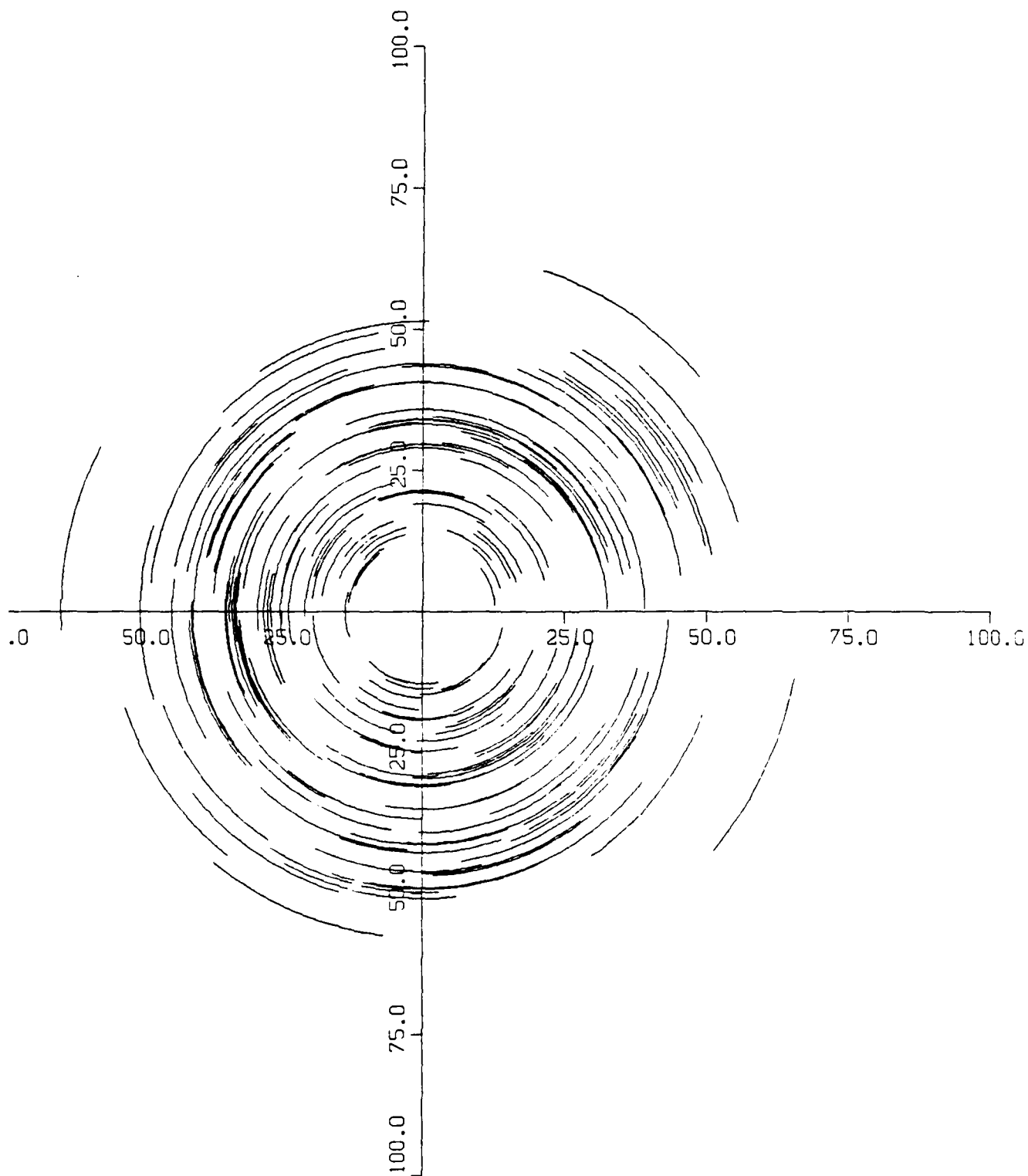


Fig. 5c

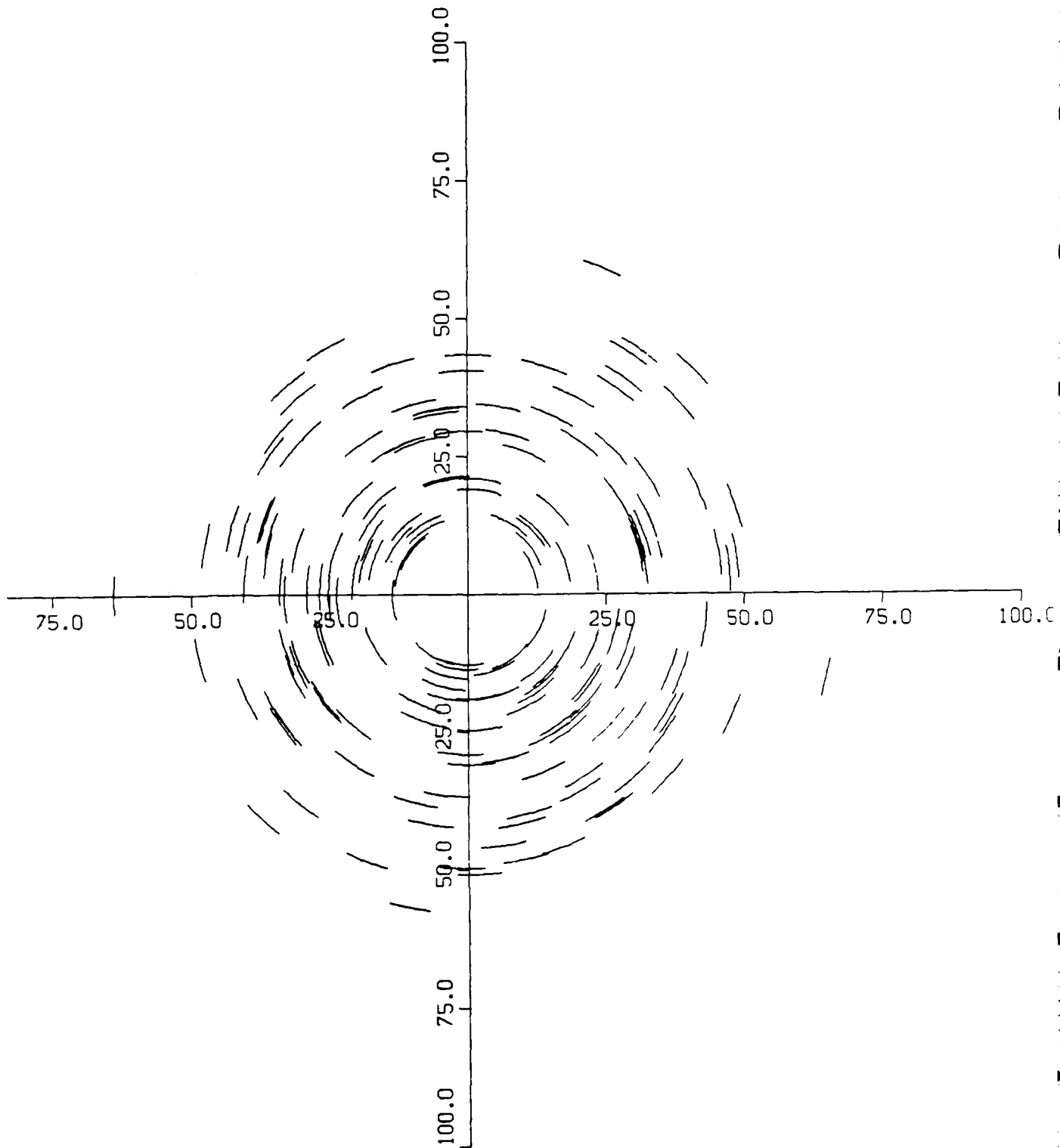


Fig. 5b

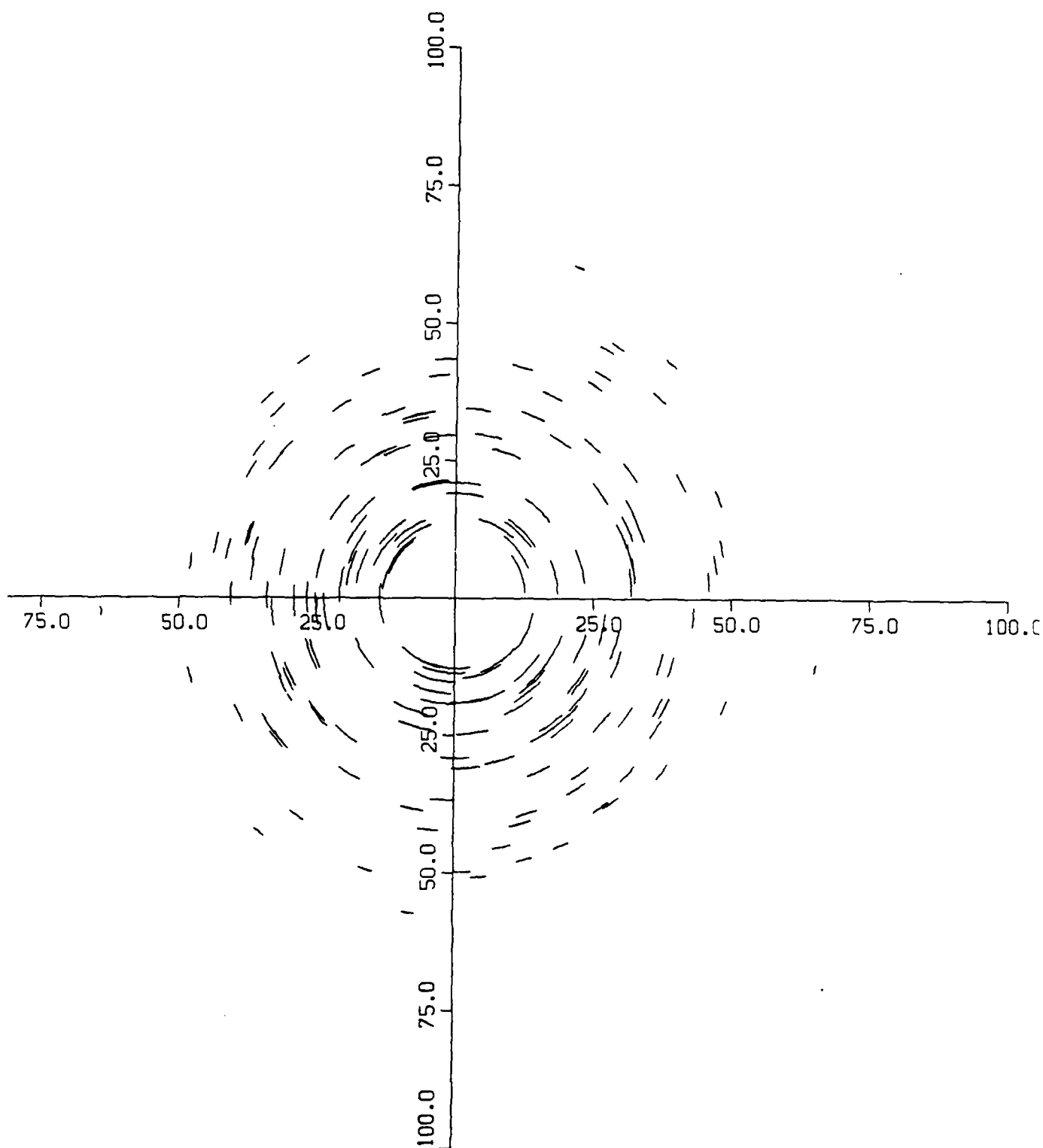


Fig. 5a

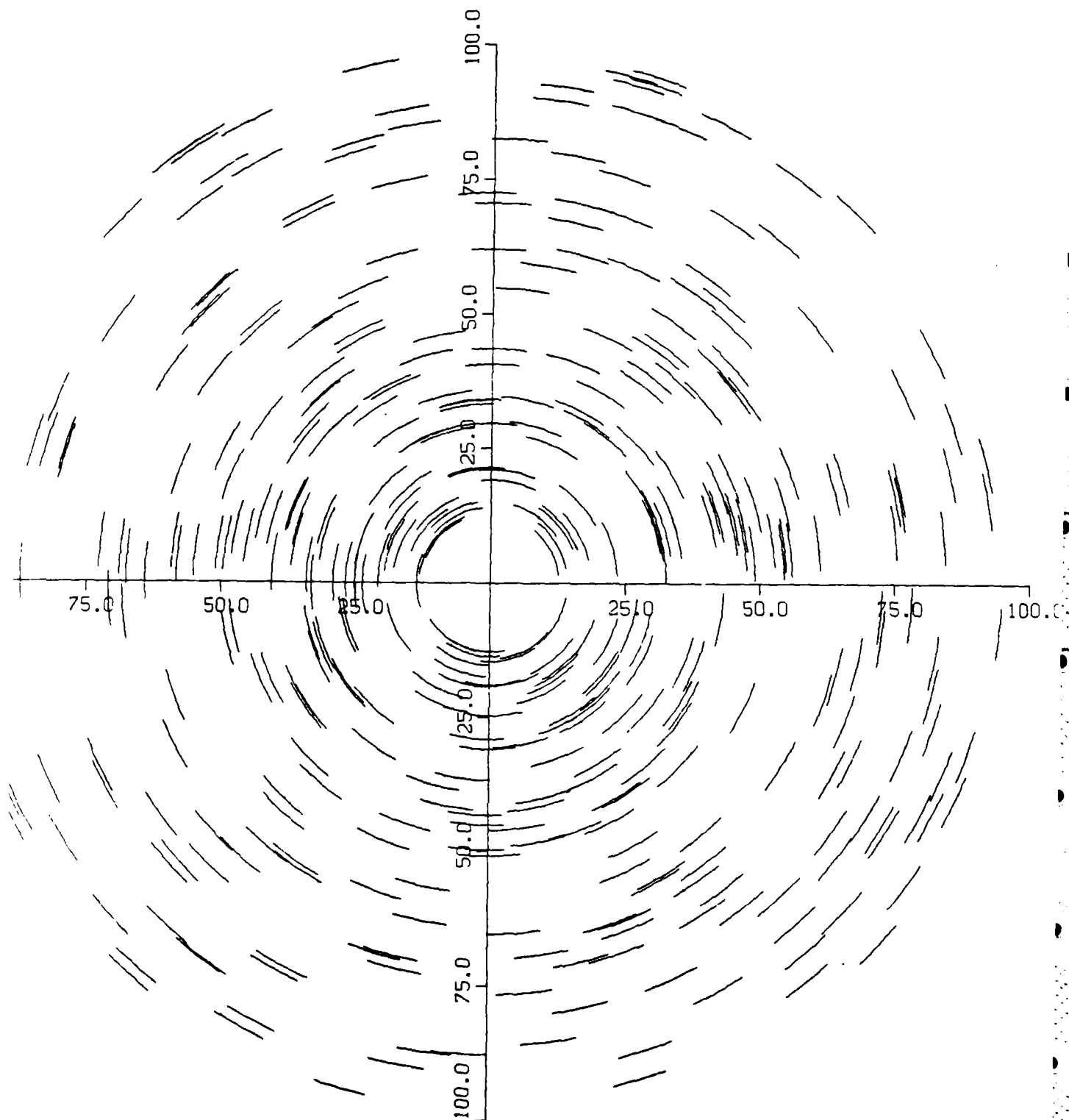
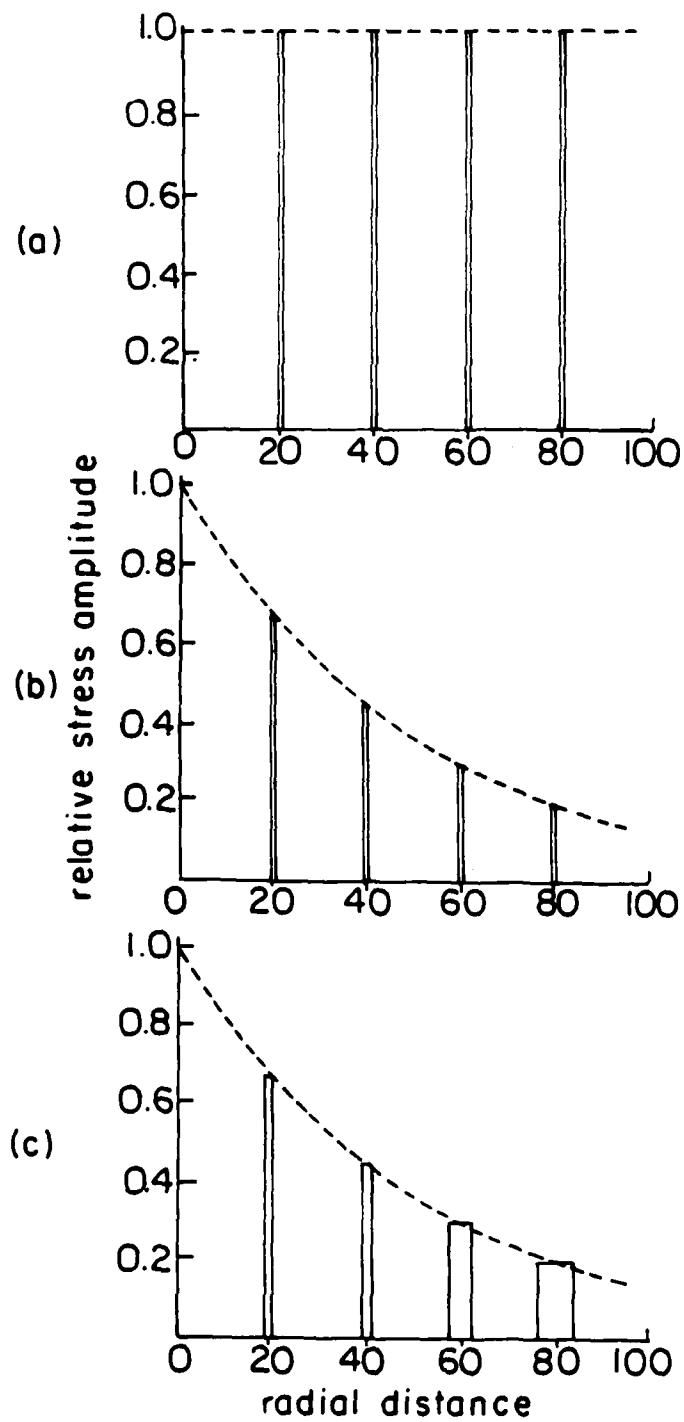
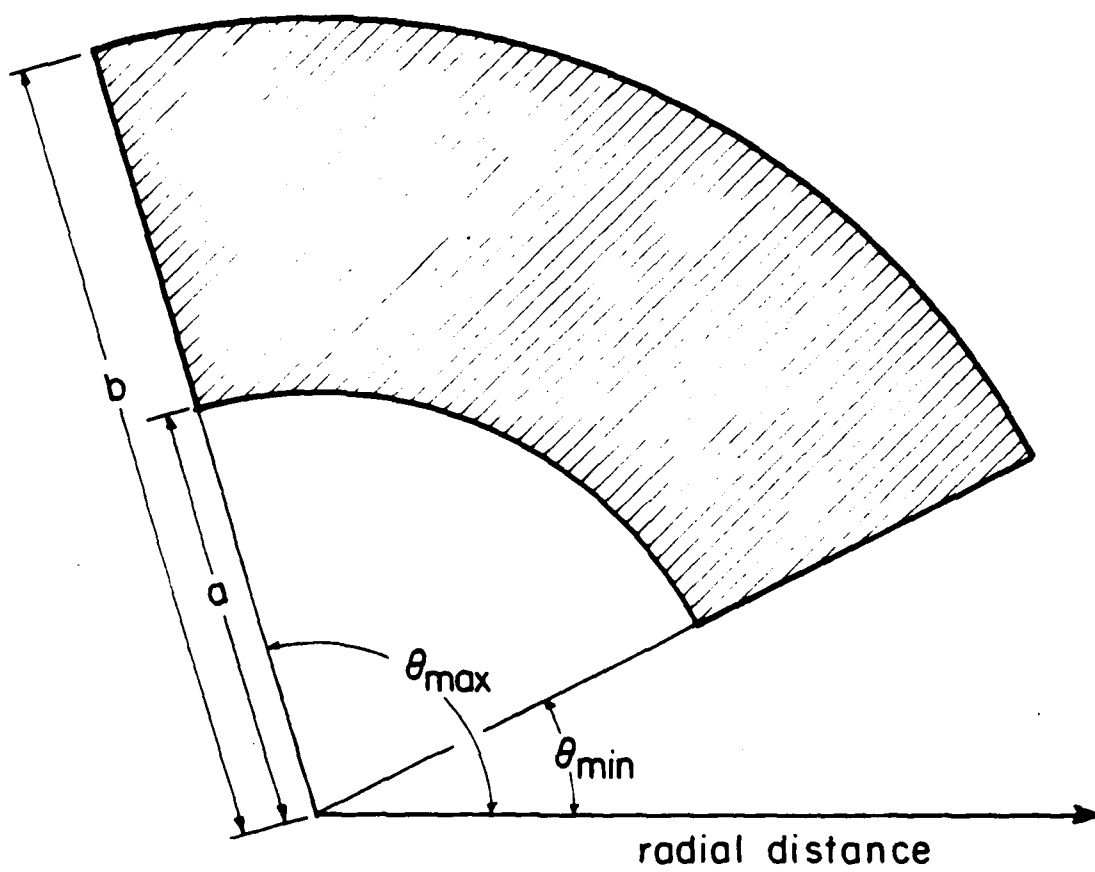


Fig. 4



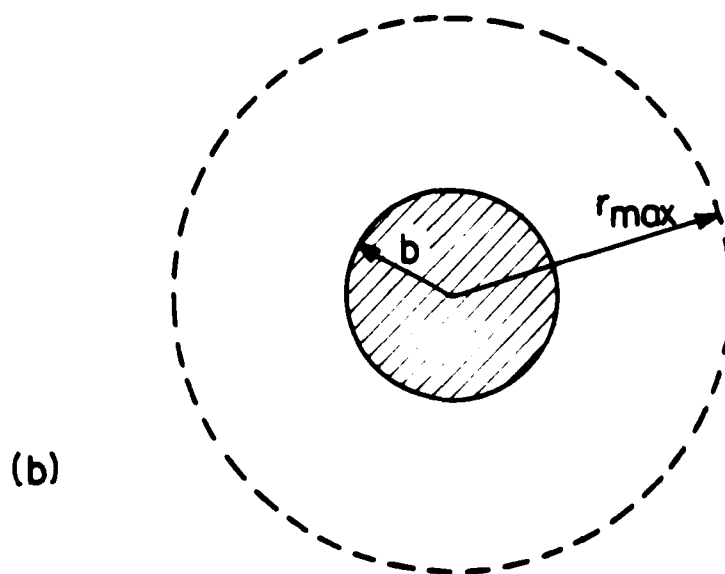
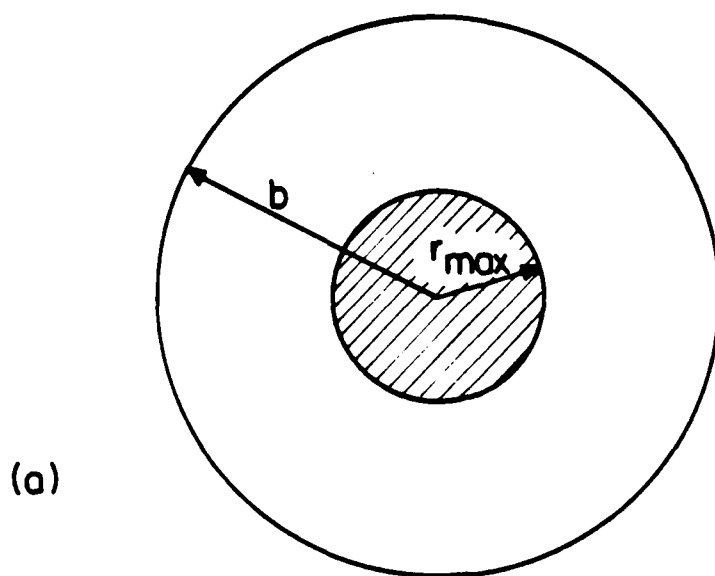
XBL842-6651

Fig. 3



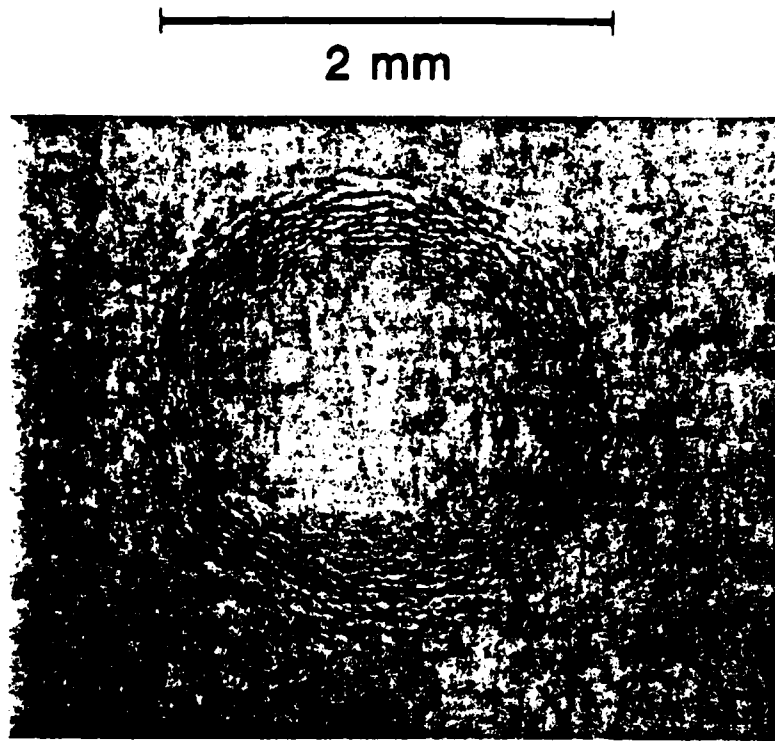
XBL 842-6649

Fig. 2



XBL 842-6650

Fig. 1



ZnS water jet impact
Impact velocity = 350 m/sec
Equivalent drop diameter = 4.5 mm

- 5c. Computer-generated impact crack array, for both amplitude attenuation and temporal spreading. (In this case, at $r = 100$, $\Delta t = 3\Delta t_0$ and $\sigma \approx 0.1 \sigma_0$, where Δt_0 is the initial stress pulse duration.
- 5d. Computer-generated impact crack array, where at $r = 100$, $\Delta t = 9\Delta t_0$ and $\sigma \approx 0.1 \sigma_0$.
6. Probability density functions for the crack number density of impact damage cracks as a function of normalized distance, n . In each graph, the solid line indicates $f(n) = \lambda \exp(-\lambda n)$, where $\lambda = 0.349$.
7. A comparison between crack number densities predicted by the simulation, and crack number densities obtained from optical micrographs of impact damage. The solid line indicates $f(n) = \lambda \exp(-\lambda n)$, where $\lambda = 0.349$.
8. Schematic showing crack sampling method used for optical micrographs of impact damage.

Figure Captions

1. Optical micrograph of impact damage for polycrystalline ZnS impacted by a water jet having a 4.5 mm equivalent water drop diameter and a velocity of 350 msec^{-1} .
2. Schematics showing errors that result from improper choices for b , the outer radius of the surface region included in the simulation. If $b \gg r_{\text{max}}$, the simulation is quite inefficient, as only a small fraction of the total initial flaw population is included in the region where crack growth can occur ($r \leq r_{\text{max}}$), as shown in (a). If $b \ll r_{\text{max}}$, (b), then the crack field is truncated in an unrealistic fashion.
3. The annular sector over which initial flaws are distributed, which is bounded by polar angles θ_{min} and θ_{max} , at radial distances $a \leq r \leq b$.
4. Temporal evolution of the initial stress pulse, for (a) no attenuation, constant pulse duration, (b) non-zero attenuation with constant pulse duration, and (c) both attenuation and a linearly increasing pulse duration.
- 5a. Computer-generated impact crack array for the case of no amplitude attenuation and no temporal spreading of the initial stress pulse.
- 5b. Computer-generated impact crack array, for no temporal spreading of the stress pulse (t is a constant), but with attenuation coefficient α such that at radial distance $r = 100$, the stress pulse amplitude $\sigma \approx 0.1 \sigma_0$ (where σ_0 is the initial stress pulse amplitude).

14. E. D. Case and A. G. Evans, Proc. 6th Conf. on Erosion by Liquid and Solid Impact, 20-1 to 20-6, Cambridge, England (1983).
15. A. G. Evans, J. Appl. Phys., 49 (6), 3304-3310 (1978).
16. L. B. Freund, J. Mech. Phys. Solids, 21, 47-61 (1973).
17. J. D. Eshelby, Mech. Phys. Solids, 17, 177-199 (1969).
18. L. R. F. Rose, Int. J. Fract. Mech., 12 799-813 (1976).
19. R. M. Blowers, J. Inst. Math. Appl. 5, 167-193 (1969).
20. A. G. Newlands, J. Inst. Math. Appl. 19, 195-203 (1977).
21. W. F. Adler, J. Mater. Sci. 12, 1253 (1977).
22. F. Adler, Final Report to the Office of Naval Research, CR-82-1075 (1982).
23. B. A. Auld, Acoustic Fields and Waves in Solids, Volume II, John Wiley and Sons, New York (1973).
24. J. A. Hudson, The Excitation and Propagation of Elastic Waves, Cambridge University Press, Cambridge, England (1980).
25. A. J. Budreau and P. H. Carr, Appl. Phys. Lett. 18, 239 (1971).
26. R. F. Wallis, Chapter 7 in Dynamical Properties in Solids, G. K. Horton and A. A. Maradudin, editors, American Elsevier Publishing Company, New York (1975).
27. I. A. Viktorov, Rayleigh and Lamb Waves, Plenum Press, New York (1967).
28. G. S. Kino, J. Appl. Phys., 49, 3190-3199 (1978).
29. B. A. Auld, Wave Motion 1, 3-10 (1979).
30. E. D. Case and A. G. Evans, unpublished work.

REFERENCES

1. A. G. Evans, J. Appl. Phys. 49 (6): 3304-3310, 1978.
2. S. van der Zwaag, J. T. Hagan, and J. E. Field, J. Mater. Sci. 15: 2965-2972, 1980.
3. E. D. Case, K. M. Louie, and A. G. Evans, accepted for publication, J. Mater. Sci. Letters.
4. W. F. Adler, Proc. Soc. Photo-Optical Instr. Eng., 297: 143-154, 1981.
5. N. S. Corney and J. S. Pippett, 24-1 to 24-7 in Proc. Sixth Int. Conf. on Erosion by Liquid and Solid Impact, ed. J. E. Field and N. S. Corney, Cavendish Laboratory, Cambridge, England, 1983.
6. S. Van der Zwaag and J. E. Field, Eng. Fract. Mech., 17 (4), 367-379.
7. F. P. Bowden and J. E. Field, Proc. R. Soc. London, A282: 321, 1965.
8. A. G. Evans and T. R. Wilshaw, J. Mater. Sci. 12: 97-116, 1977.
9. M. V. Swain and J. T. Hagan, J. Mater. Sci. 15: 387-404, 1980.
10. N. R. Mann, R. E. Schafer, and N. D. Singpurwalla, Chap. 5 in Methods of Statistical Analysis of Reliability and Life Data, John Wiley and Sons, New York, 1974.
11. A. G. Evans and R. L. Jones, J. Am. Ceram. Soc. (1978) 156.
12. A. G. Evans, B. R. Tittman, L. Ahlberg, B. T. Khuri-Yakub, and G. S. Kino, J. Appl. Phys., 49, 2669-2674 (1978).
13. R. W. Hertzberg, p. 386 in Fracture and Deformation of Engineering Materials, Second Edition, Wiley & Sons, New York, 1983.

$$r_{\text{bound}} = -\frac{1}{\alpha} \log \left[\frac{\sqrt{\pi} K_{\text{IC}}}{2 \sigma_0 (a_{\text{max}})^{1/2}} \right] + r_{\text{min}} \quad (\text{A4})$$

$$\equiv \frac{1}{\alpha} \log \left[\frac{28 z v_1 (a_{\text{max}})^{1/2}}{\sqrt{\pi} K_{\text{IC}}} \right] + r_{\text{min}} \quad (\text{A5})$$

Equation (A5) provides an analytic method for setting size limits for the region to be modeled in the damage simulation, which is of vital importance in the computer modeling process. For example, if the initial flaws are distributed over a circular region having area S_1 and radius b , then none of the flaws in the annular region described by $r_{\text{max}} < r \leq b$ (and having area S_2) will grow as a result of the impact. Assuming a constant surface number density of initial flaws, the fraction of the initial flaw population that is ultimately utilized in the damage simulation is given by the ratio of the area S_1 to the total area, S_t , included in the simulation, or

$$\frac{S_1}{S_t} = \frac{S_1}{S_1 + S_2} = \left(\frac{r_{\text{max}}}{b} \right)^2 \quad (\text{A6})$$

If b had been chosen so that $b = 5r_{\text{max}}$, then only 4 percent of the initial flaw population would lie in the region $r \leq r_{\text{max}}$ subject to crack growth. The remaining 96 percent of the initial flaw population is essentially superfluous to the damage simulation.

Fig. 7

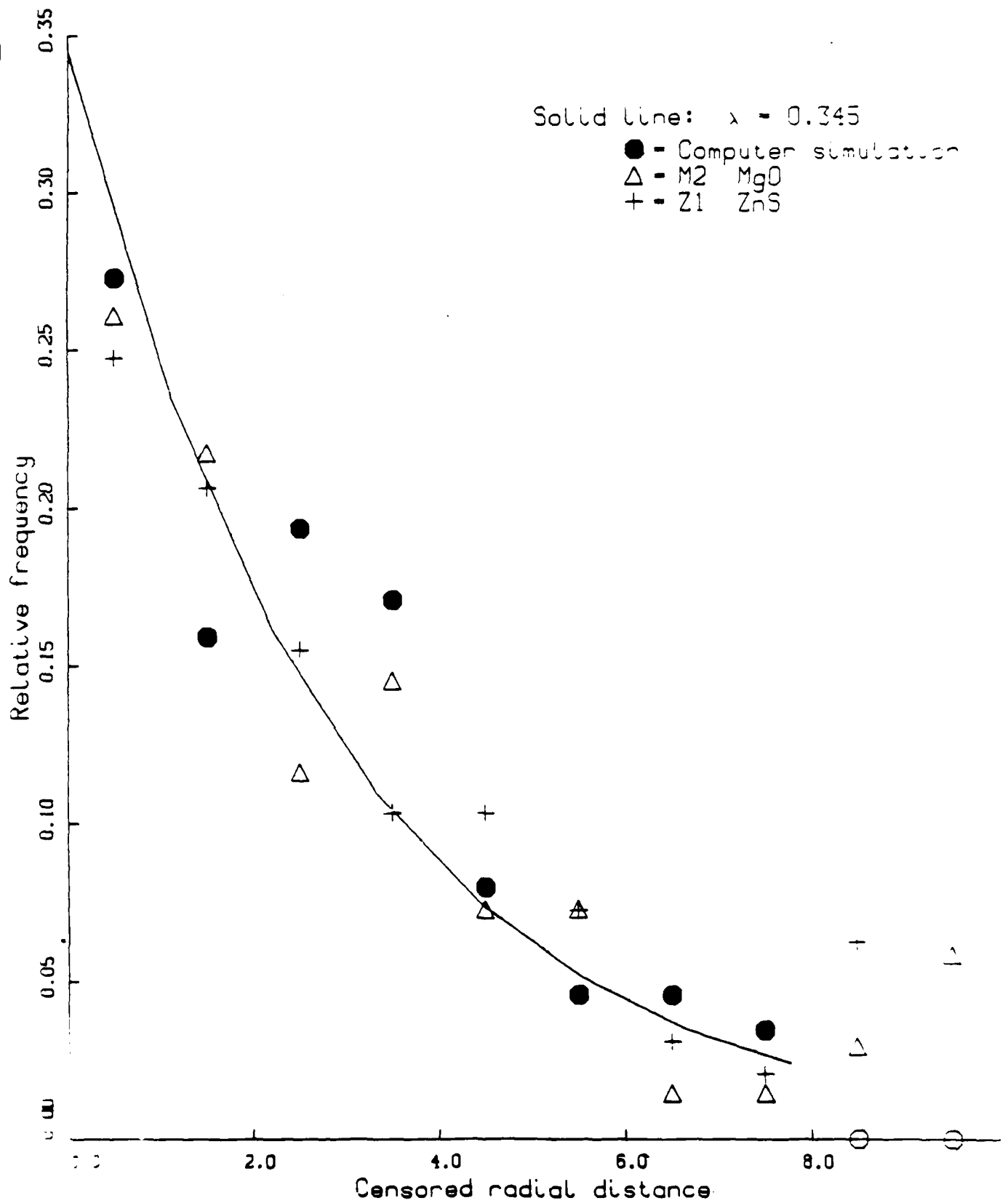
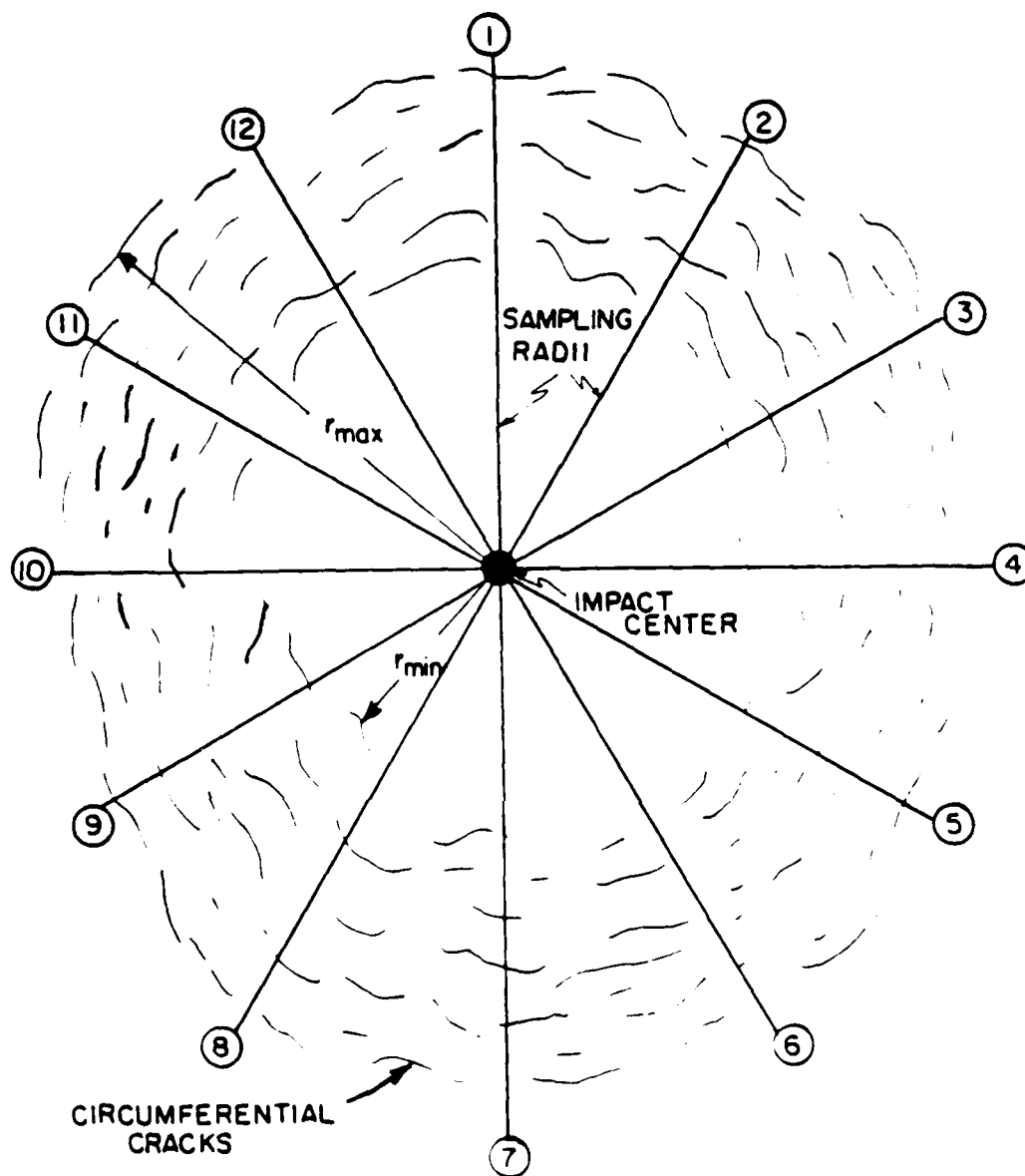


Fig. 8



XBL839-6326

CHAPTER XI

STATISTICAL ANALYSIS OF DAMAGE
INDUCED BY WATER DROP OR WATER JET IMPACT

E. D. Case, K. M. Louie and A. G. Evans

STATISTICAL ANALYSIS OF DAMAGE
INDUCED BY WATER DROP OR WATER JET IMPACT

by

E. D. Case, K. M. Louie and A. G. Evans

Department of Materials Science and Mineral Engineering

University of California

Berkeley, CA 94720

Infrared transmitting materials are susceptible to surface damage upon impact by water drops or water jets. This damage, manifest as circumferential cracks (fig. 1a) and near surface plastic deformation, can result in appreciable transmission losses (fig. 1b) at wavelengths of practical interest (4-20 μm) [1]. The magnitude of the loss is dictated by the complete damage spectrum. Hence, methods for characterizing the damage spectrum are needed in order to relate impact conditions to transmission loss and thereby, to determine the role of the important material parameters. A characterization scheme, and its utility, are investigated in this study.

Prior assessment of damage has focused on one, or a few, cracks within the crack field. In particular, measurements have been made of the maximum subsurface crack length or the crack length at the minimum distance from the impact center [2,3]. These measurements are pertinent to strength degradation, but not to transmission loss assessment. A more satisfactory approach for purposes of transmission loss analysis is to use the statistical distributions of crack length or radial position to characterize the damage state. Most of the cracks in the damaged region then contribute to the analysis.

The surface damage* resulting from impact by water jets or water drops has been investigated for 13 individual specimens of eight widely different materials** (Table 1). Among the thirteen specimens, the

*The subsurface damage characteristics are explored in a subsequent investigation.

**Micrographs of water drop damaged specimens were taken from a study by Adler [4]. Water jet damaged specimens were obtained by one of the authors (E. D. Case) at J. E. Field's water jet facilities, Cavendish Laboratory, Cambridge, England.

area included in the damage annulus, A_d , varies by more than two orders of magnitude, indicating a wide range in the spacial extent of the damage.

The crack population is sampled by superposing a polar grid on optical micrographs of the damage, followed by location of the radial position, r_i , of each crack that intersects the grid line (fig. 2). The number of cracks contained within each radial interval yields a measure of the crack number density, from which the probability density function can be evaluated.

Applying a simple coordinate transformation to the radial distance coordinate, r , produces a striking consistency among the distribution functions (fig. 3), considering the wide range of materials and impact conditions represented by the data (Table 1). The transformed coordinate, η , is obtained by setting the inner radius r_{\min} , to zero, and the outer radius, r_{\max} , to a fixed integer η_{\max} .*

Furthermore, if the data are censored to only include those measurements at radial distances equal to or beyond the mode (or maximum), η_{mode} , a unified function emerges for all materials and impact conditions, given by

$$f(\eta) = \lambda \exp[-\lambda(\eta - \eta_{\text{mode}})]$$

or equivalently

$$f(\eta_c) = \lambda \exp(-\lambda \eta_c) \quad (1)$$

* Different values of η_{\max} have been used to mitigate against the possibility of a fortuitous choice of η_{\max} affecting the data.

where η_c is the radial distance to the crack in censored coordinates. The scaling parameter, λ , may be estimated from the mean of the censored data, $\langle \eta_c \rangle$, such that

$$\lambda = 1/\langle \eta_c \rangle \quad (2)$$

Alternatively, λ depends on λ_{\max} , such that the following relation yields a satisfactory fit to the data for each of the polycrystalline materials (fig. 4) for both the water drop and water jet impacted specimens

$$\lambda = 3.49/\eta_{\max} \quad (3)$$

The current statistical sampling technique (fig. 2) yields only about 100 to 150 observations (crack positions) per specimen, which is equivalent to about 10 percent of the total population. Thus, the relative error in the crack number density is large enough that it is difficult to determine whether there are small differences among the λ 's for the various specimens. The λ values based on data from individual specimens (Eq. 2) agrees with the "average" (Eq. 3) to within a multiplicative factor of 1.4, for all polycrystalline specimens. However, in terms of the crack number density (Eq. 1) neither estimate yields a clear "best fit" for a given specimen (fig. 5). Table II summarizes the significance levels, α , obtained for a chi-squared "goodness of fit" test, using λ values computed by both equations 2 and 3. Both equations apply to all polycrystalline materials at the 0.25 significance level in most cases, and a

significance level of ≥ 0.10 in all cases. However, for the borosilicate glass, an appreciably smaller λ ($2.5/\eta_{\max}$) is needed to correlate the data.

It is noted here that, although the exponential probability density function, $\exp(-\lambda\eta)$, asymptotically approaches zero for large η , it is never identically zero. Consequently, the actual crack distribution terminates at a radial distance r_{\max} (or η_{\max} in transformed coordinates).*

The uniformity of the spatial distribution of circumferential cracks for such a wide range of materials and impact conditions has several important implications for damage characterization. A comparison of initial interest is the similarity of the damage distributions for the water drop and jet impacted specimens when viewed in the transformed coordinates.** This indicates a fundamental similarity in the damage created by these two test procedures, in the near-surface region, beyond the mode of the distribution. It remains, of course, to compare the relative sub-surface features.

These results, however, have much more importance than just the similarity between the water drop and the water jet technique. The results show that, for materials as dissimilar as ZnSe and Si_3N_4 , a

* For $\lambda = 3.49/\eta_{\max}$, the probability of finding a crack in the radial distance interval $1.5\eta_{\max} \leq \eta < \infty$ is only 0.0053. If $N = 120$, then ~ 0.64 cracks are expected in the entire interval $1.5\eta_{\max} \leq \eta < \infty$.

** Adler compared water drop and water jet damage characteristics, and concluded the test procedures are not similar in the untransformed coordinates. However, Adler did not attempt comparisons for transformed or normalized coordinates [5].

"scaling law" is operative in the impact damage problem, such that, subject to the proper coordinate transformation, the crack number density curves can be made to coincide. For discussion purposes, we presume that the existence of a unifying distribution indicates a spatial distribution of surface damage that depends on a stress field characteristic; such as the change in the stress pulse profile with radial distance from the impact center.

The dependences on material and impact parameters must be embodied within the expressions that map r_{\min} and r_{\max} back into real coordinates r_{\min} and r_{\max} . A key remaining problem thus entails deriving explicit functional forms for r_{\min} and r_{\max} in terms of such parameters as the critical stress intensity factor, the attenuation coefficient for surface acoustic waves, the impact velocity, drop size, etc. These relations, coupled with equation (1) would allow predictions of the surface damage characteristics for any set of material and impact conditions.

Acknowledgments

The authors acknowledge D. Townsend and Professor J. E. Field of Cambridge University for the use of water jet facilities at Cavendish Laboratory, Cambridge, England. Material for Si_3N_4 specimens were provided by Dr. Jay R. Smyth of Garrett Turbine Engine Co., Phoenix, Arizona.

This work was supported by the Office of Naval Research under Contract No. N00014-81-K-0362.

References

1. E. D. Case and A. G. Evans, unpublished data.
2. S. van der Zwaag and J. E. Field, *J. Materl Sci.* 17:2625, 1982.
3. J. E. Field, D. A. Gorham, J. T. Hagan, M. J. Matthewson, M. V. Swain, and S. van der Zwaag, 13-1 to 13-11, *Proc. 5th Int. Conf. on Erosion by Liquid and Solid Impact*, Cambridge, 1979.
4. W. F. Adler, Final Report to Office of Naval Research, CR-82-1075, 1983.
5. W. F. Adler and T. W. James, Technical Report to Office of Naval Research, CR-80-758, 1980.

TABLE I

| Specimen Label | Material | Impact Velocity (m/sec) | Drop Size** (mm) | $A_d(\text{mm}^2)^{***}$ |
|----------------|--|-------------------------|------------------|--------------------------|
| Z1 | ZnS | 494 | 3.07 3.19 | 6.49 |
| Z2 | ZnS | 513 | 3.36 3.65 | 19.10 |
| Z3 | ZnS | 540 | 2.30 | 3.36 |
| Z4 | ZnS | 505 | 1.44 2.02 | 7.84 |
| Z5 | ZnS | 542 | 1.73 1.79 | 2.57 |
| G1 | $3\text{Al}_2\text{O}_3 \cdot 2\text{GeO}_2$ | 759 | 3.07 | 3.61 |
| S1 | $3\text{Al}_2\text{O}_3 \cdot 2\text{SiO}_2$ | 762 | 3.10 | 3.25 |
| M1 | MgF | 578 | 2.32 | 1.53 |
| M2 | MgO | 715 | 2.04 | 2.50 |
| B1 | Borosilicate glass | 469 | 2.41 | 0.17 |
| N1* | Si_3N_4 | 925 | 4.00 | 5.80 |
| N5* | Si_3N_4 | 925 | 4.00 | 12.59 |
| E3* | ZnSe | 375 | 4.00 | 7.70 |

* Water jet impacted specimens

** When two numbers are stated for a given drop, they indicate the minor and major axis for a quasi-ellipsoidal drop. A single entry for drop size indicates the diameter of a spherical drop [4], or in the case of the water jet impacts, the size indicates an equivalent spherical diameter [3].

*** A_d , the area of the damage annulus, is given by $\pi(r_{\text{max}}^2 - r_{\text{min}}^2)$, where r_{max} and r_{min} are, respectively, the outer and inner radii of the damage annulus.

TABLE II

| <u>Specimen Label</u> | <u>λ(eq. 2)</u> | <u>α(eq. 2)</u> | <u>λ(eq. 3)</u> | <u>α(eq. 3)</u> |
|-----------------------|------------------------------------|-----------------------------------|------------------------------------|-----------------------------------|
| Z1 | 0.344 | 0.25 | 0.349 | 0.25 |
| Z2 | 0.488 | 0.10 | " | 0.25 |
| Z3 | 0.334 | 0.10 | " | 0.10 |
| Z4 | 0.470 | 0.25 | " | 0.25 |
| Z5 | 0.358 | 0.25 | " | 0.25 |
| G1 | 0.323 | 0.25 | " | 0.10 |
| S1 | 0.380 | 0.25 | " | 0.25 |
| M1 | 0.348 | 0.10 | " | 0.10 |
| M2 | 0.344 | 0.25 | " | 0.25 |
| B1 | 0.248 | 0.10 | " | 0.01 |
| N1 | 0.364 | 0.10 | " | 0.25 |
| N5 | 0.356 | 0.10 | " | 0.25 |
| E3 | 0.399 | 0.25 | " | 0.25 |

Figure Captions

- Figure 1a. Optical micrograph of impact damage for polycrystalline ZnS impacted by a water jet having a 4.0 mm equivalent drop diameter and a velocity of 350 msec^{-1} .
- Figure 1b. A Fourier Transform Infrared (FTIR) spectrograph showing the transmittance ratio $\tau_{\text{damaged}}/\tau_{\text{undamaged}}$ as a function of wave number for a 6.8 mm thick ZnSe specimen impacted by a water jet having a 4.0 mm equivalent drop diameter at a velocity of 375 msec^{-1} .
- Figure 2. Schematic showing the crack sampling method used.
- Figure 3a. Crack number density as a function of radial distance for water drop-impacted specimens.
- Figure 3b. Crack number density as a function of radial distance for water jet impacted specimens N1, N5, and E3. Water drop impacted specimen Z1 is shown for comparison.
- Figure 4. Probability density functions for crack number density data censored such that only $n \geq n_{\text{mode}}$, where n is the transformed radial distance, and n_{mode} indicates the location of the mode, or maximum, of the distribution. In each graph, the solid line indicates $f(n) = \exp(-n\lambda)$ and $\lambda = 0.349$.

Figure 5. Crack number density as a function of radial distance for three polycrystalline specimens. For each specimen the predicted number density is shown for both λ computed from Eq. 2 (dotted lines) and from Eq. 3 (solid lines). Specimens Z2 and Z4 are the two polycrystalline specimens for which the two λ estimates differ most (Table II).

AD-A151 978

MECHANICAL ASPECTS OF INTERFACES AND SURFACES IN
CERAMIC CONTAINING SYSTEMS(U) CALIFORNIA UNIV BERKELEY
DEPT OF MATERIALS SCIENCE AND MINERA.

5/5

UNCLASSIFIED

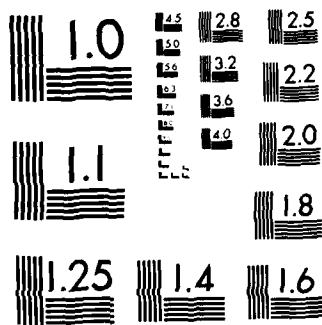
A G EVANS ET AL. 14 DEC 84 N00014-81-K-0362 F/G 20/11

NL

END

FILED

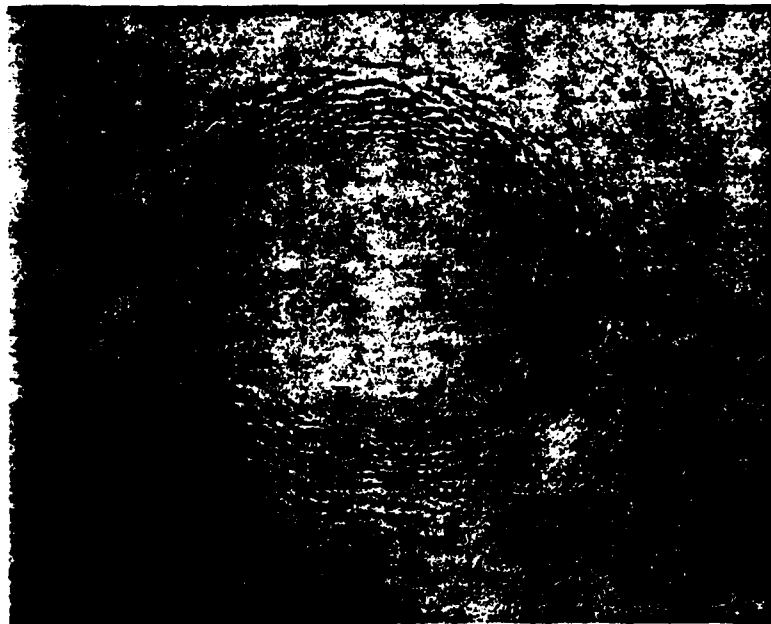
DTIC



MICROCOPY RESOLUTION TEST CHART
NATIONAL BUREAU OF STANDARDS-1963 A

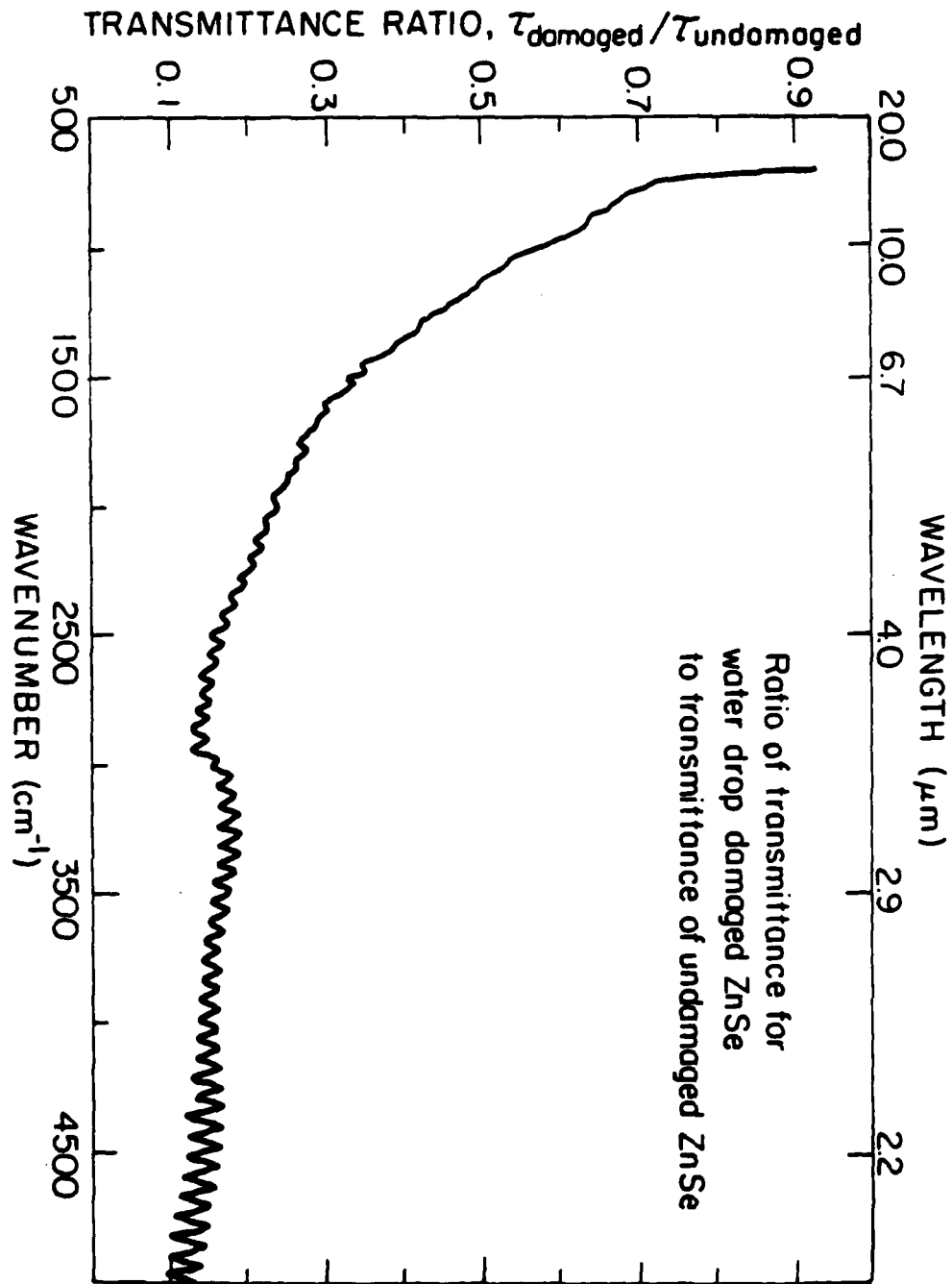
Fig. 1a

2 mm



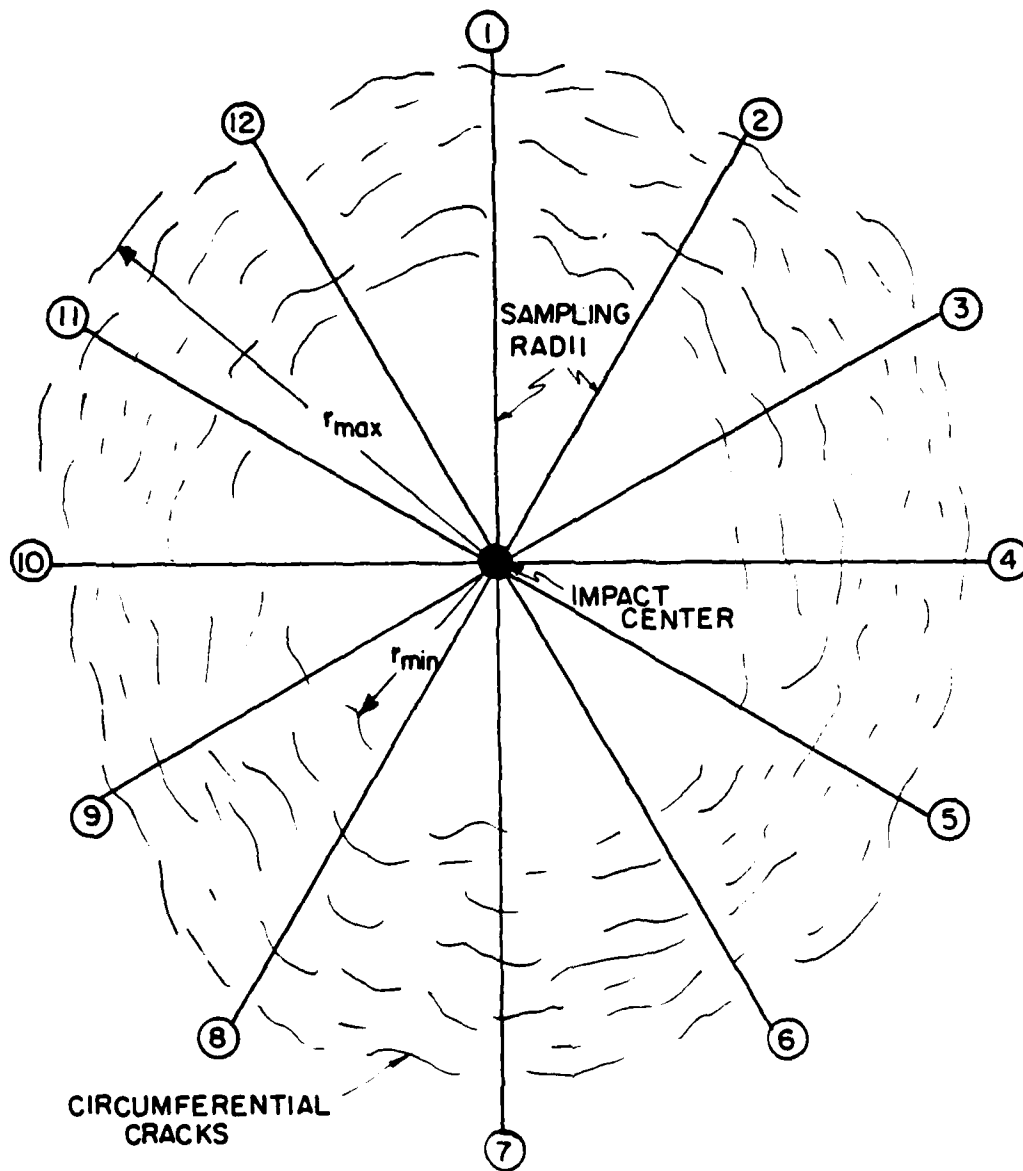
ZnS water jet impact
Impact velocity = 350 m/sec
Equivalent drop diameter = 4.5 mm

Fig. 1b



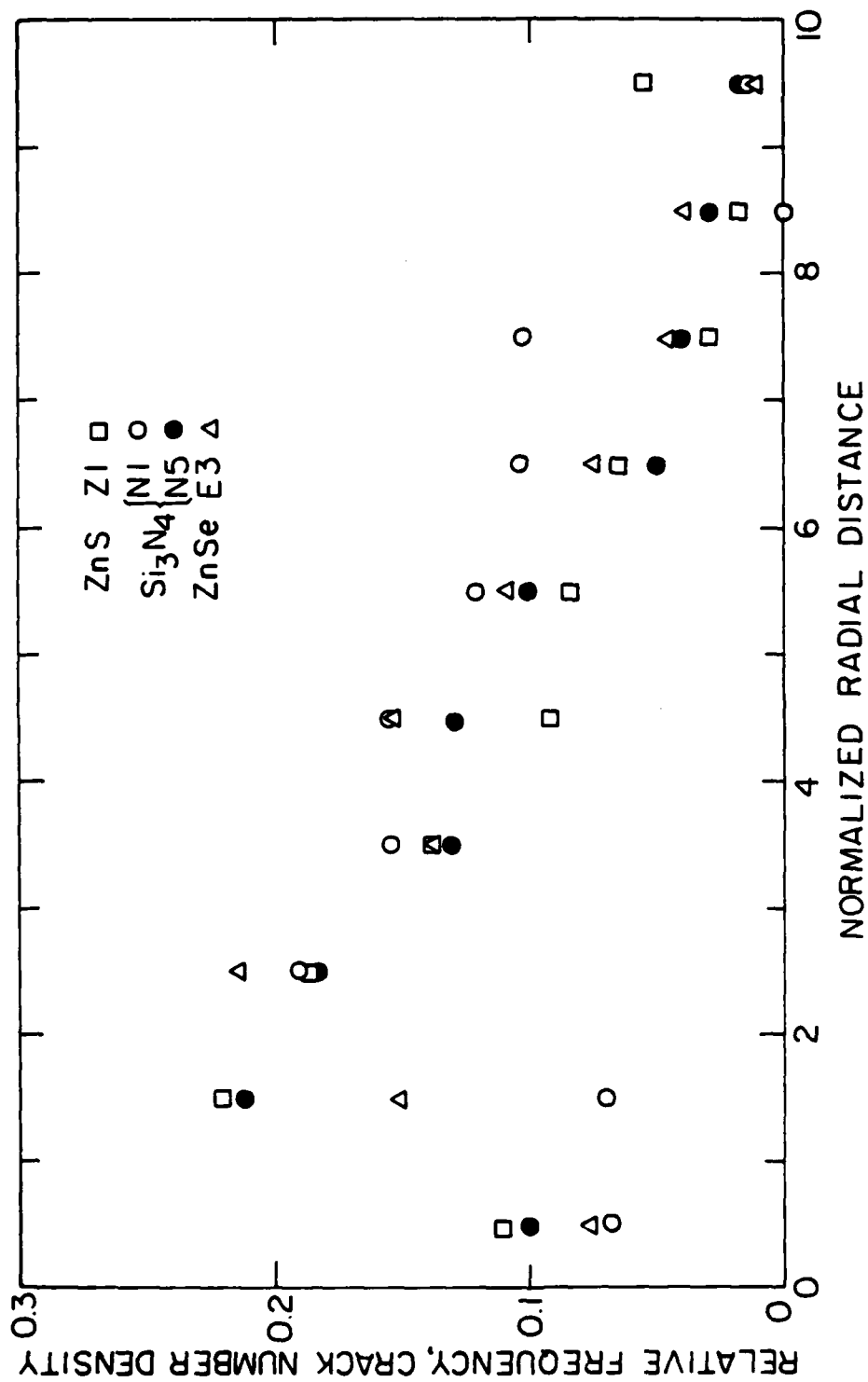
XBL 839-6330A

Fig. 2



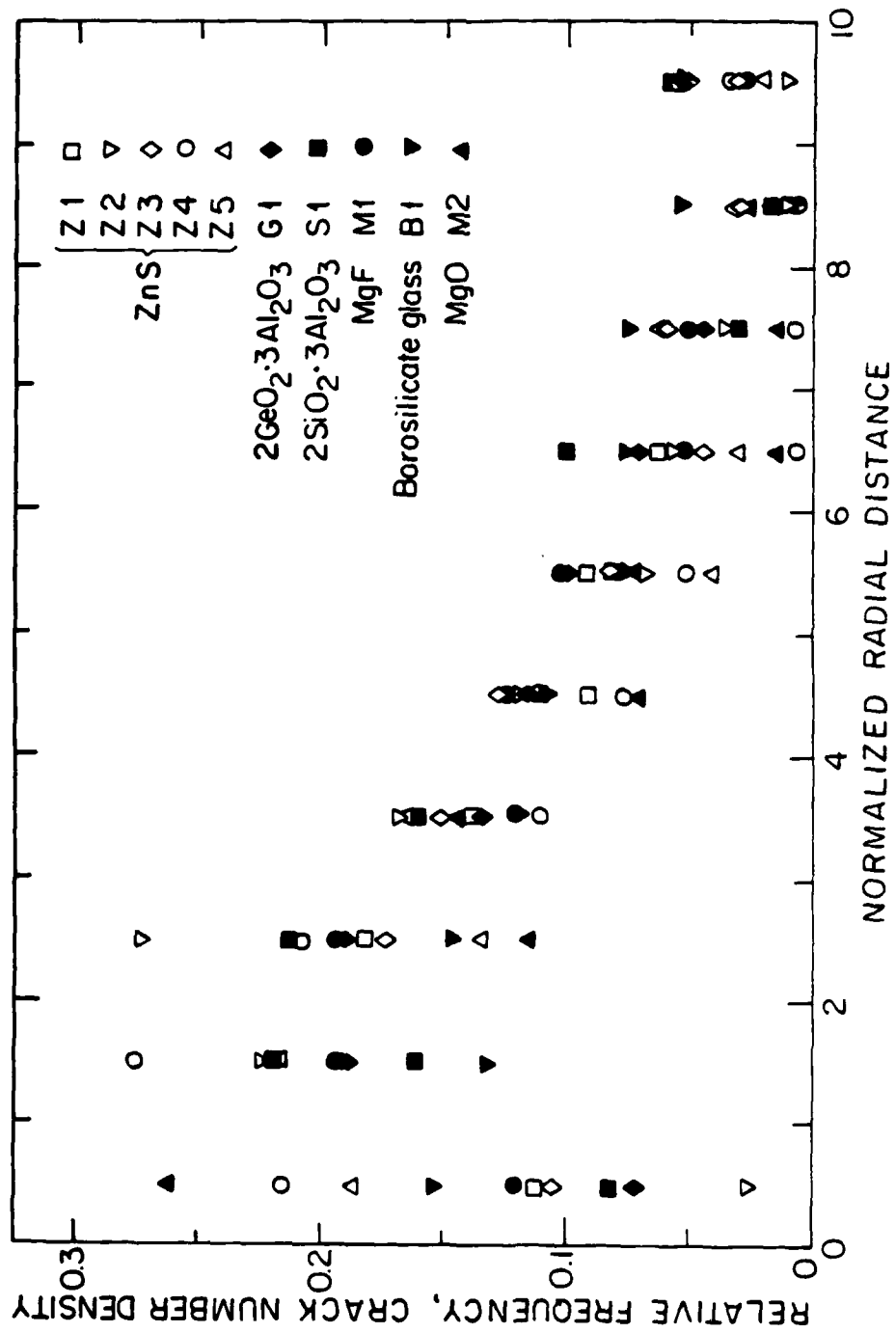
XBL839-6326

Fig. 3a



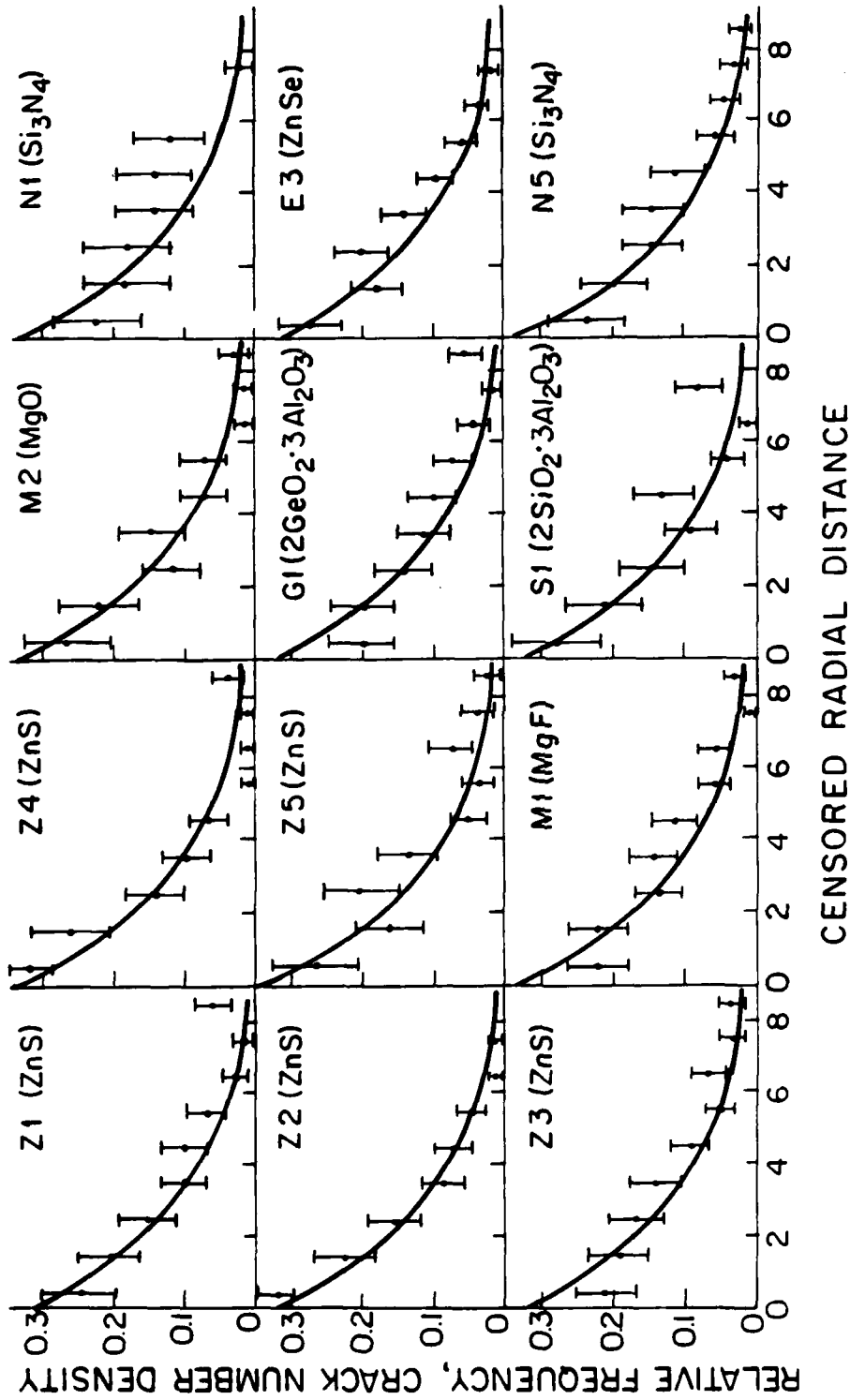
XBL 8312-4333

Fig. 3b



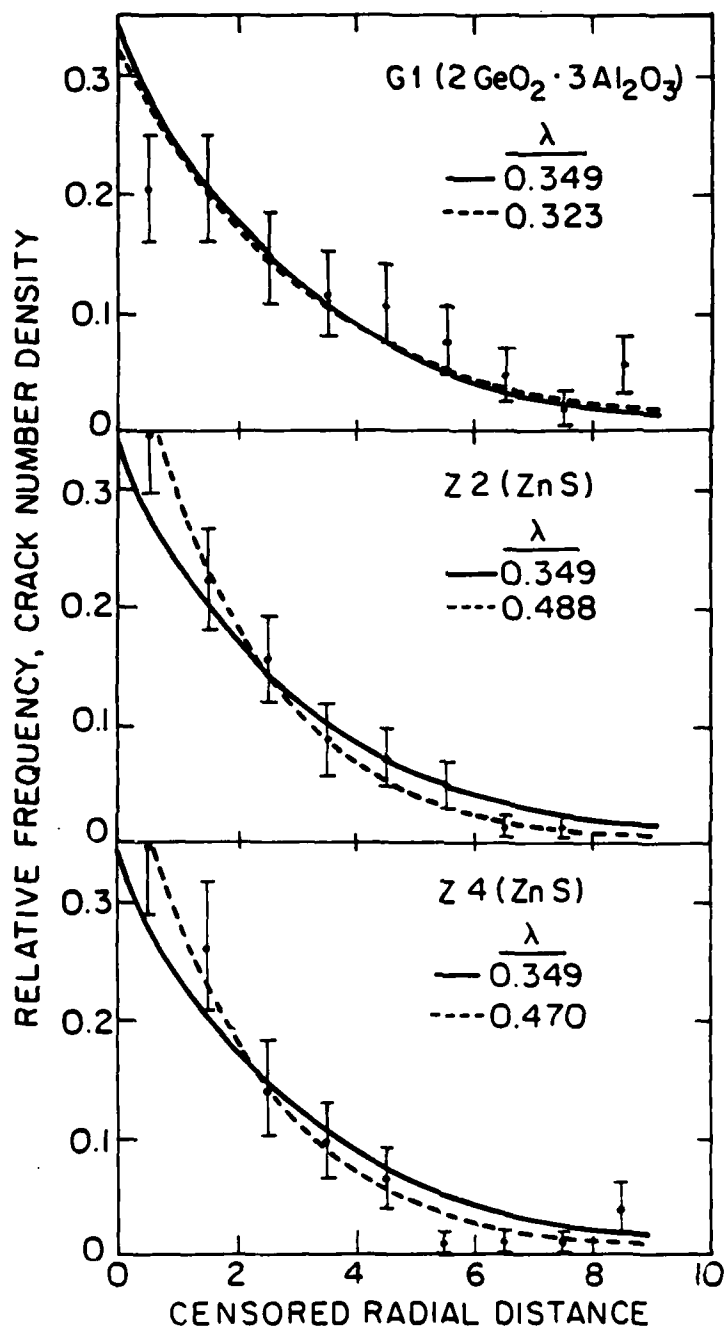
XBL 839 - 6329

Fig. 4



XBL 839-6327A

Fig. 5



XBL 8312-6899

CHAPTER XII

INNER RADIUS OF WATER DROP IMPACT DAMAGE FIELD

E. D. Case and A. G. Evans

INNER RADIUS OF WATER DROP
IMPACT DAMAGE FIELD

by

E. D. Case and A. G. Evans

Abstract

Expressions are presented for the inner radius of the crack damage field induced by water drop impact. The inner radius is expressed as a function of drop size, impact velocity and Rayleigh velocity of the target. Calculated and observed minimum radii agree well for a wide spectrum of impact conditions and target materials. Furthermore, this radius is independent of the laboratory technique used to induce the damage (water drop, water jet, and nylon bead techniques).

1. INTRODUCTION

Impact by high velocity water drops^{*} can produce annular damage fields consisting of hundreds of individual cracks (figure 1). The inner and outer radii of the damage field (labeled here as r_{\max} and r_{\min} , respectively), are thus two measures of the physical extent of the impact damage. The characterization of this damage is closely linked to the analysis of infrared transmittance losses suffered by IR windows (figure 2). For example, the optical and diffractive effects due to a given crack of simple geometry may be approximated by the solution of the electromagnetic wave equation, while multiple and non-linear interference effects can probably be determined by iterative numerical procedures already applied to ensembles of interacting electromagnetic scatterers (1). Such calculations presuppose that the scattering centers themselves (the impact cracks, in this case) have been adequately characterized. Consequently the strong link between crack characterization and transmittance calculations is established.

One step in the characterization of water-drop impact damage has been to show that an exponential distribution function of the form

$$f(n) = \lambda \exp[-\lambda n] \quad (1)$$

describes the crack number density for crack fields induced by water drop impact (2). A single value of the scaling parameter, λ_s , adequately

^{*}For the purposes of this paper, "high velocity" impact refers very roughly to the range between about 200 m/s and 100 m/s.

describes the radial crack number density distributions for several different materials (figure 3). Moreover, differences between the distributions observed for damage induced by two different laboratory impact techniques (the water drop and water jet techniques) are insignificant. The analysis entails mapping the actual inner and outer radii of the damage annulus (r_{\min} and r_{\max} , respectively), into a transformed coordinate system η , such that

$$\begin{aligned} r_{\min} &\rightarrow \eta_{\min} \\ r_{\max} &\rightarrow \eta_{\max} \end{aligned}$$

Consequently, to fully utilize the crack number density analysis, explicit functional forms are needed for the inverse mapping of η_{\min} and η_{\max} back into r_{\min} and r_{\max} , via material and drop parameters. The intent of this study is to develop a quasi-empirical expression for r_{\min} as a function of the velocity and diameter of the impacting drop, and the Rayleigh velocity of the target material. It will thereby be demonstrated for a set of 50 specimens (four different glasses, seven polycrystalline materials) and impacts via water drop, water jet and nylon bead techniques that calculated values of r_{\min} agree quite well with measured values.

2. EXPERIMENTAL PROCEDURE

The data encompass a wide spectrum of materials (table I) and impact conditions. For the 50 specimens, impact velocities and drop sizes

ranged from 240 ms^{-1} to $\sim 1000 \text{ ms}^{-1}$ and 1.6 mm to 4.5 mm, respectively. The corresponding r_{\min} span nearly an order of magnitude, from $\sim 0.1 \text{ mm}$ to $\sim 0.8 \text{ mm}$. While most of the specimens (39) were impacted via the water drop technique (3,4), seven specimens were impacted via water jet^{*} and four specimens were nylon bead impacted (3).

Table I Materials Investigated

Polycrystalline Materials:

| | |
|--|-----------------|
| ZnS | (31 specimens) |
| ZnSe | (2 specimens) |
| Si_3N_4 | (2 specimens) |
| MgF | (2 specimens) |
| $3(\text{Al}_2\text{O}_3)$ $2(\text{GeO}_2)$ | (one specimen) |
| $3(\text{Al}_2\text{O}_3)$ $2(\text{SiO}_2)$ | (one specimen) |
| CaLa_2S_4 | (two specimens) |

Glasses:

| | |
|--------------------|---------------|
| Germania glass | (2 specimens) |
| Borosilicate glass | (2 specimens) |
| Fused silica | (1 specimen) |
| Soda lime silica | (4 specimens) |

* These specimens were impacted by one of the authors (E. D. Case) at the water jet facilities of J.E. Field, Cavendish Laboratory, Cambridge, England.

Figure Captions

1. Optical micrographs of water jet impacted ZnS.
2. A Fourier Transform Infrared (FTIR) spectrograph showing the transmittance ratio $\tau_{\text{damaged}}/\tau_{\text{undamaged}}$ as a function of wavenumber for a 6.8 mm thick ZnSe specimen impacted by a water jet (having a 4.5 mm equivalent drop diameter) at 375 ms^{-1} .
3. Crack number density as a function of normalized distance, η . In each graph, the solid line indicates $f(\eta) = \lambda \exp(-\lambda \eta)$ and $\lambda = 0.349$.
4. A schematic of the water jet apparatus. A stainless steel nozzle containing a water filled chamber (sealed by a neoprene disk) is impacted by a pneumatically fired pellet. The water jet formed by the nozzle orifice then impacts the target.
5. The calculated r_{min} values versus the observed r_{min} values for 50 impacted specimens, including seven different polycrystalline materials and four glasses. The solid line is locus of points for which r_{min} calculated equals r_{min} observed.

13. E. D. Case and A. G. Evans, to be published.
14. R. W. Hertz, p. 386 in Fracture and Deformation of Engineering,
Second Edition, Wiley & Sons, New York, 1983.
15. S. van der Zwaag and J. E. Field, Eng. Fract. Mech. 17 (4), 367-379,
1983.

REFERENCES

1. S. Coen, Professor of Geophysics, University of California, Berkeley. Personal communication.
2. E. D. Case, K. M. Louie and A. G. Evans, J. Mater. Sci. Letters, in press.
3. W. F. Adler, Investigation of Liquid Drop Impacts on Ceramics, Final Report for Office of Naval Research, CR82-1075, 1982.
4. W. F. Adler, Technical Report to Naval Weapons Center, China Lake, CA, CR82-1096, 1982.
5. J. E. Field, D. A. Gorham, J. T. Hagan, M. J. Matthewson, M. V. Swain and S. Van der Zwaag, 13-1 to 13-11 in Proc. Fifth Int. Conf. on Erosion by Solid and Liquid Impact, Cavendish Laboratory, Cambridge, England, 1979.
6. J. E. Field, D. A. Gorham, and D. G. Rickerby, Proc. ASTM Conf. on Erosion, Vail Colorado, Oct. 1977, published 1979.
7. E. D. Case and A. G. Evans, unpublished data.
8. R. M. Blowers, J. Inst. Math. Appl. 5: 167-193, 1969.
9. M. Rosenblatt, G. E. Eggum, L. A. De Angelo, K. N. Kreyenhagen, Numerical Investigation of Water Drop Erosion Mechanisms in Infrared-Transparent Materials, AFML-TR-76-193, Final Report, 1976.
10. A. G. Evans, J. Appl. Phys. 49 (6), 3304, 1978.
11. I. A. Viktorov, Rayleigh and Lamb Waves, Plenum Press, New York, 1967.
12. L. B. Freund, J. Mech. Phys. Solids, 21, 47, 1973.

$$r = \frac{1}{\alpha} \ln \left[\frac{2\beta z v_o \sqrt{c}}{\sqrt{\pi} K_c a(r)} \right] + r_{\min} \quad (A5)$$

such that,

$$r_{\max} = \frac{1}{\alpha} \ln \left[\frac{2\beta z \sqrt{c} v_o}{\sqrt{\pi} K_c} \right] + r_{\min} \quad (A6)$$

Note that at the fracture threshold velocity, v_{ft} , r_{\max} must asymptotically approach r_{\min} , which in turn requires that

$$v_{ft} \approx \frac{\sqrt{\pi} K_c}{2\beta z \sqrt{c}} \quad (A7)$$

Appendix

For the calculation of r_{\max} , the maximum radius of the damage annulus, it is initially assumed that the acoustic waves of interest (the surface acoustic or, Rayleigh waves) attenuate according to

$$\sigma = \sigma_0 \exp(-\alpha[r-r_{\min}]) \quad (A1)$$

where σ_0 is the stress amplitude at r_{\min} and α is the surface acoustic wave attenuation coefficient. The mode I quasi-static stress intensity factor for the surface flaws at any stage during their propagation can then be written as (14)

$$\begin{aligned} K_I^S(r) &\equiv 1.12(2/\sqrt{\pi})\sigma(4)\sqrt{c} \\ &= 1.12(2/\sqrt{\pi})\sigma_0 \exp(-\alpha[r-r_{\min}]) \end{aligned} \quad (A2)$$

Solving for r gives

$$r = -1/\alpha \ln \left[\frac{\sqrt{\pi}K_c a(r)}{2\sigma_0\sqrt{c}} \right] + r_{\min} \quad (A3)$$

where $K_I^I(r) = a(r)K_c$, with K_c the fracture toughness. The function $a(r)$ is defined such that $a(r) = 1$ at $r = r_{\max}$ and $a(r) = a_0$ at $r = r_{\min}$. Using the approximation (8,15),

$$\sigma_0 = \beta v_0 Z$$

where Z is the drop acoustic impedance, and β is considered here to be a constant of order unity, then equation (A3) becomes

body, and the texturing within polycrystalline materials.

6. CONCLUSIONS

The analysis of r_{\max} (appendix) and r_{\min} data provides insight into the basic impact damage processes, as well as a data base allowing, for example, intercomparison of impact data and computer simulation of the damage processes (13). The minimum radius solution provides the basis for determining the inner dimension of the crack damage field, given the drop velocity, drop diameter, and the Rayleigh velocity of the target.

Furthermore, the analysis shows, as does the crack number density statistics (2), that at least to a first approximation^{*}, there is little difference in the r_{\min} values for the water drop, water jet, and nylon bead techniques. This similarity is encouraging, since it implies that less complicated laboratory techniques (namely water jet and nylon bead) may yield data similar to the more sophisticated water drop method.

The expression for r_{\max} links the crack damage equations to the initial flaw size statistics and to the surface wave attenuation coefficient, α .

where ϵ is the spatial interval (measured in the radial direction) that corresponds to a time interval τ between the appearance of the shear wave and the initiation of cracking. The temporal duration, t_0 , of the Rayleigh pulse at a given time t , is bounded by the difference between t and t_s , the time at which the Rayleigh pulse comes into existence (i.e., it separates from the contact zone). In the presence of incubation no cracking can occur until,

$$t - t_s \geq \tau \quad (13)$$

The expressions involved in determining ϵ depend on whether lateral jetting occurs at the time the shear or Rayleigh pulse separates from the contact zone. Analytical expressions for ϵ are now being developed.

The present method of calculating r_{\min} does not require data on the fracture threshold velocity for a given material, microstructural parameters such as grain size or porosity, or flaw statistics. Thus, r_{\min} is a relatively weak function of microstructure and flaw statistics. However, it does not necessarily follow that the entire damage process is insensitive to these parameters. The outer radius of the damage annulus, r_{\max} , embodies both flaw statistics and microstructural considerations (appendix). For example, at radial distances $r > r_{\min}$, the stress (and hence the stress intensity factor K) is a function of the surface acoustic wave attenuation coefficient, α . The coefficient α is in turn a function of such microstructural characteristics as the surface roughness, the size-dependent scattering from grains in a polycrystalline

where g can be any one of the three vectors v_o , d , or c_R , and where n is the number of specimens (50 in this case), U_{nc} is a measure of the empirical uncertainty involved in measuring g , and $N(0,1)$ is the normal random deviate (with zero mean and a variance of unity). After each datum has been perturbed by adding an "error" term $U_{nc}N(0,1)$, equation 10 is re-evaluated. The resulting calculated value, from the perturbed or "noisy" data is termed \tilde{r}' . The error \tilde{e} simulated by this computer experiment is then calculated using

$$\tilde{e} = \frac{\tilde{r}' - \tilde{r}}{\tilde{r}} \quad (11)$$

Equating the uncertainties in v_o , c_R and d listed in equation 8 with the standard deviation of the corresponding measured parameters, gives errors \tilde{e} very similar in magnitude and distribution to the actual errors e (Table 2).

Thus, based on two error estimates, the magnitude of the errors in the r_{min} computation are in reasonable agreement with errors arising from the uncertainties in the data.

5. DISCUSSION

The hypothesis that r_{min} is determined by the Rayleigh wave separation process ignores the existence of an incubation time, τ , for cracks induced by a stress transient (10,12). A simple generalization for equation 4 that allows for incubation has the form,

$$r_{min} = r_s + \epsilon \quad (12)$$

Thus, the maximum uncertainties in r_{\min} , v_o , d and c_R are, for the purposes of this calculation, assumed to be 10%, 2%, 2% and 10% , respectively. The uncertainties in c_R arise from at least three sources: the often imprecise measurement of Poisson's ratio, ν , the assumption of elastic isotropy (upon which equation 6 is based), and errors in the measurement of the Young's modulus E .^{*} Specifically, for materials having preferential grain orientation, such as the numerous CVD ZnS and ZnSe specimens included in this study, the appropriate surface plane values of Young's modulus and Poisson's ratio are not available (only the bulk aggregate values exist). An error level on c_R of 10% may thus be optimistic in such cases. Given the error bounds presented in equation 9, equation 8 estimates an upper bound error in the calculated r_{\min} of $\pm 22\%$.

While the propagation of error estimation only bounds the error, the following computer experiment can give a rough estimate of the distribution of the errors. Initially, it is presumed that equation 5 and the v_o , d , and c_R data are exact (no experimental error). Then r is calculated from equation 5. For the purposes of the computer experiment, r is considered an exact value. Each datum vector is then "perturbed" according to the general relation

$$g_i \rightarrow g_i + U_{nc} N(0,1) \quad i = 1,2,3 \dots, n \quad (10)$$

^{*}The uncertainties in the density, ρ , should be negligible in most cases when compared to the other uncertainties in determining c_R .

impact specimens.*

The detailed assessment of the present hypothesis for calculating r_{\min} depends on whether the observed errors (Table 1) fall within the range of errors that result directly from uncertainties in the data. Errors introduced by the experimental uncertainties in v_c , c_R , and r_{\min} data values are calculated via two estimation techniques. First, a simple propagation of error estimates is considered, and then a computer "experiment" is employed to estimate the distribution of the relative errors.

A propagation of error estimate determines an upper bound for the absolute value of error, estimated from the total differential $\Delta f(x,y,z)$ for the multivariate function $f(x,y,z)$ using

$$\Delta f(x,y,z) = \left| \frac{\partial f}{\partial x} \right| \Delta x + \left| \frac{\partial f}{\partial y} \right| \Delta y + \left| \frac{\partial f}{\partial z} \right| \Delta z \quad (8)$$

where Δx , Δy , and Δz are estimates of the error bounds on the variables x , y , and z , respectively. The individual errors (that is, the experimental uncertainties) Δx , Δy , and Δz , are assumed to be uncorrelated. The bounds assumed for the uncertainties in each of the data vectors are:

$$r_{\min} = 0.1 r_{\min}$$

$$v_o = 0.02 v_o$$

$$d = 0.02d$$

$$c_R = 0.10 c_R$$

* Adler formed the nylon beads used in his experimentation from nylon resin supplied by Rilsan Corporation, Glenbrook, New Jersey (3).

where r_{obs} is the observed value of r_{min} and r_{cal} the value of r_{min} calculated from equation 5. The maximum and minimum relative errors determined in this manner are 0.231 and -0.239, respectively. The distribution of the absolute value of relative error, $|e|$, shows that more than half of the calculated r_{min} agree with the observed values to within $\pm 10\%$. For 43 specimens (86% of the total), the calculated and observed values agree to within $\pm 20\%$. Note that for the entire set of 50 specimens, none of the errors exceeded 25% (Table II).

Although the data represent three different laboratory impact testing techniques (water jet, water drop, and nylon bead), there are no systematic differences in the magnitude of the errors with respect to the three techniques. For example, errors for the four nylon-bead impacted ZnS specimens are all less than $\pm 10\%$, while the errors for the three water jet impacted polycrystalline specimens (two Si_3N_4 specimens and one ZnSe specimen) ranged from $\pm 5\%$ for the Si_3N_4 specimens to 20% for the ZnSe specimen. Four water jet impacted soda lime silica glass specimens show a maximum relative error of about 6%. Thus, both the nylon bead and water jet data seem to display the same r_{min} trend as that observed using the water drop technique. No attempt was made to normalize the nylon bead data to account for the differences in density (and, presumably, the sonic velocity) between nylon and water. The diameter and velocity of the nylon bead used for the calculation of r_{min} are the experimental values recorded by Adler (3). The agreement between the nylon bead and water drop data presumably stem from a near equivalence in the acoustic impedance of water and the particular nylon Adler employed for his

fitting procedure. Consequently, if the exponents of v_o , d , and c_R are allowed to be different than unity, the least-squares procedure yields

$$r_{\min} = \frac{A v_o^{n_1} d^{n_2}}{c_R^{n_3}} \quad (5)$$

where exponents n_1 , n_2 , and n_3 have the values $n_1 = 0.753$, $n_2 = 1.662$, $n_3 = 0.512$ and the constant $A = 2.78 \text{ sec}^{0.24}/\text{m}^{0.90}$. The present data set includes impact damage information wherein v_o , d and r_{\min} are measured values, and Rayleigh velocity c_R is calculated from the expression

$$c_R = \left[\frac{0.87 + 1.12\nu}{1+\nu} \right] \left[\frac{E}{2\rho(1+\nu)} \right]^{1/2} \quad (6)$$

where ν , E and ρ are, respectively, the Poisson's ratio, Young's modulus and density of the target (4).

4. RESULTS

4.1 The Minimum Radius, r_{\min}

The relation between the observed r_{\min} and that calculated from eqn (5) is plotted in fig. 5. Evidently in view of the differing materials, impact conditions, and impact techniques encompassed by the data, the Rayleigh wave separation hypothesis provides a surprisingly good model for determining r_{\min} . However, further insight is provided by conducting a detailed error analysis.

The relative error, e , in the r_{\min} calculations, is defined as

$$e = \frac{(r_{\text{obs}} - r_{\text{cal}})}{r_{\text{obs}}} \quad (7)$$

nondimensional spatial coordinate R and temporal coordinate T (8,10) by

$$R = \frac{4c_i r}{k^2} \quad (2)$$

$$T = 4c_i^2 t / k^2$$

where $k^2 \sim dv_0$, and c_i is one of the acoustic wave velocities (longitudinal, shear, or Rayleigh), v_0 is the impact velocity, d is the drop diameter and r and t are respectively, the radial distance along the sample surface and the time after impact. Furthermore, Blowers (8) shows that

$$R = \begin{cases} 2\sqrt{T} & T \leq 1 \\ T + 1 & T \geq 1 \end{cases} \quad (3)$$

where $T = 1$ (or, thus, $R = 2$) gives the temporal (and spatial) coordinates for the separation of the contact zone from the acoustic wave of velocity C_i . The radial distance r_s , at which the Rayleigh wave separates from the contact zone is thus obtained from eqns (2) and (3) as,

$$r_s \equiv \frac{R' v_0 d}{4c_R} = \frac{v_0 d}{2c_R} \quad (4)$$

where $R' = R$ evaluated at $r = r_s$. By assuming that the first cracks appear as the Rayleigh wave separates from the contact zone, such that $r_s = r_{\min}$, equation 4 can be used as a trial function for the least-squares

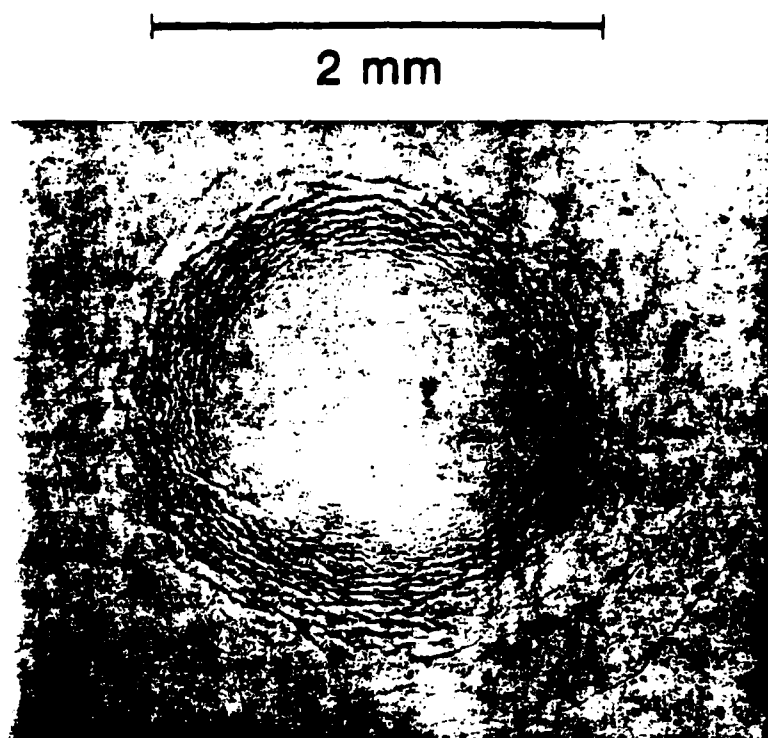
The water jet impact procedure involves firing a lead pellet into a stainless steel nozzle containing a water filled chamber (figure 4). A neoprene disk seals the water chamber in the rear of the nozzle, and a small orifice* in the nozzle front forms the jet as the water is ejected. The water then impacts the target material, held about 1 cm away from the nozzle orifice. Ideally, the jet has a hemispherical front surface (5, 6), leading to a damage similar in several aspects to damage induced by spherical drops (7). Details of the water drop and nylon bead impact techniques are given by Adler (3).

3. THEORETICAL CONSIDERATIONS

When a water drop impacts a surface, initially the velocity of the spreading contact zone exceeds the local sound velocity (8). As the contact zone expands, the Rayleigh and shear waves separate from the leading edge of the contact zone. A two-dimensional Lagrangian finite difference model by Rosenblatt, Eggum, De Angelo and Kreyenhagen (9) shows that tensile cracks due to water drop impact propagate in the vicinity of the shear wave front. The lateral distance at which the sonic waves separate from the contact zone thus appears as a plausible estimate of r_{\min} . This distance can be expressed in terms of the

*The orifice diameter determines the "equivalent spherical diameter" of the jet. For example, an orifice of ~ 0.8 mm produces a water jet that produces impact damage roughly equivalent to the damage caused by a 4.5 mm diameter spherical drop (6).

Fig. 1



ZnS water jet impact
Impact velocity = 350 m/sec
Equivalent drop diameter = 4.5 mm

Fig. 2

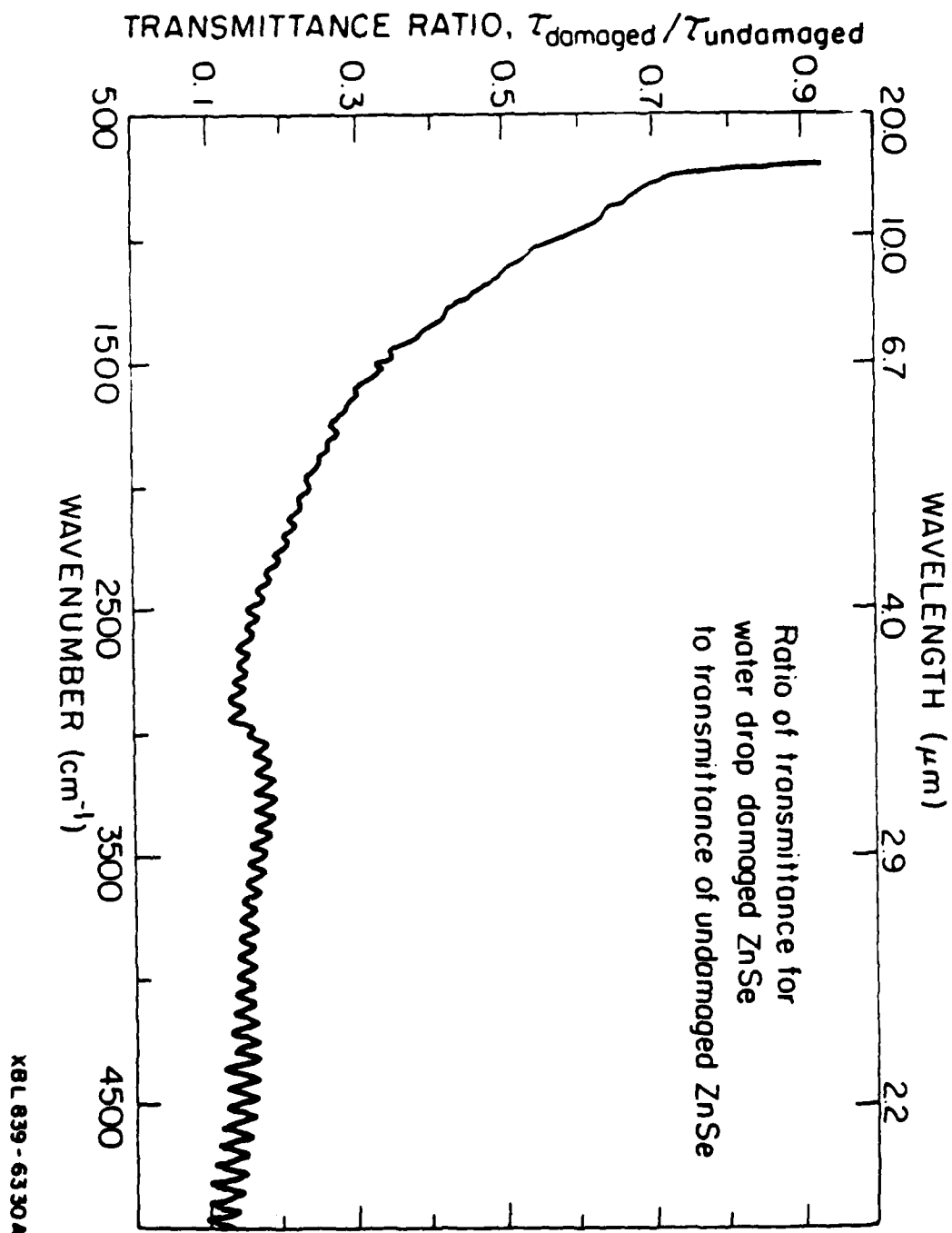
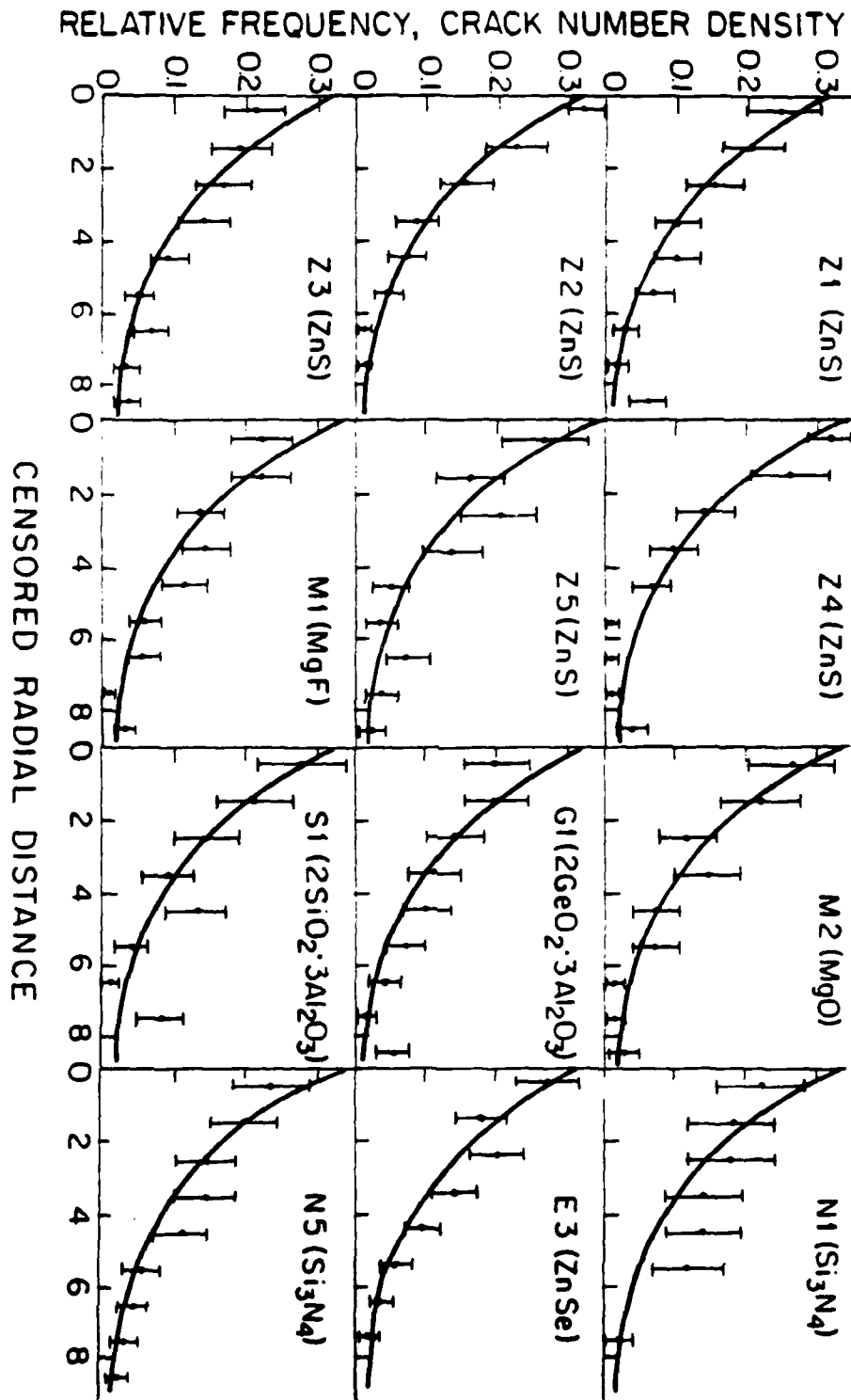


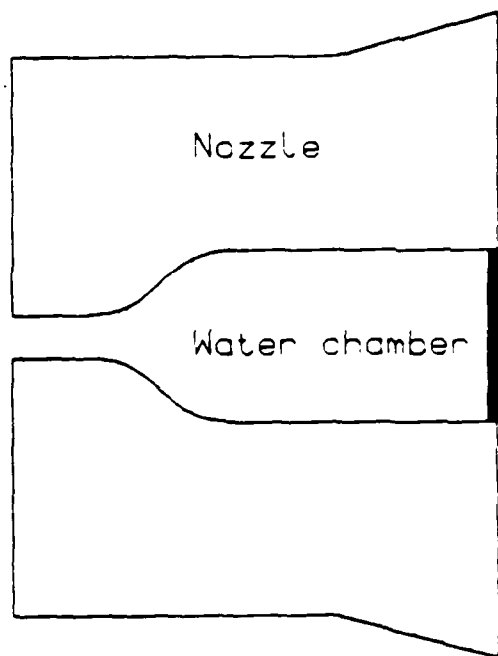
Fig. 3



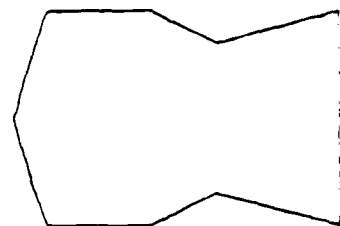
XRL 839-6327A

Fig. 4

Target

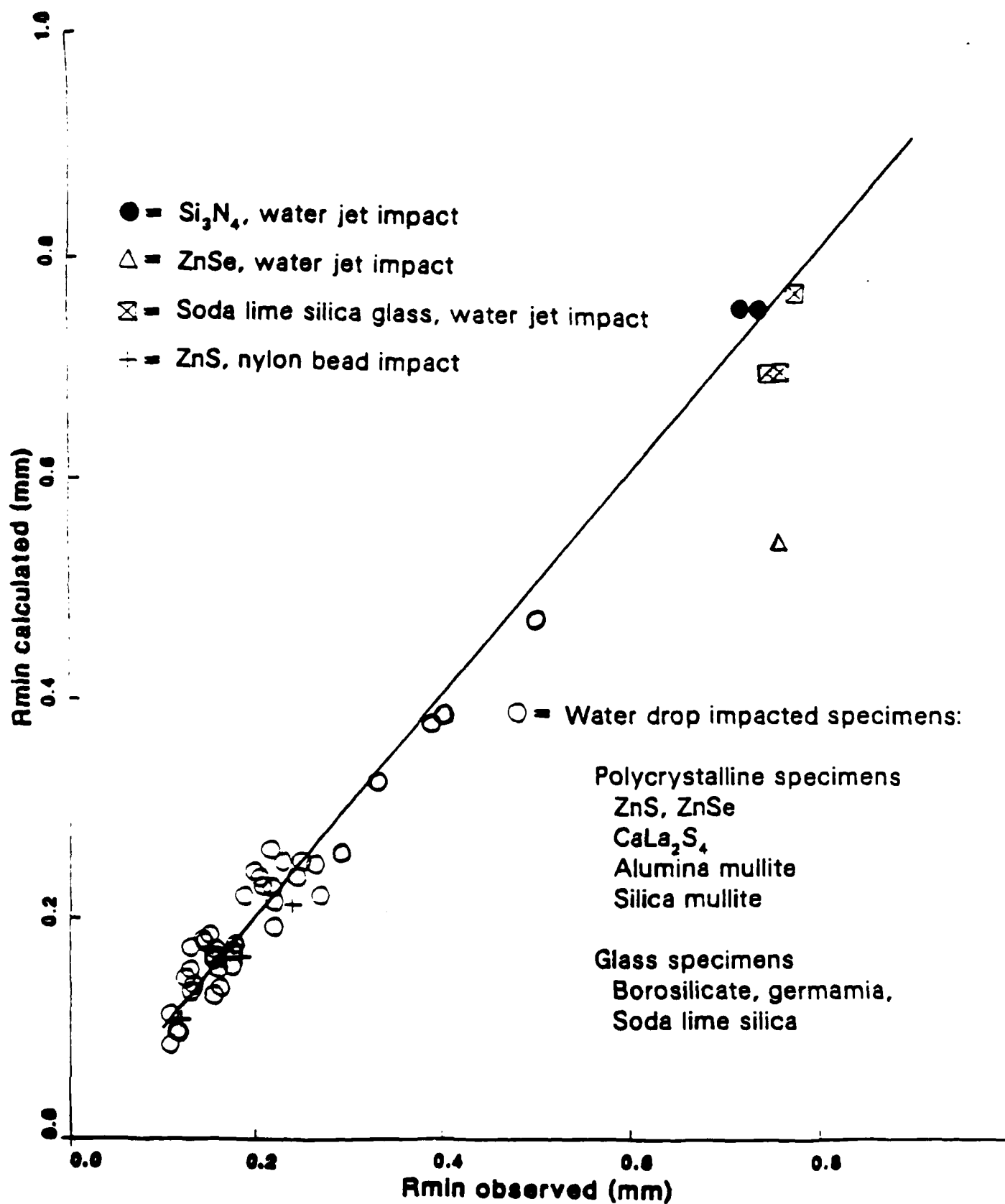


Neoprene disk



Pellet

Fig. 5



END

FILMED

4-85

DTIC